

Linking simple molecules to grain evolution across
planet-forming disks.

Linking simple molecules to grain evolution across planet-forming disks.

Proefschrift

ter verkrijging van
de graad van Doctor aan de Universiteit Leiden,
op gezag van Rector Magnificus prof. mr. C.J.J.M. Stolker
volgens besluit van het College voor Promoties
te verdedigen op maandag 18 december 2017
klokke 10:00 uur

door

Vachail Nicolás Salinas Poblete

geboren te Santiago, Chile
in 1990

Promotiecommissie

Promotores:	Prof. dr.E.F. van Dishoeck	
	Prof. dr. M.R. Hogerheijde	
Overige leden:	Prof. dr. Y. Aikawa	Univeristy of Tokyo
	Prof. dr. T.J. Millar	Queen's University Belfast
	Dr. C. Walsh	University of Leeds
	Prof. dr. I.A.G. Snellen	
	Prof. dr. H.J.A. Röttgering	

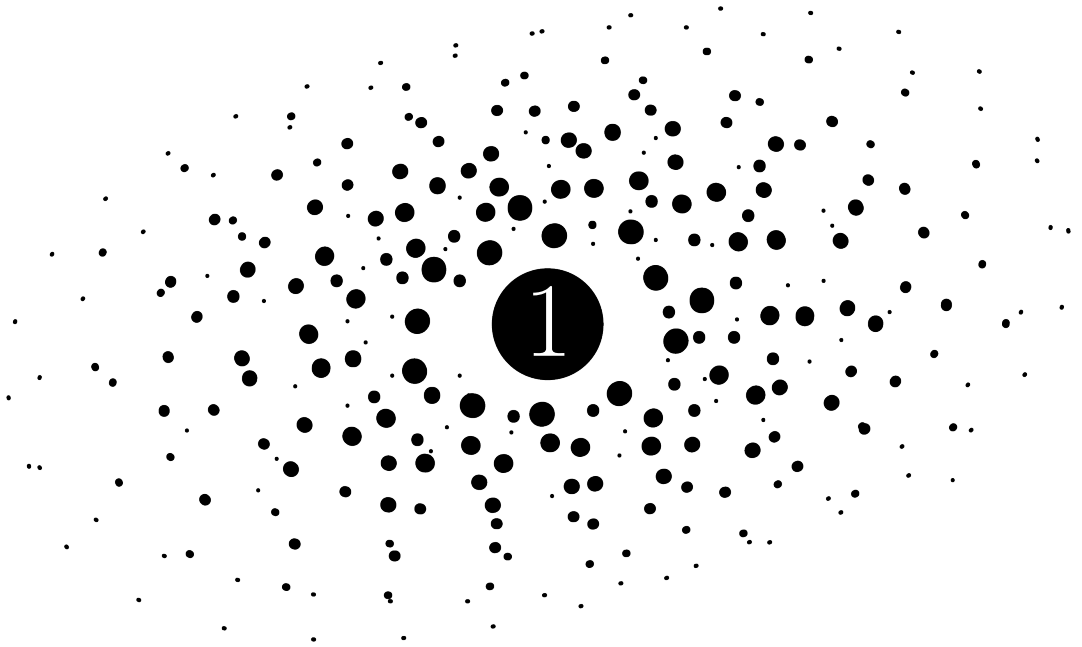
*To my beloved mother,
whose passion for the universe ignited my curiosity.*

Contents

1 Introduction	1
1.1 Disk formation	2
1.1.1 Collapse phase	2
1.1.2 Embedded phase	3
1.1.3 Observational characterization	3
1.2 Physical properties of protoplanetary disks	4
1.2.1 Mass	4
1.2.2 Radial structure	6
1.2.3 Vertical structure	7
1.2.4 Temperature structure	7
1.2.5 Ultraviolet and X-Ray radiation	8
1.3 Disk evolution	9
1.3.1 What happens to the gas?	9
1.3.2 What happens to the dust?	9
1.4 Dust in disks	11
1.4.1 Composition	11
1.4.2 Radial drift	11
1.4.3 Settling	12
1.4.4 Mixing	13
1.5 Disk chemistry	13
1.5.1 Material inventory	15
1.5.2 Water	17
1.5.3 Ammonia	17
1.5.4 Deuterium chemistry in Disks	18
1.6 Methods	20
1.6.1 Observations	20
1.6.2 Modeling	22
1.7 This thesis	23
1.7.1 Aim	23
1.7.2 Overall conclusions	25
1.7.3 Future outlook	25
2 Steepening of the 820 μm continuum surface brightness profile signals dust evolution in TW Hya's disk	35
2.1 Introduction	36
2.2 Observations and data reduction	37
2.3 Model fitting	40
2.4 Discussion	42

2.4.1	Dust drift	42
2.4.2	The presence of unseen gaps	43
2.4.3	Dust temperature and the CO snow line	44
2.5	Summary	44
2.A	Results of the emcee model fitting	47
3	First detection of gas-phase ammonia in a planet-forming disk	49
3.1	Introduction	50
3.2	Observations	51
3.3	Modeling approach	51
3.3.1	Physical structure	51
3.3.2	Chemical model	54
3.3.3	Line excitation and radiative transfer	55
3.4	Results	57
3.5	Discussion	60
3.5.1	Ice reservoirs and total gass masses	60
3.5.2	Gas-phase chemistry	60
3.5.3	Collisions of large bodies as a production mechanism	61
3.6	Conclusions	62
4	Comparing detections and upper limits of NH₃ and NH₂D in the disks of TW Hya and HD163296	65
4.1	Introduction	66
4.2	Observations	67
4.3	Modeling Approach	68
4.3.1	Physical structure	68
4.3.2	Parametric abundance models	71
4.3.3	Line excitation and radiative transfer	71
4.4	Results	73
4.5	Discussion	73
4.5.1	Total gass masses and deuteration estimates	73
4.5.2	ALMA predictions	75
4.6	Summary & Conclusions	76
5	DCO⁺, DCN, and N₂D⁺ reveal three different deuteration regimes in the disk around the Herbig Ae star HD163296	81
5.1	Introduction	82
5.2	Observations	82
5.3	Results	83
5.3.1	Detections	83
5.3.2	Column densities and deuterium fractionation	86
5.4	Parametric modeling	87
5.4.1	Deuterium chemistry	87
5.4.2	Motivation	88
5.4.3	Physical model	88
5.4.4	N ₂ D ⁺ , DCN, and DCO ⁺ abundance models	90
5.4.5	Line excitation	90
5.4.6	Abundance estimates	91
5.4.7	Best-fit parameters	91
5.5	Discussion	94

5.5.1	The inner depression	94
5.5.2	Limitation of DCO ⁺ as a CO snowline tracer	94
5.5.3	The origin of the third ring	95
5.5.4	Deuterium fractionation	95
5.6	Summary	96
5.A	Keplerian Masking	97
6	Exploring DCO⁺ as a tracer of thermal inversion in the disk around the Herbig Ae star HD163296	101
6.1	Introduction	102
6.2	Methods	103
6.2.1	Previous observation of HD 163296	103
6.2.2	Chemical model	104
6.2.3	Implementation	105
6.2.4	Radiative transfer	106
6.3	Results	107
6.3.1	Standard model (CD)	107
6.3.2	Thermal inversion model (CD+TI)	108
6.3.3	The CD+WD+TI model	110
6.4	Discussion	110
6.4.1	DCO ⁺ Outer radius	110
6.4.2	Low vs high temperature deuteration pathways	113
6.5	Summary	113
6.A	Residual channel maps	114
	Samenvatting	117
	English Summary	121
	Resumen en Español	125
	Curriculum Vitae	129
	Acknowledgments	131



Introduction

Our very existence as sentient beings has prompted us to question our place in the Universe. Ancient transcendental questions have found their way into astronomy in the following forms: What are the conditions for life? How did our Solar System form? How did the Earth form? How do other planets form? What sets the chemical composition and the ingredients for life throughout the star and planet formation process? The very first attempt to understand the formation of our Solar System was made by the French mathematician and philosopher René Descartes in his book 'Traité du monde et de la lumière'. His publication was delayed several years, feared by the Roman Inquisition because of its heliocentric view of the Universe, but was finally made available post-mortem in 1664. His theory comprised of colliding corpuscular particles in space, constantly swirling around in a continuous fashion with no vacuum inbetween. The continuous nature of his colliding particles provided the necessary force for the movement of planets around the Sun. Although incorrect, his work paved the way for the generally accepted Nebular Hypothesis, formulated first by Emanuel Swedenborg and expanded by Immanuel Kant in 1755 and (independently) by Pierre-Simon Laplace in 1796. This hypothesis consisted of a gaseous cloud of matter slowly collapsing and rotating, eventually becoming flat due to gravity, culminating in the formation of the Sun and planets.

Two more centuries had to pass until the first empirical evidence supporting this theory was discovered. Low-mass T Tauri stars (Herbig 1977) and other young objects (Cohen & Kuhl 1979) were first observed in the infrared (IR) and optical regimes. The observed IR excess could only come from material at much lower temperatures than the star. A major breakthrough came a decade later when the InfraRed Astronomical Satellite (IRAS) detected the first circumstellar disk around Vega. Although this is a rather old disk, many other young objects were found to harbor circumstellar disks through subsequent surveys by IRAS, ISO, the *Hubble Space Telescope* and the *Spitzer Space Telescope* in many star formation regions.

The next decade brought the discovery of the first planet orbiting a star other than the Sun, 51 Pegasi (Mayor & Queloz 1995). In the last two decades more than 3000 exoplanets, and about 2000 more candidates, have been found. Now that we are certain of the existence of exoplanets, and that most of the young stellar objects (YSOs) contain circumstellar material, the scientific community has been trying to understand the processes involved in the formation of planets. The study of so-called protoplanetary disks aims to explain the missing link between star formation and planet formation and the composition of other planetary systems as well as our own Solar System's history. This thesis will focus on understanding the processes that shape the distributions of key molecular species, such as water and ammonia, and simple deuterated species, by contrasting them with the spatial structures produced by dust evolution, photo-processes and gas-phase chemistry.

1.1 Disk formation

1.1.1 Collapse phase

The first step toward understanding the formation of planets is understanding the formation of circumstellar disks. The star formation process starts with a gravitationally unstable molecular cloud that collapses first onto a hydro-static core due to gravity (Ebert 1955; Bonnor 1956; Jeans 1902). A rotationally supported disk quickly forms within 10^4 yrs (Yorke et al. 1993; Hueso & Guillot 2005) as more distant material, with higher angular momentum, falls in (Figure 1.1). At this stage, the newly formed disk is fully embedded in an envelope of gas and dust. The rotation of the envelope has been measured up to scales

of ~ 0.1 pc (Goodman et al. 1993), with typical rotation rates of 10^{-15} – 10^{-12} Hz (Burkert & Bodenheimer 2000; Dib et al. 2010). Infall models were first used by Ulrich (1976) to describe the continuum and line-emission features of T Tauri disks. The viscous accretion disk theory (Lynden-Bell & Pringle 1974; Shakura et al. 1978) was later used to derive a formalism of the radial structure of disks in the context of star formation considering conservation of mass, momentum and energy (Cameron 1978; Cassen & Moosman 1981; Terebey et al. 1984)

Molecular clouds have typical specific angular momenta of $\sim 10^{21-22}$ cm² s⁻¹ (Goodman et al. 1993), which is 6-7 orders of magnitude higher than that of the Sun (Pinto et al. 2011). The removal of the angular momentum can be achieved through winds and jets or through viscous accretion. The disk viscosity is mainly dominated by the mixing of fluid elements. Several processes, such as magnetorotational instability (MRI), have been proposed as the dominating mechanisms driving the viscous transport through the disk (for a review, see Armitage 2011). The efficiency of the MRI depends on the degree of ionization because it requires the gas and the magnetic field to be well coupled. However, protoplanetary disks are only weakly ionized. Moreover, MRI is damped or suppressed by non-ideal magnetohydrodynamical effects and a magnetized disk wind has been recently suggested as the primary mechanism driving disk accretion (Bai 2016, and references therein). It is important to notice that magnetic fields could also dissipate angular momentum at large scales, since the beginning of the collapsing phase, through twisted magnetic field lines (Königl & Salmeron 2011) but the efficiency of this process is not clear. The wide range of initial angular momenta and variations in the infall duration give birth to disks that are different in size and mass (Terebey et al. 1984).

1.1.2 Embedded phase

The embedded phase typically lasts ~ 0.5 Myr (Evans et al. 2009; Carney et al. 2016). Infall describes the trajectory of material from the envelope to the disk while the material of the disk is slowly accreted onto the protostar. The disk is heated through both the infall process and the accretion. The accretion rate of material being transported into the protostar is crucial to determine the dust temperature structure of the disk and the inner envelope at this stage. This process is probably episodic to avoid the luminosity problem (see Kenyon & Hartmann 1990; Evans et al. 2009; Dunham et al. 2014). This problem concerns the discrepancy between the observed low luminosity of embedded objects and the higher luminosity predicted by accretion at a constant rate. Episodic accretion models can transfer sufficient mass to the central star without requiring sustained accretion rates larger than observed. The material of the core's envelope is gradually dispersed through outflows and jets or accreted on the disk. Eventually, the outflows produce a cavity in the envelope that grows to leave a disk behind (see work by Velusamy & Langer 1998; Arce & Sargent 2004, 2006; Salter 2010; Harsono 2014).

1.1.3 Observational characterization

The protostellar stages leave distinctive observational features that can be used to classify them. The first method proposed by Lada (1987) classifies YSOs into three different classes (I-II-III see Table 1.1) by measuring the slope of the spectral energy distribution (SED) in the mid-IR. This classification was later expanded to include a class 0 as new instruments were able to detect weaker (sub)millimeter emission of more deeply embedded objects (André et al. 1993).

Table 1.1: Classification of young stellar objects, taken from Williams & Cieza (2011).

Class	Physical properties	Observational characteristics
0	$M_{\text{env}} > M_{\text{star}} > M_{\text{disk}}$	No optical or near-IR emission
I	$M_{\text{star}} > M_{\text{env}} \sim M_{\text{disk}}$	Generally optically obscured
II	$M_{\text{disk}}/M_{\text{star}} \sim 1\%$, $M_{\text{env}} \sim 0$	Accreting disk; strong $\text{H}\alpha$ and UV
III	$M_{\text{disk}}/M_{\text{star}} \ll 1\%$, $M_{\text{env}} \sim 0$	Passive disk; no or very weak accretion

1.2 Physical properties of protoplanetary disks

After the end of Class I the disk is no longer embedded and the disk mass is only a small fraction of the stellar mass. The beginning of Class II marks the end of the star formation phase and the circumstellar disk can be considered truly planet forming and not protostellar. Protoplanetary disks have a rich and complex physical structure. This section describes the quantities that characterize planet-forming disks.

1.2.1 Mass

Traditionally, disk masses have been determined from the thermal emission of the dust, and multiplied by an assumed gas-to-dust mass ratio of 100. The (sub)millimeter emission arises from the thermal emission of the dust particles. As a rule of thumb, observations at a wavelength λ are only sensitive to the properties of dust grains of a maximum size $a_{\text{max}} \sim 3\lambda$ (Draine 2006). The dust dominates the opacity (κ_{ν}) at (sub)millimeter wavelengths and we can express the dependency of its emission on the frequency as a power law $\kappa_{\nu} \propto \nu^{\beta}$. A commonly used prescription for the dust opacity is given by Beckwith et al. (1990) and Hildebrand (1983),

$$\kappa_{\nu} = 0.1 \left(\frac{\nu}{10\text{MHz}} \right)^{\beta} \text{ cm}^2 \text{ g}^{-1}. \quad (1.1)$$

In the Rayleigh-Jeans limit, the spectral index α is related to the opacity index β by the following expression

$$\alpha = 2 + \beta. \quad (1.2)$$

The typical value for the opacity index of interstellar dust material is $\beta_{\text{ISM}} \sim 1.7$. A power-law dust size distribution of the form $n(a) \propto a^{-3.5}$ (Mathis et al. 1977) that has experienced grain growth, up to a maximum particle size of $a_{\text{max}} = 1 \text{ mm}$, results in $\beta \lesssim 1$. We can then

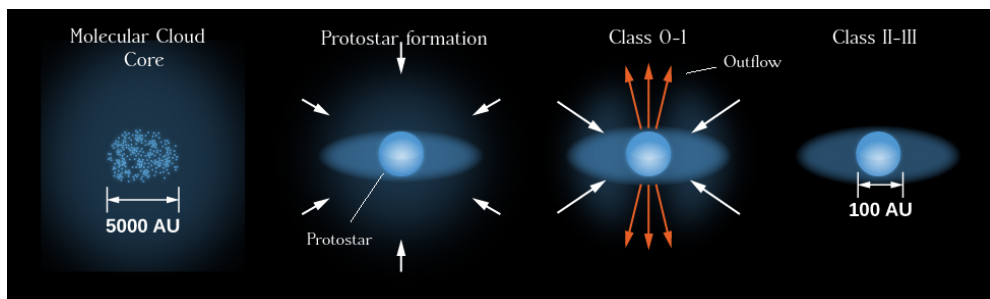


Figure 1.1: Cartoon showing the star and disk formation process. Adapted from LibreText Physics: Astronomy and Cosmology Textmaps:21.1 Star Formation (<https://phys.libretexts.org/>).

use Eq.1.2 for the spectral index as a diagnostic of grain growth at millimeter wavelengths. Continuum observations at multiple wavelengths are required for the extraction of the α parameter.

If we assume that most of the emission arises from optically thin material in the (sub)mm regime, a useful expression can be derived to calculate the disk mass by assuming a characteristic temperature T_c (Williams & Cieza 2011)

$$M(\text{gas} + \text{dust}) = \frac{F_\nu d^2}{\kappa_\nu B_\nu(T_c)}, \quad (1.3)$$

where d is the distance to the source, B_ν is the Planck function, F_ν the millimeter flux and κ_ν is the mass opacity that assumes a given gas-to-dust ratio. Detailed modelling of the mid-IR SED of disks towards the Ophiuchus region carried by Andrews & Williams (2005) showed that Eq. 1.3 is indeed a good approximation.

A number of caveats have to be taken into consideration when using Eq.1.3 to determine the disk mass. First, a large portion of the disk mass could be hidden in grains larger than a centimeter. The millimeter emission is not sensitive to this grain population. For the power-law grain size distribution given above, the total mass scales as $a_{\text{max}}^{1/2}$. Second the opacity index β depends on the size distribution of the dust particles (Ossenkopf & Henning 1994; Pollack et al. 1994; D'Alessio et al. 2001). As discussed above dust evolution processes, such as grain growth, can significantly change the opacity κ_ν at the (sub)millimeter regime. Finally, this method indirectly assumes a gas-to-dust ratio, canonically taken to be equal to the ISM value of 100; an assumption that might not hold for evolved disks. Disk masses derived from accretion rates and disk life-times are in the range of 0.01-0.2 M_\odot (Hartmann et al. 1998) while the inferred disk masses in Taurus from continuum observations using a gas-to-dust ratio of 100 show a median value of $5 \times 10^{-3} M_\odot$ (Andrews & Williams 2005).

Observing more direct gas tracers, such as CO, can constrain the disk mass without the assumption of a gas-to-dust ratio. Disk masses derived from less abundant CO isotopologues, that are optically thin, toward a sample of T Tauri disks are on average below the Minimum Mass Solar Nebula (MMSN) of $10^{-2} M_\odot$ (Williams & Best 2014) and their average gas-to-dust ratio of 16 is 6 times lower than in the ISM. The observations of other planetary systems suggest that disk masses larger than the ones derived by these methods are required to form many of the extrasolar planet systems (Greaves & Rice 2010; Mordasini et al. 2012). Although these results do not depend on an assumed gas-to-dust ratio they do depend on the assumed relative abundance of the CO and its isotopologues to H_2 (Miotello et al. 2016). A correct determination of the disk mass is essential to determine the potential of a protoplanetary disk to form planets. Recently HD, whose abundance is more directly correlated to that of H_2 , has been used to constrain the mass of the disk around TW Hya (Bergin et al. 2013). Unfortunately the emission of HD lines is usually weak, cannot be observed from the ground and is only sensitive to warm gas.

Observations in the (sub)millimeter regime of disks around Class II YSOs show a positive correlation between disk mass and stellar mass (Natta et al. 2000; Andrews et al. 2009; Lee et al. 2011; Andrews et al. 2013; Williams et al. 2013; Ansdell et al. 2015, 2016, 2017). This behavior is expected since higher mass stars require more material to pass through the disk. For more massive stars this correlation breaks down. The Orion proplyd survey (Mann & Williams 2009) constrains this relation to $M_{\text{disk}}/M_{\text{star}} \lesssim 10^{-4}$ for stellar masses $> 2M_\odot$. No signature of (sub)millimeter emission has been detected around optically visible O stars. This could be due to very high photoevaporation rates or to a totally different star-formation mechanism (Zinnecker & Yorke 2007). Environmental influences, such as dynamical disruption in binaries or by another passing star (Pfalzner et al. 2005a,b; Thies

et al. 2010) or photoevaporation by massive stars (Bally et al. 2000; Adams et al. 2004) can influence the size and mass of the disk.

1.2.2 Radial structure

The radial distribution of the mass of the disk can be described through its surface density $\Sigma(r)$, defined as

$$\Sigma(r) = \int_{-\infty}^{\infty} \rho(r, z) dz, \quad (1.4)$$

where ρ is the density of the disk in cylindrical coordinates. We can derive an analytical expression of $\Sigma(r)$ by looking at the radial component of the viscous accretion model of Shakura et al. (1978),

$$\frac{\partial \Sigma}{\partial t} + \frac{1}{r} \frac{\partial (\Sigma r v_r)}{\partial r} = 0, \quad (1.5)$$

$$v_r = -\frac{3}{\Sigma \sqrt{r}} \frac{\partial}{\partial r} (\Sigma v \sqrt{r}), \quad (1.6)$$

$$v = \alpha \frac{c_s^2}{\Omega_K} \quad (1.7)$$

where Eqs. 1.5, 1.6, 1.7 are obtained by integrating the continuity, radial momentum and tangential momentum equation over z respectively, v_r is the radial component of the velocity, Ω_K is the Keplerian angular velocity, α is a dimensionless parameter characterizing the turbulence of the disk and the speed of sound c_s is a function of the temperature of the disk. A constant $\alpha \sim 0.01$ reproduces the observed disk evolution and physical structure of protoplanetary disks (Hartmann et al. 1998; Hughes et al. 2011). If we take as ansatz that both the surface density and the temperature are power-laws of the form $\Sigma(r) \propto r^{-p}$ and $T(r) \propto r^{-q}$ respectively the solution for the steady-state of Eq. 1.5 is $\Sigma(r) \propto r^{q-3/2}$. The temperature power-law index q is equal to $3/4$ considering only viscous heating, but flattens to $q = 1/2$ at larger radii where the temperature profile is dominated by stellar irradiation (see Sec. 1.2.4). This leads to a radial distribution of the mass of the disk with power-law indexes ranging from $p \sim 1 - 3/4$.

Resolved millimeter observations of disks allow to constrain the radial distribution of the dust material. The radial extent of the disk is difficult to constrain since it emits faintly due to low temperatures and column densities in the outer regions. In the optical regime the outer parts of the disk can be seen in absorption. The *Hubble Space Telescope* found that on average disk sizes toward the Orion region are ~ 75 AU (Vicente & Alves 2005). Until recently most of the disks were modeled as pure power-laws but observations of CO and the millimeter continuum are difficult to reconcile with such a simple treatment. CO observations are consistently more extended than the continuum emission at millimeter wavelengths (Piétu et al. 2005; Isella et al. 2007; Panić et al. 2009; Isella et al. 2016) and a sharp cut-off of the surface density power-law is unable to explain both observations without relying on changing the gas-to-dust ratio or dust opacity at the edge of the continuum emission. An exponential taper at a characteristic radius R_c was needed to explain this behavior (McCaughrean & O'dell 1996; Hughes et al. 2008) of the form

$$\Sigma(r) = (2 - \gamma) \frac{M_d}{2\pi R_c^2} \left(\frac{r}{R_c} \right)^{-\gamma} \exp \left[- \left(\frac{r}{R_c} \right)^{2-\gamma} \right]. \quad (1.8)$$

This solution of Eq. 1.5 is known as the self-similar solution (Lynden-Bell & Pringle 1974), and is different from the single power-law solution because it considers the viscous coefficient ν to be a power-law with exponent γ .

1.2.3 Vertical structure

Disks are not flat. Observational evidence can be found in the Hubble images of scattered light from the central star forming characteristic silhouettes around disks in the Taurus and Orion regions (Burrows et al. 1996; Stapelfeldt et al. 1998; Padgett et al. 1999; Smith et al. 2005). The vertical distribution of dust and gas in protoplanetary disks follows from the balance between the gas pressure and the vertical component of the gravitational force. If we assume that the disk is geometrically thin, then the vertical structure is in quasi-static equilibrium compared to the timescales that govern the radial motion of the disk. The vertical temperature gradient is complex and depends on viscous energy dissipation and radiative transfer. But for simplicity, if we consider the disk to be isothermal in the vertical axis the hydro-static equilibrium equation is given by

$$\frac{kT}{\mu m_u} \frac{d\rho(z)}{dz} = -\rho(z)\Omega_K^2 z, \quad (1.9)$$

where k is the Boltzmann constant, μ is the mean molecular weight and m_u is the atomic mass unit. This has a Gaussian solution of the form

$$\rho(z) = \rho_0 \exp\left(-\frac{z^2}{2h(r)^2}\right) \quad \text{with} \quad h(r) = \sqrt{\frac{kT(r)r^3}{\mu m_p G M_{\text{star}}}}, \quad (1.10)$$

where $h(r)$ is the scale height of the disk at a radius r , which depends on the competition between disk thermal pressure and the vertical component of stellar gravity. The disk thermal pressure depends on the amount of stellar radiation absorbed at the disk surface and it is discussed in the following section. The temperature dependence can be solved analytically by considering a hot surface layer that captures and reprocesses the starlight thereby heating the gas and resulting in a flared interior (Kenyon & Hartmann 1987; Natta 1993; Calvet et al. 1994; Chiang & Goldreich 1997). The scale height can then be parametrized as a power law of the form $h(r) \propto r^\psi$ with $\psi \sim 1.3 - 1.5$.

Flared disks reproduce the far-IR excess better than spatially flat disks (Kenyon & Hartmann 1987). All observed disks to date exhibit some degree of flaring, therefore they intercept and reprocess more stellar radiation than flattened disks. Most T Tauri stars exhibit less mid-IR emission than what is expected from a disk in hydrostatic equilibrium. This can be interpreted as a consequence of a reduced flaring angle due to settling of dust particles at very short timescales (see Sec.1.4.3). Observational evidence of settling in protoplanetary disks can be found by measuring the slope at mid-IR wavelengths (Chiang et al. 2001). The median mid-IR slopes of classical T Tauri stars imply that in these disks more than 90% of their μm -sized grains have settled into the midplane (D'Alessio et al. 2006).

1.2.4 Temperature structure

The temperature structure of disks is dominated by the mechanical heating produced by the viscous nature of the disk only in the innermost dense regions, reaching temperatures as high as 1000 K. The formalism derived by Shakura et al. (1978) considering only viscous heating and dissipation mechanisms such as thermal radiation and convection gives an

effective temperature for the disk as a function of radius of the form

$$T_{eff} \propto \dot{M}^{1/4} r^{-3/4}, \quad (1.11)$$

where \dot{M} is the accretion rate of the star. If we consider a simple model for disk irradiation from the central star then the expression is modified to (Chiang & Goldreich 1997)

$$T_{eff} \propto \dot{M}^{1/4} r^{-3/4} + L_{star}^{1/4} r^{-1/2}, \quad (1.12)$$

where L_{star} is the luminosity of the star. At the outer disk, for large r , the first term corresponding to the mechanical heating drops faster than the irradiation term. This effective temperature does not take into account the vertical structure of the temperature. The processing of stellar and external radiation by the dust material determines the vertical and radial temperature profile at large radii and in the upper layers of the inner disk (Dullemond et al. 2007; Hirose & Turner 2011). A two-layer approximation of this problem, which solves the vertical temperature gradient analytically, can be found in Appendix A of Chiang et al. (2001). Nowadays, many 2D and axisymmetric 3D models (pioneered by D'Alessio et al. 1998, in 1+1-D) solve the complete disk structure problem with diffusive radiative transfer, including stellar irradiation and viscous dissipation.

The computation of the temperature structure requires knowledge of the opacity, dominated by the dust for the iterative radiative process and many models calculate the temperature structure $T(r)$ self-consistently for a given dust density distribution (see Sec. 1.6.2). It is generally assumed that gas is well coupled with the dust thus $T_{gas} = T_{dust}$. This assumption is not valid within the super-heated surface layer of the disk but is true for most of the optically thick matter at the UV and IR regimes inside the midplane region of the disk where the gas density is sufficiently high. The gas temperature above the surface layer of the disk is determined by various heating and cooling processes. These processes depend on the chemical composition of main atomic and molecular species that in turn depend on the gas temperature. Some molecular species, such as H_2 , CO or C_2H , probe the region where the gas is decoupled from the dust, but other species emit from deeper and colder regions where the aforementioned assumption is still valid.

1.2.5 Ultraviolet and X-Ray radiation

Protoplanetary disks are exposed to intense ultraviolet (UV) and X-ray radiation. For T Tauri disks, at 100 AU, the UV radiation from the accretion onto the star is a factor of 100-1000 stronger than in the ISM (Bergin et al. 2003). For the much hotter Herbig Ae disks ($M_{star} > 2M_{\odot}$), the UV radiation has a photospheric origin and is factor of 10^5 stronger than the ISM (Semenov et al. 2005; Jonkheid et al. 2006). The median value for the X-ray luminosity of T Tauri stars is $\log(L_X/L_{bol}) \approx 3.5$ or $L_X \approx 3 \times 10^{29}$ erg s^{-1} (Preibisch et al. 2005; Getman et al. 2009) which is generated by the magnetic activity produced due to the convective nature of the stellar interior. The more massive Herbig Ae stars are usually non-convective resulting in X-ray luminosities more than 10 times lower than those found in T Tauri stars (Güdel & Nazé 2009). Unlike UV radiation, X-rays can penetrate deeper in the disk and, together with cosmic rays, ionize He which is fundamental to drive chemistry. In the midplane, secondary UV radiation emitted by molecular hydrogen after ionization by X-rays or cosmic rays is the only UV source. The photo-processes triggered by UV and X-ray radiation, such as ionization and the release of radicals and free electrons, fuel the chemistry deep within the disk (see Sec.1.5).

1.3 Disk evolution

1.3.1 What happens to the gas?

Class III YSOs are characterized by weak far-IR emission coming from small cold dust that is left after most of the gas has been accreted into the central star or dissipated by stellar winds (Matsuyama et al. 2009) and/or FUV and X-ray radiation coming from the central star or external sources (Gorti et al. 2009; Owen et al. 2010). The evolution of the gas content in protoplanetary disks is driven, in a first order approximation, by viscous accretion. There is no single physical mechanism dominating the transport of angular momentum throughout the disk, although a magnetized disk wind has been recently suggested as the primary mechanism driving disk accretion (see Sec.1.1.1 and Bai 2016; Turner et al. 2014).

Extensive modeling of viscous transport, and in particular the α parameter as a representation of the turbulence that gives origin to viscosity, has been done in 3D including self-gravity and MRI as well as convection and planet-disk interaction (see references in Armitage 2011). Although this model correctly predicts observable accretion indicators, such as the H α line, it fails at predicting the sudden and very quick disk dissipation that occurs after the typical disk lifetime of a few Myr (Fedele et al. 2010). Right after the accretion onto the central star stops, it is estimated that it only takes $\lesssim 0.5$ Myr to dissipate all the material from the primordial disk (Calvet et al. 2002; Cieza et al. 2007). The photoevaporation by UV and X-ray radiation from the central star overtakes viscous accretion in the outer regions of the disk, opening a gap and cutting off accretion, while the inner disk is rapidly accreted onto the star (Clarke 2007; Clarke et al. 2001). Immediately after, the outer disk is exposed to energetic UV photons and X-ray radiation and the disk is quickly photoevaporated from the inside out. A schematic of this process is shown in Fig. 1.2.

1.3.2 What happens to the dust?

In parallel, the dust also evolves to eventually form planets. More than 13 orders of magnitude separate the size of the interstellar dust with planets. The core accretion scenario (Safronov 1972; Lissauer 1993; Pollack et al. 1996; Haghighipour 2013) describe this process in three steps.

First, small grains coagulate to form cm-sized particles (Dullemond & Dominik 2005, 2008). Evidence for the formation of μm -sized particles is abundant, even at early stages, from amorphous silicate features in the IR (Kessler-Silacci et al. 2007; McClure et al. 2010). The evidence for millimeter and centimeter sized particles comes from the impact of opacity on the shape of the SED at millimeter wavelengths (Andrews & Williams 2005). As the population of centimeter sized particles grows, the dust opacity decreases and the slope of the SED becomes shallower at millimeter wavelengths (Natta et al. 2004; Draine 2006).

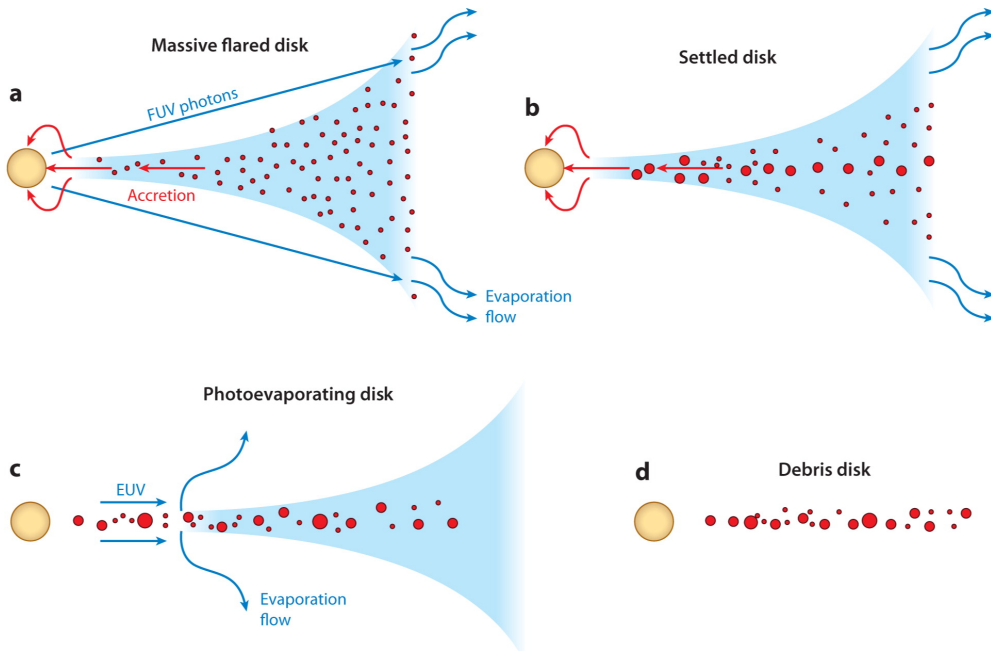
Second, the grains continue to grow to form km-sized bodies. This step is less understood than the previous one as it involves dynamical processes that arise due to the decoupling of gas and dust (Dubrulle et al. 1995; Birnstiel et al. 2011), namely settling and radial drift that are discussed in detail in the next section. Decoupled grains start experiencing a radial inward drift that is much faster than the coagulation time scales, thus preventing them from growing larger than a few meters. As dust particles begin to grow and the impact velocities increase, the outcome of their collisions results in bouncing. In the bouncing regime dust particles do not stick together but are compacted due to the collision. In addition, fragmentation of large dust grains, close to the inner regions of the disk, becomes efficient as the relative velocities between grains are enhanced by these dynamical processes (Weidenschilling 1984; Birnstiel et al. 2012). The combination of fragmentation,

bouncing and radial drift for meter-sized bodies is commonly called the meter-sized barrier.

A radial pressure maximum in the gaseous content of the disk, caused by density variations, is capable of stopping the radial migration of dust (e.g. Lyra et al. 2009; Brauer et al. 2008). Azimuthal vortices can arise once the dust has stopped migrating which are an effective way to trap the dust particles and allow them to grow (Pinilla et al. 2015). These vortices have been observed toward a couple of disks at millimeter wavelengths (e.g. van der Marel et al. 2013).

For a given distribution of dust sizes and velocities, some particles will collide with velocities that are below the critical velocities of the bouncing and fragmentation regimes. These 'lucky' particles can overcome the bouncing barrier and grow further (Garaud et al. 2013; Windmark et al. 2012). Collections of pebbles resulting from streaming instabilities in the disk can collapse to quickly form bodies as large as the asteroid Ceres in one step (Johansen et al. 2007). This process is a consequence of the so-called streaming instability and is an effective mechanism to concentrate dust particles at super-critical densities overcoming the fragmentation barrier.

Finally, once planetesimals of a few kilometers in size have formed, they grow further by sweeping up and gravitationally attracting smaller particles. At early stages of planetary accretion, the gravitational attraction of large planetesimals leads to runaway accretion while small planetesimals remain unchanged (Greenberg et al. 1978; Barnes et al. 2009). The resulting largest bodies, known as planetary embryos or protoplanets, start to dominate the viscous stirring produced by the gravitational scattering effect (Ida & Makino 1993). The formation of these large planetesimals at time scales shorter than the lifetime of the disk




 Williams JP, Cieza LA. 2011. *Annu. Rev. Astron. Astrophys.* 49:67–117

Figure 1.2: Cartoon showing the evolutionary path of a disk around a low-mass star, taken from Williams & Cieza (2011)

is challenging, but mechanisms like pebble accretion can aid to overcome this problem (Ormel & Klahr 2010; Lambrechts & Johansen 2014). In the presence of gas, massive cores of several Earth masses attract a gaseous envelope to form Jupiter like planets (Lissauer et al. 2012; Lissauer 1993).

1.4 Dust in disks

Although dust particles contain only 1% of the initial mass of protoplanetary disks, they are the precursors of planets and are fundamental in the formation of complex molecules through grain-surface chemical reactions. Moreover, they dominate the opacity of the disk. In Sec. 1.3.2 we briefly discussed dust coagulation processes that allow (sub)micron dust particles to grow to millimeter/centimeter sized particles and their impact on dust opacity. The dynamical processes that shape the dust spatial distribution are different from the ones that affect the gas. This thesis focuses in understanding the link of the spatial distribution of dust grains of different sizes and the formation mechanism and spatial distribution of key volatiles in the gas. This section will focus on the physical processes that affect dust grains in disks and their composition.

1.4.1 Composition

Dust, in the diffuse ISM, is mainly composed of silicates with an admixture of graphite grains and polycyclic aromatic hydrocarbons (PAHs) (Draine 2003). These are easily identified through spectral features at 10 and 18 μm (silicates, Henning et al. 2010) and through a series of features in the mid-IR (PAHs, Tielens 2008).

Observations of the disks around T Tauri and Herbig Ae/Be stars typically show spectral features corresponding to a mixture of amorphous silicates with olivine and pyroxene stoichiometry (being 1%-30% of the content), crystalline forsterite and enstatite, and in some cases silica (see references in Henning & Semenov 2013). In the warm inner regions of protoplanetary disks up to a few AU, the dust has been processed via thermal annealing or shock heating resulting in a higher crystallinity fraction (Harker & Desch 2002; van Boekel et al. 2005; Olofsson et al. 2009, 2010; Oliveira et al. 2011). Features of molecular ices, such as H_2O and CO_2 , have been detected in absorption toward edge-on disks and in emission toward face-on disks, including the 63 μm feature of crystalline water (Malfait et al. 1999; Thi et al. 2002; Pontoppidan et al. 2005; Terada et al. 2007; Terada & Tokunaga 2017; Aikawa et al. 2012; McClure et al. 2012; Riviere-Marichalar et al. 2016). The freeze-out and desorption processes of the ice reservoir in protoplanetary disks are further discussed in Sec.1.5.1.

1.4.2 Radial drift

Small dust particles of $\sim 1\mu\text{m}$ are well coupled to the gas in protoplanetary disks, and are supported by the gas pressure. As the particles grow to sizes $a \gg 1\mu\text{m}$ their surface-to-mass ratio decreases and the dust particles dynamically decouple from the gas. If particles get bigger than their mean free path through the gas they will feel a friction when moving through it. Due to its radial pressure gradient, the gas orbits at sub-Keplerian velocity while large dust grains move almost at Keplerian velocities. This friction will create a drag force of the form

$$F_D = -\frac{1}{2}C_D\pi a^2\rho_g v^2 \quad (1.13)$$

where πa^2 is the cross-section of the dust grain, ρ_g is the gas density, v is the relative velocity between the gas and the dust and C_D is the drag coefficient that depends on v and the relative size of the dust grain with respect to the mean free path of the gas. The drag force induced by the sub-Keplerian gas disk removes angular momentum from the dust particles and slows them down. This translates into a headwind that moves the decoupled dust particles inward. The drift velocity depends on the gas pressure gradient because it is what causes the gas to move at sub-Keplerian velocities (Nakagawa et al. 1986; Weidenschilling 1977).

A useful dimensionless parameter is the Stokes number (S_t) defined as

$$S_t = \Omega_K \tau_S, \quad (1.14)$$

where $\tau_S = mv/F_D$ is the stopping or friction time of a particle with mass m and velocity v due to drag forces (F_D) and Ω_K is the Keplerian angular velocity. Particles with the same Stokes number have identical aerodynamical behavior. Small particles with $S_t \ll 1$ will adapt to the gas velocity on shorter timescales than the orbital time scale. Similarly, big particles with $S_t \gg 1$ will adapt to the gas velocity at much longer timescales than the orbital time scale. In the regime where $S_t < 1$ the radial velocity satisfies $v_r \simeq -2S_t \eta V_K$, which means that small particles drift inwards at lower velocities than larger particles.

Observational evidence of radial drift can be found by comparing the millimeter continuum emission in resolved disks, which roughly traces the distribution of mm-sized dust grains, to the extent of the molecular gas usually traced by CO (Panić et al. 2009). Protoplanetary disks usually exhibit a larger radial extent of their gas content, traced by CO, than that of the mm-sized dust grains, traced by the millimeter continuum. Although this difference can be explained as a consequence of optically thick CO emission (Hughes et al. 2008), detailed modeling of optically thin CO isotopes and (sub)millimeter continuum has shown that, for some disks, radial drift is a natural explanation of the difference in the radial extent of CO and continuum emission (Andrews et al. 2012; Isella et al. 2016). Moreover, it is the sharp steepening of the mm-sized grain distribution, rather than its smaller radial size, that is truly characteristic of radial drift.

1.4.3 Settling

In addition to drag forces, large grains of dust will experience a vertical gravitational force. For small vertical displacements ($z \ll r$) we can write this force as

$$F_g = -m\Omega_K^2 z. \quad (1.15)$$

By equating the vertical component of the stellar gravity to the drag force an expression for the settling time scale can be obtained

$$\tau_{\text{settling}} = (S_t \Omega_K)^{-1}. \quad (1.16)$$

For small particles ($a \ll 0.1 \mu\text{m}$) this settling time will always be much larger than the orbital time, $\tau_{\text{orbit}} = \Omega_K^{-1}$. The time scale for radial drift is much shorter, about 100 years for m-sized particles, than the time scale for dust settling, which is about 10^5 years. We can therefore consider that all grains that have settled have also migrated inwards. However, a fraction of the dust grains may not stay permanently settled since turbulent velocities produce vertical stirring and mixing of small particles (Dullemond & Dominik 2004b, 2005, 2008; Birnstiel et al. 2016).

1.4.4 Mixing

The gas evolution within the disk is thought to be driven by viscous accretion. The viscous nature of the gas will induce random motions in the dust that will act as a mixing mechanism on the dust. Just like vertical settling and radial drift, the mixing process is dependent on the size of the dust particles. A useful number is the Schmidt number, the ratio of dust diffusivity to gas diffusivity, defined as (Youdin & Lithwick 2007)

$$S_c = \frac{D_g}{D_d} \approx 1 + S_t^2, \quad (1.17)$$

where it is usually assumed that the diffusivity of the gas equals its viscosity (Pavlyuchenkov & Dullemond 2007). This ratio is high for large particles and low for small particles, consistent with the notion of larger particles suffering less diffusion than small particles due to gas motions. This mixing results in the smoothing of the concentration of small dust grains and gas.

1.5 Disk chemistry

So far we have only discussed the physical structures and dynamical processes of protoplanetary disks. The large range of physical conditions throughout the disk implies an equally diverse chemistry produced by reactions ranging from photo-processes in the hot and irradiated regions to grain chemistry in the cold and dense disk. Because the disk temperature decreases with radius, we can roughly divide the chemistry into two regions: the inner warm disk at $r \lesssim 20$ AU and the outer cold disk at larger radii.

The inner disk hosts a high temperature environment at 100-5000 K with densities as high as 10^{12} cm^{-3} . The dense midplane regions of the inner disk are shielded from high-energy ionization sources and the chemistry is driven by 3-body neutral-neutral reactions (Harada et al. 2010; Aikawa et al. 1999), such as the formation of molecular hydrogen. Chemical models predict a high abundance of H_2O , CO , NH_3 , HCN and simple hydrocarbons, being destroyed only at very high temperatures by thermal dissociation (Willacy & Millar 1998; Markwick et al. 2002; Ilgner et al. 2004; Woods & Willacy 2007; Agúndez et al. 2008; Bethell & Bergin 2009; Najita et al. 2011; Walsh et al. 2015).

In the outer cold disk high-energy radiation and cosmic rays drive the chemistry of the disk dominated by ion-molecule reactions (Aikawa et al. 2002; van Zadelhoff et al. 2003; Gorti & Hollenbach 2004; van Dishoeck et al. 2006; van Dishoeck 2006; Fogel et al. 2011; Vasyunin et al. 2011; Walsh et al. 2012; Akimkin et al. 2013). Section 1.2.4 discusses the vertical gradient of the gas and dust temperature which is determined by the heating and cooling of the gas and dust triggered by the irradiation of the central star. The vertical positive gradient coupled with the UV radiation field result in three characteristic chemical regimes (Aikawa et al. 2002). Figure 7.1 shows a cartoon of these three regions: a cold chemistry region in the midplane dominated by surface processes in icy mantles, a rich warm molecular region where gas chemistry is active, and a restricted photon-dominated surface region where UV radiation dissociates and ionizes molecules driving an ion-molecule chemistry.

The cold outer midplane has temperatures below ~ 20 -50 K with most of the molecules frozen out (with the exception of H_2) and hydrogenation reactions on the surfaces of the grains dominating the chemistry. The only ionization sources in these dense and cold region are cosmic ray particles and the secondary UV photons they produce. Molecules like CO , N_2 and simple hydrocarbons evaporate at temperatures around ~ 20 K. The local

UV radiation field might also contribute to the release of icy molecules to the gas-phase in cold environments through photodesorption.

Gas-phase chemistry in the intermediate warm molecular layer is dominated by ion-molecule processes, such as proton transfer from species like H_3^+ (Herbst & Klemperer 1973; Watson 1974; Woodall et al. 2007; Wakelam et al. 2012). This region is only partially shielded from high-energy radiation and temperatures are high enough, even at large radii, for molecules such as CO and N_2 to evaporate from icy dust grains. Water has a higher sublimation temperature, around 170 K (Hayashi 1981) dependent on the pressure, and thus remains mostly frozen-out. The location of this temperature threshold is commonly known as the molecule's snowline, to refer to its radial location in the midplane, or snow surface, since the vertical temperature structure of the disk will define an isothermal surface across the radial axis.

This snowline is a function of the luminosity of the central star and the evolutionary stage of the disk. The water snowline likely moves inward from larger radii in the early hotter embedded phase (Kennedy & Kenyon 2008; Zhang & Jin 2015). Additionally, protostellar outbursts can abruptly heat the disk moving its location (e.g. Cieza et al. 2016). The water snowline is difficult to probe because is usually too close to the central star. The CO snowline, that occurs at around ~ 20 K, is further out at a few tens of AU. It has been indirectly imaged through chemical tracers in a couple of disks (e.g. Qi et al. 2013, 2015; Mathews et al. 2013).

The upper region in the disk atmosphere is dominated by the stellar UV radiation and the interstellar radiation that ionizes and dissociates molecules. These processes depend

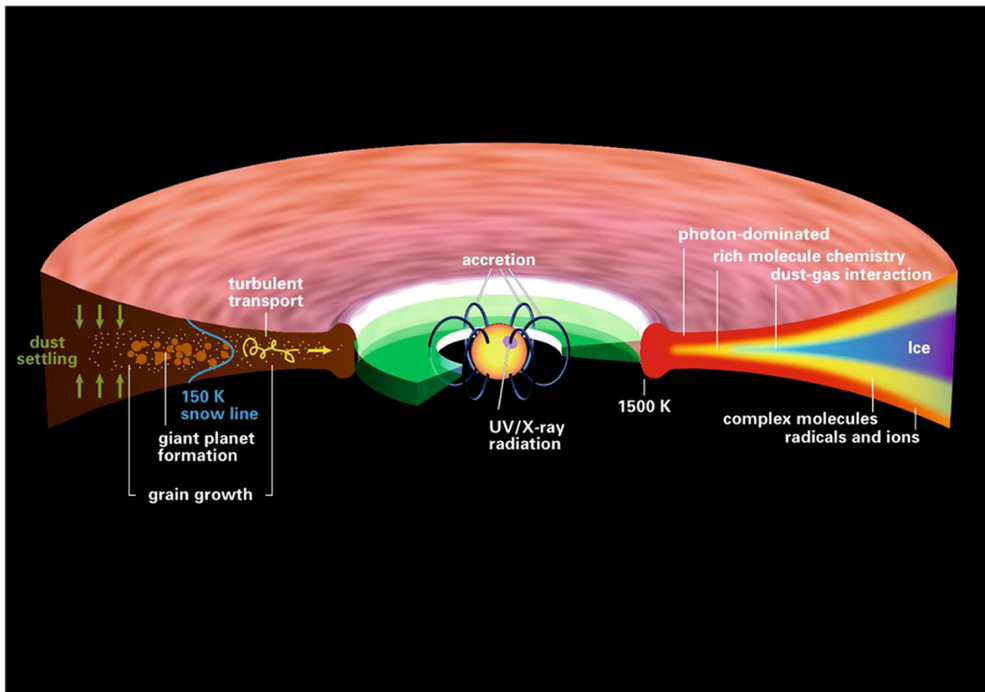


Figure 1.3: Cartoon of dust evolution and chemical regions in the disk. Taken from Henning & Semenov (2013).

strongly on the shape and intensity of the high-energy radiation field. For example, Lyman α photons will dissociate HCN and H₂O, while other molecules such as CO and H₂ are protected by self-shielding and mutual shielding (van Dishoeck & Black 1988; van Dishoeck et al. 2006; Heays et al. 2017).

1.5.1 Material inventory

Gas

To construct an inventory of chemical species high spectral resolution is needed. Disks are optically thick at IR wavelengths and emission lines can only be seen from the upper warm layers, but the disk is mostly optically thin in the (sub)millimeter regime and there we can trace molecular lines throughout the entire disk. Figure 1.4 shows a schematic summary of the main molecular diagnostic of disks.

A large body of observational work has provided an inventory of the molecular content of disks (e.g. Dutrey et al. 1997; Thi et al. 2004; Schreyer et al. 2008; Henning et al. 2010; Öberg et al. 2010, 2011b,c, 2015; Dutrey et al. 2011; Chapillon et al. 2012a,b). Molecules such as CO, HCN, HCO⁺, H₂O and recently the complex organic CH₃OH (Walsh et al. 2016) have been found toward protoplanetary disks. Their line intensities can be transformed to abundances if a density and temperature is provided. One of the most important results of this work is the depletion of molecules in comparison with ISM abundances due to low temperatures (freeze out) or photodissociation within the disk (Kastner et al. 1997; Dutrey et al. 1997; van Zadelhoff et al. 2001).

In the Far-IR regime, the PACS and HIFI instruments aboard *Herschel* have detected higher rotational transitions of CO, that account for gas at $T \sim 100 - 1000$ K, hydroxyl,

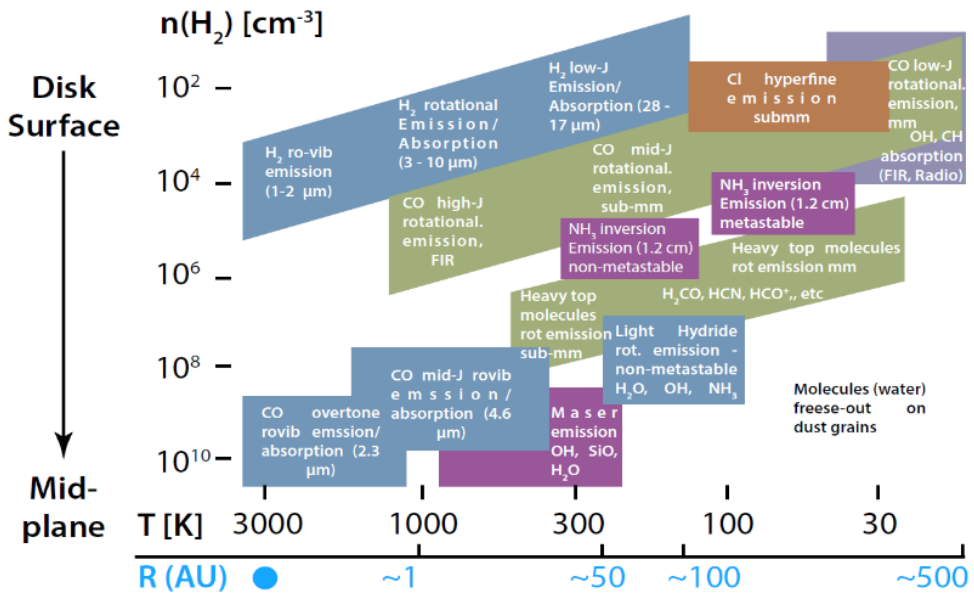


Figure 1.4: Schematic representation of the radial and vertical locations in a disk where molecular species are expected to dominate the line emission taken from Dionatos (2015) based on Genzel (1992).

water, atomic oxygen and CH^+ toward several protoplanetary disks (Fedele et al. 2012; Meeus et al. 2012; Riviere-Marichalar et al. 2012; Fedele et al. 2013; Hogerheijde et al. 2011; Sturm et al. 2010; Meeus et al. 2013). In the mid- and near-IR regimes, *Spitzer* and ground-base telescopes provided a forest of H_2O and OH line in many disks, along with CO, and organic molecules such as HCN and C_2H_2 (Lahuis et al. 2006; Carr & Najita 2008; Salyk et al. 2008; Pascucci et al. 2009; Pontoppidan et al. 2010; Carr & Najita 2011; Salyk et al. 2011; Mandell et al. 2012).

Ice

The major components of astronomical ices, such as H_2O , CO, CO_2 , CH_4 , CH_3OH , NH_3 and HCOOH , have been detected through their IR features toward embedded protostar and background stars (van Dishoeck 2004; Gibb et al. 2004; Whittet et al. 2007; Boogert et al. 2015). The icy mantles grow by accretion of atoms and molecules from the gas where molecules like CO_2 , H_2CO and CH_3OH are formed through atom addition reactions, CO and O_2 (van de Hulst 1946; Watson 1976; Ioppolo et al. 2008; Miyauchi et al. 2008; Dulieu et al. 2010). A rich surface chemistry, even at low temperatures of ~ 10 K, forms more complex molecules (e.g. Fedoseev et al. 2017) and these are subsequently processed by high energy photons and cosmic rays present in the ISM (Benz et al. 2010; Bernstein et al. 1995; Moore & Hudson 1998; Bennett et al. 2005). In the high temperature environments of massive and low-mass protostars, these icy mantels sublimate. In these so-called hot cores and hot corinos, major ice species as well as minor constituents, like some complex organics and nitrogen-bearing species, return to the gas where they can be easily identified through rotational gas-phase spectroscopy (Herbst & van Dishoeck 2009).

Some of this icy reservoir is reprocessed in the early stages of protoplanetary disks through thermal desorption followed by gas chemistry. They are ultimately frozen out again in the outer colder region of the disk where they potentially mix with pristine ices still present there (Caselli & Ceccarelli 2012; Brownlee 2014; Cleeves et al. 2014; Furuya & Aikawa 2014). Models by Visser (2009) suggest that most of the material that ends up in the comet-forming region experiences a large degree of chemical reprocessing, a result supported by the crystallinity fraction found in solar system comets. However, at the same time, comets also contain material very similar to young protostars. Comets may have mixed material from both pristine regions in the outer parts of the disk and from heavily reprocessed regions.

The freeze-out time scale t_{freeze} for the standard gas-to-dust mass ratio of 100 and a sticking probability of 1 can be roughly estimated by the following expression

$$t_{\text{freeze}} \approx \frac{10^9 \text{cm}^{-3}}{n_{\text{H}}} \frac{a}{0.1 \mu\text{m}} \text{yrs} \quad (1.18)$$

where n_{H} is the gas particle density (in cm^{-3}) and a is the typical grain radius (in μm). The freeze-out time scales in the cold midplanes of protoplanetary disks (with typical densities of $\sim 10^6$ – 10^8cm^{-3}) are of the order of 10 – 10^3 years, indicating that most of the material in the gas phase is frozen-out within a tiny fraction of the disk lifetime.

The most important desorption process for volatiles such as CO, N_2 , and CH_4 is thermal desorption. In regions where UV radiation can penetrate, photodesorption of these ices also becomes important. Additionally, cosmic ray and X-ray spot heating may release mantle material back to the gas phase in cold regions deep in the midplane (Leger et al. 1985; Hasegawa & Herbst 1993; Najita et al. 2001). The photodesorption rates of CO, H_2O , CH_4 , and NH_3 have recently been derived experimentally (Öberg et al. 2007; Öberg 2009; Öberg

et al. 2009a,b; Fayolle et al. 2011; Cruz-Diaz et al. 2012; Fedoseev et al. 2015). Observations of NH_3 in ices suggest that it is usually intermixed with H_2O on interstellar ices (Merrill et al. 1976; Knacke et al. 1982; Smith et al. 1989; Bottinelli et al. 2010). Chemical models of protoplanetary disks show that photodesorption by UV radiation significantly affects molecular column densities of the most abundant molecules such as HCN, CS, H_2O , NH_3 and CO_2 (Willacy 2007; Semenov & Wiebe 2011; Walsh et al. 2010).

Dust evolution processes and the intrinsic characteristics of the physical structure of disks drive the subsequent reprocessing of some of these species by changing the penetration of UV photons. This thesis explores the interrelationship between the dust, the temperature structure and the chemistry driving the formation of observable molecules. In particular, it explores the link between the location of the main oxygen- and nitrogen-bearing species (H_2O and NH_3) and the mm-sized dust particle distribution.

1.5.2 Water

Water was detected in the ISM more than 40 years ago (Cheung et al. 1969) and, subsequently in vapor and ice form, toward a number of YSOs and protoplanetary disks (Gillett & Forrest 1973; Cernicharo & Crovisier 2005; Boogert et al. 2008; Melnick 2009; Hogerheijde et al. 2011; Bergin & van Dishoeck 2012). Water is the most abundant volatile in interstellar and cometary ices (see reviews by Mumma & Charnley 2011; Boogert et al. 2015). At temperatures higher than 230 K water is the dominant gas-phase oxygen carrier. It forms through neutral-neutral reactions of $\text{O}+\text{H}_2 \rightarrow \text{OH}+\text{H}$ followed by $\text{OH}+\text{H}_2 \rightarrow \text{H}_2\text{O}+\text{H}$ (Elitzur & Watson 1978; Atkinson et al. 2004). At temperatures below 100 K water forms through ion-neutral reaction and dissociative reactions. It starts with $\text{H}_3^++\text{O} \rightarrow \text{H}_2+\text{OH}^+$ followed by a series of reactions of OH^+ or H_2O^+ with H_2 , leading to H_3O^+ that is finally recombined to $\text{H}_2\text{O}+\text{H}$ (Herbst & Klemperer 1973). In addition, H_2O can form on grains surfaces through hydrogenation of O, O_2 and O_3 . The whole chemical network involves photo-dissociation, photo-desorption and freeze-out summarized in Fig.1.5 (see van Dishoeck et al. 2014, and references therein). Water ice is known to be frozen out already in pre-stellar and protostellar phases and it is only thermally evaporated in the disk within ~ 10 AU from the star.

1.5.3 Ammonia

NH_3 was one of the first molecules identified in the ISM (Cheung et al. 1968) and is readily detected in star forming regions (Morris et al. 1973; Irvine et al. 1987; Persson et al. 2010; Bottinelli et al. 2010; Daranlot et al. 2012). In disks, detailed chemical models have shown ammonia to form as a product of warm gas-phase reactions and ion-molecule reactions (see Fig. 1.6). On grains, ammonia forms through atomic nitrogen hydrogenation (Brown & Millar 1989; Fedoseev et al. 2015). About 10%-20% of nitrogen is contained in ices such as NH_3 , NH_4^+ , and XCN, the latter mostly in the form of OCN^- (Öberg et al. 2011a). Processes to release NH_3 from ice to gas, at temperatures below the thermal desorption, include cosmic-ray desorption (Hasegawa & Herbst 1993), reactive desorption (Garrod et al. 2007) and photodesorption (Prasad & Tarafdar 1983). This process dominates during the very early stages of star formation. In more evolved stages, where protoplanetary disks are formed, the bulk of ammonia is locked in the ice and gas-phase formation is the only process left active (Sipilä et al. 2015; Harju et al. 2017). This process occurs through a well-known chain of reactions, starting with the dissociation of N_2 (by photo-processes or He^+) and terminating in $\text{NH}_4^+ + \text{e} \rightarrow \text{NH}_3 + \text{H}$ (Le Gal et al. 2014; Roueff et al. 2015; Walsh et al. 2014).

1.5.4 Deuterium chemistry in Disks

The initial cosmic elemental D/H fraction, produced in the Big Bang, was $\sim 2.5 \times 10^{-5}$ (Cooke et al. 2016). In present days the D/H ratio in the cold ISM is $\sim 2.0 \times 10^{-5}$ (Prodanović et al. 2010). The D/H ratio of H_2 in the solar surroundings is similar to that of the diffuse ISM. Simple molecular species, such as DCO^+ , DCN and HDCO , have D/H ratios that are higher than the cosmic and cold ISM values by two order of magnitude (Roberts et al. 2002; Bacmann et al. 2003; Vastel et al. 2006). The temperature of the regions where key molecular species, present in protoplanetary disks and solar system bodies, were formed (or processed) can be traced by measuring their D/H ratio. The high deuterium fractionation at low temperatures is a consequence of the lower zero-point vibrational energy of simple deuterated molecules in comparison to their non-deuterated counterparts (Combes et al. 1985; Millar et al. 1989; Turner 2001; Gerner et al. 2015). We can distinguish three main

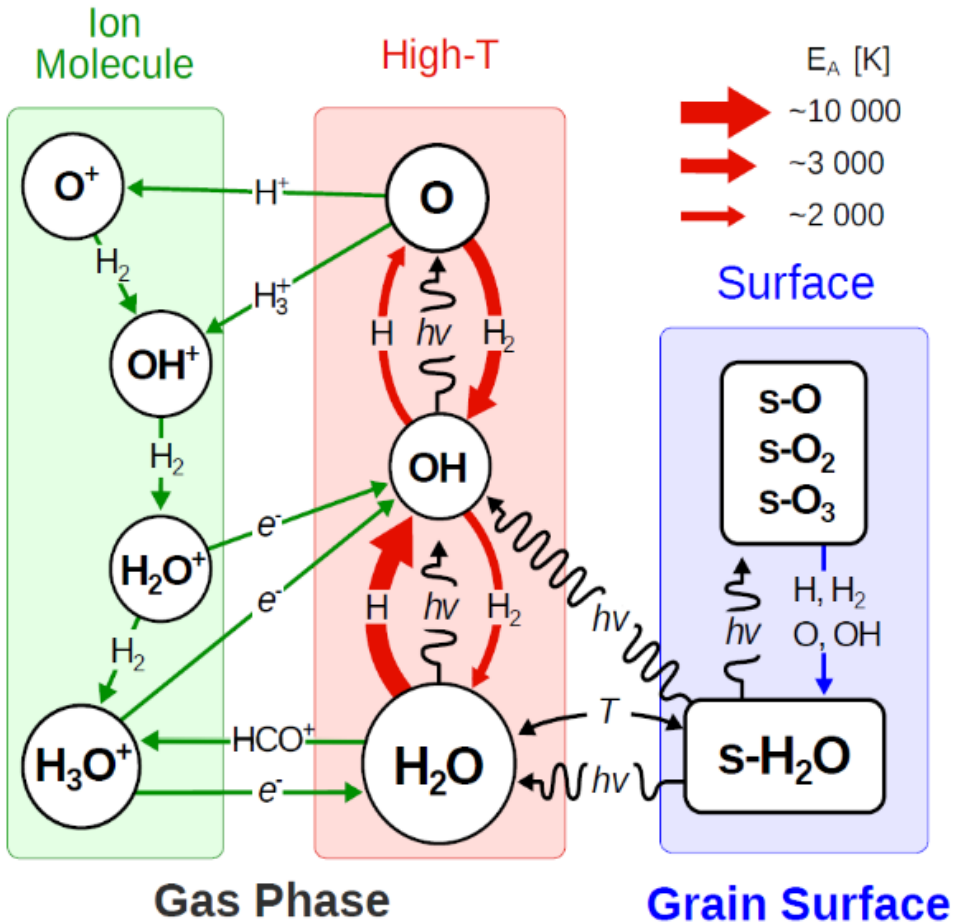
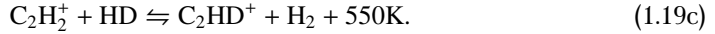
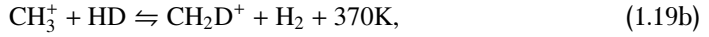
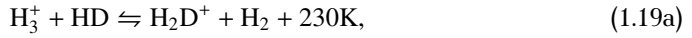


Figure 1.5: Summary of the main gas-phase and solid-state chemical reactions leading to the formation and destruction of H_2O . e stands for electron, ν for photon and s-X indicates that species X is on the grains. This figure was taken from (van Dishoeck et al. 2014).

reactions through which deuterium is injected into the chemistry,



Equation 1.19a is preceded by cosmic ray ionization of H_2 producing the H_3^+ ion. The left-to-right reaction of Eq. 1.19a is exothermic and strongly enhances the D/H ratio of H_2D^+ , and species that derive from it, at temperatures below ~ 30 K (Millar et al. 1989; Albertsson et al. 2013). This regime corresponds to the so-called low temperature deuteration channel. In contrast, the left-to-right reactions of Eq. 1.19b and 1.19c, involving light hydrocarbons, effectively enhance the deuterium fractionation at higher temperatures than Eq. 1.19a but below ~ 80 K. This regime corresponds to the high temperature deuteration channel. Deuterium fractionation initiated by the H_2D^+ is particularly effective at low temperatures in disk midplanes. In these regions CO is frozen out, otherwise it would react with H_3^+ before HD. Similarly, at low temperatures, grain surface reactions may also contribute enhance the D/H molecular ratio of selected species (Tielens 1983). Recently it was realized that the ortho-to-para ratio of molecular H_2 can hinder the deuterium enhancement because of the differences in internal energies of o- H_2 and p- H_2 (Flower et al. 2006; Pagani et al. 2009). The reverse endothermic reactions of Eq. 1.19a, 1.19b and 1.19c proceed more rapidly for the reaction involving o- H_2 than the corresponding reaction involving p- H_2 .

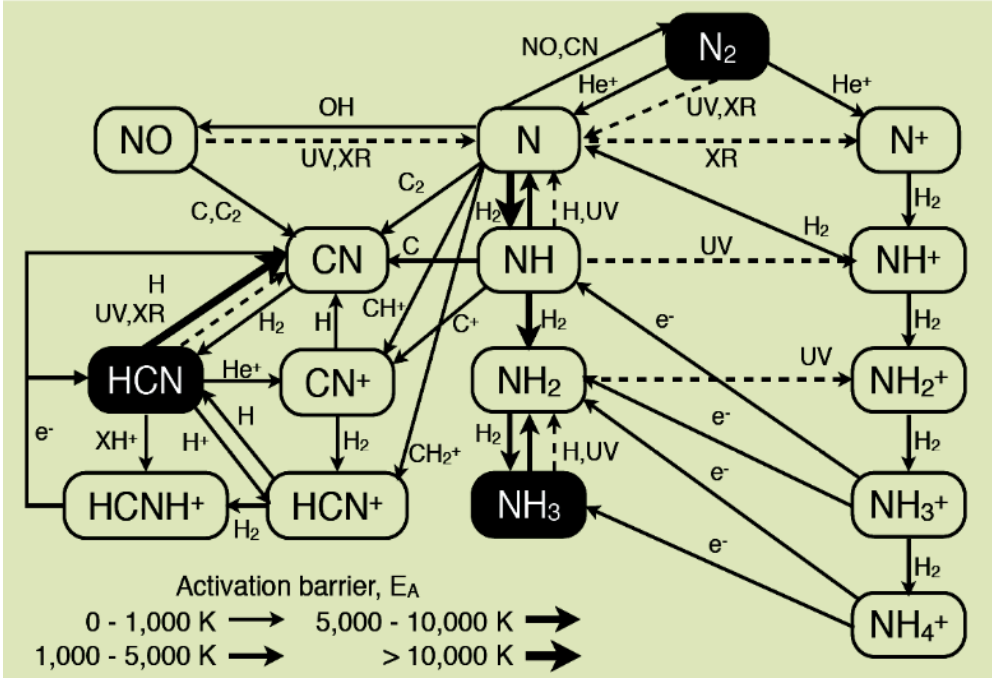


Figure 1.6: Schematic chemical network of the main gas-phase processes that involve NH_3 , taken from Walsh et al. (2015).

Cold ISM regions show D/H molecular ratios a factor of 100-300 higher than the elemental D/H (Roberts et al. 2002; Bacmann et al. 2003; Vastel et al. 2006). In contrast, the D/H molecular ratios found in meteorites and comets from the Oort cloud are a factor of 10-30 higher than the elemental D/H ratio (Irvine et al. 2000), but about an order of magnitude lower than in the cold ISM. The D/H ratio in Earth can be probed by measuring the HDO/H₂O ratio of about $\sim 1.6 \times 10^{-4}$, consistent with the idea of a dry proto-Earth that got most of its oceans from asteroids as opposed to long-period comets in the last phase of its formation (Morbidelli et al. 2000). Long period comets have a water deuterium enrichment a factor of two higher than that of Earth, suggesting that the bulk of Earth's water was delivered at early stages through massive planetary embryos, with lower HDO/H₂O ratios, in the asteroid belt. Chemical models, including a comprehensive treatment of disk ionization, show that the ion-driven deuterium pathways are inefficient to explain the observed enriched HDO/H₂O ratio of solar system bodies (Cleeves et al. 2014), implying that a considerable fraction of the water reservoir of the solar nebula was inherited from the ISM.

Other deuterated molecules, such as DCN and DCO⁺, have been detected toward protoplanetary disks. The D/H ratios of DCN and DCO⁺ in TW Hya (Öberg et al. 2012) are much higher than elemental D/H ratios, by several orders of magnitude. DCN is more centrally peaked than DCO⁺, suggesting different fractionation pathways. DCN is believed to be formed mainly through Eq. 1.19b while DCO⁺ is thought to form through Eq. 1.19a. However, recent chemical models have proposed reactions involving Eq. 1.19b and 1.19c leading to production of DCO⁺ at higher temperatures than Eq. 1.19a (Favre et al. 2015).

1.6 Methods

1.6.1 Observations

This thesis makes use of the available data from the HIFI instrument aboard the *Herschel Space Telescope* in the far-IR regime and the Atacama Large Millimeter/submillimeter Array (ALMA) in the (sub)millimeter regime toward two disks. *Herschel* had a 3.5 m single mirror and operated between 2009 and 2013. It carried three detectors: the Photodetector Array Camera and Spectrometer (PACS) (Poglitsch et al. 2010), covering wavelengths from 55 to 210 μm ; SPIRE (Griffin et al. 2010), an imaging camera covering wavelengths from 194 to 672 μm ; and HIFI (de Graauw et al. 2010) an heterodyne detector operating in two wavelengths bands from 157 to 212 and 240 to 625 μm . At these wavelengths, the primary beam size is 11"-19" and 21"-43", respectively. The *Herschel* beam cannot provide resolved spatial information of protoplanetary disks but it is capable of observing the far-IR regime that hosts several interesting molecular and atomic transitions only attainable from space. The HIFI instrument has very high spectral resolution, which can be used for reasonable inclined disks to pinpoint the location of the emission.

The guaranteed-time *Herschel* key programme "Water In Star-forming regions with *Herschel*" (WISH van Dishoeck et al. 2011) observed fundamental water rotational transitions and high-*J* CO transitions with unprecedented spectral resolution toward sources related to star formation including several protoplanetary disks using HIFI and PACS. *Herschel* provided unique spectral coverage and sensitivity, unmatched by earlier missions and not surpassed in the near future. The far-IR regime, probed by the HIFI instrument, hosts unique ground level transitions of key molecules in disks, such as NH₃ and H₂O. This thesis analyses *Herschel* HIFI data in relation to the resolved millimeter continuum emission (from ALMA) to provide constraints on the amount of volatile water and ammonia, and the

mechanisms responsible for their release in the gas phase.

ALMA is an interferometric facility of sixty-six 12 m and 7 m radio telescopes at ~ 5000 m of altitude in the Chilean Andes. Compared to the modest eight antennas of 6 m of the SMA, ALMA is a huge improvement for the observation of the cold universe in the (sub)millimeter regime. The ambitious set up of ALMA allows it to reach spatial resolutions of a few milli-arcseconds for its most extended configuration and spectral resolutions better than $\sim 0.05 \text{ km s}^{-1}$. The (sub)millimeter regime probed by ALMA has many rotational transitions of simple (e.g. CO) and complex (e.g. CH₃OH) molecules that give valuable information of the gas dynamical and chemical processes occurring in planet-forming disks.

The analysis of interferometric data is best done in the uv -space. The uv -space is the Fourier space of the coordinates (x, y) in the sky. Interferometers measure the interference pattern, or visibilities, of the image plane in a discrete sample of the uv -space defined by the available baselines. An interferometer has as many baselines as permutations of pairs of its antennas. The resolution of a particular set of baselines (B) is given by λ/B_{max} , where λ is the observed wavelength and B_{max} is the longest available baseline. Because of this relationship, baselines are usually given in $k\lambda$ rather than the standard SI units.

In the pre-ALMA era most of the spatially resolved observations of disks in the millimeter regime were obtained with interferometric arrays such as the PdBI, CARMA and SMA to a resolution of about $0.5\text{--}1''$. In addition to molecular transitions, several resolved millimeter images of disks showed ring-like structures (Piétu et al. 2006; Brown et al. 2009; Andrews et al. 2011; Williams & Cieza 2011). These structures were modeled in the Fourier space

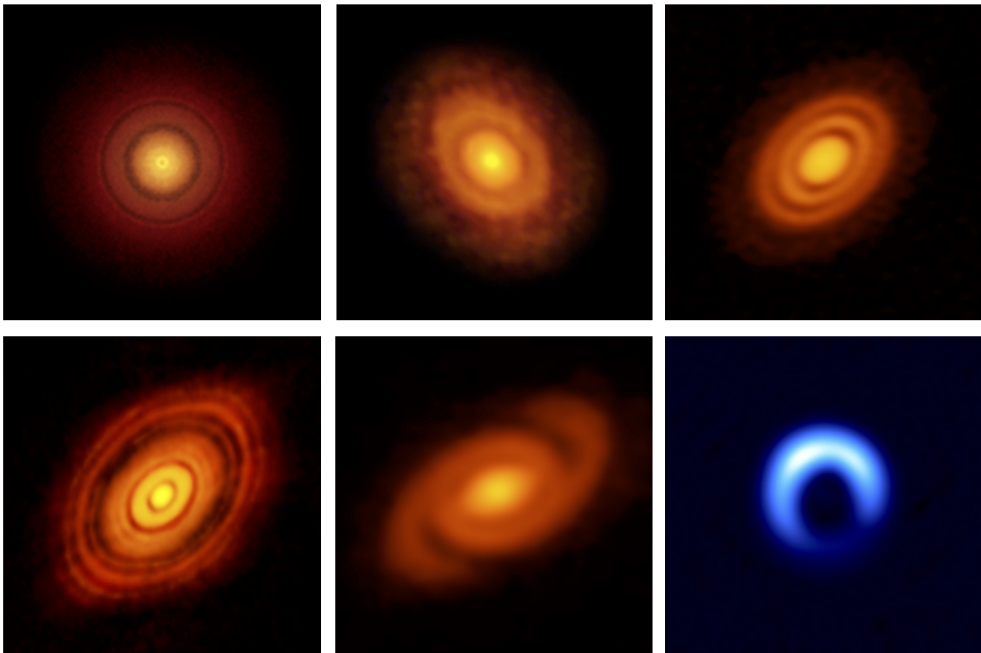


Figure 1.7: Gallery of high angular resolution continuum observations of planet forming disks obtained with ALMA. From left to right and from top to bottom: TW Hya (Andrews et al. 2016), V883 Ori (Cieza et al. 2016), HD163296 (Isella et al. 2016), HL Tau (ALMA Partnership et al. 2015), Elias 2-27 (Pérez et al. 2016), HD142527 (Kataoka et al. 2016). Credits: S. Andrews, L. Cieza, A. Isella, A. Kataoka, B. Saxton (NRAO/AUI/NSF), and ALMA (ESO/NAOJ/NRAO).

with simple parametric models but the modest uv -coverage and low sensitivity made the disentanglement of several degenerate disk models difficult (Andrews et al. 2009, 2010; Isella et al. 2009). ALMA has already reached an unprecedented spatial resolution (see Fig. 1.7) and has revealed substructures, in the continuum emission of disks, that can trace various dust evolution processes. This thesis will use both molecular and continuum observations taken with ALMA to determine the formation origin of simple deuterated molecules.

1.6.2 Modeling

Each of the chapters in this thesis analyses molecular transitions obtained with the instruments presented in the previous section. The general methodology to model them includes first the adoption of pre-existent physical models from the literature. These models are obtained by fitting the SED with a parametric model of the dust surface density and a temperature profile calculated self-consistently with radiative transfer codes. The observed molecular lines are then interpreted using abundance models to calculate their resulting line emission that are either parametric or follow from detailed chemical calculations. The line radiative transfer is performed using the 3D radiative transfer code Line Modeling Engine (LIME) capable of calculating the population levels out of local thermodynamical equilibrium (LTE). In LTE the population of the molecular energy states is given by a Boltzmann distribution of the form

$$\frac{n_u}{n_l} = \exp\left(-\frac{E_u - E_l}{k_B T_K}\right) \quad (1.20)$$

where T_K is the kinetic temperature of the gas and k_B is the Boltzmann constant. In non-LTE the population energy levels are calculated by solving the population number of the levels in statistical equilibrium

$$\frac{\partial n_u}{\partial t} = -n_u(A_{ul} + B_{ul}\bar{J} + C_{ul}) + n_l(B_{lu}\bar{J} + C_{lu}) = 0 \quad (1.21)$$

where A_{ul} and B_{ul} are the Einstein coefficients, C_{ul} are the collisional rates and \bar{J} is the line profile integrated mean intensity. The first term accounts for spontaneous emission, induced emission and collisional de-excitation and the second term for absorption and collisional excitation, respectively. We can define an excitation temperature (T_{ex}) for the molecular transition calculating the population ratio of the upper and lower energy levels as $n_u/n_l = \exp(-(E_u - E_l)/k_B T_{\text{ex}})$. In the limit where the density of the collisional partner exceeds a critical density, defined as $n_{\text{crit}} = A_{ul}/C_{ul}$, collisions drive the excitation to LTE and we recover the LTE distribution of Eq. 1.20 with $T_{\text{ex}} = T_K$. The following sections briefly describe the radiative transfer codes used in this thesis.

Physical models

The TORUS code (Pinte et al. 2009; Harries et al. 2004; Harries 2000) is a Monte Carlo radiative transfer code in 3D that fully treats polarization and multiple scattering. It can use either Mie or Rayleigh scattering. The temperatures are computed treating the dust in local thermodynamic equilibrium being only heated by stellar radiation. Radiative equilibrium is computed using the continuous absorption algorithm from Lucy (1999). All the calculations are performed on a cylindrical adaptive-mesh in 2D. The temperature structure is computed with a diffusion approximation method.

The RADMC code (Dullemond & Dominik 2004a) is a Monte Carlo continuum axisymmetric 3D radiative transfer code. It employs the algorithm from Bjorkman & Wood (2001)

but with a continuous treatment of energy instead of the discrete original one. The radiation is propagated using isotropic scattering, unlike the TORUS code that performs anisotropic scattering, and it computes the dust temperature.

Radiative transfer (LIME)

LIME is a non-LTE radiation transfer code for (sub)millimeter, far-IR continuum and spectral lines, that has the advantage of working with an arbitrary 3D geometry faster than other radiative transfer codes. It was developed by Christian Brinch (Brinch 2008; Brinch & Hogerheijde 2010) as a derivation from the RATRAN code (Hogerheijde & van der Tak 2000). Whereas RATRAN uses a Cartesian grid, LIME uses a random grid that adapts to the provided density structure or other aspects of interest (e.g. the molecular abundances). After the points have been chosen LIME constructs a Delaunay triangulation (Barber et al. 1996) and its corresponding Voronoi tessellation that define the cells that are represented by the physical properties of the grid points.

LIME requires the rate coefficients of the line transitions and dust opacities as separate inputs. Throughout this thesis the Einstein A_{ul} and collisional C_{ul} coefficients are taken from the LAMBDA database (Schöier et al. 2005). The opacities are taken from Ossenkopf & Henning (1994) for a standard dust size grain distribution.

1.7 This thesis

1.7.1 Aim

The rapid advance of observational techniques has unveiled very rich and complex structures in protoplanetary disks. The arrival of ALMA revealed exquisite substructure in the mm-grain distribution (e.g. Zhang et al. 2016; Isella et al. 2016; ALMA Partnership et al. 2015) and in molecular emission (e.g. Qi et al. 2015; Carney et al. 2017; Öberg et al. 2015). This makes ALMA an excellent instrument to explore the impact of the radial and vertical distributions of mm-sized dust into the distribution of molecules and their formation pathways. This thesis aims to understand the processes and formation origins that shape the structures and distributions seen in major nitrogen, oxygen and carbon species by contrasting them with the structures produced by dust evolution, photo-processes and gas-phase chemistry. Specifically we aim to answer two questions: **what is the spatial distribution of the main oxygen- and nitrogen-bearing species in planet-forming disks as probed by water and ammonia?** and **what is the relationship between physical features, such as the location of the CO snowline and substructures of temperature and the distribution of large dust grains, and the formation and chemistry of common molecular species?**

To this end we focus on two case studies: the disks surrounding TW Hya, a T Tauri star, and HD163296, a Herbig Ae star. Their high disk mass and proximity makes them excellent laboratories to explore the structure of the dust and simple molecules. These disks have been widely studied and modeled in past literature. TW Hya is a close (56 pc van Leeuwen 2007) low-mass star ($\sim 0.8 M_{\odot}$) hosting a disk of mass $\sim 0.04 M_{\odot}$ (Cleeves et al. 2014; Bergin et al. 2013; Webb et al. 1999). It is estimated from stellar evolutionary tracks to be between 8-10 Myr old (Hoff et al. 1998; Webb et al. 1999; de la Reza et al. 2006; Debes et al. 2013) with some uncertainties depending on the assumed stellar type (Vacca & Sandell 2011). The TW Hya disk is almost face on (7°) and its gas content extends radially to ~ 200 AU (Qi et al. 2004). The Herbig Ae star HD163296 is an intermediate-mass star ($2.3 M_{\odot}$) at 122 pc (Perryman et al. 1997) surrounded by a disk with a mass of $\sim 0.09 M_{\odot}$ (Qi et al. 2011).

Unlike TW Hya, it is inclined by 44° and its gas content extends up to 500 AU in radius (Mathews et al. 2013). This thesis uses data from the HIFI instrument on board *Herschel* and ALMA data of molecular lines and millimeter continuum toward these sources.

In **Chapter 2** we use ALMA Band 7 continuum data at $820\ \mu\text{m}$ of TW Hya to fit a model of the surface density to probe the mm-sized dust radial distribution. The interferometric visibilities are described by a model with a broken power law with slopes of -0.57 and -8.0 and a turn-over radius of ~ 47 AU. This is consistent with the expected shape of the surface distribution in the presence of grain growth and radial migration (Birnstiel & Andrews 2014). However, the derived turn-over radius and the total surface brightness are too large for a disk of 8-10 Myr. This could be reconciled considering a much larger initial disk size and disk mass, a gap halting the inward radial drift opened by an unseen embedded planet or a locally enhanced production rate of mm-sized grains due to the higher sticking efficiency of icy grains in the region outside the CO snowline.

In **Chapter 3**, the detection of the *o*-NH₃ $1_0 - 0_0$ line with the HIFI instrument on board *Herschel* toward TW Hya is presented; the first ever toward a planet-forming disk. Together with past detections of the ground-state rotational lines of *o*-H₂O and *p*-H₂O towards the same source, this chapter explores the radial and vertical distribution of these species under the assumption that water and ammonia ices are intermixed and co-desorbing. Only a compact and settled distribution of gas-phase NH₃ and H₂O, following the millimeter continuum emission radial extent of $r \lesssim 60$ AU, is consistent with the NH₃/H₂O ratio of interstellar ices and solar system bodies of $\sim 5\%$ - 10% . Additional gas-phase formation of NH₃ is needed to reconcile the observed emission with any other possible configuration. The total reservoir of water and ammonia in the disk is estimated to be about six orders of magnitude higher than the gas-phases masses of NH₃ and H₂O for any of the explored distributions indicating that the majority of these molecules are locked up in ices.

Chapter 4 continues to explore the spatial location of gas-phase NH₃, this time in the disk around HD163296. Both *Herschel* data of the *o*-NH₃ $1_0 - 0_0$ line and ALMA data of the *p*-NH₂D $1_0 - 0_0$ line result in non-detections, that still provide meaningful upper limits. Two radial distribution models of the distribution of these molecules are considered: one following the millimeter continuum emission at $r \lesssim 290$ AU, like the preferred TW Hya model from Chapter 3, and another one extending up to $r \lesssim 500$ AU, the full extent of the disk. The derived upper limits for the total mass of gas-phase *o*-NH₃ and *p*-NH₂D suggest that this disk is NH₃-poor, by a factor of 5 at least, compared to the similar-mass disk of TW Hya. Comparing other nitrogen-bearing species found in the literature toward these two disks indicates that this difference is due to the formation pathway of ammonia and not an overall lack of elemental nitrogen.

Chapter 5 focuses in the radial characterization of three simple deuterated species, DCO⁺, DCN, and N₂D⁺ detected with ALMA in Band 6 in the disk of HD163296. Assuming optically thin lines and LTE to convert line fluxes to column densities, the radial emission profile of the DCO⁺, DCN and N₂D⁺ lines is fitted using parametric abundance profiles. The DCO⁺ radial emission profile is described by three consecutive radial regions with different constant abundances from ~ 50 AU to ~ 316 AU with two radial breaks at ~ 118 AU and ~ 245 AU. The best-fit models of the radial emission profiles of DCN and N₂D⁺ correlate spatially with the first two radial regions of the best-fit model of DCO⁺. We interpret this as an indication of the correlation of their chemical pathways; DCN and N₂D⁺ form through the warm and cold deuteration channel, respectively, while DCO⁺ is thought to form through both channels. The origin of the third DCO⁺ radial region, from ~ 245 AU to ~ 316 AU, may trace a thermal inversion at large radii, a local decrease of the ortho-to-para ratio of H₂ or a decrease of the UV opacity due to grain growth.

Chapter 6 continues the analysis of the DCO^+ radial emission profile through simple chemical modelling of the cold deuteration channel and a parametric treatment of the warm deuteration channel in 2D. This simple chemical model coupled with a thermal inversion at ~ 260 AU reproduces the third radial region identified in Chapter 5. Radial thermal inversions are predicted by theoretical models as a direct consequence of radial drift and settling of dust grains (Facchini et al. 2017).

1.7.2 Overall conclusions

The above summaries contain the specific conclusions drawn from the data and modelling of each chapter. This section presents the overall conclusions of this thesis aimed at answering the two questions posed in our initial goal (see Sec. 1.7.1). First, regarding the location of NH_3 and H_2O in planet forming disks we conclude that:

- Gas-phase NH_3 and H_2O in TW Hya emit from a compact and settled spatial configuration that follows the ice reservoir trapped in large bodies which is several orders of magnitude higher than the amount of gas-phase material. This means that the location of oxygen- and nitrogen-bearing volatiles in disks are set by grain evolution, in particular radial drift (Chapter 3).
- Additional spatially resolved observations of these molecules toward these planet-forming disks are crucial to confirm these scenarios. The deuterated isotopologues of NH_3 and H_2O are readily detected with ALMA in a few hours toward TW Hya and HD163296 (Chapters 3 & 4).

Second, regarding the effect of the physical structures on the distribution of simple molecules (and vice versa) we can conclude that:

- The spatial location of temperature-sensitive species, such as DCO^+ , trace substructures in the temperature profile of protoplanetary disks and therefore (indirectly) the impact of dust evolution process on its morphology. Although to first order the temperature profile is determined by the disk's exposure to stellar radiation, dust grain evolution models show that settling and radial drift have an important role in creating substructures in the temperature profile (Chapters 5 & 6).
- The inverse process, namely how the location of simple molecules can impact dust evolution, can be studied by comparing the location of the snowline of main molecular species and the shape of the millimeter emission in planet-forming disks (Chapter 2).

1.7.3 Future outlook

ALMA has brought us impressively high spatial resolution images of protoplanetary disks these past six years. The recent effort to push its limits delivered an incredibly detailed image of a set of rings in the embedded disk around HL Tau as part of the Long Baseline Campaign (ALMA Partnership et al. 2015). Rich structures are hidden below the resolution of the observations presented in this thesis that affect the observed molecules. This is especially true for single-dish observation in the far-IR where no spatial information can be recovered. The high sensitivity and spatial resolution of ALMA can provide the means to disentangle both the distribution of key molecules, e.g. deuterated isotopologues of H_2O and NH_3 , as well as the distribution of the millimeter-sized dust in the continuum. In addition,

multifrequency analysis of ALMA data can put a constraint on dust evolution indicators, such as the degree of dust growth toward planet-forming disks.

New mid and far infrared space facilities, with higher sensitivities than *Herschel*, will allow us to expand the detection sample of key carbon-, oxygen- and nitrogen-bearing species toward disks. So far key features of disks, such as the location of snowlines, the millimeter and infrared emission profile, and the distribution of main volatiles have been determined in a handful of disks with very different physical properties. This is in part due to the limited capabilities of the current instruments. Instruments like the mid-infrared MIRI instrument on board the future James Webb Space Telescope (JWST), the SMI on board the planned Space Infrared Telescope for Cosmology and Astrophysics (SPICA) and the Origins Space Telescope (OST) will be able to observe rotational and vibrational molecular transitions of key molecules such as HD, CO and H₂O in the warm environments of the disk, ice features and resolved images of scattered light.

New infrared and visible light instruments, like METIS at the future Extremely Large Telescope (ELT), will probe the disk surface through scattered light revealing signatures of dynamical interactions. SPHERE, at the Very Large Telescope (VLT) has already produced protoplanetary disks images in polarized light with high spatial resolution showing partially shadowed disks and spiral structures (e.g. Stolker et al. 2016a,b). Observations of polarized scattered light can be used to probe the complex small dust structure of the disk surface that respond to planet-disk interactions. In addition, direct-imaging of potential companions, with techniques such as polarized differential imaging, can help in distinguishing the different scenarios that shape the structures in the millimeter regime.

The interpretation of the observables presented in this thesis rely on state-of-the-art dust evolution models. At this stage, most models are not tailored to individual sources and their input variables are poorly constrained. A comprehensive treatment of gas and dust temperature coupled with chemistry and grain evolution is necessary to fully understand individual sources. Although individual sources are good laboratories to try detailed models, a statistically relevant large sample of different protoplanetary disks would average out individual differences. Large surveys would allow the disk community to focus on general trends in the structure of disks that can potentially lead to stronger conclusions and a more comprehensive understanding of the planet formation process.

Bibliography

- Adams, F. C., Hollenbach, D., Laughlin, G., & Gorti, U. 2004, *ApJ*, 611, 360
 Agúndez, M., Cernicharo, J., & Goicoechea, J. R. 2008, *A&A*, 483, 831
 Aikawa, Y., Umebayashi, T., Nakano, T., & Miyama, S. M. 1999, *ApJ*, 519, 705
 Aikawa, Y., van Zadelhoff, G. J., van Dishoeck, E. F., & Herbst, E. 2002, *A&A*, 386, 622
 Aikawa, Y., Kamuro, D., Sakon, I., et al. 2012, *A&A*, 538, A57
 Akimkin, V., Zhukovska, S., Wiebe, D., et al. 2013, *ApJ*, 766, 8
 Albertsson, T., Semenov, D. A., Vasyunin, A. I., Henning, T., & Herbst, E. 2013, *ApJS*, 207, 27
 ALMA Partnership, Brogan, C. L., Pérez, L. M., et al. 2015, *ApJ*, 808, L3
 André, P., Ward-Thompson, D., & Barsony, M. 1993, *ApJ*, 406, 122
 Andrews, S. M., Rosenfeld, K. A., Kraus, A. L., & Wilner, D. J. 2013, *ApJ*, 771, 129
 Andrews, S. M., & Williams, J. P. 2005, *ApJ*, 631, 1134
 Andrews, S. M., Wilner, D. J., Espaillat, C., et al. 2011, *ApJ*, 732, 42
 Andrews, S. M., Wilner, D. J., Hughes, A. M., Qi, C., & Dullemond, C. P. 2009, *ApJ*, 700, 1502
 Andrews, S. M., Wilner, D. J., Hughes, A. M., Qi, C., & Dullemond, C. P. 2010, *ApJ*, 723, 1241

- Andrews, S. M., Wilner, D. J., Hughes, A. M., et al. 2012, *ApJ*, 744, 162
- Andrews, S. M., Wilner, D. J., Zhu, Z., et al. 2016, *ApJ*, 820, L40
- Ansdell, M., Williams, J. P., & Cieza, L. A. 2015, *ApJ*, 806, 221
- Ansdell, M., Williams, J. P., Manara, C. F., et al. 2017, *AJ*, 153, 240
- Ansdell, M., Williams, J. P., van der Marel, N., et al. 2016, *ApJ*, 828, 46
- Arce, H. G., & Sargent, A. I. 2004, *ApJ*, 612, 342
- Arce, H. G., & Sargent, A. I. 2006, *ApJ*, 646, 1070
- Armitage, P. J. 2011, *ARA&A*, 49, 195
- Atkinson, R., Baulch, D. L., Cox, R. A., et al. 2004, *Atmospheric Chemistry & Physics*, 4, 1461
- Bacmann, A., Lefloch, B., Ceccarelli, C., et al. 2003, *ApJ*, 585, L55
- Bai, X.-N. 2016, *ApJ*, 821, 80
- Bally, J., O'Dell, C. R., & McCaughrean, M. J. 2000, *AJ*, 119, 2919
- Barber, C. B., Dobkin, D. P., & Huhdanpaa, H. 1996, *ACM Trans. Math. Softw.*, 22, 469
- Barnes, R., Quinn, T. R., Lissauer, J. J., & Richardson, D. C. 2009, *Icarus*, 203, 626
- Beckwith, S. V. W., Sargent, A. I., Chini, R. S., & Guesten, R. 1990, *AJ*, 99, 924
- Bennett, C. J., Osamura, Y., Lebar, M. D., & Kaiser, R. I. 2005, *ApJ*, 634, 698
- Benz, A. O., Bruderer, S., van Dishoeck, E. F., et al. 2010, *A&A*, 521, L35
- Bergin, E., Calvet, N., D'Alessio, P., & Herczeg, G. J. 2003, *ApJ*, 591, L159
- Bergin, E. A., & van Dishoeck, E. F. 2012, *Philosophical Transactions of the Royal Society of London Series A*, 370, 2778
- Bergin, E. A., Cleeves, L. I., Gorti, U., et al. 2013, *Nature*, 493, 644
- Bernstein, M. P., Sandford, S. A., Allamandola, L. J., Chang, S., & Scharberg, M. A. 1995, *ApJ*, 454, 327
- Bethell, T., & Bergin, E. 2009, *Science*, 326, 1675
- Birnstiel, T., & Andrews, S. M. 2014, *ApJ*, 780, 153
- Birnstiel, T., Fang, M., & Johansen, A. 2016, *Space Sci. Rev.*, 205, 41
- Birnstiel, T., Klahr, H., & Ercolano, B. 2012, *A&A*, 539, A148
- Birnstiel, T., Ormel, C. W., & Dullemond, C. P. 2011, *A&A*, 525, A11
- Bjorkman, J. E., & Wood, K. 2001, *ApJ*, 554, 615
- Bonnor, W. B. 1956, *MNRAS*, 116, 351
- Boogert, A. C. A., Gerakines, P. A., & Whittet, D. C. B. 2015, *ARA&A*, 53, 541
- Boogert, A. C. A., Pontoppidan, K. M., Knez, C., et al. 2008, *ApJ*, 678, 985
- Bottinelli, S., Boogert, A. C. A., Bouwman, J., et al. 2010, *ApJ*, 718, 1100
- Brauer, F., Henning, T., & Dullemond, C. P. 2008, *A&A*, 487, L1
- Brinch, C. 2008, PhD thesis, Leiden University
- Brinch, C., & Hogerheijde, M. R. 2010, *A&A*, 523, A25
- Brown, J. M., Blake, G. A., Qi, C., et al. 2009, *ApJ*, 704, 496
- Brown, P. D., & Millar, T. J. 1989, *MNRAS*, 240, 25P
- Brownlee, D. 2014, *Annual Review of Earth and Planetary Sciences*, 42, 179
- Burkert, A., & Bodenheimer, P. 2000, *ApJ*, 543, 822
- Burrows, C. J., Stapelfeldt, K. R., Watson, A. M., et al. 1996, *ApJ*, 473, 437
- Calvet, N., D'Alessio, P., Hartmann, L., et al. 2002, *ApJ*, 568, 1008
- Calvet, N., Hartmann, L., Kenyon, S. J., & Whitney, B. A. 1994, *ApJ*, 434, 330
- Cameron, A. G. W. 1978, *Moon and Planets*, 18, 5
- Carney, M. T., Hogerheijde, M. R., Loomis, R. A., et al. 2017, *A&A*, 605, A21
- Carney, M. T., Yildiz, U. A., Mottram, J. C., et al. 2016, *A&A*, 586, A44
- Carr, J. S., & Najita, J. R. 2008, *Science*, 319, 1504
- Carr, J. S., & Najita, J. R. 2011, *ApJ*, 733, 102
- Caselli, P., & Ceccarelli, C. 2012, *A&A Rev.*, 20, 56

- Cassen, P., & Moosman, A. 1981, *Icarus*, 48, 353
- Cernicharo, J., & Crovisier, J. 2005, *Space Sci. Rev.*, 119, 29
- Chapillon, E., Guilloteau, S., Dutrey, A., Piétu, V., & Guélin, M. 2012a, *A&A*, 537, A60
- Chapillon, E., Dutrey, A., Guilloteau, S., et al. 2012b, *ApJ*, 756, 58
- Cheung, A. C., Rank, D. M., Townes, C. H., Thornton, D. D., & Welch, W. J. 1968, *Physical Review Letters*, 21, 1701
- Cheung, A. C., Rank, D. M., Townes, C. H., Thornton, D. D., & Welch, W. J. 1969, *Nature*, 221, 626
- Chiang, E. I., & Goldreich, P. 1997, *ApJ*, 490, 368
- Chiang, E. I., Joungh, M. K., Creech-Eakman, M. J., et al. 2001, *ApJ*, 547, 1077
- Cieza, L., Padgett, D. L., Stapelfeldt, K. R., et al. 2007, *ApJ*, 667, 308
- Cieza, L. A., Casassus, S., Tobin, J., et al. 2016, *Nature*, 535, 258
- Clarke, C. J. 2007, *MNRAS*, 376, 1350
- Clarke, C. J., Gendrin, A., & Sotomayor, M. 2001, *MNRAS*, 328, 485
- Cleeves, L. I., Bergin, E. A., Alexander, C. M. O. ., et al. 2014, *Science*, 345, 1590
- Cohen, M., & Kuhl, L. V. 1979, *ApJS*, 41, 743
- Combes, F., Boulanger, F., Encrenaz, P. J., et al. 1985, *A&A*, 147, L25
- Cooke, R. J., Pettini, M., Nollett, K. M., & Jorgenson, R. 2016, *ApJ*, 830, 148
- Cruz-Díaz, G. A., Muñoz Caro, G. M., & Jiménez-Escobar, A. 2012, in *EAS Publications Series*, Vol. 58, *EAS Publications Series*, ed. C. Stehlé, C. Joblin, & L. d'Hendecourt, 333–336
- D'Alessio, P., Calvet, N., & Hartmann, L. 2001, *ApJ*, 553, 321
- D'Alessio, P., Calvet, N., Hartmann, L., Franco-Hernández, R., & Servín, H. 2006, *ApJ*, 638, 314
- D'Alessio, P., Cantö, J., Calvet, N., & Lizano, S. 1998, *ApJ*, 500, 411
- Daranlot, J., Hincelin, U., Bergeat, A., et al. 2012, *Proceedings of the National Academy of Science*, 109, 10233
- de Graauw, T., Helmich, F. P., Phillips, T. G., et al. 2010, *A&A*, 518, L6
- de la Reza, R., Jilinski, E., & Ortega, V. G. 2006, *AJ*, 131, 2609
- Debes, J. H., Jang-Condell, H., Weinberger, A. J., Roberge, A., & Schneider, G. 2013, *ApJ*, 771, 45
- Dib, S., Hennebelle, P., Pineda, J. E., et al. 2010, *ApJ*, 723, 425
- Dionatos, O. 2015, in *European Physical Journal Web of Conferences*, Vol. 102, *European Physical Journal Web of Conferences*, 00008
- Draine, B. T. 2003, *ARA&A*, 41, 241
- Draine, B. T. 2006, *ApJ*, 636, 1114
- Dubrulle, B., Morfill, G., & Sterzik, M. 1995, *Icarus*, 114, 237
- Dulieu, F., Amiaud, L., Congiu, E., et al. 2010, *A&A*, 512, A30
- Dullemond, C. P., & Dominik, C. 2004a, *A&A*, 417, 159
- Dullemond, C. P., & Dominik, C. 2004b, *A&A*, 421, 1075
- Dullemond, C. P., & Dominik, C. 2005, *A&A*, 434, 971
- Dullemond, C. P., & Dominik, C. 2008, *A&A*, 487, 205
- Dullemond, C. P., Henning, T., Visser, R., et al. 2007, *A&A*, 473, 457
- Dunham, M. M., Arce, H. G., Mardones, D., et al. 2014, *ApJ*, 783, 29
- Dutrey, A., Guilloteau, S., & Guélin, M. 1997, *A&A*, 317, L55
- Dutrey, A., Wakelam, V., Boehler, Y., et al. 2011, *A&A*, 535, A104
- Ebert, R. 1955, in *Liege International Astrophysical Colloquia*, Vol. 6, *Liege International Astrophysical Colloquia*, 666–672
- Elitzur, M., & Watson, W. D. 1978, *ApJ*, 222, L141
- Evans, N. J., Dunham, M. M., Jorgensen, J. K., et al. 2009, *VizieR Online Data Catalog*, 218

- Facchini, S., Birnstiel, T., Bruderer, S., & van Dishoeck, E. F. 2017, *A&A*, 605, A16
- Favre, C., Bergin, E. A., Cleeves, L. I., et al. 2015, *ApJ*, 802, L23
- Fayolle, E. C., Öberg, K. I., Cuppen, H. M., Visser, R., & Linnartz, H. 2011, *A&A*, 529, A74
- Fedele, D., Bruderer, S., van Dishoeck, E. F., et al. 2012, *A&A*, 544, L9
- Fedele, D., van den Ancker, M. E., Henning, T., Jayawardhana, R., & Oliveira, J. M. 2010, *A&A*, 510, A72
- Fedele, D., Bruderer, S., van Dishoeck, E. F., et al. 2013, *A&A*, 559, A77
- Fedoseev, G., Chuang, K.-J., Ioppolo, S., et al. 2017, *ApJ*, 842, 52
- Fedoseev, G., Ioppolo, S., Zhao, D., Lamberts, T., & Linnartz, H. 2015, *MNRAS*, 446, 439
- Flower, D. R., Pineau Des Forêts, G., & Walmsley, C. M. 2006, *A&A*, 449, 621
- Fogel, J. K. J., Bethell, T. J., Bergin, E. A., Calvet, N., & Semenov, D. 2011, *ApJ*, 726, 29
- Furuya, K., & Aikawa, Y. 2014, *ApJ*, 790, 97
- Garaud, P., Meru, F., Galvagni, M., & Olczak, C. 2013, *ApJ*, 764, 146
- Garrod, R. T., Wakelam, V., & Herbst, E. 2007, *A&A*, 467, 1103
- Genzel, R. 1992, in *Saas-Fee Advanced Course 21: The Galactic Interstellar Medium*, ed. W. B. Burton, B. G. Elmegreen, & R. Genzel, 275–391
- Gerner, T., Shirley, Y. L., Beuther, H., et al. 2015, *A&A*, 579, A80
- Getman, K. V., Feigelson, E. D., Luhman, K. L., et al. 2009, *ApJ*, 699, 1454
- Gibb, E. L., Whittet, D. C. B., Boogert, A. C. A., & Tielens, A. G. G. M. 2004, *ApJS*, 151, 35
- Gillett, F. C., & Forrest, W. J. 1973, *ApJ*, 179, 483
- Goodman, A. A., Benson, P. J., Fuller, G. A., & Myers, P. C. 1993, *ApJ*, 406, 528
- Gorti, U., Dullemond, C. P., & Hollenbach, D. 2009, *ApJ*, 705, 1237
- Gorti, U., & Hollenbach, D. 2004, *ApJ*, 613, 424
- Greaves, J. S., & Rice, W. K. M. 2010, *MNRAS*, 407, 1981
- Greenberg, R., Hartmann, W. K., Chapman, C. R., & Wacker, J. F. 1978, *Icarus*, 35, 1
- Griffin, M. J., Abergel, A., Abreu, A., et al. 2010, *A&A*, 518, L3
- Güdel, M., & Nazé, Y. 2009, *A&A Rev.*, 17, 309
- Haghighipour, N. 2013, *Annual Review of Earth and Planetary Sciences*, 41, 469
- Harada, N., Herbst, E., & Wakelam, V. 2010, *ApJ*, 721, 1570
- Harju, J., Daniel, F., Sipilä, O., et al. 2017, *A&A*, 600, A61
- Harker, D. E., & Desch, S. J. 2002, *ApJ*, 565, L109
- Harries, T. J. 2000, *MNRAS*, 315, 722
- Harries, T. J., Monnier, J. D., Symington, N. H., & Kurosawa, R. 2004, *MNRAS*, 350, 565
- Harsono, D. 2014, PhD thesis, Leiden University, doi:10.5281/zenodo.29224
- Hartmann, L., Calvet, N., Gullbring, E., & D'Alessio, P. 1998, *ApJ*, 495, 385
- Hasegawa, T. I., & Herbst, E. 1993, *MNRAS*, 261, 83
- Hayashi, C. 1981, *Progress of Theoretical Physics Supplement*, 70, 35
- Heays, A. N., Bosman, A. D., & van Dishoeck, E. F. 2017, *A&A*, 602, A105
- Henning, T., & Semenov, D. 2013, *Chemical Reviews*, 113, 9016
- Henning, T., Semenov, D., Guilloteau, S., et al. 2010, *ApJ*, 714, 1511
- Herbig, G. H. 1977, *ApJ*, 214, 747
- Herbst, E., & Klemperer, W. 1973, *ApJ*, 185, 505
- Herbst, E., & van Dishoeck, E. F. 2009, *ARA&A*, 47, 427
- Hildebrand, R. H. 1983, *QJRAS*, 24, 267
- Hirose, S., & Turner, N. J. 2011, *ApJ*, 732, L30
- Hoff, W., Henning, T., & Pfau, W. 1998, *A&A*, 336, 242
- Hogerheijde, M., & van der Tak, F. 2000, *RATTRAN: Radiative Transfer and Molecular Excitation in One and Two Dimensions*, Astrophysics Source Code Library, ascl:0008.002
- Hogerheijde, M. R., Bergin, E. A., Brinch, C., et al. 2011, *Science*, 334, 338

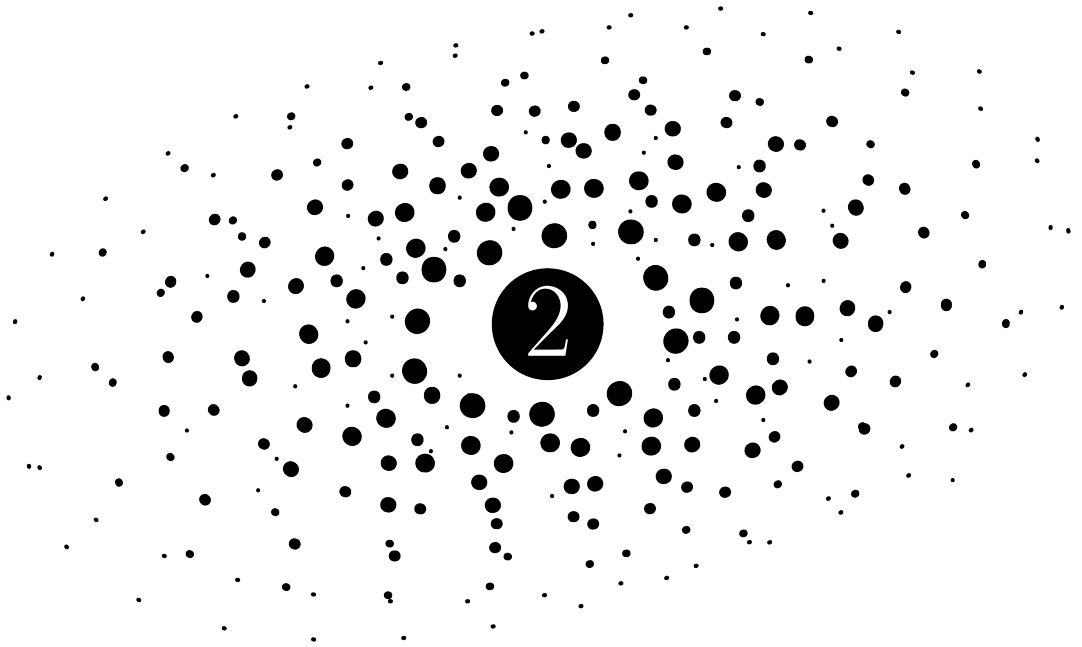
- Hueso, R., & Guillot, T. 2005, *A&A*, 442, 703
- Hughes, A. M., Wilner, D. J., Andrews, S. M., Qi, C., & Hogerheijde, M. R. 2011, *ApJ*, 727, 85
- Hughes, A. M., Wilner, D. J., Qi, C., & Hogerheijde, M. R. 2008, *ApJ*, 678, 1119
- Ida, S., & Makino, J. 1993, *Icarus*, 106, 210
- Ilgner, M., Henning, T., Markwick, A. J., & Millar, T. J. 2004, *A&A*, 415, 643
- Ioppolo, S., Cuppen, H. M., Romanzin, C., van Dishoeck, E. F., & Linnartz, H. 2008, *ApJ*, 686, 1474
- Irvine, W. M., Goldsmith, P. F., & Hjalmarnson, A. 1987, in *Astrophysics and Space Science Library*, Vol. 134, *Interstellar Processes*, ed. D. J. Hollenbach & H. A. Thronson, Jr., 561–609
- Irvine, W. M., Schloerb, F. P., Crovisier, J., Fegley, Jr., B., & Mumma, M. J. 2000, *Protostars and Planets IV*, 1159
- Isella, A., Carpenter, J. M., & Sargent, A. I. 2009, *ApJ*, 701, 260
- Isella, A., Testi, L., Natta, A., et al. 2007, *A&A*, 469, 213
- Isella, A., Guidi, G., Testi, L., et al. 2016, *Physical Review Letters*, 117, 251101
- Jeans, J. H. 1902, *Philosophical Transactions of the Royal Society of London Series A*, 199, 1
- Johansen, A., Oishi, J. S., Mac Low, M.-M., et al. 2007, *Nature*, 448, 1022
- Jonkheid, B., Kamp, I., Augereau, J.-C., & van Dishoeck, E. F. 2006, *A&A*, 453, 163
- Kastner, J. H., Zuckerman, B., Weintraub, D. A., & Forveille, T. 1997, *Science*, 277, 67
- Kataoka, A., Tsukagoshi, T., Momose, M., et al. 2016, *ApJ*, 831, L12
- Kennedy, G. M., & Kenyon, S. J. 2008, *ApJ*, 673, 502
- Kenyon, S. J., & Hartmann, L. 1987, *ApJ*, 323, 714
- Kenyon, S. J., & Hartmann, L. W. 1990, *ApJ*, 349, 197
- Kessler-Silacci, J. E., Dullemond, C. P., Augereau, J.-C., et al. 2007, *ApJ*, 659, 680
- Knacke, R. F., McCorkle, S., Puetter, R. C., Erickson, E. F., & Kraetschmer, W. 1982, *ApJ*, 260, 141
- Königl, A., & Salmeron, R. 2011, *The Effects of Large-Scale Magnetic Fields on Disk Formation and Evolution*, ed. P. J. V. Garcia, 283–352
- Lada, C. J. 1987, in *IAU Symposium*, Vol. 115, *Star Forming Regions*, ed. M. Peimbert & J. Jugaku, 1–17
- Lahuis, F., van Dishoeck, E. F., Boogert, A. C. A., et al. 2006, *ApJ*, 636, L145
- Lambrechts, M., & Johansen, A. 2014, *A&A*, 572, A107
- Le Gal, R., Hily-Blant, P., Faure, A., et al. 2014, *A&A*, 562, A83
- Lee, N., Williams, J. P., & Cieza, L. A. 2011, *ApJ*, 736, 135
- Leger, A., Jura, M., & Omont, A. 1985, *A&A*, 144, 147
- Lissauer, J. J. 1993, *ARA&A*, 31, 129
- Lissauer, J. J., Marcy, G. W., Rowe, J. F., et al. 2012, *ApJ*, 750, 112
- Lucy, L. B. 1999, *A&A*, 345, 211
- Lynden-Bell, D., & Pringle, J. E. 1974, *MNRAS*, 168, 603
- Lyra, W., Johansen, A., Zsom, A., Klahr, H., & Piskunov, N. 2009, *A&A*, 497, 869
- Malfait, K., Waelkens, C., Bouwman, J., de Koter, A., & Waters, L. B. F. M. 1999, *A&A*, 345, 181
- Mandell, A. M., Bast, J., van Dishoeck, E. F., et al. 2012, *ApJ*, 747, 92
- Mann, R. K., & Williams, J. P. 2009, *ApJ*, 699, L55
- Markwick, A. J., Ilgner, M., Millar, T. J., & Henning, T. 2002, *A&A*, 385, 632
- Mathews, G. S., Klaassen, P. D., Juhász, A., et al. 2013, *A&A*, 557, A132
- Mathis, J. S., Rumpl, W., & Nordsieck, K. H. 1977, *ApJ*, 217, 425
- Matsuyama, I., Johnstone, D., & Hollenbach, D. 2009, *ApJ*, 700, 10

- Mayor, M., & Queloz, D. 1995, *Nature*, 378, 355
- McCaughrean, M. J., & O'dell, C. R. 1996, *AJ*, 111, 1977
- McClure, M. K., Furlan, E., Manoj, P., et al. 2010, *ApJS*, 188, 75
- McClure, M. K., Manoj, P., Calvet, N., et al. 2012, *ApJ*, 759, L10
- Meeus, G., Montesinos, B., Mendigutía, I., et al. 2012, *A&A*, 544, A78
- Meeus, G., Salyk, C., Bruderer, S., et al. 2013, *A&A*, 559, A84
- Melnick, G. J. 2009, in *Astronomical Society of the Pacific Conference Series*, Vol. 417, *Submillimeter Astrophysics and Technology: a Symposium Honoring Thomas G. Phillips*, ed. D. C. Lis, J. E. Vaillancourt, P. F. Goldsmith, T. A. Bell, N. Z. Scoville, & J. Zmuidzinas, 59
- Merrill, K. M., Russell, R. W., & Soifer, B. T. 1976, *ApJ*, 207, 763
- Millar, T. J., Bennett, A., & Herbst, E. 1989, *ApJ*, 340, 906
- Miotello, A., van Dishoeck, E. F., Kama, M., & Bruderer, S. 2016, *A&A*, 594, A85
- Miyauchi, N., Hidaka, H., Chigai, T., et al. 2008, *Chemical Physics Letters*, 456, 27
- Moore, M. H., & Hudson, R. L. 1998, *Icarus*, 135, 518
- Morbidelli, A., Chambers, J., Lunine, J. I., et al. 2000, *Meteoritics and Planetary Science*, 35, 1309
- Mordasini, C., Alibert, Y., Benz, W., Klahr, H., & Henning, T. 2012, *A&A*, 541, A97
- Morris, M., Zuckerman, B., Palmer, P., & Turner, B. E. 1973, *ApJ*, 186, 501
- Mumma, M. J., & Charnley, S. B. 2011, *ARA&A*, 49, 471
- Najita, J., Bergin, E. A., & Ullom, J. N. 2001, *ApJ*, 561, 880
- Najita, J. R., Ádámkóvics, M., & Glassgold, A. E. 2011, *ApJ*, 743, 147
- Nakagawa, Y., Sekiya, M., & Hayashi, C. 1986, *Icarus*, 67, 375
- Natta, A. 1993, *ApJ*, 412, 761
- Natta, A., Grinin, V., & Mannings, V. 2000, *Protostars and Planets IV*, 559
- Natta, A., Testi, L., Neri, R., Shepherd, D. S., & Wilner, D. J. 2004, *A&A*, 416, 179
- Öberg, K. I. 2009, PhD thesis, Leiden University
- Öberg, K. I., Boogert, A. C. A., Pontoppidan, K. M., et al. 2011a, *ApJ*, 740, 109
- Öberg, K. I., Fuchs, G. W., Awad, Z., et al. 2007, *ApJ*, 662, L23
- Öberg, K. I., Furuya, K., Loomis, R., et al. 2015, *ApJ*, 810, 112
- Öberg, K. I., Linnartz, H., Visser, R., & van Dishoeck, E. F. 2009a, *ApJ*, 693, 1209
- Öberg, K. I., Qi, C., Wilner, D. J., & Andrews, S. M. 2011b, *ApJ*, 743, 152
- Öberg, K. I., Qi, C., Wilner, D. J., & Hogerheijde, M. R. 2012, *ApJ*, 749, 162
- Öberg, K. I., van Dishoeck, E. F., & Linnartz, H. 2009b, *A&A*, 496, 281
- Öberg, K. I., Qi, C., Fogel, J. K. J., et al. 2010, *ApJ*, 720, 480
- Öberg, K. I., Qi, C., Fogel, J. K. J., et al. 2011c, *ApJ*, 734, 98
- Oliveira, I., Olofsson, J., Pontoppidan, K. M., et al. 2011, *ApJ*, 734, 51
- Olofsson, J., Augereau, J.-C., van Dishoeck, E. F., et al. 2010, *A&A*, 520, A39
- Olofsson, J., Augereau, J.-C., van Dishoeck, E. F., et al. 2009, *A&A*, 507, 327
- Ormel, C. W., & Klahr, H. H. 2010, *A&A*, 520, A43
- Ossenkopf, V., & Henning, T. 1994, *A&A*, 291, 943
- Owen, J. E., Ercolano, B., Clarke, C. J., & Alexander, R. D. 2010, *MNRAS*, 401, 1415
- Padgett, D. L., Brandner, W., Stapelfeldt, K. R., et al. 1999, *AJ*, 117, 1490
- Pagani, L., Vastel, C., Hugo, E., et al. 2009, *A&A*, 494, 623
- Panić, O., Hogerheijde, M. R., Wilner, D., & Qi, C. 2009, *A&A*, 501, 269
- Pascucci, I., Apai, D., Luhman, K., et al. 2009, *ApJ*, 696, 143
- Pavlyuchenkov, Y., & Dullemond, C. P. 2007, *A&A*, 471, 833
- Pérez, L. M., Carpenter, J. M., Andrews, S. M., et al. 2016, *Science*, 353, 1519
- Perryman, M. A. C., Lindegren, L., Kovalevsky, J., et al. 1997, *A&A*, 323, L49

- Persson, C. M., Black, J. H., Cernicharo, J., et al. 2010, *A&A*, 521, L45
- Pfalzner, S., Umbreit, S., & Henning, T. 2005a, *ApJ*, 629, 526
- Pfalzner, S., Vogel, P., Scharwächter, J., & Olczak, C. 2005b, *A&A*, 437, 967
- Piétu, V., Dutrey, A., Guilloteau, S., Chapillon, E., & Pety, J. 2006, *A&A*, 460, L43
- Piétu, V., Guilloteau, S., & Dutrey, A. 2005, *A&A*, 443, 945
- Pinilla, P., van der Marel, N., Pérez, L. M., et al. 2015, *A&A*, 584, A16
- Pinte, C., Harries, T. J., Min, M., et al. 2009, *A&A*, 498, 967
- Pinto, R. F., Brun, A. S., Jouve, L., & Grappin, R. 2011, *ApJ*, 737, 72
- Poglitsch, A., Waelkens, C., Geis, N., et al. 2010, *A&A*, 518, L2
- Pollack, J. B., Hollenbach, D., Beckwith, S., et al. 1994, *ApJ*, 421, 615
- Pollack, J. B., Hubickyj, O., Bodenheimer, P., et al. 1996, *Icarus*, 124, 62
- Pontoppidan, K. M., Dullemond, C. P., van Dishoeck, E. F., et al. 2005, *ApJ*, 622, 463
- Pontoppidan, K. M., Salyk, C., Blake, G. A., & Käufl, H. U. 2010, *ApJ*, 722, L173
- Prasad, S. S., & Tarafdar, S. P. 1983, *ApJ*, 267, 603
- Preibisch, T., Kim, Y.-C., Favata, F., et al. 2005, *ApJS*, 160, 401
- Prodanović, T., Steigman, G., & Fields, B. D. 2010, *MNRAS*, 406, 1108
- Qi, C., D'Alessio, P., Öberg, K. I., et al. 2011, *ApJ*, 740, 84
- Qi, C., Öberg, K. I., Andrews, S. M., et al. 2015, *ApJ*, 813, 128
- Qi, C., Ho, P. T. P., Wilner, D. J., et al. 2004, *ApJ*, 616, L11
- Qi, C., Öberg, K. I., Wilner, D. J., et al. 2013, *Science*, 341, 630
- Riviere-Marichalar, P., Merín, B., Kamp, I., Eiroa, C., & Montesinos, B. 2016, *A&A*, 594, A59
- Riviere-Marichalar, P., Ménard, F., Thi, W. F., et al. 2012, *A&A*, 538, L3
- Roberts, H., Fuller, G. A., Millar, T. J., Hatchell, J., & Buckle, J. V. 2002, *Planet. Space Sci.*, 50, 1173
- Roueff, E., Loison, J. C., & Hickson, K. M. 2015, *A&A*, 576, A99
- Safronov, V. S. 1972, *Evolution of the protoplanetary cloud and formation of the earth and planets*. (Israel Program for Scientific Translations, Keter Publishing House, 212 p.)
- Salter, D. M. 2010, PhD thesis, Leiden University
- Salyk, C., Pontoppidan, K. M., Blake, G. A., et al. 2008, *ApJ*, 676, L49
- Salyk, C., Pontoppidan, K. M., Blake, G. A., Najita, J. R., & Carr, J. S. 2011, *ApJ*, 731, 130
- Schöier, F. L., van der Tak, F. F. S., van Dishoeck, E. F., & Black, J. H. 2005, *A&A*, 432, 369
- Schreyer, K., Guilloteau, S., Semenov, D., et al. 2008, *A&A*, 491, 821
- Semenov, D., Pavlyuchenkov, Y., Schreyer, K., et al. 2005, *ApJ*, 621, 853
- Semenov, D., & Wiebe, D. 2011, *ApJS*, 196, 25
- Shakura, N. I., Sunyaev, R. A., & Zilitinkevich, S. S. 1978, *A&A*, 62, 179
- Sipilä, O., Harju, J., Caselli, P., & Schlemmer, S. 2015, *A&A*, 581, A122
- Smith, N., Bally, J., Licht, D., & Walawender, J. 2005, *AJ*, 129, 382
- Smith, R. G., Sellgren, K., & Tokunaga, A. T. 1989, *ApJ*, 344, 413
- Stapelfeldt, K. R., Burrows, C. J., Krist, J. E., et al. 1998, *ApJ*, 508, 736
- Stolker, T., Dominik, C., Min, M., et al. 2016a, *A&A*, 596, A70
- Stolker, T., Dominik, C., Avenhaus, H., et al. 2016b, *A&A*, 595, A113
- Sturm, B., Bouwman, J., Henning, T., et al. 2010, *A&A*, 518, L129
- Terada, H., & Tokunaga, A. T. 2017, *ApJ*, 834, 115
- Terada, H., Tokunaga, A. T., Kobayashi, N., et al. 2007, *ApJ*, 667, 303
- Terebey, S., Shu, F. H., & Cassen, P. 1984, *ApJ*, 286, 529
- Thi, W. F., Pontoppidan, K. M., van Dishoeck, E. F., Dartois, E., & d'Hendecourt, L. 2002, *A&A*, 394, L27
- Thi, W.-F., van Zadelhoff, G.-J., & van Dishoeck, E. F. 2004, *A&A*, 425, 955
- Thies, I., Kroupa, P., Goodwin, S. P., Stamatellos, D., & Whitworth, A. P. 2010, *ApJ*, 717, 577

- Tielens, A. G. G. M. 1983, *A&A*, 119, 177
Tielens, A. G. G. M. 2008, *ARA&A*, 46, 289
Turner, B. E. 2001, *ApJS*, 136, 579
Turner, N. J., Fromang, S., Gammie, C., et al. 2014, *Protostars and Planets VI*, 411
Ulrich, R. K. 1976, *ApJ*, 210, 377
Vacca, W. D., & Sandell, G. 2011, *ApJ*, 732, 8
van Boekel, R., Min, M., Waters, L. B. F. M., et al. 2005, *A&A*, 437, 189
van de Hulst, H. C. 1946, *Recherches Astronomiques de l'Observatoire d'Utrecht*, 11, 2.i
van der Marel, N., van Dishoeck, E. F., Bruderer, S., et al. 2013, *Science*, 340, 1199
van Dishoeck, E. F. 2004, *ARA&A*, 42, 119
van Dishoeck, E. F. 2006, *Proceedings of the National Academy of Science*, 103, 12249
van Dishoeck, E. F., Bergin, E. A., Lis, D. C., & Lunine, J. I. 2014, *Protostars and Planets VI*, 835
van Dishoeck, E. F., & Black, J. H. 1988, *ApJ*, 334, 771
van Dishoeck, E. F., Jonkheid, B., & van Hemert, M. C. 2006, *Faraday Discussions*, 133, 231
van Dishoeck, E. F., Kristensen, L. E., Benz, A. O., et al. 2011, *PASP*, 123, 138
van Leeuwen, F. 2007, *A&A*, 474, 653
van Zadelhoff, G.-J., Aikawa, Y., Hogerheijde, M. R., & van Dishoeck, E. F. 2003, *A&A*, 397, 789
van Zadelhoff, G.-J., van Dishoeck, E. F., Thi, W.-F., & Blake, G. A. 2001, *A&A*, 377, 566
Vastel, C., Caselli, P., Ceccarelli, C., et al. 2006, *ApJ*, 645, 1198
Vasgounis, A. I., Wiebe, D. S., Birnstiel, T., et al. 2011, *ApJ*, 727, 76
Velusamy, T., & Langer, W. D. 1998, *Nature*, 392, 685
Vicente, S. M., & Alves, J. 2005, *A&A*, 441, 195
Visser, R. 2009, PhD thesis, Ph. D. thesis, Leiden University
Wakelam, V., Herbst, E., Loison, J.-C., et al. 2012, *ApJS*, 199, 21
Walsh, C., Millar, T. J., & Nomura, H. 2010, *ApJ*, 722, 1607
Walsh, C., Millar, T. J., Nomura, H., et al. 2014, *A&A*, 563, A33
Walsh, C., Nomura, H., Millar, T. J., & Aikawa, Y. 2012, *ApJ*, 747, 114
Walsh, C., Nomura, H., & van Dishoeck, E. 2015, *A&A*, 582, A88
Walsh, C., Loomis, R. A., Öberg, K. I., et al. 2016, *ApJ*, 823, L10
Watson, W. D. 1974, *ApJ*, 188, 35
Watson, W. D. 1976, *Reviews of Modern Physics*, 48, 513
Webb, R. A., Zuckerman, B., Platais, I., et al. 1999, *ApJ*, 512, L63
Weidenschilling, S. J. 1977, *MNRAS*, 180, 57
Weidenschilling, S. J. 1984, *Icarus*, 60, 553
Whittet, D. C. B., Shenoy, S. S., Bergin, E. A., et al. 2007, *ApJ*, 655, 332
Willacy, K. 2007, *ApJ*, 660, 441
Willacy, K., & Millar, T. J. 1998, *MNRAS*, 298, 562
Williams, J. P., & Best, W. M. J. 2014, *ApJ*, 788, 59
Williams, J. P., & Cieza, L. A. 2011, *ARA&A*, 49, 67
Williams, J. P., Cieza, L. A., Andrews, S. M., et al. 2013, *MNRAS*, 435, 1671
Windmark, F., Birnstiel, T., Güttler, C., et al. 2012, *A&A*, 540, A73
Woodall, J., Agúndez, M., Markwick-Kemper, A. J., & Millar, T. J. 2007, *A&A*, 466, 1197
Woods, P. M., & Willacy, K. 2007, *ApJ*, 655, L49
Yorke, H. W., Bodenheimer, P., & Laughlin, G. 1993, *ApJ*, 411, 274
Youdin, A. N., & Lithwick, Y. 2007, *Icarus*, 192, 588
Zhang, K., Bergin, E. A., Blake, G. A., et al. 2016, *ApJ*, 818, L16
Zhang, Y., & Jin, L. 2015, *ApJ*, 802, 58

Zinnecker, H., & Yorke, H. W. 2007, ARA&A, 45, 481



Steepening of the $820 \mu\text{m}$
continuum surface
brightness profile signals
dust evolution in TW
Hya's disk

2.1 Introduction

Within the core accretion scenario, the formation of planets starts inside disks around newly formed stars with the coagulation of (sub)micron-sized dust grains into larger objects (see, e.g., Lissauer & Stevenson 2007, for a review). Evidence for grain growth follows from the spectral slope from submillimeter to centimeter wavelengths (e.g., Draine 2006) and has been found toward many disks (Beckwith et al. 1990; Andrews & Williams 2005; Rodmann et al. 2006; Lommen et al. 2009; Ricci et al. 2010a,b, 2011; Mann & Williams 2010; Guilloteau et al. 2011; Ubach et al. 2012). As grains grow to millimeter sizes, they start to decouple dynamically from the gas and, no longer supported by gas pressure, begin to feel the headwind of the gas and drift inward (Whipple 1972; Weidenschilling 1977). This results in radially more compact millimeter continuum emission (roughly probing millimeter-sized dust) than near-infrared scattered light (probing sub-micron-sized dust) and CO (probing the cold gas), as detected in an increasing number of disks (Panić et al. 2009; Andrews et al. 2012; de Gregorio-Monsalvo et al. 2013; Walsh et al. 2014). The high sensitivity of the Atacama Large Millimeter / submillimeter Array (ALMA) allows detailed investigation of the radial distribution of millimeter-sized grains and critical comparison to theoretical expectations of their growth and dynamics.

One of the first disks for which radial migration of millimeter-sized dust was inferred is found around the nearby T Tauri star TW Hya (Andrews et al. 2012). At a distance of 53.7 ± 6.2 pc (Hipparcos; van Leeuwen 2007), TW Hya is the closest gas- and dust-rich planet-forming disk; it is observed close to face-on with an inclination of $7^\circ \pm 1^\circ$ (Qi et al. 2004; Hughes et al. 2011; Rosenfeld et al. 2012). TW Hya has a mass of $0.55 \pm 0.15 M_\odot$ and, although some uncertainty exists (Vacca & Sandell 2011), an estimated age of 8–10 Myr (Hoff et al. 1998; Webb et al. 1999; de la Reza et al. 2006; Debes et al. 2013). Its disk has a gas mass of at least $0.05 M_\odot$ as inferred from the emission of HD (Bergin et al. 2013), consistent with a gas-to-dust ratio of 100 and the derived dust mass of $2\text{--}6 \times 10^{-4} M_\odot$ (Calvet et al. 2002; Thi et al. 2010). The outer radius of the disk as seen at near-infrared wavelengths and in the emission of CO is $\sim 200\text{--}280$ au (Weinberger et al. 2002; Qi et al. 2004; Andrews et al. 2012; Debes et al. 2013). From the spectral energy distribution (SED) an inner hole in the disk of ~ 4 au was found (Calvet et al. 2002; Hughes et al. 2007; Menu et al. 2014). Andrews et al. (2012) show that millimeter-sized grains, as traced by $870 \mu\text{m}$ SMA observations, extend out only to ~ 60 au, indicating significant radial inward drift. Menu et al. (2014) found a population of even larger grains at smaller radii from 7 mm JVLA observations. At near-infrared wavelengths, Debes et al. (2013) show a depression of emission around 80 au, while Akiyama et al. (2015) detected structure in polarized scattered light at radii of 10–20 au possibly indicating a gap, or changes in the scale height or opacity of micron-sized grains.

In this paper we reanalyze archival ALMA Cycle 0 data of the $820 \mu\text{m}$ (365.5 GHz) continuum emission of TW Hya with an angular resolution of $\sim 0''.4$. This observing wavelength is near $870 \mu\text{m}$, the wavelength used by Andrews et al. (2012) to infer the 60 au outer radius for millimeter-sized grains. We do not consider available ALMA continuum data at 106 GHz and 663 GHz because we aim to make a direct comparison to the $870 \mu\text{m}$ SMA data without the added degeneracy between dust surface density and dust emissivity as a function of wavelength. The sensitivity of the archival ALMA data allows detailed comparison of the continuum visibilities as a function of deprojected baseline length with parameterized models of the disk. Section 2.2 presents the data and describes how the visibilities vary with deprojected baseline length. Section 2.3 describes our disk model and the fitting methods, yielding the radial surface brightness profile of millimeter-sized grains as well as the underlying dust surface density and opacity. Section 2.4 discusses our results

in the light of theoretical models of dust grain growth, fragmentation, and transport, and Section 2.5 summarizes our findings.

2.2 Observations and data reduction

The ALMA archive contains two Cycle 0 data sets with continuum observations of TW Hya near $870 \mu\text{m}$. These data sets are 2011.0.00340.S (hereafter 340.S), covering wavelengths of $804\text{--}837 \mu\text{m}$ (frequencies of $348\text{--}373 \text{ GHz}$), a total bandwidth of 0.94 GHz , baselines up to 370 m ($460 \text{ k}\lambda$), and a total on-source integration time of 5449 s ; and 2011.0.00399.S (hereafter 399.S), covering $867\text{--}898 \mu\text{m}$ ($334\text{--}346 \text{ GHz}$), a total bandwidth of 0.24 GHz , baselines up to 345 m ($430 \text{ k}\lambda$), and a total on-source integration time of 4615 s . For both data sets, 3C279 and J0522–364 served as bandpass calibrators; Ceres, and for a part of data set 399.S, Titan, as flux calibrators; and J1037–295 as gain calibrator. Median system temperatures were $230\text{--}260 \text{ K}$ for S.340 and $110\text{--}130 \text{ K}$ for S.399. The 340.S data were previously presented by Qi et al. (2013), who do not analyze the continuum emission in detail.

After verifying the calibration of these data sets, to improve the complex gain calibration we iteratively performed self-calibration on the continuum down to solution intervals of 60 s . We use CASA 4.2.1 for the calibration. We reach noise levels of $0.50 \text{ mJy beam}^{-1}$ (340.S) and $0.59 \text{ mJy beam}^{-1}$ (399.S). Uniformly weighted synthesized beams are $0'.45 \times 0'.37$ (340.S) and $0'.45 \times 0'.40$ (399.S). Integrated fluxes of 1.7 Jy (340.S) and 1.3 Jy (399.S) are found.

In the remainder of this paper, we focus on data set 340.S which has slightly higher resolution and lower noise. Although we can combine both data sets into a single set at an effective observing wavelength, with a $\sim 30\%$ lower resulting noise, we instead prefer to use data set 399.S to independently confirm our results and other than that, we do not discuss this data set further in this paper. Figure 2.1 shows the continuum image obtained from data set 340.S.

Adopting a position angle for the disk's major axis of 155° (east of north) and an inclination of $+6^\circ$ (Qi et al. 2013; Rosenfeld et al. 2012), we derive average continuum visibilities (real and imaginary part) in 41 $10\text{-k}\lambda$ wide radial bins of deprojected baseline length. We use the equations of Berger & Segransan (2007) (as referenced in Walsh et al. 2014) to carry out the deprojection. Given the near face-on orientation of TW Hya's disk, the deprojection corrections are small.

Figure 2.2 plots the real and imaginary parts of the continuum visibilities against the deprojected baseline length. The imaginary parts are all zero to within the accuracy, indicating that the emission is symmetric around the source center at the resolution of our observations. Apart from the much higher signal-to-noise ratio, the real part of the visibilities show a behavior similar to that shown by Andrews et al. (2012), with a drop off from 1.72 Jy at the shortest baselines to a minimum of 0.057 Jy near $190 \text{ k}\lambda$, followed by a second maximum of 0.123 Jy around $275 \text{ k}\lambda$ and a subsequent decrease to 0.028 Jy at our longest baseline of $410 \text{ k}\lambda$. The data of Andrews et al. (2012) continue to longer baselines of $600 \text{ k}\lambda$ with fluxes approaching 0 Jy .

We overplot the data with the model presented by Andrews et al. (2012) (their model pC) which they find to best fit the continuum data. We recalculate the model at the exact observing wavelengths of the ALMA data. Our model is geometrically thin and uses only the midplane temperatures as calculated by Andrews et al. (2012) (see Section 2.3). Our model curve therefore differs in detail from the one shown by Andrews et al. (2012), but qualitatively shows the same behavior. In particular, it fits the data well out to baselines of $290 \text{ k}\lambda$ but severely underpredicts the emission on baselines of 300 and $400 \text{ k}\lambda$, corre-

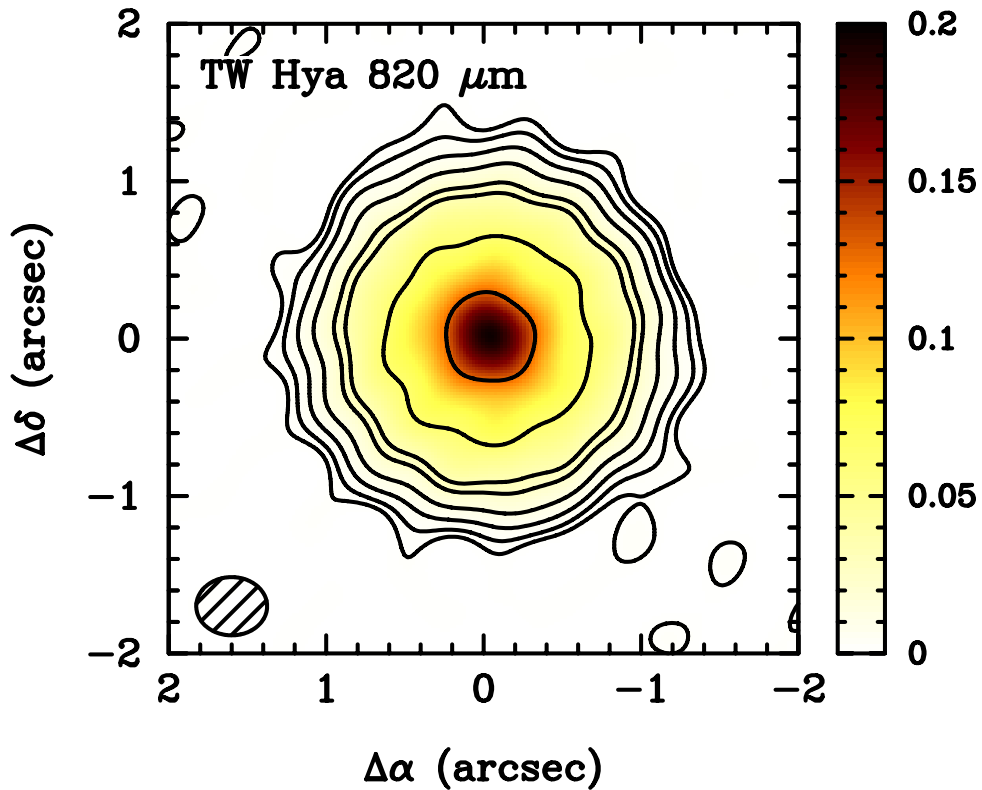


Figure 2.1: Image of the 820 μm (365.5 GHz) continuum of TW Hya based on data set 2011.0.00340.S. We reimagined these data, and obtain a result indistinguishable from (Qi et al. 2013). The image construction employed self-calibration and uniform weighting. The resulting beam size, indicated in the lower left, is $0''.45 \times 0''.37$ at a position angle of -56° . The color scale is in units of Jy beam^{-1} and contours are drawn at 1.5, 6.0, 12.0, 24.0, 48.0, 64.0, and 128. mJy beam^{-1} . The peak intensity is $195.8 \text{ mJy beam}^{-1}$ and the rms noise level is $0.50 \text{ mJy beam}^{-1}$.

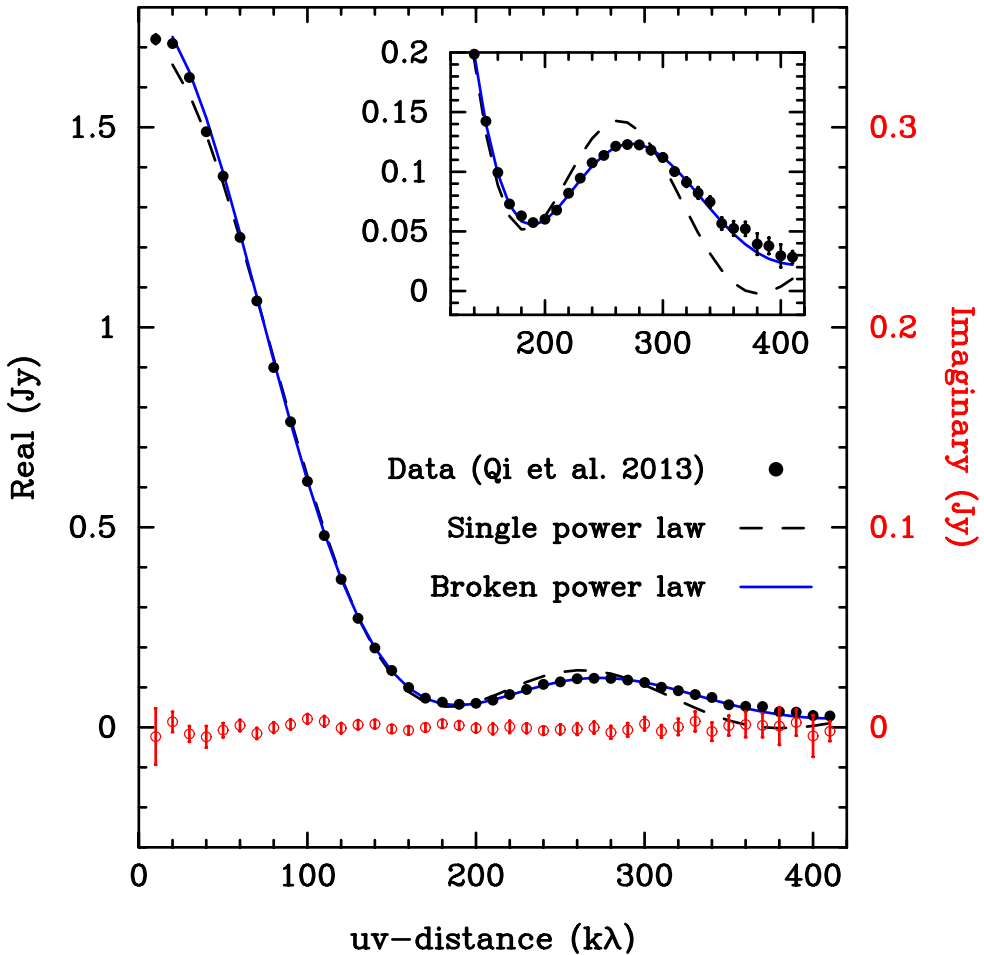


Figure 2.2: Real (black points) and imaginary (red points) parts of the visibilities of project 340.S (previously presented in Qi et al. 2013) in Jy vs deprojected baseline length in $k\lambda$. The inset shows the region of 120–420 $k\lambda$ in greater detail. The dashed black curve shows the recalculated single power-law model of Andrews et al. (2012) (their model pC), which fails to reproduce the data on baselines $> 290 k\lambda$. A much better fit is found for a broken power-law model described in Section 2.3 (solid blue curve). Because both models are symmetric, the imaginary parts of their visibilities are all 0 (not shown).

sponding to angular scales of $0'.5$ – $0'.7$ (27–37 au). In the next section we attempt to find a model description that provides a better fit.

2.3 Model fitting

To further investigate the disk structure that best describes the observed emission, we consider the deprojected and radially binned real visibilities of data set 340.S. We fit to the 41 data points plotted in Fig. 2.2 rather than the full set of complex visibilities to speed up calculations. Since the observed emission is symmetric (imaginary visibilities are all 0) and the 41 data points in Fig. 2.2 fully sample the curve and do not average out any detected asymmetric structure, this simplification is allowed. As a consequence of using only the binned visibilities, our fitting places relatively little weight on the shortest baselines, which represent the total flux. Because we are primarily interested in the spatial distribution of the emission, rather than the total amount, our results are not affected. However, even a small discrepancy in total flux would be accentuated if we would calculate a residual image. For this reason, we refrain from imaging the residuals and exclusively work with the visibilities.

The real part of the visibilities, V , are related to the intensity distribution of the source by

$$V(r_{in}) = 2\pi \int_0^\infty I_\nu(R) J_0(2\pi R r_{in}) R dR, \quad (2.1)$$

where r_{in} is the baseline length, $I_\nu(R)$ is the intensity as a function of radius R , and J_0 the zeroth order Bessel function of the first kind (see, e.g., Hughes et al. 2007). We solve the integral in equation (2.1) by summation using a step size of 0.1 au, which was found to be sufficiently small.

The intensity $I_\nu(R)$ follows from the expression

$$I_\nu(R) = B_\nu(T(R)) \left(1 - \exp(-\tau(R))\right), \quad (2.2)$$

where $B_\nu(T(R))$ is the Planck function, $T(R)$ is the dust temperature, and $\tau(R)$ is the dust optical depth which is given by the product of the dust surface density Σ , the dust opacity κ at the observing wavelength, and $\cos i$, where i is the inclination. The factor $\cos i$ is very close to unity for TW Hya.

We follow the midplane temperature as calculated by Andrews et al. (2012), which reproduces the observed SED. Here, $T(R)$ is characterized by a very steep drop off in the inner few au, with $T(R) \propto R^{-q_0}$ with $q_0 = 2.6$, followed by a very shallow decrease across the remainder of the disk, with $T(R) \propto R^{-q_1}$ and $q_1 = 0.26$. Physically, this corresponds to the stellar radiation being stopped by the high opacity in the inner few au of the disk just outside the inner hole, and the remainder of the disk being heated indirectly by stellar radiation absorbed in the disk surface and reradiated vertically (e.g., Chiang & Goldreich 1997). In our model, the temperature at the turnover radius, R_0 (7 au), T_0 , is a free parameter. In all cases, we find best-fit values for T_0 close to the values found by Andrews et al. (2012). Furthermore, R_0 is much smaller than the resolution of our data, and T_0 is degenerate with the optical depth $\tau(R)$. Therefore their exact values do not change our results. The steep rise of the temperature in the inner few au adds an unresolved component to the continuum emission. This provides a vertical offset to the real part of the visibilities. Indeed, the observed real part of the visibilities never become negative (Fig. 2.2), showing that the sharp increase in temperature at small radii is essential in our model even if we do not resolve these scales.

We choose to describe the optical depth $\tau(R)$ as the product of a constant dust opacity $\kappa_{365.5}$ and a radially varying dust surface density distribution $\Sigma(R)$. For the dust opacity at the average observing wavelength of 365.5 GHz $\kappa_{365.5}$, we adopt the same value as employed by Andrews et al. (2012), $\kappa_{365.5} = 3.4 \text{ cm}^2 \text{ g}^{-1}$ (dust). We describe the dust surface density $\Sigma(R)$ as a (set of) radial power law(s) between an inner radius R_{in} and an outer radius R_{out} . In Section 2.4.1 we further discuss what happens if also κ varies radially, as would be naturally expected.

Table 2.1 lists the fixed and 4 or 6 (depending on the model) free parameters of our model. Estimates of the parameters follow from a Markov chain Monte Carlo (MCMC) exploration of the parameter space, minimizing $\Sigma(x_i - y_i)^2 / 2\sigma_i^2$, where x_i and y_i are the 41 observed and modeled binned real visibilities, and σ_i the observed dispersion in each of the bins. These σ_i correspond to the error on the averaged real visibilities and follow from the dispersion of the data points in the bin divided by the square root of the number of data points. Any undetected asymmetric structures also contribute to σ_i , which ranges from 2.0 to 12.0 mJy, with a median value of 3.0 mJy. We use the `emcee`¹ implementation of the MCMC method, which uses affine invariant ensemble sampling (Goodman & Weare 2010; Foreman-Mackey et al. 2013). Figure 2.3 in Appendix 2.A plots the results.

Assuming a single radial power law for the surface density, the relevant free parameters in our model are the surface density distribution $\Sigma(R)$, the inner hole radius R_{in} , and the outer radius R_{out} . In all cases we find inner radii on the order of a few au, consistent with SED estimates of the inner hole. The best-fit model of Andrews et al. (2012) (their model pC) has $\Sigma(R) \propto R^{-0.75}$ and a surface density of Σ_0 of 0.39 g cm^{-2} at 10 au. Keeping this Σ_0 fixed and using a single power law for the radial dependence ($\Sigma \propto R^{-p_0}$), we find very similar values as Andrews et al. (2012) for the slope ($p_0 = 0.70 \pm 0.01$ vs 0.75) and outer radius ($R_{\text{out}} = 55.7 \pm 0.1$ au vs 60 au; see Table 2.1). The quoted errors on the parameters are formal fitting errors, only meaningful within the model assumptions. The emission in Fig. 2.1 is convolved with the synthesized beam and therefore appears to extend beyond the value for R_{out} found from the visibilities (57 au, corresponding to $1''.1$). Figure 2.2 shows the model curve corresponding to the single power law fit. This curve is similar, but not identical, to the curve for model pC in Andrews et al. (2012). Although the parameters are nearly identical, our model is vertically isothermal, unlike model pC, resulting in a slightly different curve. Regardless, both models have equal problems in reproducing the visibilities on baselines of 300–400 k λ .

After this single radial power law as a description for the surface density, the next simplest model consists of a broken power law, with $\Sigma(R) \propto R^{-p_0}$ inside a radius R_{break} and $\Sigma(R) \propto R^{-p_1}$ outside this radius. This adds two free parameters to the model p_1 and R_{break} . A very good fit to the data is found (Fig. 2.2, Table 2.1 and Fig. 2.4). In this best-fit model, the radial drop off of the surface density is initially modest ($p_0 = 0.53 \pm 0.01$) out to a radius of 47.1 ± 0.2 au, followed by a very sharp drop at larger radii ($p_1 = 8.0 \pm 0.1$). Given the fast drop of the surface density, no useful constraint on the outer radius is found (200 ± 55 au), as the emission drops below the detection limit. This fit is significantly better than the single power law fit, with respective χ^2 values of 1437 and 283. A likelihood ratio test indicates that the broken power law model describes the data better than the single power law model with a probability larger than 0.999.

The broken power law solution found above should not be confused with the exponentially tapered models that are often used (see, for example, Hughes et al. 2008). Such models are described by a surface density $\Sigma = \Sigma_c (R/R_c)^{-\gamma} \exp[-(R/R_c)^{2-\gamma}]$. Andrews et al. (2012) already show that exponentially tapered models do not fit the millimeter continuum

¹<http://dan.iel.fm/emcee>

Table 2.1: Model Parameters

Parameter	Single power law	Broken power law
Fixed parameters:		
$\Sigma_{10 \text{ au}}$ (g cm^{-2})	0.39	0.39
$\kappa_{365.5}$ ($\text{cm}^2 \text{g}^{-1}$)	3.4	3.4
q_0	2.6	2.6
q_1	0.26	0.26
R_0 (au)	7.0	7.0
Free parameters:		
R_{in} (au)	4.44 ± 0.02	4.07 ± 0.03
R_{out} (au)	55.7 ± 0.1	200 ± 55
p_0	0.70 ± 0.01	0.53 ± 0.01
p_1		8.0 ± 0.1
T_0 (K)	28.4 ± 0.2	26.7 ± 0.2
R_{break} (au)		47.1 ± 0.2

Notes. Quoted uncertainties are formal fitting errors only, and do not include the effect of the model assumptions or the distance to TW Hya.

visibilities of TW Hya: there are no values of γ that give a sufficiently shallow drop off of Σ at small R and a sufficiently steep fall off at large R . Only our broken power law can combine these slopes.

In this analysis, we have parameterized the emission with a constant dust opacity κ and a radially varying surface density $\Sigma(R)$. We stress that our real constraints are on the dust optical depth $\tau(R) = \kappa\Sigma$. This optical depth follows the same radial broken power law found above. The functional description of the surface brightness profile is more complex, since following equation (2.2) it also includes the slope of the temperature via the Planck function and the slope of the optical depth via the factor $(1 - \exp(-\tau))$. The optical depth drops from 2.1 at 4.1 au to 0.57 at 47 au, making the emission moderately optically thick and preventing us from taking the limit for small τ , $\lim_{\tau \rightarrow 0}(1 - \exp(-\tau)) = \tau$.

2.4 Discussion

2.4.1 Dust drift

The broken power law distribution obtained for the dust surface density resembles predictions from Birnstiel & Andrews (2014) who consider the effects of radial drift and gas drag on the growing grains. At late time (~ 0.5 – 1 Myr in their models), the dust surface density follows a slope of approximately -1 out to ~ 50 au, after which it steepens to approximately -10 . Our inferred surface density profile, although different in detail, shows a similar steepening, further strengthening the suggestion of Andrews et al. (2012) that the grains in TW Hya’s disk have undergone significant growth and drift. However, Birnstiel & Andrews (2014) consider the total dust surface density while our fit is essentially to the $820 \mu\text{m}$ continuum optical depth profile. This is dominated by grains of roughly 0.1 – 10 mm (Draine 2006) but grains of all sizes contribute. As noted by Birnstiel & Andrews (2014), the total dust surface density consist of a radially varying population of dust at different sizes, with larger grains having more compact distributions than smaller grains. This is

certainly the case for TW Hya, given that grains small enough to scatter near-infrared light extend out to 200–280 au (Debes et al. 2013) while 7 mm observations by Menu et al. (2014) show emission concentrated toward only the inner several au. From observations at a single wavelength we cannot infer both the dust surface density and the dust opacity as a function of radius.

Various authors describe simulations of grain evolution including growth, fragmentation, and drift (e.g., see Testi et al. 2014, for a review). Pinilla et al. (2015) follow the description of Birnstiel et al. (2010) to describe the advection-diffusion differential equation for the dust surface density simultaneously with the growth, fragmentation, and erosion of dust grains via grain-grain collisions. We do not perform a detailed simulation of the TW Hya disk here, since this would require knowledge of the gas surface density distribution and comparison to multiwavelength continuum observations. Instead, we note that any simulation of realistic disks using the prescriptions of Pinilla et al. (2015) results in a very low 820 μm continuum surface brightness and in radial profiles that have turnover radii $R_{\text{break}} \lesssim 20$ au at ages >5 Myr and therefore cannot explain the observations for the 8–10 Myr of TW Hya. This age vs surface brightness (extent) problem was already noted before (e.g., Pinilla et al. 2012, 2015; Testi et al. 2014). The conundrum of TW Hya’s surface brightness profile is that it resembles *in shape* the signatures of grain evolution and drift while in *in flux and size* it is too bright and extended for these same mechanisms to have operated over the 8–10 Myr lifetime of the disk.

One possible explanation is that TW Hya’s disk was originally much more massive and larger than the 200–280 au now seen. However, to have a turn-over radius of ~ 50 au, after 10 Myr, requires an initial disk size of 800–1000 au and a mechanism to remove all CO and small dust outside 200 au over the past 10 Myr to match current observations of CO line emission and near-infrared scattered light. We do not consider this a likely scenario.

2.4.2 The presence of unseen gaps

Another possibility to explain the apparent youth of TW Hya’s disk both in terms of the turn-over radius of the surface brightness distribution of the millimeter continuum and its significant gas and dust content lies in comparison to the recent high resolution imaging results of millimeter continuum emission of HL Tau (ALMA Partnership et al. 2015). HL Tau is a very young disk (<1 Myr), but its millimeter continuum image shows a remarkable set of bright and dark rings. The presence of these rings have been variously interpreted as the result of gap clearing by embedded planets (Dipierro et al. 2015; Dong 2015; Pinte et al. 2015), secular gravitational instabilities (Youdin 2011; Takahashi & Inutsuka 2014), or emissivity depressions due to accelerated grain growth to decimeter sizes at the location of the frost lines of dominant ices and clathrates (Zhang et al. 2015; Okuzumi et al. 2015).

Millimeter-sized grains are known to become trapped outside gaps in so-called transitional disks because of the reversed pressure gradient (e.g., van der Marel et al. 2013; Casassus et al. 2013). Therefore, one or more embedded planets inside the TW Hya disk could have trapped millimeter-sized grains and prevented further inward migration. This mechanism has been invoked by Pinilla et al. (2012), who show that even small pressure maxima are sufficient to slow down the inward migration of millimeter-sized dust.

We investigated if the currently available ALMA data place constraints on the presence of gaps inside the TW Hya disk, other than the known gap inside ~ 4 au. Starting with the two-slope model, we include a gap centered on 20 au characterized by a Gaussian width and a depth. We choose the value of 20 au to be near the center of the extent of the millimeter-sized grains. We then repeat the procedure of the previous section to find the best-fit parameters for a series of gap widths and depths. By optimizing the other free

model parameters we allow these to maximally compensate for the effect of the presence of the gap on the visibilities. We find that we can exclude, as defined by an increase of the χ^2 value by a factor of two or more, models with gaps that are entirely empty with FWHM widths of more than 6.6 au and models with gaps that have only a depth of 80% to widths of 16.6 au. Assuming a gap width of 5 Hill radii, such gaps correspond to planet masses of 0.7–10 M_{Jup} (Dodson-Robinson & Salyk 2011). For comparison, the widths and depths of the gaps in HL Tau are well within the allowed range. We conclude that TW Hya’s disk may very well contain planet-induced gaps as detected toward HL Tau, which are capable of halting further inward migration of grains and explain the observed millimeter continuum surface brightness profile.

2.4.3 Dust temperature and the CO snow line

The discussion above attributes the characteristics of the distribution of the millimeter-wave continuum to the surface density distribution and opacity of the grains. According to equation (2.2) the explanation could equally well lie with the dust temperature. At radii inside the turn-over of the emission, up to 47 au, the disk is known to be cold, $< 20\text{K}$, as witnessed by the CO freeze-out probed by N_2H^+ emission (Qi et al. 2013). A shallow surface density distribution combined with a steep temperature drop off outside 47 au cannot explain the observations, since this requires unrealistically low temperatures ($\ll 10\text{K}$). A steeper density distribution combined with a temperature rise around 30–40 au followed by a return to nominal temperatures can fit the observations, but requires temperatures as high as 70 K, clearly inconsistent with the detection of N_2H^+ that would be rapidly destroyed by gas-phase CO at such temperatures.

The N_2H^+ data from Qi et al. (2013) place the CO snow line at 30 au. Just outside this snow line, grain growth may receive a boost by the accumulation of frost resulting from mixing of material across the snow line. This cold-finger effect was earlier described by Meijerink et al. (2009) and invoked by Zhang et al. (2015) to explain the dark rings in the HL Tau millimeter continuum image as locations of growth to decimeter-sized particles at the location of frost lines. Similarly in TW Hya, the location of the turn-over radius in the millimeter emission may be determined, not by the inward migration of millimeter-sized grains, but by a local enhancement of growth of (sub) micron-sized grains to millimeter sized grains in the 30–47 au region outside the CO snow line. If the efficiency of grain growth is locally sufficiently enhanced, this may increase the dust opacity at 820 μm and explain the observed surface brightness profile. Zhang et al. (2016) present an analysis of four protoplanetary disks with high resolution continuum observations, and find that regions just beyond CO snow lines show locally enhanced continuum emission. Detailed modeling of grain growth and drift in the presence of ices and the resulting dust opacity is required to further explore this mechanism. If this mechanism is indeed effective, population studies of disks should reveal a correlation between the location of the CO snow lines² and the sizes of the millimeter continuum emission disk.

2.5 Summary

We analyzed archival ALMA Cycle 0 365.5 GHz continuum data with baselines up to 410 $k\lambda$ and conclude the following.

²In the case of a disk with a temperature structure that varies with time, the *effective* (or time averaged) location of the CO snow line is what matters here.

1. The interferometric visibilities are described by a disk with a broken power law radial surface density distribution and constant dust opacity, with slopes of -0.53 ± 0.01 and -8.0 ± 0.2 and a turn-over radius of 47.1 ± 0.2 au. The outer radius is unconstrained as the emission drops below the detection limit beyond ~ 57 au.
2. Under the assumption of a constant dust opacity κ , the shape of the corresponding surface density distribution resembles the one expected in the presence of grain growth and radial migration for late times as calculated by Birnstiel & Andrews (2014).
3. The total surface brightness and the turn-over radius of 47 au are too large for a source age of 8–10 Myr. This implies that either the disk formed with a much larger size and mass, that one or more unseen embedded planets have opened gaps and halted inward drift of millimeter-sized grains, or that the region outside the CO snow line at radii of 30–47 au has a significantly locally enhanced production rate of millimeter-sized grains boosting the dust opacity at $820 \mu\text{m}$.

Higher resolution observations with ALMA are essential to explore the reason for the location of the turnover at 47 au (see, e.g., Zhang et al. in prep.). Such observations can easily show the presence of one or more gaps, as shown by the HL Tau image. Near-infrared observations (Debes et al. 2013; Akiyama et al. 2015; Rapson et al. 2015) suggest the presence of structures at, respectively, 80 au, 10–20 au, and ~ 23 au that are consistent with partially filled gaps. Whether these correspond to unresolved structures of millimeter-wave emitting grains is unknown but likely. If, in spite of this, no gaps in the millimeter emission are found, high resolution multiwavelength observations of the brightness distribution can be compared to models of grain growth and migration in the presence of the CO snow line to explore whether an increase in grain growth in the 30–47 au region can be sufficiently efficient to create the observed millimeter continuum brightness profile. There is even the possibility that both scenarios operate: increased grain growth outside the CO snow line has led to the formation of a planet that subsequently has halted further migration of millimeter-sized grains. If so, the correlation mentioned above between CO snow line locations and the sizes of the millimeter continuum emission disks should extend to the locations of gaps as well.

Acknowledgements. This paper makes use of the following ALMA data: ADS/JAO.ALMA#2011.0.00340.S and ADS/JAO.ALMA#2011.0.00399.S. ALMA is a partnership of ESO (representing its member states), NSF (USA) and NINS (Japan), together with NRC (Canada), NSC and ASIAA (Taiwan), and KASI (Republic of Korea), in cooperation with the Republic of Chile. The Joint ALMA Observatory is operated by ESO, AUI/NRAO and NAOJ. The research of MRH and VNS is supported by grants from the Netherlands Organization for Scientific Research (NWO) and the Netherlands Research School for Astronomy (NOVA). This work made use of PyAstronomy.

Bibliography

- Akiyama, E., Muto, T., Kusakabe, N., et al. 2015, *ApJ*, 802, L17
 ALMA Partnership, Brogan, C. L., Pérez, L. M., et al. 2015, *ApJ*, 808, L3
 Andrews, S. M. & Williams, J. P. 2005, *ApJ*, 631, 1134
 Andrews, S. M., Wilner, D. J., Hughes, A. M., et al. 2012, *ApJ*, 744, 162
 Beckwith, S. V. W., Sargent, A. I., Chini, R. S., & Guesten, R. 1990, *AJ*, 99, 924
 Berger, J. P. & Segransan, D. 2007, *New Astronomy Reviews*, 51, 576
 Bergin, E. A., Cleeves, L. I., Gorti, U., et al. 2013, *Nature*, 493, 644
 Birnstiel, T. & Andrews, S. M. 2014, *ApJ*, 780, 153
 Birnstiel, T., Dullemond, C. P., & Brauer, F. 2010, *A&A*, 513, A79
 Calvet, N., D'Alessio, P., Hartmann, L., et al. 2002, *ApJ*, 568, 1008
 Casassus, S., van der Plas, G., M. S. P., et al. 2013, *Nature*, 493, 191
 Chiang, E. I. & Goldreich, P. 1997, *ApJ*, 490, 368

- de Gregorio-Monsalvo, I., Ménard, F., Dent, W., et al. 2013, *A&A*, 557, A133
- de la Reza, R., Jilinski, E., & Ortega, V. G. 2006, *AJ*, 131, 2609
- Debes, J. H., Jang-Condell, H., Weinberger, A. J., Roberge, A., & Schneider, G. 2013, *ApJ*, 771, 45
- Dipierro, G., Price, D., Laibe, G., et al. 2015, *MNRAS*, 453, L73
- Dodson-Robinson, S. E. & Salyk, C. 2011, *ApJ*, 738, 131
- Dong, R. 2015, *ApJ*, 810, 6
- Draine, B. T. 2006, *ApJ*, 636, 1114
- Foreman-Mackey, D., Hogg, D. W., Lang, D., & Goodman, J. 2013, *PASP*, 125, 306
- Goodman, J. & Weare, J. 2010, *Commun. Appl. Math. Comput. Sci.*, 5, 65
- Guilloteau, S., Dutrey, A., Piétu, V., & Boehler, Y. 2011, *A&A*, 529, A105
- Hoff, W., Henning, T., & Pfau, W. 1998, *A&A*, 336, 242
- Hughes, A. M., Wilner, D. J., Andrews, S. M., Qi, C., & Hogerheijde, M. R. 2011, *ApJ*, 727, 85
- Hughes, A. M., Wilner, D. J., Calvet, N., et al. 2007, *ApJ*, 664, 536
- Hughes, A. M., Wilner, D. J., Qi, C., & Hogerheijde, M. R. 2008, *ApJ*, 678, 1119
- Lissauer, J. J. & Stevenson, D. J. 2007, *Protostars and Planets V*, 591
- Lommen, D., Maddison, S. T., Wright, C. M., et al. 2009, *A&A*, 495, 869
- Mann, R. K. & Williams, J. P. 2010, *ApJ*, 725, 430
- Meijerink, R., Pontoppidan, K. M., Blake, G. A., Poelman, D. R., & Dullemond, C. P. 2009, *ApJ*, 704, 1471
- Menu, J., van Boekel, R., Henning, T., et al. 2014, *A&A*, 564, A93
- Okuzumi, S., Momose, M., Sirono, S.-i., Kobayashi, H., & Tanaka, H. 2015, *ArXiv e-prints* [[arXiv:1510.03556](https://arxiv.org/abs/1510.03556)]
- Panić, O., Hogerheijde, M. R., Wilner, D., & Qi, C. 2009, *A&A*, 501, 269
- Pinilla, P., Birnstiel, T., Ricci, L., et al. 2012, *A&A*, 538, A114
- Pinilla, P., Birnstiel, T., & Walsh, C. 2015, *A&A*, 580, A105
- Pinte, C., Dent, W. R. F., Menard, F., et al. 2016, *ApJ*, 816, 25P
- Qi, C., Ho, P. T. P., Wilner, D. J., et al. 2004, *ApJ*, 616, L11
- Qi, C., Öberg, K. I., Wilner, D. J., et al. 2013, *Science*, 341, 630
- Rapson, V. A., Kastner, J. H., Millar-Blanchaer, M. A., & Dong, R. 2015, *ApJ*, 815, L26
- Ricci, L., Testi, L., Natta, A., & Brooks, K. J. 2010a, *A&A*, 521, A66
- Ricci, L., Testi, L., Natta, A., et al. 2010b, *A&A*, 512, A15
- Ricci, L., Testi, L., Williams, J. P., Mann, R. K., & Birnstiel, T. 2011, *ApJ*, 739, L8
- Rodmann, J., Henning, T., Chandler, C. J., Mundy, L. G., & Wilner, D. J. 2006, *A&A*, 446, 211
- Rosenfeld, K. A., Andrews, S. M., Wilner, D. J., & Stempels, H. C. 2012, *ApJ*, 759, 119
- Takahashi, S. Z. & Inutsuka, S.-i. 2014, *ApJ*, 794, 55
- Testi, L., Birnstiel, T., Ricci, L., et al. 2014, *Protostars and Planets VI*, 339
- Thi, W.-F., Mathews, G., Ménard, F., et al. 2010, *A&A*, 518, L125
- Ubach, C., Maddison, S. T., Wright, C. M., et al. 2012, *MNRAS*, 425, 3137
- Vacca, W. D. & Sandell, G. 2011, *ApJ*, 732, 8
- van der Marel, N., van Dishoeck, E. F., Bruderer, S., et al. 2013, *Science*, 340, 1199
- van Leeuwen, F. 2007, *A&A*, 474, 653
- Walsh, C., Juhász, A., Pinilla, P., et al. 2014, *ApJ*, 791, L6
- Webb, R. A., Zuckerman, B., Platais, I., et al. 1999, *ApJ*, 512, L63
- Weidenschilling, S. J. 1977, *MNRAS*, 180, 57
- Weinberger, A. J., Becklin, E. E., Schneider, G., et al. 2002, *ApJ*, 566, 409
- Whipple, F. L. 1972, in *From Plasma to Planet*, ed. A. Elvius, 211
- Youdin, A. N. 2011, *ApJ*, 731, 99

Zhang, K., Blake, G. A., & Bergin, E. A. 2015, ApJ, 806, L7

Zhang, K., Bergin, E. A., Blake, G. A., Cleeves, L. I., Hogerheijde, M., Salinas, V., & Schwarz, K. R. 2016, ApJ, 818, L16

2.A Results of the emcee model fitting

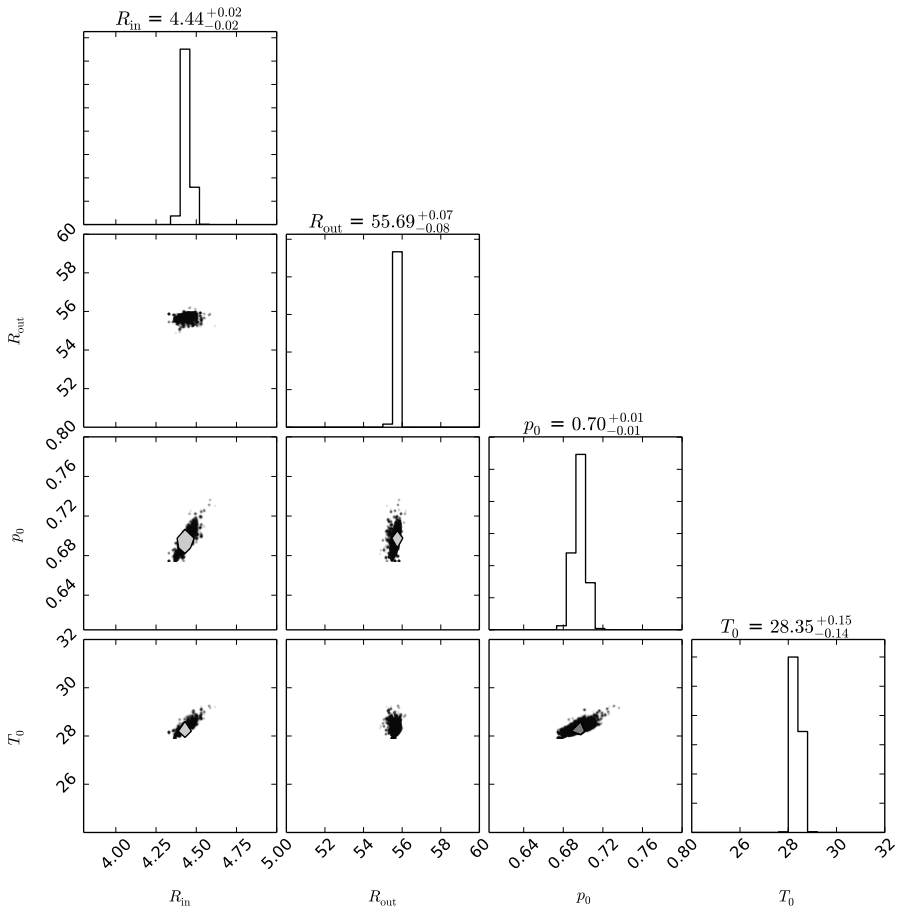


Figure 2.3: Results of the emcee MCMC optimization using a single radial power law for the surface density. The panels show one- and two-dimensional projections of the posterior probability functions of the free model parameters. The panels along the diagonal show the marginalized distribution of each of the parameters as histograms; the other panels show the marginalized two-dimensional distributions for each set of two parameters. Contours (barely visible in the tightly constrained probability distributions) and associated greyscale show 0.5, 1, 1.5 and 2σ levels. Best-fit values and error estimates are listed above the panels along the diagonal.

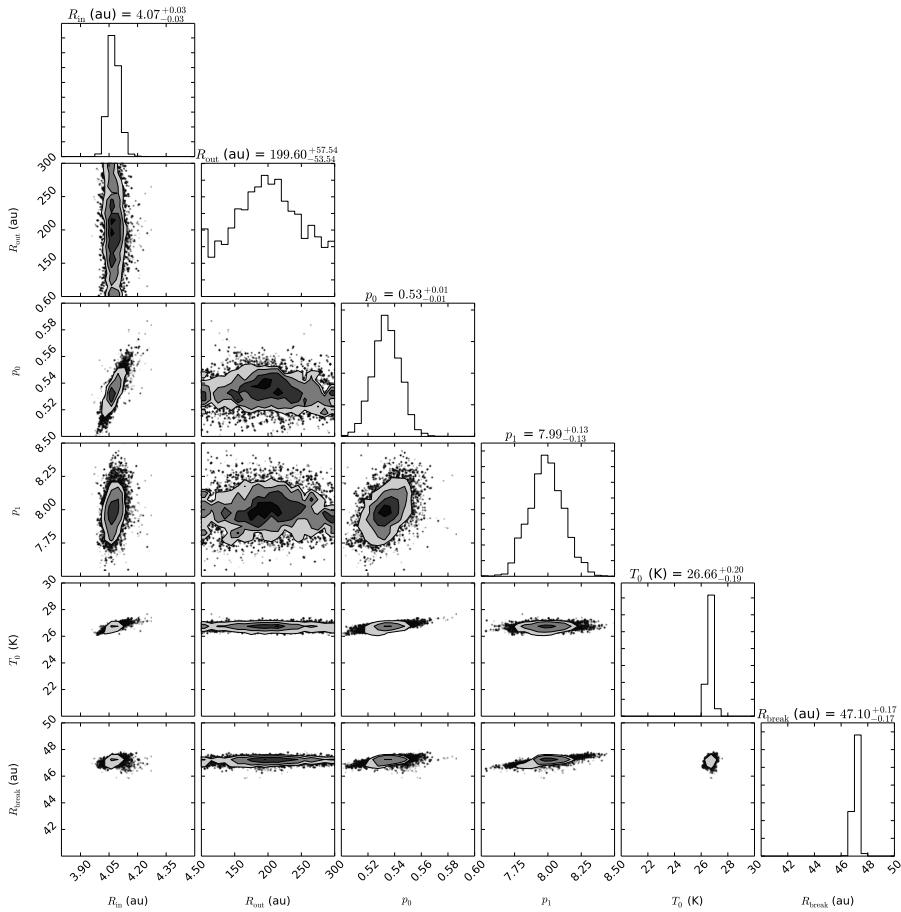
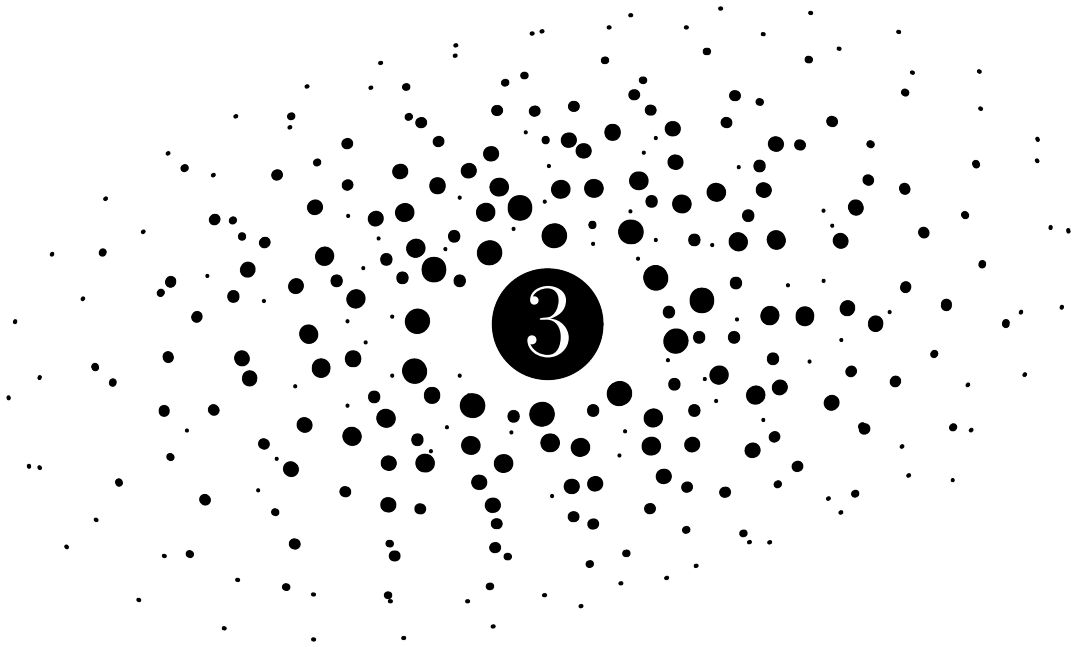


Figure 2.4: Results of the emcee MCMC optimization using a broken radial power law for the surface density. Otherwise, the figure is similar to 2.3. No useful constraints on the outer radius R_{out} are obtained.



First detection of gas-phase ammonia in a planet-forming disk

Salinas, V. N., Hogerheijde, M. R., Bergin, E. A., Cleeves, L. I., Brinch, C., Blake, G. A., Lis, D. C., Melnick, G. J., Panić, O., Pearson, J. C., Kristensen, L., Yıldız, U. A., van Dishoeck, E. F. 2016, *A&A*, 591, A122.

3.1 Introduction

The main reservoir of nitrogen-bearing species in most solar system bodies is unknown. The dominant form of nitrogen on these bodies is inherited from the chemical composition of the solar nebula when planetesimals were formed (Schwarz & Bergin 2014; Mumma & Charnley 2011). This composition strongly depends on the initial abundances, which are difficult to probe since N and N₂ are not directly observable in the interstellar medium (ISM). The Spitzer program ‘Cores to Disks’ found that on average 10% to 20% of nitrogen is contained in ices such as NH₃, NH₄⁺, and XCN, mostly in the form of OCN⁻ (Öberg et al. 2011a). Water is the most abundant volatile in interstellar ices and cometary ices. The relative abundance of the main nitrogen-bearing species compared to water are on the order of a few percent; ~ 5% for ammonia and ~ 0.3% for XCN (Bottinelli et al. 2010; Öberg et al. 2011a). CN and HCN have been detected in later stages of star formation toward protoplanetary disks (see Dutrey et al. 1997; Thi et al. 2004; Öberg et al. 2011b; Guilloteau et al. 2013) along with resolved N₂H⁺ emission in TW Hya (Qi et al. 2013) and unresolved N₂H⁺ emission in several other disks (Dutrey et al. 2007; Öberg et al. 2010, 2011b). Although some upper limits exist for NH₃ in protoplanetary disks in the near-infrared (Salyk et al. 2011; Mandell et al. 2012), there are currently no published detections.

Here we report the first detection of NH₃ along with the N₂H⁺ 6–5 line in the planet-forming disk around TW Hya using the HIFI instrument on the *Herschel* Space Observatory. This disk has already been well studied. It was first imaged by the Hubble Space Telescope (HST) (Krist et al. 2000; Weinberger et al. 2002), which revealed a nearly face-on orientation. Roberge et al. (2005) took new HST images that confirmed this orientation and measured scattered light up to 280 au. Submillimeter interferometric CO data suggest an inclination of 6° to 7° (Qi et al. 2004; Rosenfeld et al. 2012). The age of TW Hya is estimated to be 8–10 Myr (Hoff et al. 1998; Webb et al. 1999; de la Reza et al. 2006; Debes et al. 2013) at a distance of 54 ± 6 pc (Rucinski & Krautter 1983; Wichmann et al. 1998; van Leeuwen 2007).

We here model the ammonia emission from TW Hya assuming that it is desorbed simultaneously with water. The thermal desorption characteristics of ammonia are similar to those of water (Collings et al. 2004). The nonthermal desorption of ammonia through photodesorption has a similar rate to that of water, within a factor of three (Öberg 2009). Ammonia is frozen in water-rich ice layers on interstellar dust particles. Therefore, we can expect both molecules to be absent from the gas phase in similar regions. In order to properly constrain the NH₃/H₂O ratio we need to revisit past models of water emission in the disk surrounding TW Hya.

The ground-state rotational emission for both of the water spin isomers has been found around TW Hya by Hogerheijde et al. (2011) (from now on H11), also using the HIFI instrument onboard the *Herschel* Space Observatory. The authors explained this emission using the physical model from Thi et al. (2010) to calculate the amount of water that can be produced by photodesorption from a hidden reservoir of water in the form of ice on dust grains (Bergin et al. 2010; van Dishoeck et al. 2014). Their model overestimates the total line flux by a factor of 3–5. They explored different ways to reduce the amount of water flux and concluded that settling of large icy grains is the only viable way to fit the data.

Here, we rederive estimates of the amount of water vapor, using an updated estimate of the disk gas mass. We also consider the effect of a more compact distribution of millimeter-sized grains that are moved by radial drift and settling. These dust processes are relevant for the molecular abundance of water because they can potentially move the bulk of the ice reservoir away from regions where photodesorption is effective. Simultaneously, we estimate the amount of NH₃ using the detection of ammonia in the *Herschel* spectra and

derive constraints on the $\text{NH}_3/\text{H}_2\text{O}$ ratio in the disk gas, assuming that NH_3 and H_2O are co-spatial. We also estimate the amount of N_2H^+ and compare it to the amount of NH_3 using a simple parametric model. Section 3.2 presents our data and their reduction. Section 3.3 contains our modeling approach and Sect. 3.4 the resulting ammonia and water vapor masses. Section 3.5 discusses the validity of our models and compares these predictions to standard values. Finally, Sect. 3.6 summarizes our conclusions.

3.2 Observations

Observations of TW Hya ($\alpha_{2000} = 11^{\text{h}}01^{\text{m}}51^{\text{s}}.91$, $\delta_{2000} = -34^{\circ}42'17''.0$) were previously presented by H11 and obtained using the Heterodyne Instrument for the Far-Infrared (HIFI) as part of the key program ‘Water in Star-Forming Regions with *Herschel*’ (WISH) (van Dishoeck et al. 2011). We now present observations taken on 2010 June 15 of the NH_3 $1_0 - 0_0$ line at 572.49817 GHz simultaneously with o- H_2O at 556.93607 GHz using receiver band 1b and a local oscillator tuning of 551.895 GHz (OBS-ID 1342198337). We also present the detection of N_2H^+ 6–5 at 558.96651 GHz in the same spectrum. With a total on-source integration of 326 min, the observation was taken with system temperatures of 360–400 K. The data were recorded in the Wide-Band Spectrometer (WBS) which covers 4.4 GHz with 1.1 MHz resolution. This corresponds to 0.59 km s^{-1} at 572 GHz. The data were also recorded in the High-Resolution Spectrometer (HRS) which covers 230 MHz at a resolution of 0.25 MHz resulting in 0.13 km s^{-1} at the observed frequency of the NH_3 $1_0 - 0_0$ line. The calibration procedure is identical to the one of H11, but employs an updated beam efficiency of $\eta_{\text{mb}} = 0.635$ and a HPBW of $36''.1^1$, which increases the reported water line fluxes by about 17% with respect to the values of H11. Table 3.1 summarizes the line fluxes of ammonia, water and N_2H^+ 6–5. Figure 3.1 shows the calibrated spectra of ortho-ammonia, ortho-water, and the N_2H^+ 6–5 lines.

3.3 Modeling approach

Since NH_3 is intermixed with H_2O on interstellar ices and is thought to desorb simultaneously (Öberg 2009), our modeling approach focuses on deriving a $\text{NH}_3/\text{H}_2\text{O}$ ratio in the TW Hya disk assuming that the NH_3 emission comes from the same location as the H_2O emission. We adopt a physical model for the gas density and temperature and rederive the amount of water vapor from literature results (H11). After we define our H_2O model, we use it to model NH_3 emission by adopting the same spatial distribution as the water but scaling the overall abundance as a free parameter. We also take into account the effect of radial drift and vertical settling of dust grains on our abundance profiles. Additionally, we model the N_2H^+ 6–5 emission by assuming a constant abundance throughout the disk where the temperature is below the CO freeze-out temperature (17 K) following Qi et al. (2013). The total amount of N_2H^+ in this model is also a free parameter. The following sections describe the physical and chemical structure of our models.

3.3.1 Physical structure

Recently, Cleeves et al. (2015) used HD measurements (Bergin et al. 2013) to constrain the total gas mass for the disk of TW Hya of $0.04 \pm 0.02 M_{\odot}$, which is twice as massive as the

¹HIFI-ICC-RP-2014-001 on

<http://herschel.esac.esa.int/twiki/bin/view/Public/HifiCalibrationWeb>

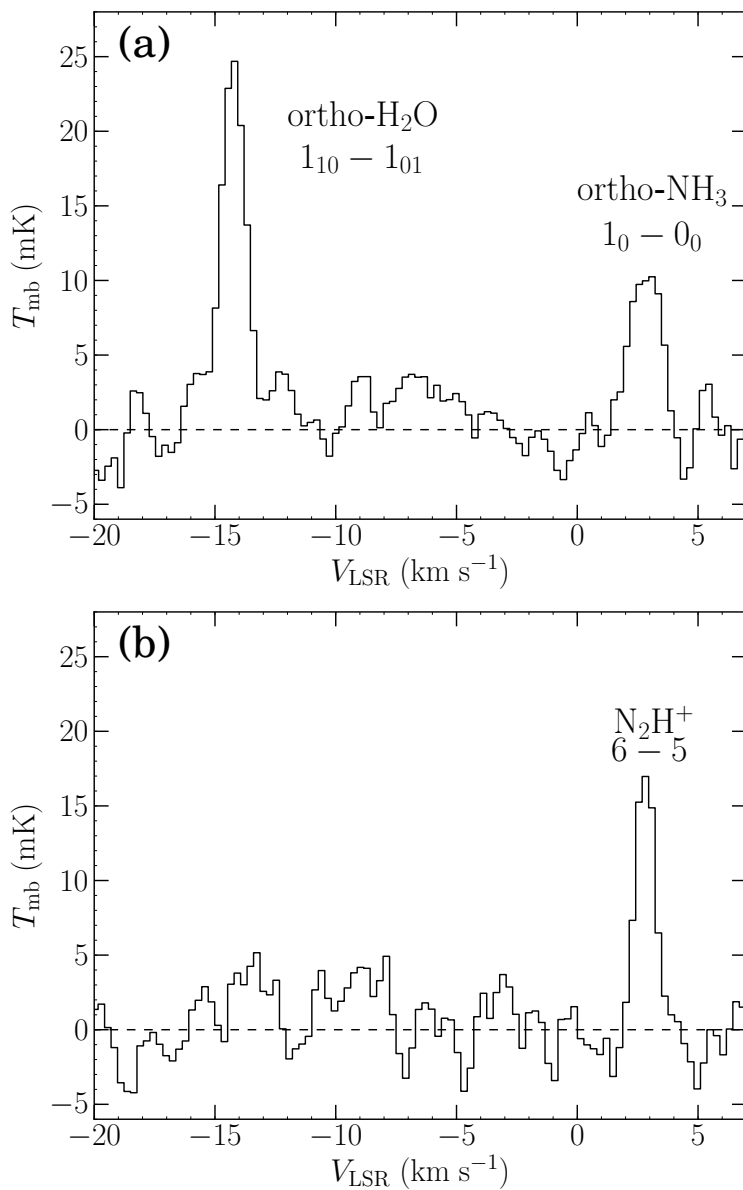


Figure 3.1: Observed spectra of (a) ortho-NH $_3$ $1_0 - 0_0$, ortho-H $_2$ O $1_{10} - 1_{01}$ (previously presented by H11), and (b) N $_2$ H $^+$ $6-5$, using *Herschel* WBS. The dashed line shows the continuum-subtracted spectral baseline. The o-H $_2$ O and o-NH $_3$ lines are observed in opposite sidebands, causing the o-H $_2$ O to be detected at a velocity of -14 km s $^{-1}$ in panel (a).

Table 3.1: Observed line parameters.

Transition	F_{line} (10^{-19} W m $^{-2}$) ^{a,b}	V_{LSR} (km s $^{-1}$) ^b	FWHM (km s $^{-1}$) ^c	T_{mb} (mK) ^c
NH ₃ 1 ₀ - 0 ₀ (HRS)	1.1±0.13	3.0±0.06	0.9±0.06	15.3±3.6
NH ₃ 1 ₀ - 0 ₀ (WBS)	1.1±0.10	2.9±0.06	1.4±0.06	11.3±2.0
N ₂ H ⁺ 6-5 (WBS)	1.0±0.11	2.9±0.03	0.9±0.04	18.1±2.4
o-H ₂ O 1 ₁₀ - 1 ₀₁ (HRS)	1.8±0.11	2.8±0.02	0.9±0.02	30.7±3.7
o-H ₂ O 1 ₁₀ - 1 ₀₁ (WBS)	1.9±0.09	2.9±0.03	1.3±0.03	24.0±2.0
p-H ₂ O 1 ₁₁ - 0 ₀₀ (HRS)	6.7±0.62	2.7±0.05	1.1±0.05	41.0±8.1
p-H ₂ O 1 ₁₁ - 0 ₀₀ (WBS)	6.7±0.44	2.7±0.04	1.3±0.04	39.0±5.2

Notes. ^(a) The errors listed are calculated taking the random errors due to noise only and do not include the calibration uncertainty, estimated to be about 20% of the total flux; the sideband ratio has an uncertainty of 3-4%. ^(b) F_{line} is the integrated flux from $V_{\text{LSR}} = +1.5$ to $+4.1$ km s $^{-1}$. ^(c) Results of a gaussian fit. Errors on V_{LSR} and FWHM are formal fitting errors and much smaller than the spectral resolution of 0.26 km s $^{-1}$.

model used by H11. We adopted the physical structure of their best-fit model defined by a dust surface density profile of

$$\Sigma_d(R) = 0.04 \text{ g cm}^{-2} \left(\frac{R}{R_c}\right)^{-1} \exp\left[-\left(\frac{R}{R_c}\right)\right], \quad (3.1)$$

and a scale height for small grains (and gas) given by

$$H(R) = 15 \text{ au} \left(\frac{R}{R_c}\right)^{0.3}, \quad (3.2)$$

where the critical radius R_c is 150 au. We also adopted their estimated temperature profile $T(R, z)$ calculated from the ultraviolet radiation field throughout the disk (see Appendix A of Cleeves et al. 2015). Cleeves and collaborators did not consider a radial separation between large and small grains because the small grains dominate the dust surface area, which is most important for the chemistry. Many models for the TW Hya SED include an inner hole with a radius of a few au that is depleted of dust. Slight variations of this gap size have been proposed (Calvet et al. 2002; Eisner et al. 2006; Hughes et al. 2007; Ratzka et al. 2007; Arnold et al. 2012; Menu et al. 2014). However, the observations in the large *Herschel* beam are not sensitive to these small scales, and we ignore the inner hole in our model.

3.3.2 Chemical model

Gas temperatures throughout the disk in previous models and ours are typically below 200 K, which means that they exclude high-temperature gas-phase water formation. We consider thermal evaporation and photodesorption by ultraviolet radiation as H_2O production mechanisms and ultraviolet photodissociation and freeze-out and as H_2O destruction mechanisms together with ion-molecule reactions, for both formation and destruction of H_2O , using the time-dependent chemical model of Cleeves et al. (2015). Thermal desorption is only dominant in the innermost disk up to a few au. Most of the water in this chemical model is released to the gas-phase through photodesorption in the outer disk. Compared to the chemistry used in H11, this model uses a more realistic water grain chemistry and updated gas-phase reactions. Figure 3.2 summarizes the physical conditions of the model and the location of the bulk of the water vapor. A significant decrease in the midplane abundance of water vapor can be seen in comparison to the model proposed by H11, which is due to a lower rate of cosmic-ray (CR) driven water formation. Two layers of water abundance can be distinguished in Fig. 3.2(b). The upper layer is the product of gas-phase chemistry and photodesorption whereas the layer at larger radii but smaller height is dominated by photodesorption.

Since our observations are spatially unresolved and the disk is observed nearly face on, no information of the spatial location of the emitting molecules can be retrieved directly from our spectrally resolved data. The following sections describe two processes (radial drift and settling) that are due to grain growth that affects the radial and vertical configuration of dust grains. These in turn determine the distribution of the ices. We consider two scenarios for the vertical location and two scenarios for the radial location of the molecules, resulting in four different configurations.

Vertical settling

For the vertical distribution, we considered two extreme cases. In the first scenario (p), the vertical distribution of the ammonia and water follows that found by the location of

water released through photodesorption (i.e., in the upper and intermediate disk layers) as described above. In the second extreme scenario (m) we assume that the $\text{H}_2\text{O}/\text{H}_2$ and NH_3/H_2 abundances are constant. We distribute the species vertically out to one scale height of the millimeter grains following Andrews et al. (2012),

$$H(R) = 10.31 \left(\frac{R}{100 \text{ au}} \right)^{1.25} \text{ au.} \quad (3.3)$$

Because the column density is dominated by the dense layers near the midplane, this model represents emission dominated by the midplane (hence: model m). The latter is motivated by H11, where they tried to explain water emission from TW Hya using the physical model from Thi et al. (2010) to calculate the amount of water vapor that can be produced by photodesorption. But their model overestimates the total line flux by a factor of 3-5. They concluded that settling of large(r) icy grains could be acting as a mechanism to hide the icy grains from the reach of ultraviolet photons resulting in the lower-than-expected water line fluxes. We do not make any assumptions about the production mechanism of the gas-phase ammonia and water in the absence of photodesorption in the midplane (m), but discuss possible mechanisms in Sect. 3.5.

Radial drift

For the radial location we considered an extended model (E) with ammonia and water across the entire disk out to 196 au, corresponding to the extent of μ -size grains (Debes et al. 2013), and a compact model (C) with NH_3 and H_2O confined to the location of the millimeter grains (<60 au). Andrews et al. (2012) found that the millimeter-sized grains are located within 60 au, probably as the result of radial drift causing a separation between the large and small-size population of dust that remains coupled to the gas. The compact model (C) is also motivated by H11, since grain settling operates faster than drift because the vertical pressure gradient is larger than the radial one. Any grains large enough to drift radially will certainly have settled vertically first. This means that the molecules are already locked up in large(r) grains when they experience (or not) a radial drift. Our compact model (C) represents the extreme case where all water and ammonia ice has been transported to within 60 au and is (partially) returned to the gas phase only there. In the same way, our extended model (E) represents the other extreme where the water and ammonia reservoir, locked up in icy dust particles, extends across the full disk.

As Fig. 3.2 shows, water vapor is mostly present in a thin photo-dominated layer (models p) or near the midplane (models m) following total H_2 density profile. Figure 3.3 summarizes the resulting four different scenarios (Em, Ep, Cm and Cp). In all scenarios, the total amount of ammonia and water vapor is a free parameter constrained by fitting the observed line fluxes. In particular, for the p-models, this means that we use the radial and vertical density distribution from the detailed calculations but scale the total amount of ammonia and water vapor up or down as necessary.

3.3.3 Line excitation and radiative transfer

We used LIME (v1.3.1), a non-LTE 3D radiative transfer code (Brinch & Hogerheijde 2010) that can predict line and continuum radiation from a source model. All of our models use 15000 grid points. Doubling the number of grid points does not affect the outcome of the calculations. Grid points are distributed randomly in R using a logarithmic scale. This means in practice that inner regions of the disk have a finer sampling than the outer parts of the disk. Since it is difficult to establish reliable convergence criteria, LIME requires

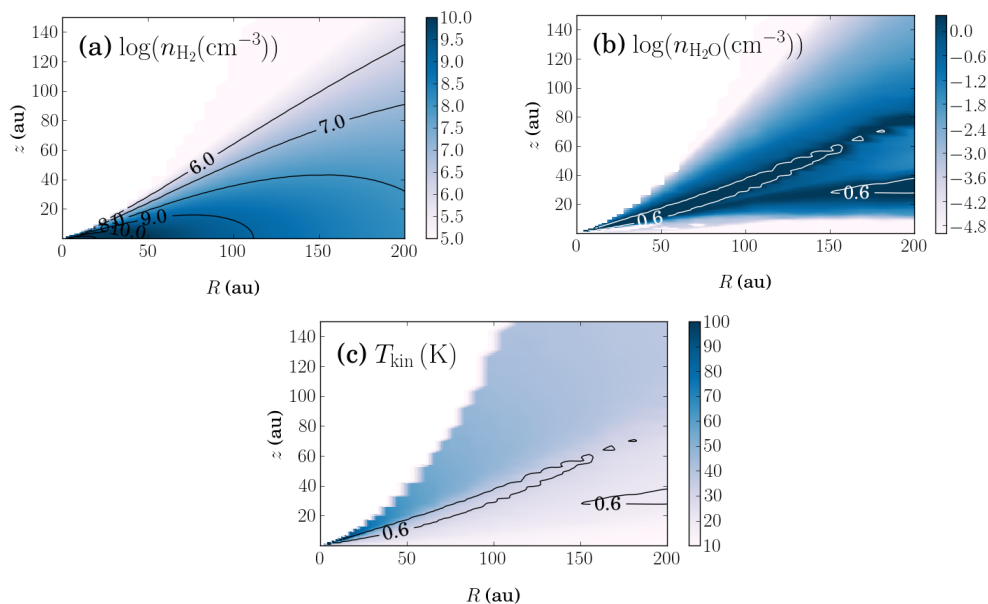


Figure 3.2: Overview of the adopted model structure. (a) Logarithm of the molecular hydrogen density in cm^{-3} with black contours. (b) Logarithm of the water vapor density with white contours at 0.6 cm^{-3} . (c) Gas temperature in K. Black contours represent the logarithm of the water abundance at 0.6 cm^{-3} .

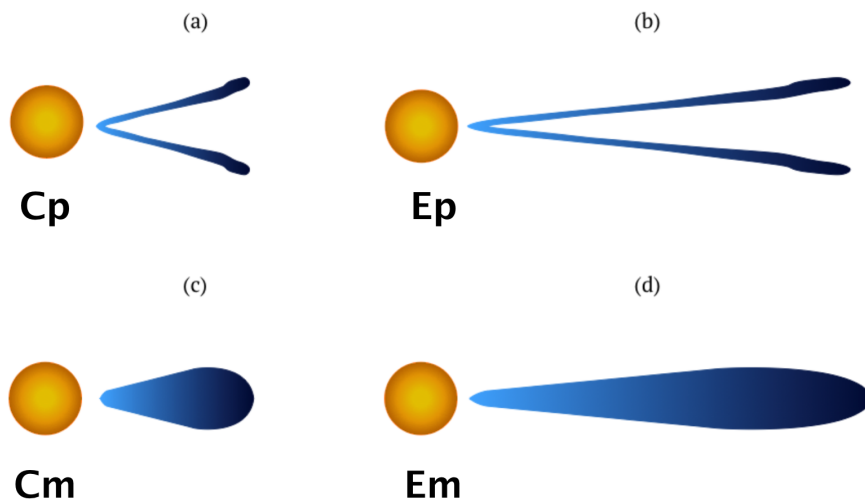


Figure 3.3: Schematic illustration of the location of water vapor in our models: (a) Compact photodesorption-layer configuration (Cp). (b) Extended photodesorption-layer configuration (Ep). (c) Compact with a constant abundance configuration (Cm). (d) Extended with a constant abundance configuration (Em).

that the number of iterations of each point are set manually. We set this number to 12 and confirmed convergence in our models by performing consecutive iterations. Forty channels of 110 m s^{-1} each were used for all line models with 200 pixels of 0.05 arcsec. Because we aimed at comparing these models with spatially unresolved data, we calculated the total flux by summing all the pixels after subtracting the continuum.

Rate coefficients for ortho-ammonia, N_2H^+ , and both spin isomers of water were taken from the Leiden Atomic and Molecular Database (Schöier et al. 2005)². The excitation levels of para- H_2O and ortho- H_2O have separate coefficients for o- H_2 and p- H_2 (Daniel et al. 2011). The o- NH_3 collision rates are only available for p- H_2 , therefore we considered the total H_2 as p- H_2 to calculate their population levels (see Danby et al. 1988). The N_2H^+ collision rates were adopted from HCO^+ following Flower (1999). We assumed that the H_2 ortho-to-para ratios are in local thermal equilibrium. Given the low dust temperatures, this implies H_2 OPR < 0.3 . If instead we increase the H_2 ortho-to-para ratio to 3, the high-temperature limit for formation on grains (Flower et al. 1996), it will increase the H_2O line fluxes by a factor ~ 2 . We discuss the effect of this on the inferred water vapor mass below.

3.4 Results

Figure 3.4 shows the emerging line flux in the *Herschel* beam as a function of ammonia and water vapor mass. These curves of growth (flux (F) vs mass \propto column density(N)) are consistent with saturated lines: the slopes go from linear ($F \propto N$) in the low-opacity regime to saturated ($F \propto \sqrt{\ln(N)}$). The latter behavior is due to the line becoming gradually optically thick in its wings, resulting in a steady flux growth.

Our four models predict different asymptotic values for high vapor masses. In the asymptotic regimes, the lines are fully thick and probe only a very thin region near the surface of the disk. The larger E models therefore result in more flux than the smaller C models. The m models trace higher H_2 densities but lower temperatures than the corresponding p models, resulting in different predicted fluxes. This has a strong effect on the water lines, which have critical densities and upper level energies higher than the conditions prevalent in the regions where the lines originate. This effect is strongest for the Cm models because in this regime densities are considerably higher and the lines become thermalized and opaque, resulting in higher required water-vapor masses.

Table 3.2 summarizes the best-fit vapor masses; error estimates include statistical errors on the observations and the systematic errors on the total line flux, estimated to be about 20%. The ammonia-to-water ratios shown in Table 3.2 assume an OPR of ammonia of either ∞ or 1. As stated above in Sect. 3.3.3, we assumed that H_2 ortho-to-para ratios are in local thermal equilibrium. If we increase this value to 3 (the high-temperature limit), the derived masses would decrease by a little more than one order of magnitude in our most massive and optically thick model (Cm) and by less than one order of magnitude in the remaining models (Cp, Em, and Ep). We do not include this in the error budget of our reported values because the NH_3 and N_2H^+ might be equally affected.

All four models yield o- NH_3 masses ranging from $(0.7\text{--}1.2)\times 10^{21}$ g for models Ep, Em, and Cp, to 1.1×10^{22} g. These correspond to ammonia abundances ranging from $(2.0\text{--}9.5)\times 10^{-12}$ (E models) to $(0.6\text{--}1.7)\times 10^{-10}$ (C models), relative to H_2 . For water, a higher range of masses is inferred, ranging from $(2.2\text{--}4.5)\times 10^{21}$ g for models Ep, Em, and Cp, to 1.6×10^{23} g for model Cm. These correspond to water abundances ranging from $(1.1\text{--}3.0)\times 10^{-11}$ (E models) to $(4.5\text{--}9.0)\times 10^{-10}$ (C models), relative to H_2 . The water OPR is found to range from

²www.strw.leidenuniv.nl/~moldata/

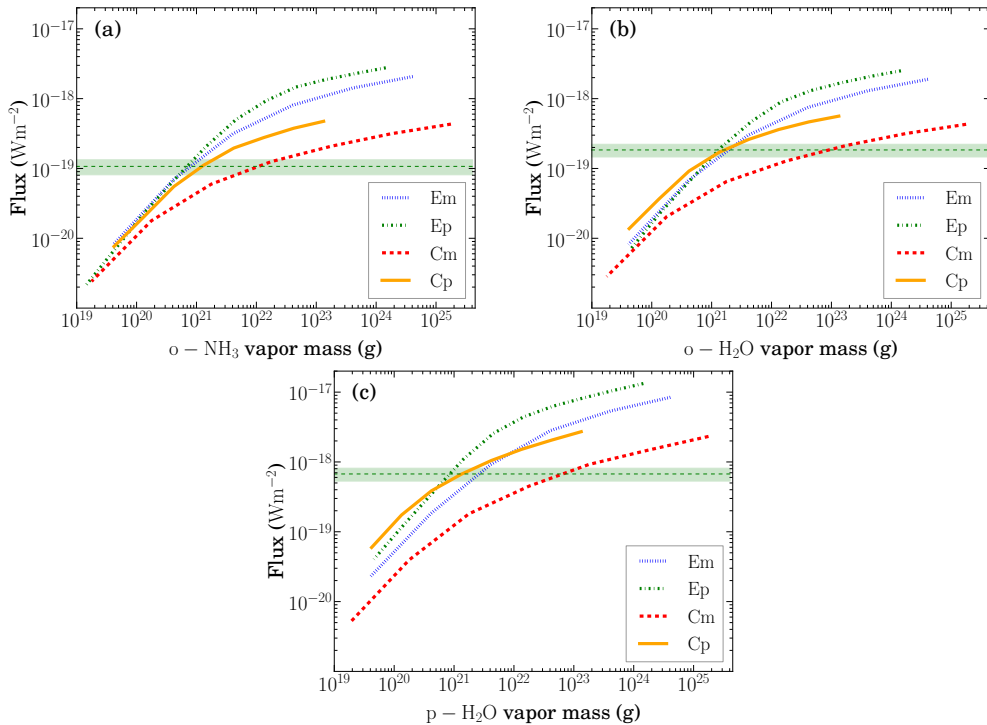


Figure 3.4: Panels (a), (b) and (c) show the LIME (Brinch & Hogerheijde 2010) output of the total line fluxes of ortho-NH₃, ortho-H₂O, and para-H₂O, respectively, as a function of the total water vapor mass. The blue, green, red, and yellow curves correspond to the Em, Ep, Cm, and Cp models, respectively. The dashed lines and horizontal green bar show the observed line fluxes and their 3 σ ranges, with sigma having two sources of noise added in quadrature; the systematic error of the observations, estimated to be about 20% of the total flux, and the rms of the spectra.

0.73 to 1.52. If the associated errors are considered, the range is much wider (0.2-3.0) with model Ep, Cp and Cm in agreement with the interstellar and cometary range of 2.0-3.0 for the OPR of water. The ammonia-to-water ratio ranges from 7%^{+9%}_{-5%} to 84%^{+61%}_{-36%}.

Calculations using a simple escape-probability code (RADEX, van der Tak et al. 2007) reproduce the observed line fluxes adopting the inferred vapor masses and using densities and temperatures representative for the emitting regions. But only a full 3D calculation can reproduce the exact line fluxes because of the wide range in densities and temperatures. These simple calculations also show that, under the conditions of the four models, equal amounts of o-H₂O and o-NH₃ give approximately equal line strengths (within 50%). This means that we can relate the observed line ratios of $F_{\text{o-NH}_3}/F_{\text{o-H}_2\text{O}} \sim 0.6$ to estimate the actual overall NH₃/H₂O abundance fraction of about 0.35-0.65 as confirmed by the detailed LIME modeling below. The high NH₃/H₂O ratios suggested by most models are therefore a direct consequence of the near-equal observed line fluxes of H₂O and NH₃; only in the Cm model where lines are opaque, are much lower NH₃/H₂O values consistent with the observed fluxes.

Our best-fit model result for N₂H⁺ agrees with the N₂H⁺ 4–3 emission reported in Qi et al. (2013). The fit to the N₂H⁺ 6–5 emission yields a total N₂H⁺ vapor mass of 4.9×10^{21} g, which is ~50% higher than the model of Qi et al. (2013) obtained from integrating their best-fit model ($z_{\text{big}}(H) = 3$ in Table S2).

Table 3.2: Summary table of our results in different regimes.

	Ep	Em	Cp	Cm
Total o – H ₂ O vapor mass (10 ²¹ g)	1.3 ^{+0.4} _{-0.3}	1.9 ^{+0.6} _{-0.5}	1.6 ^{+1.1} _{-0.6}	94 ^{+111.2} _{-5.8}
Total p – H ₂ O vapor mass (10 ²¹ g)	0.9 ^{+0.2} _{-0.2}	2.6 ^{+0.8} _{-0.7}	1.4 ^{+0.7} _{-0.6}	65 ^{+5.4} _{-3.4}
Total o – NH ₃ vapor mass (10 ²⁰ g)	7.0 ^{+1.8} _{-1.9}	8.0 ^{+0.3} _{-0.3}	12 ⁺⁷ ₋₄	110 ⁺¹³⁰ ₋₆₀
OPR	1.52 ^{+0.58} _{-0.49}	0.73 ^{+0.32} _{-0.28}	1.14 ^{+0.97} _{-0.65}	1.38 ^{+2.07} _{-1.15}
NH ₃ /H ₂ O ^a	33% ^{+11%} _{-11%} ~ 66% ^{+21%} _{-22%}	19% ^{+8%} _{-7%} ~ 38% ^{+17%} _{-15%}	42% ^{+30%} _{-18%} ~ 84% ^{+61%} _{-36%}	7% ^{+9%} _{-5%} ~ 15% ^{+20%} _{-11%}

Notes. The errors on the masses include noise and 20% calibration error. ^(a) The values correspond to the number ratio, not the mass ratio, and are calculated with two extreme OPR of ammonia ∞ and 1. Errors are calculated propagating the noise and calibration error of each total abundance.

3.5 Discussion

3.5.1 Ice reservoirs and total gaseous masses

The inferred NH_3 vapor masses from 7.0×10^{20} g to 1.1×10^{22} g are much lower than the potential ammonia ice reservoir of $\sim 3.0 \times 10^{28}$ g. This ice reservoir mass estimate was obtained assuming an elemental nitrogen abundance relative to H of 2.25×10^{-5} and a disk mass of $0.04 \pm 0.02 M_{\odot}$, and assuming that 10% of nitrogen freezes out on grains as NH_3 (Öberg et al. 2011a). In the same way, we estimate a water ice mass reservoir of 3.4×10^{29} g, adopting an oxygen elemental abundance of 3.5×10^{-4} relative to H, assuming that 70% of O is locked up in water (Visser et al. 2009) and all of it is frozen out. Both mass estimates indicate that the detected vapor masses are only tiny fractions ($\lesssim 10^{-6}$) of the available ice reservoirs.

The total water mass of our original chemistry model (4.6×10^{24} g) is 2.5 to 25 times (Cm and Ep models respectively) more massive than the values derived from our reanalysis of the water detection toward TW Hya. H11 reported a model 16 times more massive than their original chemistry model to fit the water emission from the disk of TW Hya. This value is significantly lower than the value of our analogous Ep model, which indicates an even higher degree of settling of the icy grains than previously proposed. This is consistent with earlier conclusions that most volatiles are locked up in large grains near the midplane (Hogerheijde et al. 2011; Du et al. 2015).

3.5.2 Gas-phase chemistry

The reported ammonia-to-water ratios are considerably higher than those found for ices in solar system comets and interstellar sources (Mumma & Charnley 2011), which are typically below 5%. Our model-derived ratios assume that the NH_3 and H_2O emission originates from the same regions; however, if this is not the case, expressing the relative amounts of ammonia and water as a ratio is not very useful. Then, it is better to work with their (disk averaged) abundances of $0.2\text{--}17.0 \times 10^{-11}$ and $0.1\text{--}9.0 \times 10^{-10}$ respectively.

An obvious conclusion from the large amount of NH_3 is that other routes exist for gas-phase NH_3 in addition to evaporating $\text{NH}_3/\text{H}_2\text{O}$ ice mixtures. In the colder outer disk the synthesis of ammonia in the gas phase relies on ion-molecule chemistry. This means that N_2 needs to be broken apart (to release N or N^+) first, but N_2 can self-shield against photodissociation (Li et al. 2013). The chemistry in the disk of TW Hya seems to reflect an elevated X-ray state of the star (Cleeves et al. 2015). This strong X-ray field scenario could be invoked to break N_2 apart. The models of Schwarz & Bergin (2014) for a typical T Tauri disk (with a FUV field measured in TW Hya) give values for the abundance of NH_3 as high as $\sim 10^{-8}$ (the models of Walsh et al. 2015, also produce the same abundance), which would be sufficient to explain the emission. Modeling tailored to TW Hya with the correct stellar and disk parameters, as well as appropriate initial conditions is required to fully address the question of the origin of the large NH_3 abundance.

Of our four models, the Cm model stands out in that it yields much lower $\text{NH}_3/\text{H}_2\text{O}$ ratios that are consistent with the low values found in solar system bodies and interstellar ices. It is also the only model where the (large uncertainties of the) derived water OPR overlap with the 2-3 range commonly found in solar system comets. Recent laboratory work by Hama et al. (2015) shows that water in ices efficiently attains an OPR of 3 upon release into the gas-phase, indicating that the OPR is not a reflection of the physical temperature and that high OPR values are naturally expected. The $\text{NH}_3/\text{H}_2\text{O}$ values and the water OPR values together can be taken as evidence that the Cm model is a correct description for

the distribution of H₂O and NH₃ in the disk. If so, a mechanism to release water in the midplane is required.

3.5.3 Collisions of large bodies as a production mechanism

In the midplane models (Em and Cm), photodesorption cannot explain the abundance of water and ammonia in the gas phase because ultraviolet radiation cannot penetrate these depths. CR-induced H₂O desorption, such as modeled in H11, cannot produce the required amount of H₂O. The typical water vapor abundances found in the H11 chemical model near the midplane are on the order of $X_{\text{H}_2\text{O}} \sim 10^{-13}$, much smaller than the corresponding best-fit midplane abundances in the Em and Cm models of $X_{\text{H}_2\text{O}} \sim 10^{-10} - 10^{-9}$. How can volatiles such as ammonia and water exist near the midplane where low temperatures and high densities would ensure rapid freeze-out?

One way of releasing such a vapor mass from the icy reservoir would be through collisions of larger icy bodies. We can calculate how much water needs to be released through these collisions if we assume steady-state with freeze-out to retain the observed amount of volatiles in the gas phase. Freeze-out is calculated using the freeze-out rate expression for neutral species derived in Charnley et al. (2001). For typical temperatures of 12 K and densities of $1.7 \times 10^9 \text{ cm}^{-3}$, the freeze-out rate of water vapor is $2.5 \times 10^{13} \text{ g s}^{-1}$ if we consider the (Em) model to match the observations. That is equivalent to completely destroying $\sim 7,000$ comets per year, with a mass similar to Halley's comet and assuming they consist of 50% water. After 10 Myr roughly 5% of the water previously locked up in icy grains would be back to the gas phase if an ice reservoir of $3.4 \times 10^{29} \text{ g}$ were present in the disk. In the case of the (Cm) model a higher production of water vapor $1.6 \times 10^{16} \text{ g s}^{-1}$ is needed to match the observations. This would mean destroying $\sim 5 \times 10^6$ comets per year. After 10 Myr we would have produced ten times more water vapor than its total ice reservoir. Such large numbers of collisions and the significant (or even unrealistic) amount of released water suggest that collisions between icy bodies are an unlikely explanation for the observed amount of water and ammonia vapor in the midplane models.

The freeze-out rates used above have been calculated assuming a typical grain size distribution $n(a) \propto a^{-3.5}$ (Mathis et al. 1977) with smallest and largest grains sizes of 10^{-8} m and 10^{-1} m . Since the majority of the surface for freeze-out is on (sub) μm -sized grains, we can expect this surface to be substantially reduced if these smaller grains are removed thus reducing the freeze-out rate significantly. Small grains may be removed by photoevaporating winds (Gorti et al. 2015), when transported to the upper layers by vertical mixing, or have coagulated into larger grains. In the extreme case where all of the μm -size grains have grown into larger bodies the freeze-out rate can be reduced by two orders of magnitude.

We can achieve a drop by a factor of 100 in the freeze-out rate by directly calculating the mean grain surface in Eq.6 from Charnley et al. (2001) by setting $a_{\text{min}}=10^{-4} \text{ m}$ for our Em model, $a_{\text{min}}=10^{-3} \text{ m}$ for our Cm model (see calculations of Vasyunin et al. 2011) and $a_{\text{max}}=10^{-1} \text{ m}$ for both. If this assumption holds, then our model with the highest production rate (Cm) will have processed only 10% of its water reservoir into water vapor in the span of 10 Myr, equivalent to destroying only ~ 5000 comets per year. In the same way, the amount of water processed in the span of 10 Myr in our (Em) will be only 0.5% of its ice reservoir, equivalent to destroying only ~ 70 comets per year. These numbers are much more realistic, making this a viable mechanism for releasing volatiles in the midplane.

Nevertheless, for this scenario to be viable, the system must meet some criteria. First, the comets (or planetesimals) must have a high enough collision rate that accounts for the numbers estimated above. In the outer disk this can be enhanced through shepherding by planets, that is, sweeping up the planetesimals into one proto-debris belt. Acke et al. (2012)

calculated a collision rate of $6.3 \times 10^{13} \text{ g s}^{-1}$ in Fomalhout's debris disk to reproduce the thin dust belt seen in far-infrared images (70-500 μm). This rate is similar to our estimated rate even in the absence of a reduction in grain surface available for freeze-out. For Fomalhout, this rate corresponds to a population of 2.6×10^{11} comets with a size of 10 km, which is similar to the number of comets in the Oort cloud of $10^{12} - 10^{13}$ (Weissman 1991). Second, the collisions must release enough energy to sublimate the ices. This is only achieved if the relative velocities of the parent bodies are sufficiently high. If the colliding bodies have high eccentricities their relative velocities can be high. But in the presence of gas, we expect their orbits to be circularized. If this is the case, then the relative velocities will be dominated by the radial drift in the outer parts of the disk and enhanced in the very inner regions by turbulence. Finally, the small dust produced in the cometary (or planetesimal) collisions themselves must not provide a surface for the volatiles to freeze back onto.

If a sufficient number of small grains ($\lesssim \mu\text{m}$) are removed by coagulation into larger grains ($\gtrsim \text{mm}$) and the relative velocities and rates of the collisions between larger bodies ($\gtrsim \text{m}$) in the midplane are sufficiently high to meet the conditions above, then collisions between icy bodies are a plausible mechanism for releasing (and keeping in the gas phase for long enough) the amount of water and ammonia that we observe. The treatment above is simplistic and there are many other ways to achieve this (e.g., changing the slope of the grain distribution or by photoevaporation of grains along with the gas). A full treatment of the combined effect of grain growth, drift, settling, collisions and volatile freeze-out is needed to confirm this scenario, but is beyond the scope of this paper.

3.6 Conclusions

We have successfully detected NH_3 and N_2H^+ in the disk surrounding TW Hya. We used a non-LTE excitation and radiative transfer code and a detailed physical and chemical disk structure to derive the amount of NH_3 , N_2H^+ , and (for comparison) H_2O adopting four different spatial distributions of the molecules. Our main conclusions are as follows.

1. The NH_3 emission corresponds to an ammonia vapor mass that ranges from $7.0 \times 10^{20} \text{ g}$ (Ep model) to $1.1 \times 10^{22} \text{ g}$ (Cm model).
2. We used the above values and the same approach to derive H_2O vapor masses to derive $\text{NH}_3/\text{H}_2\text{O}$ ratios ranging from 7% to 15% (Cm model) and 42% to 84% (Cp model), adopting a NH_3 OPR of ∞ or 1, respectively. These ratios are higher than those observed in solar system and interstellar ices, with the exception of our most massive and compact configuration (Cm model).
3. Of our four models, only model Cm gives $\text{NH}_3/\text{H}_2\text{O}$ ratios as low as observed in interstellar ices and solar system comets. It is also the only model that within the errors gives a water OPR of 2-3, which is similar to solar system comets. This can be taken as evidence that H_2O and NH_3 are indeed located near the midplane at radii $< 60 \text{ au}$.
4. If the H_2O and NH_3 follow the Cp, Ep, or Em spatial distributions, the implied high $\text{NH}_3/\text{H}_2\text{O}$ ratio requires an additional mechanism to produce gas-phase NH_3 . A strong X-ray field may provide the necessary N atoms or radicals to form NH_3 in the gas.
5. If NH_3 and H_2O emission comes from the midplane, where photodesorption does not operate (models m), collisions of larger bodies can release NH_3 and H_2O and explain

the observed vapor. This requires a reduction of the total grain surface available for freeze-out, for example, through the growth of grains into pebbles and larger; and a sufficiently high collision rate and sufficiently violent collisions to release the volatiles.

6. The ammonia vapor mass is similar to the N_2H^+ mass derived with our simple model and to that inferred by Qi et al. (2013) (see Sect. 3.4) within 50%.

Additional spatially resolved observations of ammonia would help to constrain the radial extent of ammonia (and perhaps vertical structure) and refine our current limits. We can observe ammonia isotopes with ALMA in band 7 (ortho- NH_2D $1_{01} - 0_{00}$ at 332.781 GHz and para- NH_2D $1_{01} - 0_{00}$ at 332.822 GHz) and band 8 (ortho- NH_2D $1_{10} - 0_{00}$ at 470.271 GHz and para- NH_2D $1_{10} - 0_{00}$ at 494.454 GHz). We used our models to predict line fluxes of about 1 Jy in band 8 and 30 mJy in band 7 using LIME in all of our models, and considering a value of 0.1 for ammonia deuterium fractionation as found toward protostellar dense cores (Roueff et al. 2005; Busquet et al. 2010), and an OPR ammonia of 1. ALMA can detect such line fluxes in a few hours³. Observations with JVLA or GBT of para-ammonia (para- NH_3 $1_1 - 1_0$ at 23.694 GHz or para- NH_3 $2_1 - 2_0$ at 23.722 GHz) are not possible since our predicted line fluxes are too low (~ 10 mJy).

Acknowledgements. *Herschel* is a European Space Agency space observatory with science instruments provided by European-led principal investigator consortia and with important participation from NASA. HIPI has been designed and built by a consortium of institutes and university departments from across Europe, Canada, and the United States under the leadership of SRON Netherlands Institute for Space Research, Groningen, The Netherlands, and with major contributions from Germany, France, and the US. Consortium members are: Canada: CSA, U. Waterloo; France: IRAP (formerly CESR), LAB, LERMA, IRAM; Germany: KOSMA, MPIFR, MPS; Ireland: NUI Maynooth; Italy: ASI, IFSI-INAF, Osservatorio Astrofisico di Arcetri-INAF; Netherlands: SRON, TUD; Poland: CAMK, CBK; Spain: Observatorio Astronómico Nacional (IGN), Centro de Astrobiología (CSIC-INTA); Sweden: Chalmers University of Technology – MC2, RSS & GARD; Onsala Space Observatory; Swedish National Space Board, Stockholm University – Stockholm Observatory; Switzerland: ETH Zurich, FHNW; USA: Caltech, JPL, NHS. Support for this work was provided by NASA (*Herschel* OT funding) through an award issued by JPL/Caltech. This work was partially supported by grants from the Netherlands Organization for Scientific Research (NWO) and the Netherlands Research School for Astronomy (NOVA). The data presented here are archived at the *Herschel* Science Archive, <http://archives.esac.esa.int/hda/ui>, under OBSID 1342198337 and 1342201585.

Bibliography

- Acke, B., Min, M., Dominik, C., et al. 2012, *A&A*, 540, A125
 Andrews, S. M., Wilner, D. J., Hughes, A. M., et al. 2012, *ApJ*, 744, 162
 Arnold, T. J., Eisner, J. A., Monnier, J. D., & Tuthill, P. 2012, *ApJ*, 750, 119
 Bergin, E. A., Hogerheijde, M. R., Brinch, C., et al. 2010, *A&A*, 521, L33
 Bergin, E. A., Cleeves, L. I., Gorti, U., et al. 2013, *Nature*, 493, 644
 Bottinelli, S., Boogert, A. C. A., Bouwman, J., et al. 2010, *ApJ*, 718, 1100
 Brinch, C., & Hogerheijde, M. R. 2010, *A&A*, 523, A25
 Busquet, G., Palau, A., Estalella, R., et al. 2010, *A&A*, 517, L6
 Calvet, N., D’Alessio, P., Hartmann, L., et al. 2002, *ApJ*, 568, 1008
 Charnley, S. B., Rodgers, S. D., & Ehrenfreund, P. 2001, *A&A*, 378, 1024
 Cleeves, L. I., Bergin, E. A., Qi, C., Adams, F. C., & Öberg, K. I. 2015, *ApJ*, 799, 204
 Collings, M. P., Anderson, M. A., Chen, R., et al. 2004, *MNRAS*, 354, 1133
 Danby, G., Flower, D. R., Valiron, P., Schilke, P., & Walmsley, C. M. 1988, *MNRAS*, 235, 229
 Daniel, F., Dubernet, M.-L., & Grosjean, A. 2011, *A&A*, 536, A76
 de la Reza, R., Jilinski, E., & Ortega, V. G. 2006, *AJ*, 131, 2609
 Debes, J. H., Jang-Condell, H., Weinberger, A. J., Roberge, A., & Schneider, G. 2013, *ApJ*, 771, 45
 Du, F., Bergin, E. A., & Hogerheijde, M. R. 2015, *ApJ*, 807, L32
 Dutrey, A., Guilloteau, S., & Guelin, M. 1997, *A&A*, 317, L55
 Dutrey, A., Henning, T., Guilloteau, S., et al. 2007, *A&A*, 464, 615

³Calculations performed with the ALMA sensitivity calculator (<https://almascience.eso.org/proposing/sensitivity-calculator>)

- Eisner, J. A., Chiang, E. I., & Hillenbrand, L. A. 2006, *ApJ*, 637, L133
- Flower, D. R. 1999, *MNRAS*, 305, 651
- Flower, D. R., Pineau des Forets, G., Field, D., & May, P. W. 1996, *MNRAS*, 280, 447
- Gorti, U., Hollenbach, D., & Dullemond, C. P. 2015, *ApJ*, 804, 29
- Guilloteau, S., Di Folco, E., Dutrey, A., et al. 2013, *A&A*, 549, A92
- Hama, T., Kouchi, A., & Watanabe, N. 2015, *Science*, 351, 65
- Hoff, W., Henning, T., & Pfau, W. 1998, *A&A*, 336, 242
- Hogerheijde, M. R., Bergin, E. A., Brinch, C., et al. 2011, *Science*, 334, 338
- Hughes, A. M., Wilner, D. J., Calvet, N., et al. 2007, *ApJ*, 664, 536
- Krist, J. E., Stapelfeldt, K. R., Ménard, F., Padgett, D. L., & Burrows, C. J. 2000, *ApJ*, 538, 793
- Li, X., Heays, A. N., Visser, R., et al. 2013, *A&A*, 555, A14
- Mandell, A. M., Bast, J., van Dishoeck, E. F., et al. 2012, *ApJ*, 747, 92
- Mathis, J. S., Rumpl, W., & Nordsieck, K. H. 1977, *ApJ*, 217, 425
- Menu, J., van Boekel, R., Henning, T., et al. 2014, *A&A*, 564, A93
- Mumma, M. J., & Charnley, S. B. 2011, *ARA&A*, 49, 471
- Öberg, K. I. 2009, PhD thesis, Leiden Observatory, Leiden University, P.O. Box 9513, 2300 RA Leiden, The Netherlands
- Öberg, K. I., Boogert, A. C. A., Pontoppidan, K. M., et al. 2011a, *ApJ*, 740, 109
- Öberg, K. I., Qi, C., Fogel, J. K. J., et al. 2010, *ApJ*, 720, 480
- Öberg, K. I., Qi, C., Fogel, J. K. J., et al. 2011b, *ApJ*, 734, 98
- Qi, C., Ho, P. T. P., Wilner, D. J., et al. 2004, *ApJ*, 616, L11
- Qi, C., Öberg, K. I., Wilner, D. J., et al. 2013, *Science*, 341, 630
- Ratzka, T., Leinert, C., Henning, T., et al. 2007, *A&A*, 471, 173
- Roberge, A., Weinberger, A. J., & Malumuth, E. M. 2005, *ApJ*, 622, 1171
- Rosenfeld, K. A., Qi, C., Andrews, S. M., et al. 2012, *ApJ*, 757, 129
- Roueff, E., Lis, D. C., van der Tak, F. F. S., Gerin, M., & Goldsmith, P. F. 2005, *A&A*, 438, 585
- Rucinski, S. M., & Krautter, J. 1983, *A&A*, 121, 217
- Saljck, C., Pontoppidan, K. M., Blake, G. A., Najita, J. R., & Carr, J. S. 2011, *ApJ*, 731, 130
- Schöier, F. L., van der Tak, F. F. S., van Dishoeck, E. F., & Black, J. H. 2005, *A&A*, 432, 369
- Schwarz, K. R., & Bergin, E. A. 2014, *ApJ*, 797, 113
- Thi, W.-F., van Zadelhoff, G.-J., & van Dishoeck, E. F. 2004, *A&A*, 425, 955
- Thi, W.-F., Mathews, G., Ménard, F., et al. 2010, *A&A*, 518, L125
- van der Tak, F. F. S., Black, J. H., Schöier, F. L., Jansen, D. J., & van Dishoeck, E. F. 2007, *A&A*, 468, 627
- van Dishoeck, E. F., Bergin, E. A., Lis, D. C., & Lunine, J. I. 2014, *Protostars and Planets VI*, 835
- van Dishoeck, E. F., Kristensen, L. E., Benz, A. O., et al. 2011, *PASP*, 123, 138
- van Leeuwen, F. 2007, *A&A*, 474, 653
- Vasunin, A. I., Wiebe, D. S., Birnstiel, T., et al. 2011, *ApJ*, 727, 76
- Visser, R., van Dishoeck, E. F., Doty, S. D., & Dullemond, C. P. 2009, *A&A*, 495, 881
- Walsh, C., Nomura, H., & van Dishoeck, E. 2015, *A&A*, 582, A88
- Webb, R. A., Zuckerman, B., Platais, I., et al. 1999, *ApJ*, 512, L63
- Weinberger, A. J., Becklin, E. E., Schneider, G., et al. 2002, *ApJ*, 566, 409
- Weissman, P. R. 1991, in *Astrophysics and Space Science Library*, Vol. 167, IAU Colloq. 116: Comets in the post-Halley era, ed. R. L. Newburn, Jr., M. Neugebauer, & J. Rahe, 463–486
- Wichmann, R., Bastian, U., Krautter, J., Jankovics, I., & Rucinski, S. M. 1998, *MNRAS*, 301, 39L



4

Comparing detections and upper limits of NH_3 and NH_2D in the disks of TW Hya and HD163296

4.1 Introduction

Nitrogen within Solar System bodies, inherited from the Solar Nebula, takes a variety of forms: N_2 on Earth, organics in meteorites, and NH_3 and organics in comets (Schwarz & Bergin 2014; Mumma & Charnley 2011). Most bodies are furthermore strongly depleted in nitrogen, compared to oxygen and carbon (Pontoppidan et al. 2014). In the interstellar medium 10%-20% of nitrogen is contained in ices such as NH_3 , NH_4^+ , and XCN, the latter of which is mostly in the form of OCN^- (Öberg et al. 2011). The remainder of the nitrogen budget is thought to reside in the gas in atomic and molecular form, and does not represent a suitable reservoir to deliver nitrogen to rocky planets, meteorites, and comets. Molecular and atomic nitrogen is not directly observable in the dense interstellar medium (ISM). However, most of the simple nitrogen-bearing ices have been detected in the gas-phase toward star forming regions. Their initial abundances are critical for the understanding of the chemical composition of nitrogen-bearing species throughout the star formation process and, consequently, Solar System bodies.

Ammonia is one of the main ice reservoirs of nitrogen and is readily detected in star forming regions (Bottinelli et al. 2010; Daranlot et al. 2012; Boogert et al. 2015). It has only been recently detected, for the first time, toward the old planet-forming disk around TW Hya using *Herschel*/HIFI by Salinas et al. (2016). Our modelling, that considered different radial distributions of ammonia high in the upper layers of the disk as well as settled and compact models, showed that the total vapor mass estimates can range across two orders of magnitude. Only the most settled and compact model (Cm), following the same distribution of mm-size grains (Andrews et al. 2012), is in agreement with the expected NH_3/H_2O ratio and ortho to para ratio (OPR) of water in comets. Detailed chemical models have shown ammonia to be able to form as a product of several processes at large radii, namely warm gas-phase chemistry, ion-molecule chemistry and photodesorption processes (Walsh et al. 2015). On grains, ammonia forms through atomic nitrogen hydrogenation (Brown & Millar 1989; Hiraoka et al. 1995; Hidaka et al. 2011; Fedoseev et al. 2015). Processes to release NH_3 from ice to gas at temperatures below the thermal desorption include cosmic-ray desorption (Hasegawa & Herbst 1993), reactive desorption (Garrod et al. 2007) and photodesorption (Prasad & Tarafdar 1983; Hartquist & Williams 1990). The formation of ammonia in grains dominates in the very early stages of star formation. In more evolved stages, where protoplanetary disks are formed, the dominant process shifts to gas-phase formation (Sipilä et al. 2015; Harju et al. 2017). This process occurs through a well-known chain of reactions, starting with the dissociation of N_2 (by photo-processes or He^+) and terminating in $NH_4^+ + e \rightarrow NH_3 + H$ (Le Gal et al. 2014; Roueff et al. 2015; Walsh et al. 2015).

Observations of gas-phase ammonia in cold star-forming cores (Daniel et al. 2016; Pillai et al. 2011; Busquet et al. 2010; Crapsi et al. 2007; Roueff et al. 2005) and ices in comets (Crovisier et al. 2004) show very high NH_2D/NH_3 ratios of ~ 0.5 and ~ 0.05 respectively¹. This high NH_2D/NH_3 ratio suggests formation on cold environments. However, the deuteration of ammonia in the gas-phase is dominated by the isotopologues of H_3^+ and is faster and more efficient than deuteration on grains (Harju et al. 2017; Sipilä et al. 2015). TW Hya and HD163296 are known to harbor deuterated species, like DCN with deuterium fractionations of 0.017 and 0.016 respectively (Öberg et al. 2012; Huang et al. 2017), DCO^+ with deuterium fractionations of 0.035 and 0.048 respectively (van Dishoeck et al. 2003; Huang et al. 2017) and N_2H^+ with a deuterium fractionation of ~ 0.4 toward HD163296 (Salinas et al. 2017). In prestellar cores, NH_2D/NH_3 is found to be consistently higher than

¹The NH_2D/NH_3 ratio is different than the atomic D/H ratio of NH_3 , which accounts for the number of H atoms in NH_3 .

DCO⁺/HCO⁺ and DCN/HCN (Treviño-Morales et al. 2014). Together, this suggest that disks around HD163296 and TW Hya may be equally rich in NH₂D.

We first aim to constrain the amount of gas-phase NH₃ in HD 163296, in comparison to TW Hya. Secondly, we observed o-NH₂D towards HD 163296. Since we do not observe the same line in TW Hya, we assume that the NH₂D/NH₃ ratio in the gas-phase is 0.1 and compare the expected NH₂D mass with the upper limits derived for HD 163296. Finally, we estimate the integration time in ALMA to detect the NH₂D line in HD 163296 and TW Hya. Section 4.2 presents the data and their reduction. Section 4.3 contains our modeling approach and Section 4.4 the resulting upper limits on the NH₃ and NH₂D vapor masses. Section 4.5 discusses the implication of our models and compares the values obtained for HD163296 to those of TW Hya. We also predict line fluxes for deuterated ammonia toward TW Hya. Finally, Section 4.6 summarizes our conclusions.

4.2 Observations

Observations of o-NH₃ 1₀ – 0₀ in TW Hya ($\alpha_{2000} = 11^{\text{h}}01^{\text{m}}51^{\text{s}}.91$, $\delta_{2000} = -34^{\circ}42'17''.0$) were previously presented by Salinas et al. (2016) and were obtained using the Heterodyne Instrument for the Far-Infrared (HIFI) as part of the key program ‘Water in Star-Forming Regions with *Herschel*’ (WISH) (van Dishoeck et al. 2011). We now present observations toward the Herbig Ae star HD 163296 ($\alpha_{2000} = 17^{\text{h}}56^{\text{m}}51^{\text{s}}.21$, $\delta_{2000} = -21^{\circ}57'22''.0$) as part of the same program taken on 2010 March 21 of the o-NH₃ 1₀ – 0₀ line at 572.49817 GHz using receiver band 1b and a local oscillator tuning of 551.895 GHz (OBS-ID 1342192516). With a total on-source integration of about 20 min, the observation was taken with system temperatures of 75-95 K. The data were recorded in the Wide-Band Spectrometer (WBS) which covers 4.4 GHz with 1.1 MHz resolution. This corresponds to 0.59 km s⁻¹ at 572 GHz. A beam efficiency $\eta_{\text{nb}} = 0.64$ was used to calibrate the data and the procedure is identical to that of Du et al. (2017).

We also present ALMA Band 8 archival observations of the p-NH₂D 1₀ – 0₀ line at 494.454 GHz toward HD 163296 (project 2013.1.00527.S) taken on 2015 May 2. The total integration time on source was 14 min with thirty-six 12 m antennas. The system temperature varied from 500 to 900 K. The correlator set up had 4 different spectral windows (SPW). Two of these SPW contain the [CI] atomic line at 492.160 GHz and the p-NH₂D 1₀ – 0₀ line at 494.454 GHz with spectral resolutions of 488 kHz (0.30 km s⁻¹) and 244 kHz (0.15 km s⁻¹) respectively. The other two SPW contain wideband (2 GHz) continuum centered at 480.236 GHz and 482.047 GHz. The quasars J1256-0547 and J1733-1304 were used as bandpass and gain calibrators respectively. Titan was used as total flux calibrator using the Butler-JPL-Horizons 2012 flux models for Solar System objects available through the Common Astronomy Software Applications (CASA). The data were calibrated following the standard CASA reduction as provided in the calibration scripts by ALMA. Baselines in the antenna array configuration correspond to a range in uv -distance of 30–570 k λ , which translates into a beam of $\sim 0''.36$. Self-calibration was applied to the data using the continuum emission from the two SPW containing wideband continuum and the line-free channels of the SPW containing high-spectral resolution data. We used DV02 as a reference antenna. We calculated calibration solutions twice for phase, first using a solution interval of 125 s and secondly together with amplitude using a solution interval of 6.05 s corresponding to the integration scan. A minimum of 4 antennas and a signal-to-noise (S/N) of 2 was required for the solution to be valid. The data were continuum subtracted in the uv -space using a zero-order polynomial fit and imaged using the CLEAN task in CASA with natural weighting.

The p-NH₂D 1₀–0₀ and o-NH₃ 1₀–0₀ observations resulted in non-detections for these modest integration times. The channel maps in the spectral cube of the p-NH₂D 1₀–0₀ reached a sensitivity of 30 mJy beam⁻¹ channel⁻¹. In Table 4.1 we report upper limits for these transitions and the total line flux of the o-NH₃ 1₀–0₀ transition toward TW Hya. Figure 4.1 shows the calibrated spectra of HD163296 and TW Hya for the selected lines.

4.3 Modeling Approach

In this section we describe our adopted physical models and two different parametrizations of the abundance of ammonia and its deuterated isotope. We assume that deuterated ammonia follows the same distribution as its non-deuterated isotope to translate the derived total line flux upper limits into total masses. Although this assumption is not necessarily true if their formation pathways are different, it translates as a lower limit on the NH₂D/NH₃ ratio because gas-phase NH₂D might not be present in the regions where gas-phase NH₃ exists. By comparing the amounts of ammonia of the two disks we aim to make a prediction for upcoming observations of the expected line flux of deuterated ammonia for both disks.

4.3.1 Physical structure

We model the physical structure of both disks with models found previously in the literature. We adopt the physical models of Cleeves et al. (2015) for TW Hya and of Mathews et al. (2013) for HD163296. Cleeves et al. (2015) used HD measurements (Bergin et al. 2013) to constrain a total gas mass for the disk of TW Hya of $0.04 \pm 0.02 M_{\odot}$ whereas Mathews et al. (2013) fitted the SED of HD 163296 and used a dust to gas ratio of 0.0065 (Draine & Lee 1984). The dust surface density profile is defined by the following expression

$$\Sigma_d(R) = \begin{cases} \Sigma_c \left(\frac{R}{R_c}\right)^{\gamma} \exp\left[-\left(\frac{R}{R_c}\right)^{(2-\gamma)}\right] & \text{if } R_{\text{in}} \leq R \leq R_{\text{out}} \\ 0 & \text{if } R < R_{\text{in}} \text{ or } R > R_{\text{out}} \end{cases} \quad (4.1)$$

and their vertical distribution by a scale height of the form

$$H(R) = H_c \left(\frac{R}{R_c}\right)^{\psi}, \quad (4.2)$$

where R_c is a characteristic radius, γ represents the radial dependency of the disk viscosity, ψ describes the power law disk flaring, and R_{in} and R_{out} the inner and outer radii of the disk. The H_c takes four different values for the HD163296 model: H_{small} and H_{large} to describe the small and large population of dust grains, and H_{main} and H_{tail} that describe the gas distribution as two-component model with a term f_{tail} describing the fraction of the total gas mass in the tail component. The adopted TW Hya model makes no distinction between large and small dust populations (see Appendix A.2 of Cleeves et al. 2015). Both models do not consider a radial separation of small and large dust grain populations. Table 4.2 shows the adopted values of the parameters described above for both sources.

We also adopt their estimated gas temperature profile $T(R, z)$ calculated from the ultraviolet radiation field throughout the disk by using the radiative transfer code TORUS in the case of TW Hya (see Appendix A of Cleeves et al. 2015, and references therein) and the axisymmetric 3D radiative transfer code RADMC in the case of HD163296 (Dullemond & Dominik 2004).

Table 4.1: Observed line parameters.

Source	Transition	$F_{\text{line}} (10^{-19} \text{ W m}^{-2})^{a,b}$	$V_{\text{LSR}} (\text{km s}^{-1})^b$	FWHM (km s^{-1}) ^b	$T_{\text{mb}} (\text{mK km s}^{-1})$
TW Hya	o-NH ₃ 1 ₀ - 0 ₀	1.1±0.13	3.0±0.06	0.9±0.06	15.1±2.1
HD163296	o-NH ₃ 1 ₀ - 0 ₀	<2.1	5.8	9.0	<36.9
HD163296	p-NH ₂ D 1 ₀ - 0 ₀	<0.3	5.8	9.0	<8.8 ^c

Notes. ^(a) The upper limit for p-NH₂D 1₀ - 0₀ is equal to 3σ , where σ is the rms of the spectra from a square box of $10''0 \times 10''0$. The errors and upper limits are calculated taking the random errors due to noise only and do not include the calibration uncertainty, estimated to be about 20% of the total flux in the case of observations taken with *Herschel*. F_{line} is the integrated flux from $V_{\text{LSR}} = +1.5$ to $+4.1 \text{ km s}^{-1}$ in the case of TW Hya, and from $V_{\text{LSR}} = +1.3$ to $+10.3 \text{ km s}^{-1}$. ^(b) For TW Hya these are the results of a Gaussian fit, for HD163296 the values of V_{LSR} and FWHM are taken from Mathews et al. (2013). Errors on V_{LSR} and FWHM are formal fitting errors and much smaller than the spectral resolution of 0.26 km s^{-1} . ^(c) This integrated line flux was calculated diluting the ALMA signal to the correspondent *Herschel* beam of $44''0$ at the observed frequency of 493.454 GHz assuming a source size of $10''0 \times 10''0$.

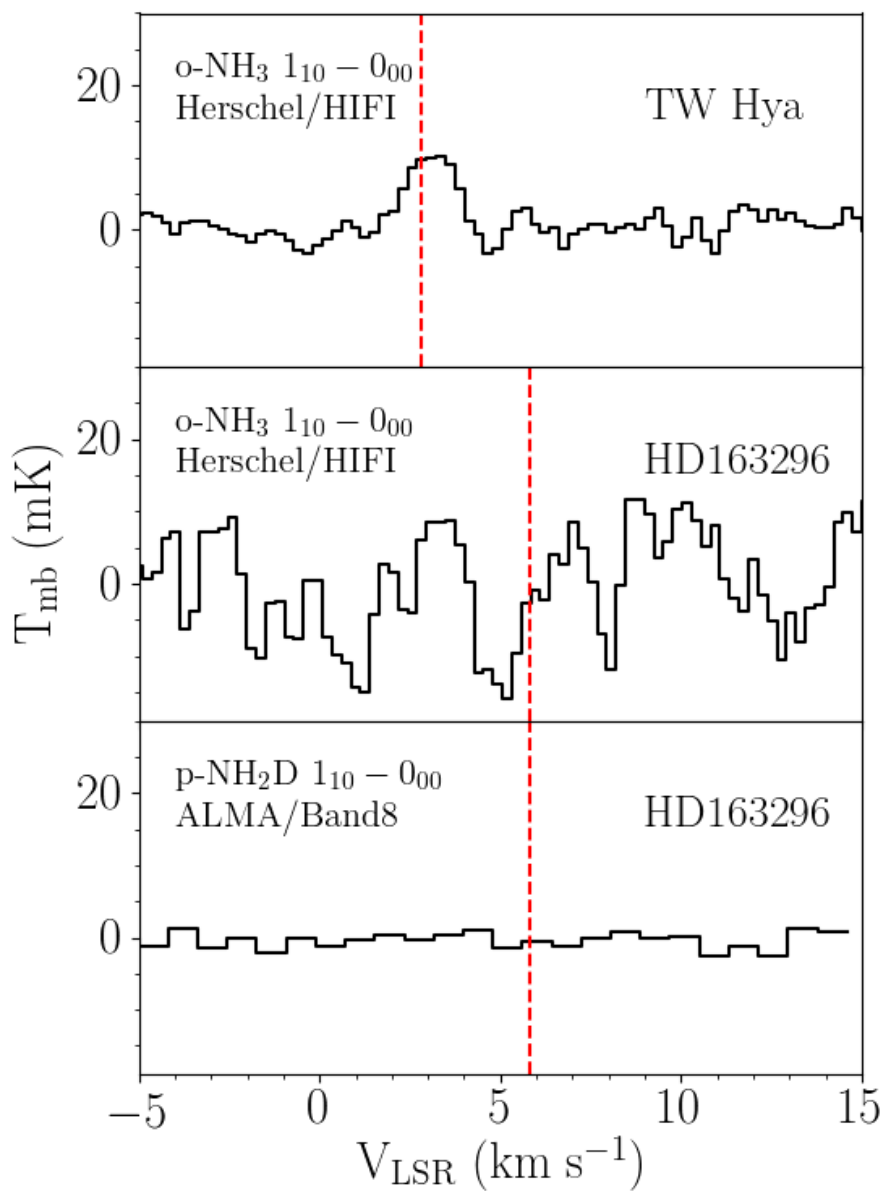


Figure 4.1: Observed spectra of o-NH_3 $1_0 - 0_0$ with *Herschel* toward TW Hya and HD163296 and of $\text{p-NH}_2\text{D}$ $1_0 - 0_0$ with ALMA Band 8 toward HD163296. The ALMA signal was beam diluted to the correspondent *Herschel* beam of $44''0$ at 493.454 GHz.

Table 4.2: Adopted model parameters.

Disk parameters	HD163296	TW Hya
Σ_c	0.037 g cm ⁻²	0.040 g cm ⁻²
R_c	150 AU	150 AU
R_{in}	0.6 AU	4.0 AU
R_{out}	540 AU	200 AU
γ	1.0	1.0
ψ	0.066	0.3
H_{small}	12 AU	15 AU
H_{large}	9 AU	3 AU
H_{main}	15 AU	15 AU
H_{tail}	30 AU	–
f_{tail}	0.016	–

4.3.2 Parametric abundance models

We consider two different abundance models for ammonia and its single deuterated isotopologues in both disks. The first model simply consists of an extended and constant (model Ec) abundance throughout the entire disk. The second model considers that, in both disks, we expect the distribution of the mm-size grains to have settled to the midplane and migrated inwards as supported by observations of the continuum emission (Andrews et al. 2016; Zhang et al. 2016). Figure 4.2 shows a diagram of these two models. They are analogues of the Cm and Em models of TW Hya presented in (Salinas et al. 2016). In TW Hya, ammonia (and water) is thought to be released to the gas-phase from its icy reservoir, possibly locked in large planetesimals bodies, that follow the distribution of mm-size dust grains (Salinas et al. 2017). Thus we set the Cm model as our preferred model. We implement this settled and compact distribution (Cm) of ammonia and its single deuterated isotope as a constant abundance with respect to $n(\text{H}_2)$ following the mm-size dust grain distribution of Andrews et al. (2012) with $H_c = 10.31$, $\psi = 1.25$ and $R_c = 100$ AU at $R < 60$ AU for TW Hya and with $H_c = 9.0$ AU, $\psi = 0.066$ and R_c at $R < 290$ AU for HD163296 (Mathews et al. 2013; Zhang et al. 2016).

4.3.3 Line excitation and radiative transfer

We used LIME (v1.5), a non-LTE 3D radiative transfer code (Brinch & Hogerheijde 2010) that can predict line and continuum radiation from a source model. All of our models use 50000 grid points. Grid points are distributed randomly in R using a logarithmic scale. This means in practice that inner regions of the disk have a finer sampling than the outer parts of the disk. We perform our calculation in LTE since non-LTE calculations of representative models are indistinguishable from their LTE counterparts. This is due to the relatively low critical density, of only a few 10^7 cm⁻³ for transitions, compared to the densities at the midplane of the adopted models of TW Hya and HD163296. The rate coefficients for o-NH₃ and p-NH₂D were taken from the Leiden Atomic and Molecular Database (Schöier et al. 2005; Daniel et al. 2014; Danby et al. 1988)².

²www.strw.leidenuniv.nl/~moldata/

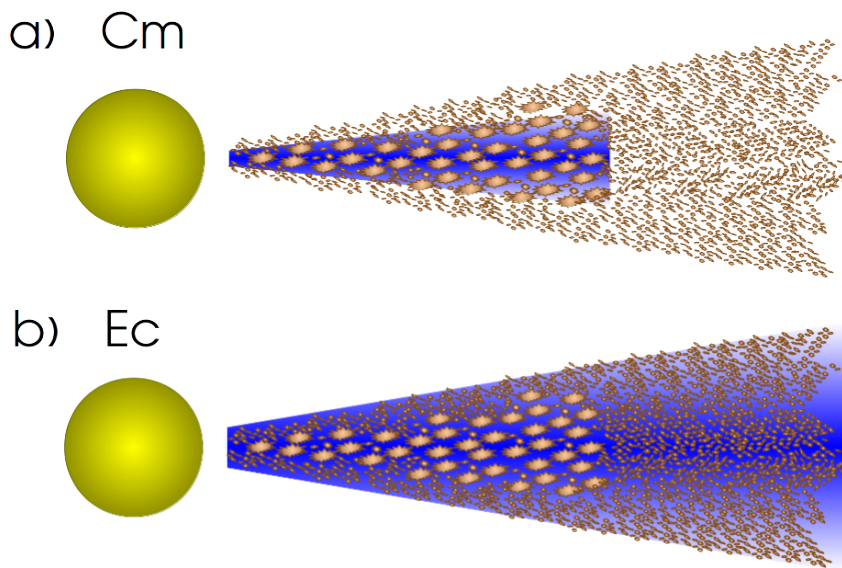


Figure 4.2: Diagram of the compact and settled (Cm), and the extended and constant (Ec) distribution of ammonia. The blue region highlights the location of ammonia following the mm-size grains (Cm) and the entire disk (Ec).

Table 4.3: Upper limits on total vapor masses in the HD163296 disk.

Species	Cm	Ec
o-NH ₃	$< 8.5 \times 10^{20}$ g	$< 1.4 \times 10^{21}$ g
p-NH ₂ D	$< 1.5 \times 10^{20}$ g	$< 6.5 \times 10^{20}$ g

Forty channels of 0.4 km s^{-1} and 0.1 km s^{-1} each, for HD163296 and TW Hya models respectively, were used for all line models with 200 pixels of 0.05 arcsec. Because we aimed at comparing these models with spatially unresolved data, we calculated the total flux by summing all the pixels after subtracting the continuum.

4.4 Results

Figure 4.3 shows the resulting line flux for the targeted lines in the *Herschel* beam as a function of o-NH₃ and p-NH₂D total vapor masses. The slope of the curves are consistent with increasing opacity going from an optically thin regime (flux (F) \propto column density(N)) to saturated ($F \propto \sqrt{\ln(N)}$) as the wings of the line become gradually optically thick.

In the optically thin regime (low total vapor masses) the Cm models result in higher line fluxes than in the Ec models for an equal total vapor mass. At lower vapor masses our radially compact (Cm) model lies within higher temperatures than a radially extended (Ec) model resulting in the observed behavior. In the asymptotic regimes (high total vapor masses), the compact Cm models result in less total flux than the larger Ec models. At higher vapor masses the lines become fully thick and trace only a very thin region at the disk surface, hence the Cm model yields less flux than the Ec because of its smaller emitting size.

Table 4.3 summarizes the upper limits on the total vapor mass of o-NH₃ and p-NH₂D in HD163296 obtained by the intersection of the total line flux for our two models, as shown in Fig. 4.3, with the upper limits on the total line fluxes listed in Table 4.1. These total line flux 3σ upper limits of o-NH₃ 1_0-0_0 and p-NH₂D 1_0-0_0 correspond to total vapor masses of $0.9-1.4 \times 10^{21}$ g and $1.5-6.5 \times 10^{20}$ g, equivalent to disk-averaged abundances of $0.8-2.7 \times 10^{-11}$ and $4.0-5.0 \times 10^{-12}$, respectively. The estimates on the total vapor mass of o-NH₃ include the statistical error on the observations and the systematic errors on the total line flux, estimated to be about 20%.

4.5 Discussion

4.5.1 Total gass masses and deuteration estimates

The upper limit on the o-NH₃ total vapor mass in HD163296 is a factor of 5-10 higher than the upper limit on the p-NH₂D total vapor mass. The upper limit on the o-NH₃ total vapor mass in HD163296 of $0.9-1.4 \times 10^{21}$ g is a factor 10 lower than the o-NH₃ total vapor mass detected in TW Hya (1.1×10^{22} g) by Salinas et al. (2016) adopting their preferred Cm model. Since the adopted disk mass of HD163296 is twice that of TW Hya, this leads us to conclude that the HD163296 disk is relatively poorer in NH₃.

The dashed vertical lines in Fig. 4.3 show different estimates of the total amount of vapor mass of o-NH₃ that could be present in HD163296. The first estimate of $\sim 2.2 \times 10^{22}$ g ($E_{\text{TW Hya}}$) corresponds to twice the o-NH₃ total vapor mass (1.1×10^{22} g) detected in TW

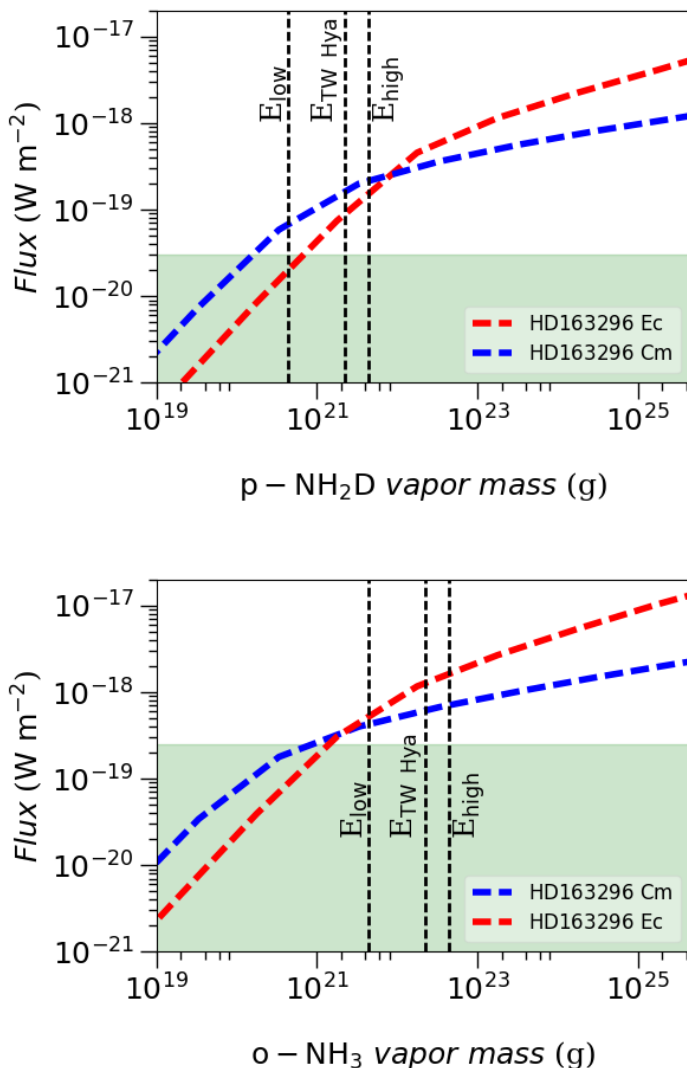


Figure 4.3: Resulting total line flux of our Cm and Ec models toward HD163296 for p-NH₂D 1_0-0_0 and o-NH₃ 1_0-0_0 as a function of total vapor mass. The green area shows the derived total line flux 3σ upper limits of $< 0.3 \times 10^{-19} \text{ Wm}^{-2}$ and $< 2.1 \times 10^{-19} \text{ Wm}^{-2}$ for the p-NH₂D 1_0-0_0 and o-NH₃ 1_0-0_0 lines, respectively. The dashed vertical lines show estimates for the vapor mass obtained by assuming that the amounts of o-NH₃ toward TW Hya and HD163296 are comparable (see Sec. 4.5.1). The estimates for p-NH₂D are scaled down versions of the o-NH₃ estimates assuming a deuterium fractionation of 10% and an OPR of ammonia of unity.

Hya since the adopted total mass of HD163296 is twice that of TW Hya. The second (E_{High}) and third (E_{Low}) estimates, of $\sim 4.4 \times 10^{22}$ g and of $\sim 4.4 \times 10^{21}$ g respectively, are calculated scaling the first $E_{\text{TW Hya}}$ estimate by factors of 2 and 0.2. These factors account for the relative amounts of other nitrogen-bearing species, namely HCN (factor of 2) and N_2H^+ (factor of 0.2), of HD163296 with respect to TW Hya. The HCN mass in TW Hya is only half that of HD163296, while the N_2H^+ in TW Hya is 5 times larger than in HD163296. The amount of HCN is calculated by scaling the H^{13}CN data of HD163296 by an adopted $^{12}\text{C}/^{13}\text{C}$ ratio of 69 (Huang et al. 2017). We therefore conclude that, for the assumed disk masses, the low o-NH_3 amount in HD163296 in comparison to that of TW Hya is due to chemical differences and not to the overall content of elemental nitrogen in these disks. If we consider desorption from ices to be the dominant mechanism to release NH_3 into the gas-phase, environmental conditions in TW Hya, such as a high X-ray radiation field or a local decrease in UV opacity, can enhance the production of gas-phase NH_3 in comparison to HD163296. In the gas-phase, formation of ammonia could also be enhanced by a higher X-ray/UV radiation field, since the chemical pathway to produce NH_3 starts by the dissociation of molecular nitrogen by either photo-processes or He^+ .

Alternatively, this difference can also be reconciled by considering a lower mass of the disk around HD163296. The work by Kama et al. (2015) suggest a lower gas-to-dust ratio for the inner disk around HD163296 as an explanation for the decreased photospheric abundance of refractory elements. They report a gas-to-dust ratio a factor of 2-4 lower than the value of our adopted model. The corrected estimates of o-NH_3 in HD163296, considering these lower gas-to-dust ratios, would be a factor of 2-4 lower than the ones presented above and consistent with our non-detections at levels similar to those of TW Hya.

The upper limit on the $\text{p-NH}_2\text{D}$ total vapor mass in HD163296 of $1.5\text{-}6.5 \times 10^{20}$ g is a factor 5-10 lower than the $\text{p-NH}_2\text{D}$ total vapor mass estimate in TW Hya of 1.1×10^{21} g. This estimate is calculated from the inferred o-NH_3 considering the Cm model of Salinas et al. (2016) and assuming a deuterium fractionation of 10%, equal to the canonical value in protostellar dense cores (Roueff et al. 2005; Busquet et al. 2010), together with an OPR of NH_2D of unity. The top panel of Figure 4.3 shows limits on the $\text{p-NH}_2\text{D}$ total vapor masses in HD163296. These are calculated by scaling down the previous estimates on the o-NH_3 total vapor masses in the same disk by a factor of 0.1 accounting for a deuterium fractionation of 10%.

The non-detection of the $\text{p-NH}_2\text{D } 1_0 - 0_0$ line at the modest integration times here presented does not add any new information on the amount of ammonia in HD163296, but is consistent with a lower amount of ammonia in this disk in comparison with TW Hya. However, other effects can be responsible for the non-detection of the $\text{p-NH}_2\text{D } 1_0 - 0_0$ line toward HD163296 such as a much lower deuterium fractionation or a lower OPR of ammonia. The expected OPR of ammonia at low spin temperatures is ~ 3 (Daniel et al. 2016) in contrast to the high temperature limit of unity at $T_{\text{spin}} > 30$ K. If $\text{p-NH}_2\text{D}$ is being released near the midplane into the gas-phase from the grains together with o-NH_3 this low value of the upper limit could reflect its formation pathway.

4.5.2 ALMA predictions

Both our compact and extended radial distributions are consistent, at low vapor masses, with the obtained o-NH_3 and $\text{p-NH}_2\text{D}$ total line flux upper limits. Nevertheless, our models predict the same total line flux for different total vapor masses depending on their radial distribution. ALMA can provide the spatial resolution needed to distinguish the radial location of NH_2D and, indirectly, of NH_3 . In addition, ALMA is also more sensitive than

Herschel (Fig. 4.1). From Fig. 4.3 our Ec model of p-NH₂D 1₀ – 0₀ line in HD163296 results in 1.9×10^{-20} W m⁻² for a deuteration fractionation of 0.1 and the lowest o-NH₃ total vapor mass estimate of 4.4×10^{20} gr. We can detect a 5 σ signal of the total integrated flux with ALMA³ of our Ec model in ~ 20 min. This calculation was made using 43 antennas and a water vapor column density of 0.66 mm corresponding to a T_{sys} of 615 K. We also assume a bandwidth equivalent to the adopted FWHM (see Table 4.1) of the line of 9 km s⁻¹. A total integrated flux detection would constrain the total amount of p-NH₂D but a spatially resolved detection in individual channels is needed to constrain the radial and vertical distribution of p-NH₂D.

Although we did not observe TW Hya, it is two times closer than HD163296 and, as stated above, has at least 5 times more o-NH₃. The expected total flux of this line is shown in Fig. 4.4 as a function of total vapor mass. We have an accepted ALMA Cycle 4 proposal that has received rank A to observe the o-NH₂D 1₀–0₀. We target this line, instead of the p-NH₂D 1₀–0₀ line, advocating for the expected higher OPR ratio of 3 for ammonia and deuterated ammonia at low temperatures (Sipilä et al. 2015) as argued above. Figure 4.5 shows simulated ALMA observations of the two radially compact models, Cm and Cp, described in Salinas et al. (2016, see Chapter 3) with 2.5 h of integration time using a deuterium fractionation of 5%. The Cm model places gas-phase ammonia in the midplane, the same way as presented in this work, while the Cp model places gas-phase ammonia in the upper photodominated layers of the disk. These radially compact models are brighter than the radially extended ones for their best-fit vapor masses. At this resolution (42 au at the source distance of 56 pc) and the proposed sensitivity, we expect to detect line emission for all four radial and vertical distributions considered by Salinas et al. (2016) if the deuteration ratio NH₂D/NH₃ is high (0.5), and to detect only the two radially compact models (<60 AU) down to a deuterium fractionation for ammonia as low as 5%. Thus, our proposed observations allow us to directly test our hypothesis that NH₂D, and by inference NH₃, is co-located with the millimeter-sized grains at radii <60 AU, for deuteration values comparable to prestellar cores.

4.6 Summary & Conclusions

We have modeled the o-NH₃ 1₀–0₀ and p-NH₂D 1₀–0₀ lines toward HD163296 considering two different models: a compact and settled configuration following the mm-size grains and an extended configuration following the full extent of the gas. We have derived upper limits on the total amount of o-NH₃ and p-NH₂D vapor mass (and disk-averaged abundances) from these models of $0.8\text{-}1.4 \times 10^{21}$ g ($0.8\text{-}2.7 \times 10^{-11}$) and $1.5\text{-}6.5 \times 10^{20}$ g ($4.0\text{-}5.0 \times 10^{-12}$) respectively, and contrasted them with the amount of nitrogen-bearing species detected in TW Hya.

We conclude that the non-detections of the o-NH₃ 1₀–0₀ and p-NH₂D 1₀–0₀ lines toward HD163296 suggest that this disk is NH₃ poor compared to the similar-mass disk of TW Hya for the adopted models. We argue that this difference is due to its chemical origin by also comparing with other nitrogen-bearing species reported in the literature toward these two sources. Full chemical modeling of these species and spatially resolved observations of these disks are needed to disentangle the different distributions and formation pathways of NH₃ and NH₂D.

³Calculations performed with the ALMA sensitivity calculator <https://almascience.eso.org/proposing/sensitivity-calculator>

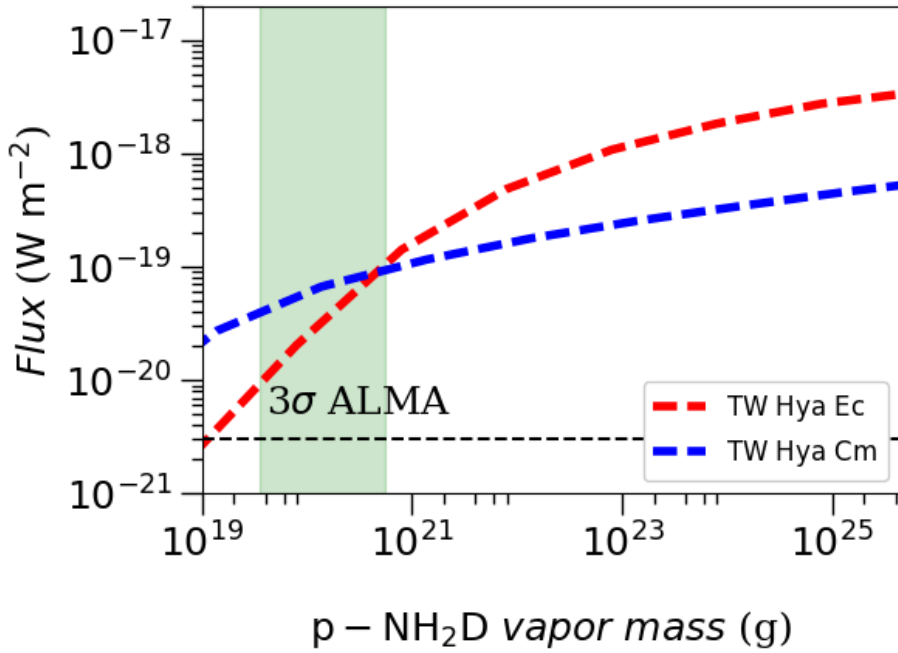


Figure 4.4: Resulting total line flux of our Cm and Ec models toward TW Hya for $p\text{-NH}_2\text{D } 1_0 - 0_0$ as a function of total vapor mass. The colored region show the expected range of vapor masses taken from the different models of Salinas et al. (2016) assuming a 5% deuterium fractionation and an OPR of unity. The dashed line shows the 3σ ALMA detection limit for an integrated line flux over a bandwidth of 1 km s^{-1} in 2.5 h.

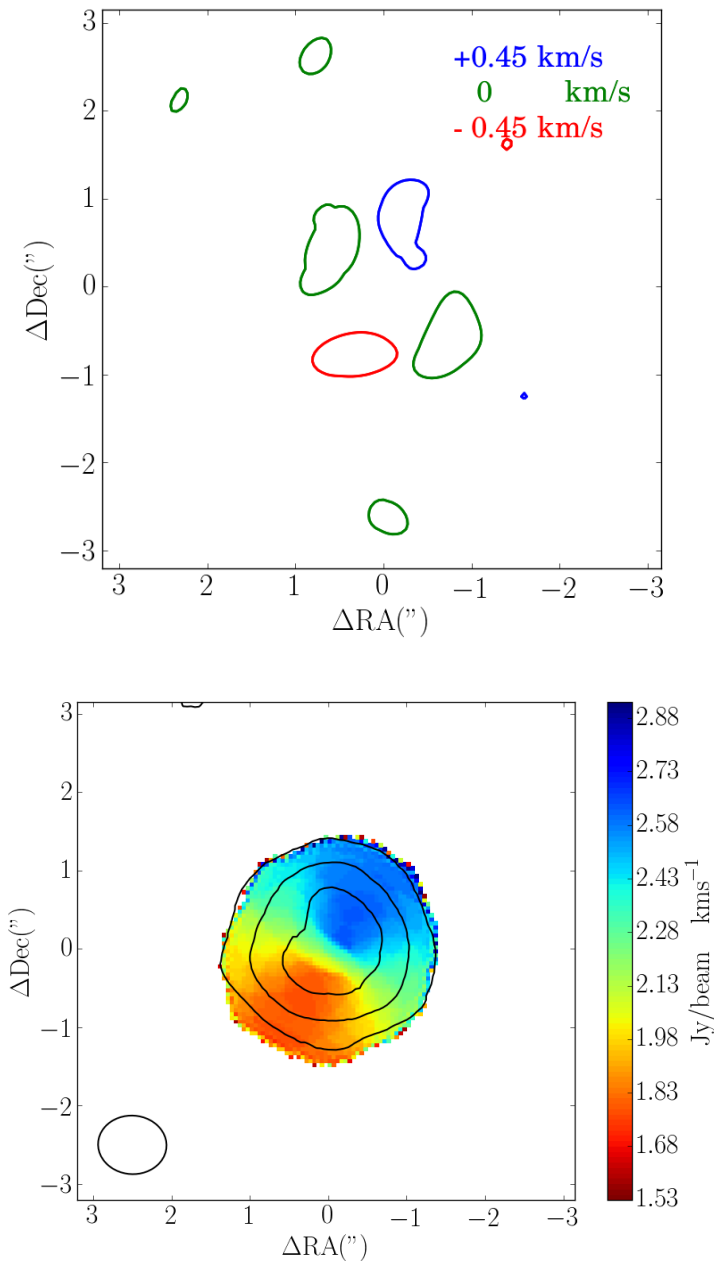


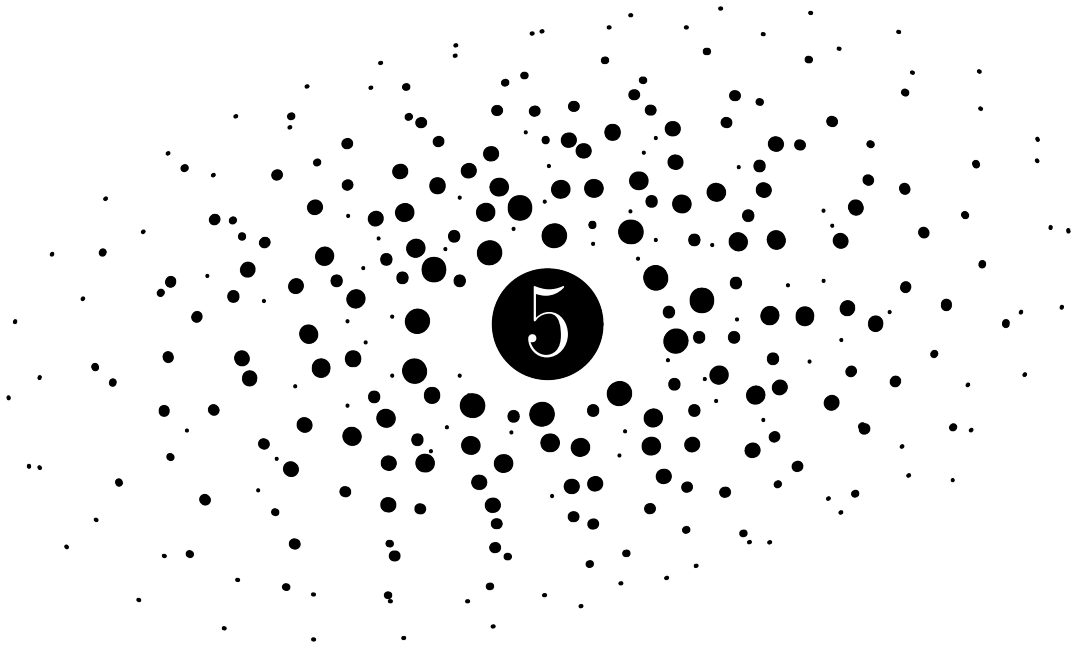
Figure 4.5: Simulated ALMA images of the expected $\text{o-NH}_2\text{D } 1_0 - -0_0$ emission for a low $\text{NH}_2\text{D}/\text{NH}_3$ ratio of 0.05 and an assumed radial distribution for ammonia <60 AU. The right panel shows the velocity-centroid (color) and integrated intensity (contours of 5, 10 and 15 σ -levels) of a model with all ammonia residing near the disk midplane; the left panel shows the detection limit of our proposed observations, corresponding to a model with all ammonia residing at radii <60 AU but at large heights in the disk ($3\text{-}\sigma$ contours at 3 different velocities).

Acknowledgements. This work was partially supported by grants from the Netherlands Organization for Scientific Research (NWO) and the Netherlands Research School for Astronomy (NOVA). This paper makes use of the following ALMA data: ADS/JAO.ALMA# 2013.1.01268.S. ALMA is a partnership of ESO (representing its member states), NSF (USA), and NINS (Japan), together with NRC (Canada), NSC and ASIAA (Taiwan), and KASI (Republic of Korea), in cooperation with the Republic of Chile. The Joint ALMA Observatory is operated by ESO, AUI/NRAO, and NAOJ. *Herschel* is a European Space Agency space observatory with science instruments provided by European-led principal investigator consortia and with important participation from NASA. HIPI has been designed and built by a consortium of institutes and university departments from across Europe, Canada, and the United States under the leadership of SRON Netherlands Institute for Space Research, Groningen, The Netherlands, and with major contributions from Germany, France, and the US. Consortium members are: Canada: CSA, U. Waterloo; France: IRAP (formerly CESR), LAB, LERMA, IRAM; Germany: KOSMA, MPIfR, MPS; Ireland, NUI Maynooth; Italy: ASI, IFSI-INAF, Osservatorio Astrofisico di Arcetri-INAF; Netherlands: SRON, TUD; Poland: CAMK, CBK; Spain: Observatorio Astronómico Nacional (IGN), Centro de Astrobiología (CSIC-INTA). Sweden: Chalmers University of Technology – MC2, RSS & GARD; Onsala Space Observatory; Swedish National Space Board, Stockholm University – Stockholm Observatory; Switzerland: ETH Zurich, PHNWX; USA: Caltech, JPL, NNS. Support for this work was provided by NASA (*Herschel* OT funding) through an award issued by JPL/Caltech. The data presented here are archived at the *Herschel* Science Archive, <http://archives.esac.esa.int/hda/ui>, under OBSID 1342198337 and 1342201585.

Bibliography

- Andrews, S. M., Wilner, D. J., Hughes, A. M., et al. 2012, *ApJ*, 744, 162
 Andrews, S. M., Wilner, D. J., Zhu, Z., et al. 2016, *ApJ*, 820, L40
 Bergin, E. A., Cleeves, L. I., Gorti, U., et al. 2013, *Nature*, 493, 644
 Boogert, A. C. A., Gerakines, P. A., & Whittet, D. C. B. 2015, *ARA&A*, 53, 541
 Bottinelli, S., Boogert, A. C. A., Bouwman, J., et al. 2010, *ApJ*, 718, 1100
 Brinch, C., & Hogerheijde, M. R. 2010, *A&A*, 523, A25
 Brown, P. D., & Millar, T. J. 1989, *MNRAS*, 240, 25P
 Busquet, G., Palau, A., Estalella, R., et al. 2010, *A&A*, 517, L6
 Cleeves, L. I., Bergin, E. A., Qi, C., Adams, F. C., & Öberg, K. I. 2015, *ApJ*, 799, 204
 Crapsi, A., Caselli, P., Walmsley, M. C., & Tafalla, M. 2007, *A&A*, 470, 221
 Crovisier, J., Bockelée-Morvan, D., Colom, P., et al. 2004, *A&A*, 418, 1141
 Danby, G., Flower, D. R., Valiron, P., Schilke, P., & Walmsley, C. M. 1988, *MNRAS*, 235, 229
 Daniel, F., Faure, A., Wiesenfeld, L., et al. 2014, *MNRAS*, 444, 2544
 Daniel, F., Coudert, L. H., Punanova, A., et al. 2016, *A&A*, 586, L4
 Daranlot, J., Hincelin, U., Bergeat, A., et al. 2012, *Proceedings of the National Academy of Science*, 109, 10233
 Draine, B. T., & Lee, H. M. 1984, *ApJ*, 285, 89
 Du, F., Bergin, E. A., Hogerheijde, M., et al. 2017, *ApJ*, 842, 98
 Dullemond, C. P., & Dominik, C. 2004, *A&A*, 417, 159
 Fedoseev, G., Ioppolo, S., & Linnartz, H. 2015, *MNRAS*, 446, 449
 Garrod, R. T., Wakelam, V., & Herbst, E. 2007, *A&A*, 467, 1103
 Harju, J., Daniel, F., Sipilä, O., et al. 2017, *A&A*, 600, A61
 Hartquist, T. W., & Williams, D. A. 1990, *MNRAS*, 247, 343
 Hasegawa, T. I., & Herbst, E. 1993, *MNRAS*, 261, 83
 Hidaka, H., Watanabe, M., Kouchi, A., & Watanabe, N. 2011, *Physical Chemistry Chemical Physics (Incorporating Faraday Transactions)*, 13, 15798
 Hiraoka, K., Yamashita, A., Yachi, Y., et al. 1995, *ApJ*, 443, 363
 Huang, J., Öberg, K. I., Qi, C., et al. 2017, *ApJ*, 835, 231
 Kama, M., Folsom, C. P., & Pinilla, P. 2015, *A&A*, 582, L10
 Le Gal, R., Hily-Blant, P., Faure, A., et al. 2014, *A&A*, 562, A83
 Mathews, G. S., Klaassen, P. D., Juhász, A., et al. 2013, *A&A*, 557, A132
 Mumma, M. J., & Charnley, S. B. 2011, *ARA&A*, 49, 471
 Öberg, K. I., Boogert, A. C. A., Pontoppidan, K. M., et al. 2011, *ApJ*, 740, 109
 Öberg, K. I., Qi, C., Wilner, D. J., & Hogerheijde, M. R. 2012, *ApJ*, 749, 162
 Pillai, T., Kauffmann, J., Wyrowski, F., et al. 2011, *A&A*, 530, A118
 Pontoppidan, K. M., Salyk, C., Bergin, E. A., et al. 2014, *Protostars and Planets VI*, 363
 Prasad, S. S., & Tarafdar, S. P. 1983, *ApJ*, 267, 603
 Roueff, E., Lis, D. C., van der Tak, F. F. S., Gerin, M., & Goldsmith, P. F. 2005, *A&A*, 438, 585
 Roueff, E., Loison, J. C., & Hickson, K. M. 2015, *A&A*, 576, A99

- Salinas, V. N., Hogerheijde, M. R., Mathews, G. S., et al. 2017, ArXiv e-prints, arXiv:1707.06475
- Salinas, V. N., Hogerheijde, M. R., Bergin, E. A., et al. 2016, *A&A*, 591, A122
- Schöier, F. L., van der Tak, F. F. S., van Dishoeck, E. F., & Black, J. H. 2005, *A&A*, 432, 369
- Schwarz, K. R., & Bergin, E. A. 2014, *ApJ*, 797, 113
- Sipilä, O., Harju, J., Caselli, P., & Schlemmer, S. 2015, *A&A*, 581, A122
- Treviño-Morales, S. P., Pilleri, P., Fuente, A., et al. 2014, *A&A*, 569, A19
- van Dishoeck, E. F., Thi, W.-F., & van Zadelhoff, G.-J. 2003, *A&A*, 400, L1
- van Dishoeck, E. F., Kristensen, L. E., Benz, A. O., et al. 2011, *PASP*, 123, 138
- Walsh, C., Nomura, H., & van Dishoeck, E. 2015, *A&A*, 582, A88
- Zhang, K., Bergin, E. A., Blake, G. A., et al. 2016, *ApJ*, 818, L16



DCO⁺, DCN, and N₂D⁺
reveal three different
deuteration regimes in the
disk around the Herbig Ae
star HD163296

Salinas, V. N., Hogerheijde, M. R., Mathews, G. S., Öberg, K. I., Qi, C., Williams, J. P., Wilner, D. J.
2017, A&A, 606, A125S.

5.1 Introduction

So far, more than 30 deuterated species have been detected toward prestellar cores and solar system bodies (Ceccarelli et al. 2007; Mumma & Charnley 2011). Their deuterium fractionation (D_f), usually higher than the D/H cosmic ratio of $\sim 10^{-5}$ (Vidal-Madjar 1991), is used to infer their thermal history, and in the case of solar system bodies, their location within the solar nebula at the time of formation. The amount of detections of deuterated species toward protoplanetary disks is not as high as in protostellar environments. DCO^+ has been detected in both T Tauri disks (Guilloteau et al. 2006; Öberg et al. 2010, 2011, 2015; van Dishoeck et al. 2003; Huang et al. 2017) and in the Herbig Ae disks HD163296 and MWC 480 (Qi et al. 2015; Mathews et al. 2013; Huang et al. 2017). DCN has been observed toward six different disks by Huang et al. (2017) and in addition DCN was previously observed toward TW Hya (Qi et al. 2008) and LkCa15 (Öberg et al. 2010). N_2D^+ has only been recently observed in the disk around the T Tauri star AS 209 (Huang & Öberg 2015).

The massive ($0.089 M_\odot$) and extended gas-rich disk around HD163296 is inclined at 44° . Its proximity (122 pc) makes it an excellent laboratory to study the spatial location of the different deuteration regimes in protoplanetary disks (Qi et al. 2011; Mathews et al. 2013; Perryman et al. 1997). DCO^+ emission was first seen in a ring toward the disk around HD163296 and suggested as a tracer of the CO snowline by Mathews et al. (2013). It was later observed that the emission extended further inward past the CO snowline at 90 AU traced by N_2H^+ (Qi et al. 2015). Atacama Large Millimeter/submillimeter Array (ALMA) cycle 2 observations toward HD163296 of DCO^+ , DCN, and N_2D^+ were presented by Yen et al. (2016) using a new stacking technique to enhance the signal to noise (S/N) of the radial profile confirming the extent of DCO^+ . The observational study of Huang et al. (2017) found that both DCO^+ and H^{13}CO^+ show an emission break around 200 AU.

The ALMA continuum emission in Band 6 of HD163296 shows a rich structure of rings and depressions extending up to 230 AU (Isella et al. 2016; Zhang et al. 2016). This substructure could have an impact on the distribution and chemistry of certain species (See Sec. 5.5). The gas, traced by C^{18}O , extends out to 360 AU, well beyond the extent of the millimeter continuum emission, and scattered light has been detected up to ~ 500 AU (Garufi et al. 2014; Wisniewski et al. 2008). By contrasting the observations of key deuterated species to a physical model of HD163296, we hope to determine the origin of their formation and their relation to the location of the CO snowline. We carried out observations toward this disk using ALMA Band 6 and obtained spectral cubes of N_2D^+ ($J=3-2$), DCO^+ ($J=3-2$) and DCN ($J=3-2$).

The goal of this study is to constrain the radial location of these deuterated species in the disk surrounding the Herbig Ae star HD 163296 that trace different deuteration pathways. In Section 5.2 we present our data and their reduction. Section 5.3 shows the spatial characterization of the line emission. Section 5.4 contains our modeling approach and the derived parameters. Section 5.5 discusses the validity of our models and an interpretation of our observed molecules as a tracer for different deuteration pathways and their relation to the CO snowline. Finally, in Section 5.6 we give our conclusions.

5.2 Observations

We carried out observations of the disk surrounding the Herbig Ae star HD163296 ($\alpha_{2000} = 17^{\text{h}}56^{\text{m}}51^{\text{s}}.21$, $\delta_{2000} = -21^\circ 57' 22''$) using ALMA in Band 6 as a part of Cycle 2 on the 27, 28, and 29 July 2014 (project 2013.1.01268.S). The total integration time on source was 4 hours and 43 min with thirty-three 12 m antennas. The correlator set up had seven

Table 5.1: Summary of our line observations.

Line transition	Frequency (GHz)	Integrated Intensity (mJy km s ⁻¹)	Beam	Channel rms (mJy/beam)
DCO ⁺ J=3–2	216.112	1270.45± 5.8	0′.53× 0′.42	3.25
DCN J=3–2	217.238	104.4± 5.6	0′.53× 0′.42	3.11
N ₂ D ⁺ J= 3–2	231.321	61.6± 7.5	0′.50× 0′.39	3.37

Notes. Line parameters of CLEAN images using natural weighting. The velocity integrated fluxes and their respective errors are calculated with a Keplerian mask as explained in Appendix 5.A.

different spectral windows (SPW); three of these contain H₂CO lines (Carney et al. 2017) while 3 others are centered on the rest frequencies of DCO⁺ ($J=3-2$), N₂D⁺ ($J=3-2$) and DCN ($J=3-2$), all of which have a resolution of 61 kHz. A final SPW contains wideband (2 GHz) continuum centered at 232.989 GHz. The quasar J1733-1304 was used as gain, bandpass, and total flux calibrator with 1.329 Jy on the lower sideband and 1.255 Jy in the upper sideband.

The data were calibrated following the standard CASA reduction as provided in the calibration scripts by ALMA. Baselines in the antenna array configuration correspond to a range in uv -distance of 20–630 $k\lambda$, which translates into a beam of $\sim 0′.33$. Self-calibration was applied to the data as implemented by Carney et al. (2017). The DCO⁺ ($J=3-2$), N₂D⁺ ($J=3-2$) and DCN ($J=3-2$) lines were continuum subtracted in the visibility plane using a linear fit to the line-free channels and imaged by the CLEAN task in CASA. Figure 5.1 shows the integrated intensity maps of each line with and without a Keplerian mask. This mask is constructed by calculating the projected Keplerian velocities of the disk and matching them with the expected Doppler shifted emission in the spectral cube of the data (see Appendix 5.A). The N₂D⁺ ($J=3-2$) emission is sitting on the edge of a strong atmospheric feature at high T_{sys} . We fit the continuum only using the least noisy line-free channels from one side of the spectra (channels 350–750) but continuum subtraction is less accurate here.

5.3 Results

5.3.1 Detections

We successfully detected all of our target emission lines. Table 5.1 shows a summary of the line emission based on integrated intensity maps with Keplerian masking (lower panels of Fig.5.1).

Figure 5.2 shows the double -peaked spectra of DCO⁺ ($J=3-2$), DCN ($J=3-2$) and N₂D⁺ ($J=3-2$) at peak fluxes of 294 mJy, 48 mJy, and 54 mJy (without binning) corresponding to detections of 11σ , 5σ , and 4σ respectively. These spectra correspond to an aperture in the sky equal to the 1σ contour of DCO⁺ in Fig. 5.1 for all lines. A simple Gaussian fit of the DCO⁺ line profile gives a full width at half maximum (FWHM) of ~ 6.0 km s⁻¹ and $+5.8$ km s⁻¹ offset or systemic velocity consistent with values in the literature.

From the integrated intensity maps, shown in Fig. 5.1, N₂D⁺ seems to be emitting from a broad ring with its peak flux at 9.3 mJy beam⁻¹ km s⁻¹ and a velocity integrated line intensity of 61.6 ± 7.5 mJy km s⁻¹. On the other hand, DCN emission is more compact, arising from within the N₂D⁺ ring. As already noted by Huang et al. (2017) in their observations, we do not see clear evidence for an offset from the center as reported by Yen et al.

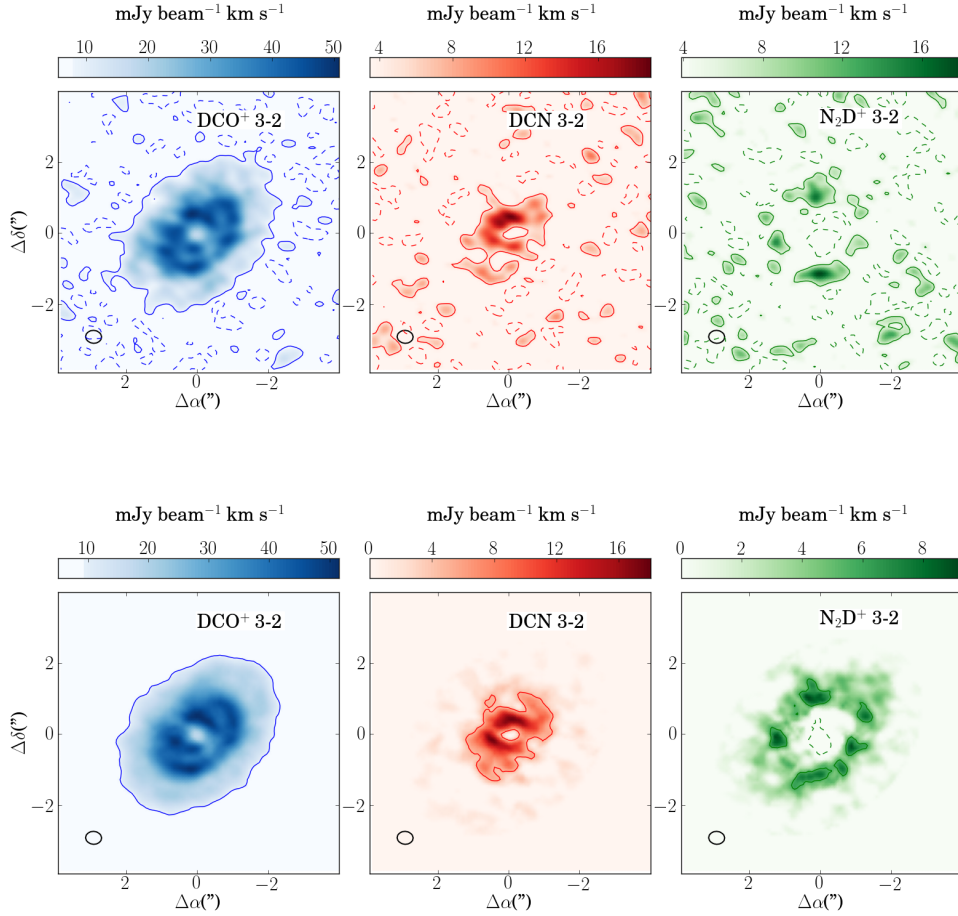


Figure 5.1: Integrated intensity maps of DCO^+ , N_2D^+ , and DCN with (lower panels) and without (upper panels) a Keplerian mask as explained in Appendix 5.A. The resulting synthesized beams of $0''.53 \times 0''.42$ for DCO^+ and DCN , and $0''.50 \times 0''.39$ for N_2D^+ , with a beam position angle of 90° , using natural weighting are shown at the lower left of each map. Contours are 1σ levels, where σ is estimated as the rms of an emission free region in the sky.

(2016). The emission peak is somewhat shifted northeast from what is observed by Huang et al. (2017). The total DCN velocity integrated line intensity is $104.4 \pm 5.6 \text{ mJy km s}^{-1}$ and the peak flux of its integrated intensity map is at $17.3 \text{ mJy beam}^{-1} \text{ km s}^{-1}$. DCO^+ extends radially further inward than what was observed by Mathews et al. (2013) as confirmed by Qi et al. (2015) and Huang et al. (2017) within both of the N_2D^+ and N_2H^+ emission rings. The DCO^+ emission peaks at $51.5 \text{ mJy beam}^{-1} \text{ km s}^{-1}$ northwest, as noted by both Yen et al. (2016) and Huang et al. (2017), and has a velocity integrated line intensity of $1270.5 \pm 5.8 \text{ mJy km s}^{-1}$.

Figure 5.3 shows the average radial profile of the integrated intensity maps of Fig. 5.1. This profile is constructed taking the average value of concentric ellipsoid annuli and their error is taken from the standard deviation. The projected linear resolution is lower along

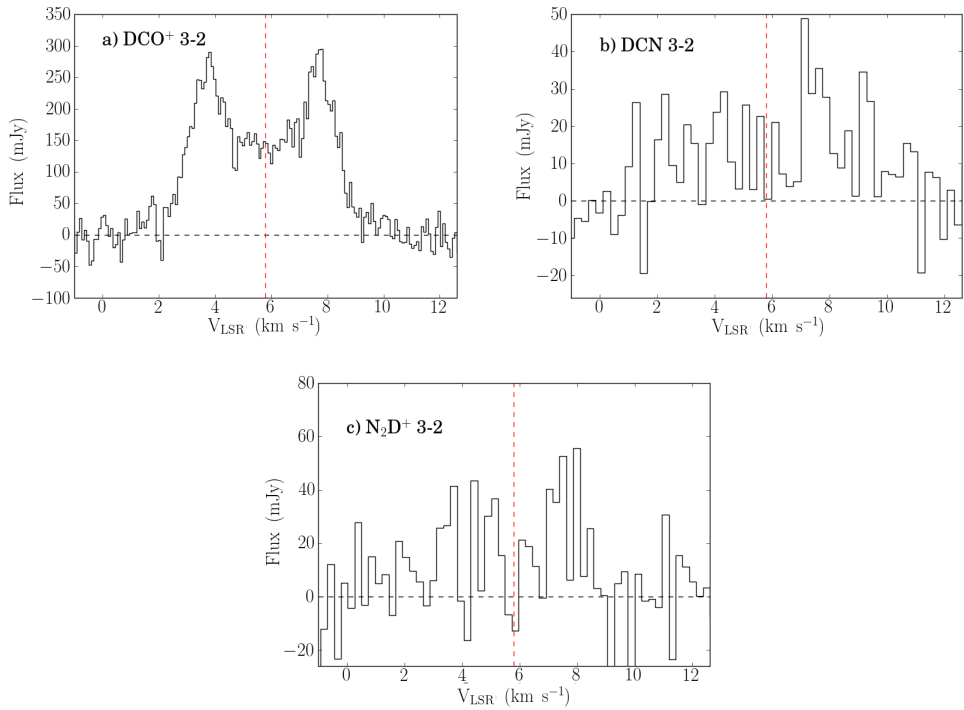


Figure 5.2: Spectra of a) DCO⁺ J=3–2, b) DCN J=3–2, and c) N₂D⁺ J= 3–2 of the disk integrated values using a Keplerian mask as shown in Fig. 5.1. The DCN and N₂D⁺ spectra have been binned to 3 times their resolution, 0.255 km/s and 0.238 km/s, respectively, to enhance their S/N ratio.

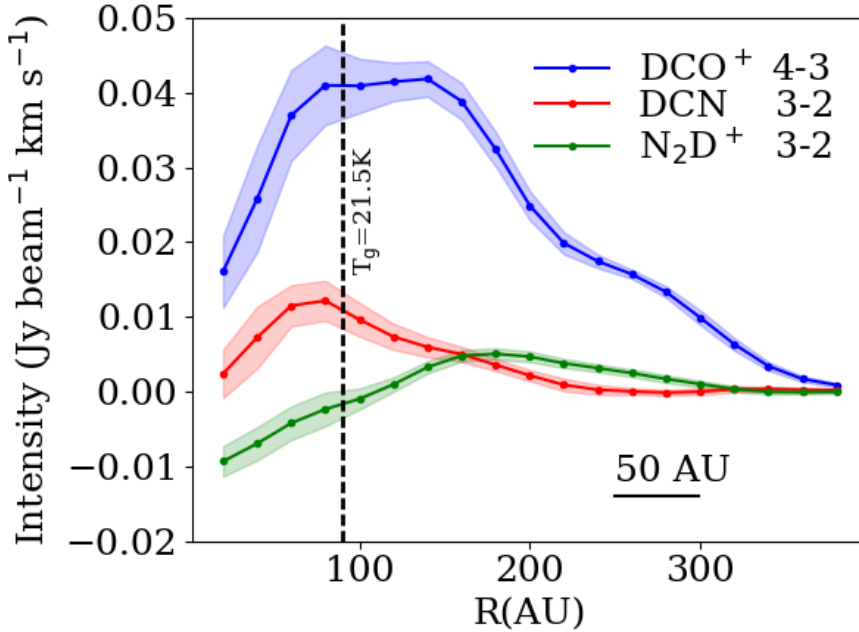


Figure 5.3: Radial profiles of the integrated intensity maps shown in Fig. 5.1. The shadowed color area represents the 3σ errors, where σ is the standard deviation in one elliptical annulus. The black dashed line corresponds to the location of the CO snowline (90 AU; Qi et al. 2015).

the semiminor axis than along the semimajor axis and therefore the resulting spatial resolution of the radial profiles is poorer than the synthesized beam. The N₂D⁺ and DCN emission peak at ~160 AU and ~60 AU, respectively. The DCO⁺ emission shows three peaks at 60 AU, 130 AU, and 250 AU, and extends up to 330 AU. Both the DCN and the DCO⁺ radial profiles show a depression toward the center of the disk that is discussed in Sec. 5.5.

5.3.2 Column densities and deuterium fractionation

We can get an estimate of the disk-averaged column densities of the observed species if we consider the analytical formula from Remijan et al. (2003) for optically thin emission,

$$N = \frac{2.04 \int \Delta I dv}{\theta_a \theta_b} \frac{Q_{rot} \exp(-\frac{E_u}{T_{ex}})}{v^3 \langle S_{ij} \mu^2 \rangle} \times 10^{20} \text{ cm}^{-2}, \quad (5.1)$$

where θ_a and θ_b (arcsec) corresponds to the semimajor and semiminor axes of the synthesized beam, $\int \Delta I dv$ is the total line flux (Jy beam⁻¹ km s⁻¹), and T_{ex} (K) is the excitation temperature. The partition function (Q_{rot}), upper energy level (E_u K), line strength (S_{ij}), and dipole moment (μ Debye) were taken from the CDMS database.

We adopt two different disk-averaged excitation temperatures for each of the molecules: 10 and 25 K for N₂D⁺ and 25 and 80 K for DCN and DCO⁺. N₂D⁺ should be abundant at temperatures $\lesssim 25$ K where CO is frozen out (Qi et al. 2015) and at temperatures $\gtrsim 10$ K where the low deuteration channel starts to be active. On the other hand, DCN and DCO⁺

Table 5.2: Column density estimates for different excitation temperatures.

T_{ex}	N_{DCO^+} (cm^{-2})	N_{DCN} (cm^{-2})	$N_{\text{N}_2\text{D}^+}$ (cm^{-2})
10 K	-	-	$2.5 \pm 0.3 \times 10^{11}$
25 K	$1.68 \pm 0.01 \times 10^{12}$	$2.9 \pm 0.2 \times 10^{11}$	$1.6 \pm 0.2 \times 10^{11}$
80 K	$2.56 \pm 0.01 \times 10^{12}$	$5.2 \pm 0.3 \times 10^{11}$	-

Table 5.3: Deuterium fractionation estimates for different excitation temperatures.

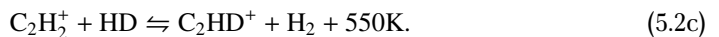
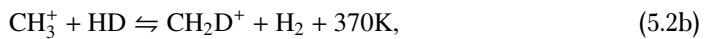
T_{ex}	$\text{DCO}^+/\text{HCO}^+$	DCN/HCN	$\text{N}_2\text{D}^+/\text{N}_2\text{H}^+$
10 K	-	-	0.34 ± 0.15
25 K	0.05 ± 0.01	0.02 ± 0.01	0.45 ± 0.21
80 K	0.06 ± 0.01	0.02 ± 0.01	-

start to be abundant at higher temperatures where the high temperature pathway starts to be active (80K; see below Sec. 5.4.1). Table 5.2 summarizes our column density estimates for the three deuterated species using the values of the velocity integrated line intensities from Table 5.1. In general, our estimates do not differ by more than a factor of 2 within the excitation temperature ranges. Table 5.3 shows estimated disk-averaged D_f values for each of our species using the disk-averaged column densities from Table 5.2. We take the velocity integrated flux values of past line detections of H^{13}CO^+ $J=3-2$ ($620 \text{ mJy beam}^{-1} \text{ km s}^{-1}$), H^{13}CN $J=3-2$ ($170 \text{ mJy beam}^{-1} \text{ km s}^{-1}$) (Huang et al. 2017), N_2H^+ $J=3-2$ ($520 \text{ mJy beam}^{-1} \text{ km s}^{-1}$) (Qi et al. 2015), and Eq. 5.1 to derive disk-average column densities assuming a $^{12}\text{C}/^{13}\text{C}$ ratio of 69 (Wilson 1999). The $^{12}\text{C}/^{13}\text{C}$ ratio can vary in disks between different C-bearing species (Woods & Willacy 2009). Higher or lower $^{12}\text{C}/^{13}\text{C}$ ratios for these species change D_f linearly. These D_f values are only lower limits as the species might not be spatially colocated.

5.4 Parametric modeling

5.4.1 Deuterium chemistry

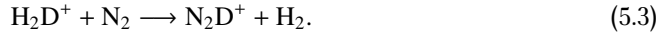
The D/H ratio is specially useful to constrain the physical conditions of protoplanetary disks since an enhancement in this ratio is a direct consequence of the energy barrier of the reactions that deuterate simple molecules. We can distinguish the following three different key reactions that introduce deuterium into the most abundant species in protoplanetary disks (Gerner et al. 2015; Turner 2001):



The right-to-left reaction of Equation 5.2a is endothermic and strongly enhances the D/H ratio of H_2D^+ , and species that derive from it, in temperatures ranging from 10-30

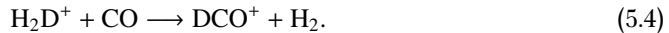
K (Millar et al. 1989; Albertsson et al. 2013). This regime corresponds to the so-called low temperature deuteration channel. In contrast, the right-to-left reactions of Eq. 5.2b and 5.2c, involving light hydrocarbons, effectively enhance the deuterium fractionation in warmer temperatures ranging from 10-80 K. This regime corresponds to the high temperature deuteration channel.

N_2D^+ forms mainly through the low temperature deuteration channel via ion-molecule reaction (Dalgarno & Lepp 1984),



Hence the formation of N_2D^+ is expected to be enhanced at the same temperature range as H_2D^+ .

DCN is formed out of two main reactions involving the low and high temperature channels with the latter being dominant (66%) (Turner 2001; Albertsson et al. 2013). Early works identify the low temperature channel as the key gas-phase formation of DCO^+ (Watson 1976; Wootten 1987). This pathway starts from Eq. 5.2a followed by the reaction



However, recently modeling efforts by Favre et al. (2015) show that the high temperature channel may be an active formation pathway. If we consider Eq. 5.2b, DCO^+ can be formed via



5.4.2 Motivation

Past observations of DCN in protoplanetary disks show centrally peaked distributions (Qi et al. 2008; Huang et al. 2017). This supports the idea that DCN is mainly formed through the high temperature deuteration pathway. If N_2D^+ and DCN are tracing the low and high temperature deuteration pathways, respectively, we can think of the DCO^+ emission as a linear combination of DCN and N_2D^+ . Figure 5.4 shows, as an illustration, the DCO^+ radial profile subtracted first by the DCN emission scaled by a factor of 3.7 and then by the N_2D^+ emission scaled by a factor of 4.9. These factors can be interpreted as the ratio of their abundances. The first ring at 115 AU in the residuals, after subtracting both the DCN and N_2D^+ radial profile, can be interpreted as DCO^+ that is formed inside the CO snowline. If N_2D^+ is formed exclusively outside the snowline, its emission peak is shifted slightly outward (van't Hoff et al. 2017; Zhang et al. 2017) and its subtraction reveals DCO^+ formed by the low temperature channel in the regions in which CO is still present in the gas phase. The second residual ring at 280 AU indicates a third regime in which DCO^+ is present in the gas phase that does not correlate with the deuteration pathways regimes probed by DCN and N_2D^+ . This analysis assumes that the line emission is optically thin and that it arises from the same disk region for the warm and cold channels.

We intend to characterize the three different regimes described above via a reasonable physical model for the disk and simple models for the column density of our species. In the following section we describe the adopted physical model and parametric abundances for N_2D^+ , DCN, and DCO^+ that are used to fit the data.

5.4.3 Physical model

We adopted the physical model used by Mathews et al. (2013). This model was constructed by approximating the semi-parametric modeling of Qi et al. (2011) fitting the SED and the extent of their mm observations. The density structure is defined by

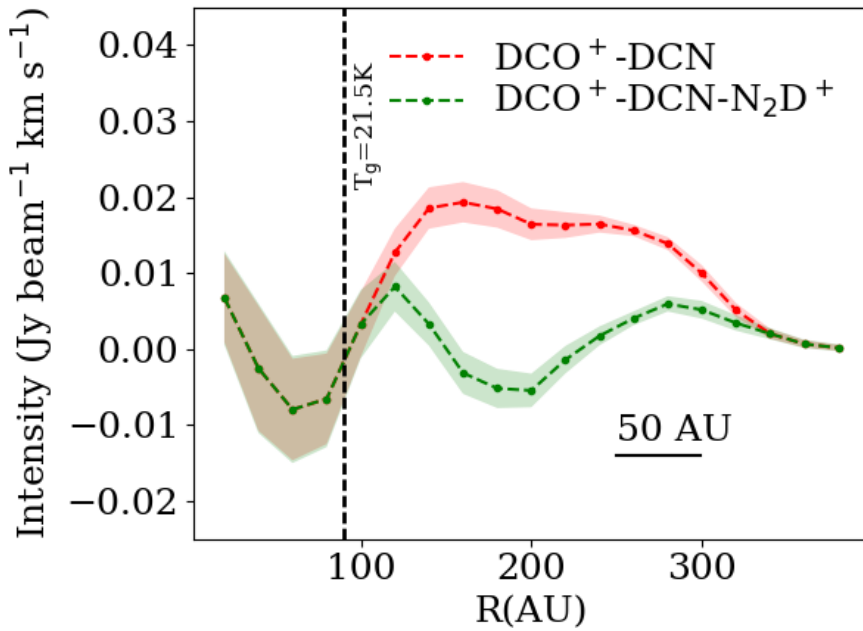


Figure 5.4: Residuals of the DCO^+ radial profile (as shown in Fig. 5.3) by subtracting first the DCN radial profile and then the N_2D^+ radial profile. The shadowed color area represents 1σ errors, where σ is the standard deviation in one elliptical annulus. The black dashed line corresponds to the location of the CO snowline (90 AU).

$$\Sigma_d(R) = \begin{cases} \Sigma_C \left(\frac{R}{R_C}\right)^{-1} \exp\left[-\left(\frac{R}{R_C}\right)\right] & \text{if } R \geq R_{\text{rim}} \\ 0 & \text{if } R < R_{\text{rim}}, \end{cases}$$

where Σ_C is determined by the total disk mass M_{disk} ($0.089 M_{\odot}$ using a gas-to-dust ratio of 0.0065), R_C (150 AU) is the characteristic radius, and R_{rim} (0.6 AU) is the inner rim of the disk. The vertical structure is treated as a Gaussian distribution with an angular scale height defined by

$$h(R) = h_C \left(\frac{R}{R_C}\right)^{\psi},$$

where ψ (0.066) is the flaring power of the disk and h_C is the angular scale height at the characteristic radius R_C . The parameter h_C takes different two values for the dust vertical distribution and two more for the gas vertical distribution. The parameters h_{small} (0.08) and h_{large} (0.06) describe the distribution of small and large dust grains, respectively, while h_{main} (0.1) and h_{tail} (0.2) describe the main bulk distribution of gas in the mid-plane of the disk and the tail of gas that continues the upper regions of the disk surface (See appendix A of Mathews et al. 2013). The gas temperature profile was computed by the 2D radiative transfer code RADMC (Dullemond & Dominik 2004) assuming $T_{\text{gas}} = T_{\text{dust}}$. This code receives the stellar parameters as listed in Mathews et al. (2013) and the dust density distribution as inputs.

5.4.4 N_2D^+ , DCN, and DCO⁺ abundance models

DCN is formed mainly (66%) through deuterated light hydrocarbons such as CH_2D (see Fig. 5c of Turner 2001). This reaction starts with the deuteration of CH_3^+ , the so-called high temperature deuteration pathway. For an enhancement of CH_2D^+ over CH_3^+ temperatures should not exceed $\sim 10\text{--}80$ K. We use a simple toy model for DCN taking the same approach as for the N_2D^+ model with three free parameters: an inner radius R_{in} beyond which it is sufficiently cold for an enhancement of the $\text{CH}_2\text{D}/\text{CH}_3^+$ ratio, an outer radius R_{out} , and a constant abundance X_{high} .

N_2D^+ is formed by the reaction of N_2 with H_2D^+ . We expected considerable abundances of N_2D^+ only outside the CO snowline because its parent molecule, H_3^+ , is readily destroyed by the proton exchange with CO. This is also true for its non-deuterated form N_2H^+ . We used a simple ring model to constrain the spatial distribution of gas N_2D^+ . The model consists of three free parameters: an inner radius R_{in} beyond the CO snowline and where conditions are sufficiently cold for a substantial enhancement of the $\text{H}_2\text{D}^+/\text{H}_3^+$ ratio, an outer radius R_{out} , and a constant abundance X_{low} .

We modeled the distribution of DCO⁺ as three separate contributions from both deuteration channels and a third region in the outer disk motivated by the radial profile of its integrated intensity map (Fig. 5.4). Our model uses a set of seven parameters describing three regions: an inner radius (R_{in}), two radial breaks (R_1 , R_2), and three constant abundances (X_{high} , X_{low} , X_3) for the inner, the middle and the outer emission region. Figure 5.5 shows abundances and column density profiles of these simple models.

5.4.5 Line excitation

Instead of a full radiative transfer modeling we opted for a more simplistic approach by considering estimates of a characteristic excitation temperature as a function of the distance to the central star to calculate the resulting line emission given an abundance profile. We used

LIME (Brinch & Hogerheijde 2010, v1.5), a 3D radiative transfer code in non-LTE that can produce line and continuum radiation from a physical model to estimate a characteristic excitation temperature as a function of radius throughout the disk for the observed transitions DCO⁺ 3–2, DCN 3–2, and N₂D⁺ 3–2. We used the physical model described above and a constant abundance equal to the disk average found in Sec. 5.3 assuming $T_{\text{ex}} = 25$ K. LIME outputs population levels in a grid of 50000 points, which are randomly distributed in R using a logarithmic scale. Establishing a convergence criteria encompassing all of the grid points is difficult. We manually set the number of iterations to 12 and confirm convergence by comparing consecutive iterations. We used the rate coefficients from the Leiden Atomic and Molecular Database (Schöier et al. 2005)¹. For N₂D⁺ and DCN we used the N₂H⁺ rate coefficients, which are adopted from HCO⁺ (Flower 1999), and HCN rate coefficients (Dumouchel et al. 2010), respectively, since the transitions between the non-deuterated and deuterated forms do not differ significantly. For DCO⁺ we use the same collision rates as those for HCO⁺ and Einstein A coefficients taken from the Cologne Database for Molecular Spectroscopy (CDMS) and Jet Propulsion Laboratory (JPL) database.

To construct the radial excitation temperature profile we take the average excitation temperature of the points below $z < 10 \times h(R)$, where $h(R)$ is the scale height of our adopted physical model. These temperature profiles are shown in red in Fig. 5.5. A drawback of this approach is that assuming an isothermal vertical structure of the temperature profile might not properly describe the vertical region over which the molecules extend.

5.4.6 Abundance estimates

We computed a radial emission profile with the radial excitation temperature profile and column densities from the parametric constant abundance profiles, shown in green in Fig. 5.5, by solving Eq. 5.1.

We then created a 2D sky image from the modeled emission profile and convolved it with the synthesized beam of the observation to fit the integrated intensity maps shown in Fig. 5.1. Since we only fit radial column density profiles the vertical distribution of these species cannot be constrained by this approach. However, past modeling of DCO⁺ shows that its vertical distribution has limited effect on constraining radial boundaries (Qi et al. 2015).

5.4.7 Best-fit parameters

We minimize $\chi^2 = (F_{\text{obs}}(x, y) - F_{\text{model}}(x, y))^2 / \sigma(x, y)^2$ values, where $F_{\text{obs}}(x, y)$ corresponds to the data points of the integrated intensity maps (as shown in Fig. 5.1), $F_{\text{model}}(x, y)$ corresponds to the points of the modeled integrated intensity map convolved with the synthesized beam and $\sigma(x, y)$ corresponds to the standard deviation of the pixels of a concentric ellipsoid (such as those used to make the radial profiles seen in Fig. 5.3) that includes the pixel (x, y) . We report best-fit parameters that correspond to a minimum of the explored parameter space. In the case of DCO⁺ we explore different configurations of rings, allowing them to have one, two or no gaps empty of material between the ring-like regions. Table 5.4 shows a summary of our preferred models and Fig. 5.6 shows radial profiles of the best-fit model's column density, integrated intensity, estimated excitation temperature, and the integrated intensity of the data for each of our detections.

In the case of DCO⁺, the location of the different radial zones are degenerate. A model with an additional two degrees of freedom, describing three radial rings separated by gaps,

¹www.strw.leidenuniv.nl/~moldata/

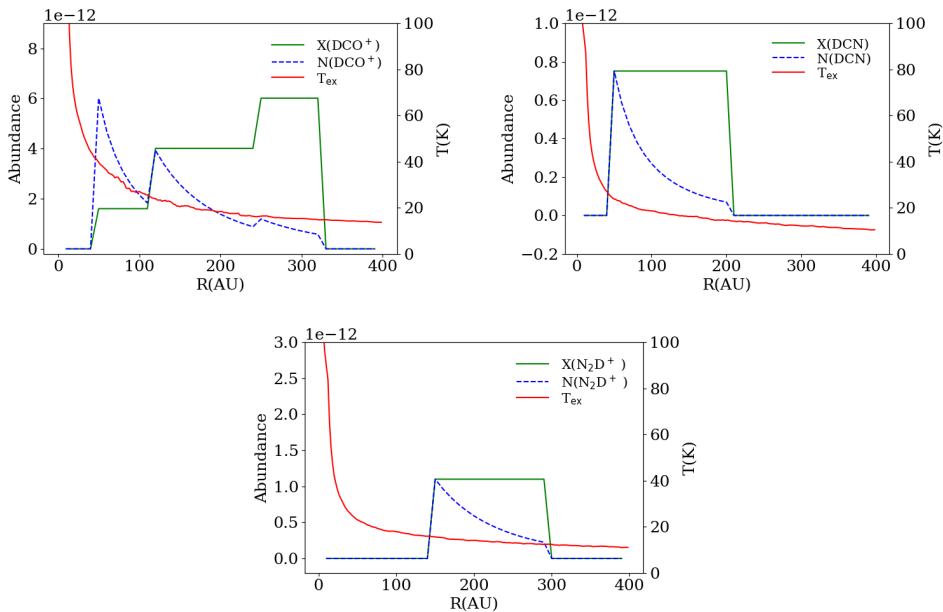


Figure 5.5: Schematics of the abundance models for the transitions of DCO^+ $J=3-2$, DCN $J=3-2$ and N_2D^+ $J=3-2$. The dashed blue line corresponds to a scaled profile of the column density of the abundance model for the purpose of illustration. The red continuous line corresponds to the assumed excitation temperature profile.

can also reproduce the data. The modest spatial resolution of our data cannot distinguish between these models. Detailed chemical modeling plus a 3D radiative treatment of DCO^+ is necessary to break the degeneracy of our toy model. The best-fit abundances for the simplest model without any gaps as described in Sec. 5.4.4 are $X_{\text{high}}=1.6^{+0.4}_{-0.5}\times 10^{-12}$, $X_{\text{low}}=4.0^{+1.0}_{-1.3}\times 10^{-12}$, $X_3=6.0^{+1.4}_{-2.0}\times 10^{-12}$, and their best-fit radial boundaries are $R_{\text{in}}=50^{+5}_{-3}$ AU, $R_1=118^{+4}_{-5}$ AU, $R_2=245^{+3}_{-13}$ AU, and $R_{\text{out}}=316^{+3}_{-10}$ AU. We do not consider a vertical distribution of the DCO^+ and DCN molecules. This results in vertically averaged abundances, which are lower limits to the maximum values expected in a full 2D treatment because in reality DCO^+ and DCN are absent where the gas temperature is higher than the activation temperature for their deuteration. In addition, DCO^+ is absent in the midplane where CO starts to freeze-out.

The best-fit model for the DCN emission profile consists of a ring with a constant abundance $X_{\text{high}}=7.5^{+0.9}_{-0.9}\times 10^{-13}$ between $R_{\text{in}}=51^{+6}_{-6}$ AU and $R_{\text{out}}=201^{+15}_{-24}$ AU, where R_{in} can be considered the radius where the gas temperature is high enough for the reaction described in Eq. 5.2b to be exothermic. The best-fit model for the N_2D^+ emission profile consists of a ring with constant abundance $X_{\text{low}}=1.1^{+0.1}_{-0.1}\times 10^{-12}$ between $R_{\text{in}}=139^{+5}_{-4}$ AU and $R_{\text{out}}=287^{+15}_{-21}$ AU, where R_{in} could be tracing the CO midplane snowline radial location.

Table 5.4: Best-fit model parameters

Parameters	DCN $J=3-2$	N_2D^+ $J=3-2$	DCO^+ $J=3-2$
R_{in}	51^{+6}_{-6} AU	139^{+5}_{-4} AU	50^{+5}_{-3} AU
R_1			118^{+4}_{-5} AU
R_2			245^{+3}_{-13} AU
R_{out}	201^{+15}_{-24} AU	287^{+15}_{-21} AU	316^{+3}_{-10} AU
X_{high}	$7.5^{+0.9}_{-0.9} \times 10^{-13}$		$1.6^{+0.4}_{-0.5} \times 10^{-12}$
X_{low}		$1.1^{+0.1}_{-0.1} \times 10^{-12}$	$4.0^{+1.0}_{-1.3} \times 10^{-12}$
X_3			$6.0^{+1.4}_{-2.0} \times 10^{-12}$

Notes. Best-fit parameters of models as shown in Fig. 5.6. DCO^+ values correspond to the model with two gaps. The formal errors are calculated at 90% confidence levels.

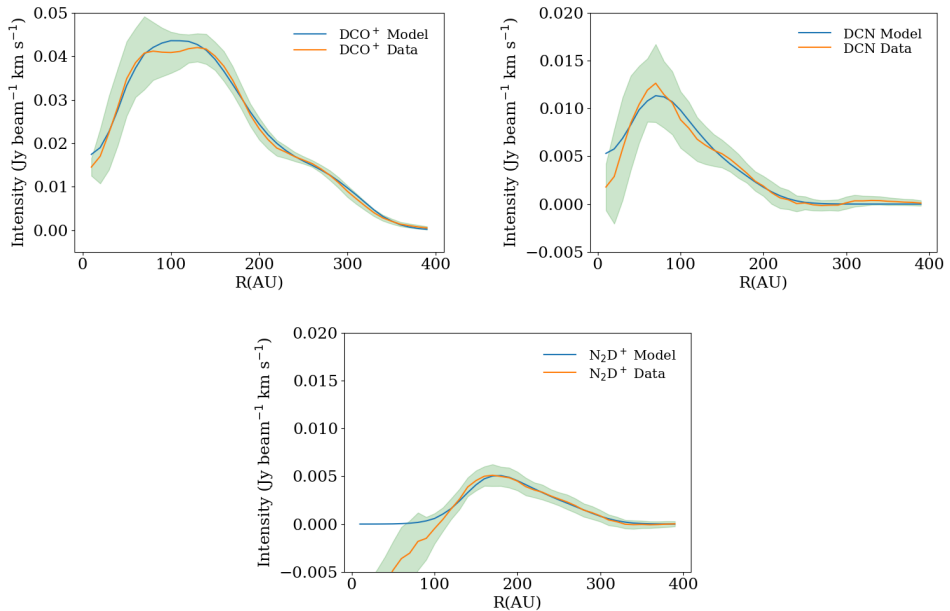


Figure 5.6: Best-fit models for the transitions of DCO^+ $J=3-2$, DCN $J=3-2$, and N_2D^+ $J=3-2$. The error bars, shown as a filled region in green, correspond to the standard deviation of the values in one annulus as seen in Fig. 5.3.

5.5 Discussion

5.5.1 The inner depression

Our best-fit models find an inner drop in emission at ~ 50 AU for both the DCN and DCO^+ line emission. This could be tracing the gas temperature required for the high temperature deuteration channel to be active (10-80 K) or an optically thick continuum region at small radii. Recent observations of C^{18}O , ^{13}CO , and continuum at 1.3 mm (Isella et al. 2016) with ALMA in higher spatial resolution also show a central depression in C^{18}O and ^{13}CO radial intensity profiles. These CO isotopes are optically thin and trace the gas near the midplane. If the dust becomes optically thick it could hide the line emission coming from deeper layers toward the midplane. Subtracting the continuum estimate in these regions then creates an apparent absence of emission. An alternative explanation is inherent to the chemistry of both species. DCN is readily destroyed by simple ions such as H_3^+ and H^+ (Albertsson et al. 2013). DCO^+ can be destroyed if H_2O is desorbed from the grains at inner radii. It is unlikely that both of these effects correlate at the same radii ($R_{\text{in}} \sim 50$ AU).

The peak value of the continuum at the center of the disk is $167 \text{ mJy beam}^{-1}$ corresponding to a brightness temperature of 25 K at 1.3 mm. This is inconsistent with the expected dust temperature derived from SED models for optically thick dust. The disk surrounding HD163296 is known to have unresolved ring-like structure at 1.3 mm (Zhang et al. 2016; Isella et al. 2016). The corresponding brightness temperature for the peak intensity in these observations at higher spatial resolution is 55 K, which is consistent with optically thick dust. The best-fit continuum models of Isella et al. (2016) show optically thick dust just inside 50 AU. We conclude that our R_{in} parameter is tracing this optically thick dust region.

5.5.2 Limitation of DCO^+ as a CO snowline tracer

N_2H^+ has been used to trace the CO snowline in protoplanetary disks before (Qi et al. 2015, 2013). We expect N_2D^+ to trace it as well using the same reasoning as for N_2H^+ (Huang & Öberg 2015). Our best-fit N_2D^+ model gives a R_{in} value of 141 AU, which is 50 AU further away than previous estimates of the CO snowline in HD 163296. This could be due to the apparent central depression in the N_2D^+ radial profile. As explained in Sec. 5.2, this line is sitting on the edge of an atmospheric feature resulting in high noise and a very weak detection, which makes it difficult to do a good continuum subtraction. The central negative bowl has the same order of magnitude as other scattered negative noise in the image plane of the resulting integrated intensity map, but, as it is located at the center, an azimuthal average does not represent as good an estimate of the radial profile in the inner disk as it does in the outer disk. We cannot rely on our best-fit value for R_{in} as a probe for the CO snowline in the midplane, although a deeper integration of the N_2D^+ $J=3-2$ line can still be used to constrain it.

On the other hand, our best-fit DCO^+ model value for R_1 of 118_{-5}^{+4} AU agrees well with the previous estimate of ~ 90 AU given our resolution. Two effects are boosting the deuterium fractionation of H_2D^+ and, in consequence, the low temperature deuteration channel. First, the gas temperature is low enough for the reaction in Eq. 5.2a to be mainly exothermic. Second, H_2D^+ is readily destroyed by CO in the gas phase which is frozen out. But CO must be present to form DCO^+ via Eq. 5.5. This could be achieved in a scenario in which DCO^+ is found in a thin layer around the CO freeze-out temperature as proposed by Mathews et al. (2013). Without previous knowledge, DCO^+ alone cannot trace the location of the CO snowline.

5.5.3 The origin of the third ring

Motivated by the reasoning in Section 5.4.2 we found a best-fit value of 245_{-13}^{+3} AU for the R_2 parameter in our DCO^+ model. At these radii the bulk of CO in the gas phase is locked up on the grains as ice. The main production route of DCO^+ in the low temperature deuteration route (Eq.5.4) requires CO in the gas-phase. This raises the question of how DCO^+ emission arises at such large radii.

Photodesorption of CO by nonthermal processes could explain an outer ring of DCO^+ emission as discussed in the case of IM Lup (Öberg et al. 2015). However the efficiency of this mechanism is very model dependent. Full chemical models of DCO^+ toward DM Tau (Teague et al. 2015) show that, although there is an enhancement of DCO^+ at large radii produced by the interstellar UV field and X-ray luminosity, the effect is not as pronounced as that seen in IM Lup. The strongly emitting outer disk seen toward IM Lup coincides with the extent of the mm-size grains. If the smaller grains also follow the steepening of the surface density of mm-size grains, UV penetration is enhanced leading to an enhancement on the DCO^+ emission. High-resolution continuum data observed with ALMA Band 6 (Isella et al. 2016) revealed three concentric sets of rings and gaps as predicted by Zhang et al. (2016). The first depression at $D_1 \sim 53$ AU and the second brightness peak centered at $B_2 \sim 120$ AU correlate well with $R_{\text{in}}=50_{-3}^{+5}$ AU and $R_1=118_{-5}^{+4}$ AU from our best-fit DCO^+ model. The extent of the continuum to about 230 AU also correlates with R_2 at 245_{-13}^{+3} AU from our best-fit DCO^+ model. Although no direct consequence of the location of the second gap can be drawn toward an enhancement in UV penetration, the scales at which these rings are seen in the (sub)mm continuum (~ 60 -50 AU) are a rough estimate of the spatial scales where rings and gaps are seen in shorter wavelengths. Full grain-surface chemical modeling is needed to identify the chemical reactions involved in this mechanism.

Cleeves (2016) have proposed a thermal inversion in the midplane as a mechanism to release CO into the gas phase at large radii. Recently, dust evolution modeling efforts by Facchini et al. (2017), coupled with chemistry models of HD 163296, shows signs of thermal inversion as a direct consequence of radial drift, grain growth, and settling. As a result, thermal CO desorption is enhanced at large radii where the dust becomes warmer. The thermal inversion in the models of Facchini et al. (2017) occurs at about 400 AU, farther away than our R_2 best-fit parameter of 245_{-13}^{+3} AU. However, the radial location of the thermal inversion is very temperature sensitive and a slightly colder disk could shift its location inward. This effect is only seen in models with a low turbulence α of 10^{-3} - 10^{-4} and when the CO ice is mixed with water ice resulting in a higher binding energy. A tailored model is necessary to confirm the viability of this mechanism as an explanation for the outer DCO^+ ring.

Finally, another plausible explanation is a local decrease of the ortho- to para- (o/p) ratio of H_2 . The reaction shown in Eq.5.2a has a higher activation barrier for p- H_2 than for o- H_2 which results in an increase in DCO^+ formation (Murillo et al. 2015; Walmsley et al. 2004). Detailed chemical modeling is needed to test this scenario.

5.5.4 Deuterium fractionation

Our estimated disk-averaged fractionation ratio $D_f(\text{DCO}^+/\text{HCO}^+)$ of 0.05 ± 0.01 agrees with previous measurements on this source (Huang et al. 2017) or even toward other disks, for example, DM Tau (Guilloteau et al. 2006) and TW Hya (van Dishoeck et al. 2003).

Our estimated value of 0.02 ± 0.01 for $D_f(\text{DCN}/\text{HCN})$ is lower than the $D_f(\text{DCO}^+/\text{HCO}^+)$ and $D_f(\text{N}_2\text{D}^+/\text{N}_2\text{H}^+)$. A lower value of $D_f(\text{DCN}/\text{HCN})$ compared to $D_f(\text{N}_2\text{D}^+/\text{N}_2\text{H}^+)$ could hint at a more efficient deuterium enrichment in the outer colder disk. On the other hand,

in comparison with $D_f(\text{DCO}^+/\text{HCO}^+)$, a lower value of $D_f(\text{DCN}/\text{HCN})$ could be explained by the different deuteration pathways that formed these species, supporting the idea of a colder formation environment for DCO^+ at large radii. Both of these values are of the same order of magnitude as for other protoplanetary disks (Öberg et al. 2012; Huang et al. 2017). The derived $D_f(\text{DCO}^+/\text{HCO}^+)$ value is one order of magnitude lower than in starless cores but similar to the value toward low-mass protostars, such as IRAS 16293-2422 (Butner et al. 1995; Caselli et al. 2002; Tafalla et al. 2006; Schöier et al. 2002). The derived $D_f(\text{DCN}/\text{HCN})$ value is the same order of magnitude toward low-mass protostars and starless cores (Wootten 1987; Roberts et al. 2002).

Our estimated value of 0.45 ± 0.21 for $D_f(\text{N}_2\text{D}^+/\text{N}_2\text{H}^+)$ is higher than $D_f(\text{DCO}^+/\text{HCO}^+)$ and $D_f(\text{DCO}^+/\text{HCO}^+)$ as predicted by the chemical models of Willacy (2007). It is also comparable to the values toward the T Tauri disk AS 209 (Huang & Öberg 2015) and consistent with the wide range of ratios, from <0.02 to 0.44, found toward starless cores (Crapsi et al. 2005). As noted in the case of AS 209, the higher D/H ratio from N_2D^+ compared to that from DCO^+ is a consequence of their formation environments. DCO^+ is formed where CO is not frozen out in the relatively warm upper layers of the disk. N_2D^+ is more abundant where CO is frozen out and deuteration is enhanced by Eq. 5.2a which, together with N_2H^+ , makes it an excellent tracer of the cold outer midplane.

5.6 Summary

We have successfully detected three deuterated species toward HD 163296: DCO^+ , N_2D^+ , and DCN. We use simple models and estimates of the midplane temperature to fit radial rings with constant abundance constraining their relative abundance and radial location. Our main conclusions are:

- We confirm the location of the CO snowline using the second ring of DCO^+ as a tracer at ~ 100 AU, which is consistent with the previously reported value of 90 AU. Our N_2D^+ detection is too noisy to effectively constrain its location, although it is still consistent given our large beam.
- DCO^+ and DCN show an inner depression that arises most likely due to optically thick dust and not due to inherent formation pathway of both species.
- DCO^+ shows a three ring-like structure, located at 70 AU, 150 AU, and 260 AU that could be linked to the structure of the μm -sized grains. The two first rings correspond to the high and low temperature deuteration pathways and are in agreement with simple DCN and N_2D^+ best-fit models.
- The origin of the third DCO^+ ring at 260 AU may be due to a local decrease of UV opacity allowing the photodesorption of CO and consequent formation of DCO^+ as seen in other disks (Öberg et al. 2015), thermal desorption of CO as proposed by Facchini et al. (2017), or a local decrease of the o/p ratio of H_2 .
- The derived D_f values are several orders of magnitude higher than the D/H cosmic ratio as expected and are in agreement with previous measurements and models. The higher D/H value for N_2D^+ in comparison with those from DCO^+ and DCN suggest a cooler formation environment for the former.

Detailed chemical modeling of these molecules is needed to confirm the origin of the DCO^+ rings.

Acknowledgements. The authors acknowledge support by Allegro, the European ALMA Regional Center node in The Netherlands, and expert advice from Luke Maud in particular. This work was partially supported by grants from the Netherlands Organization for Scientific Research (NWO) and the Netherlands Research School for Astronomy (NOVA). This paper makes use of the following ALMA data: ADS/JAO.ALMA# 2013.1.01268.S. ALMA is a partnership of ESO (representing its member states), NSF (USA), and NINS (Japan), together with NRC (Canada), NSC and ASIAA (Taiwan), and KASI (Republic of Korea), in cooperation with the Republic of Chile. The Joint ALMA Observatory is operated by ESO, AUI/NRAO, and NAOJ.

5.A Keplerian Masking

Since the emission in each channel only comes from a region in the sky where the rotational velocity of the disk matches the Doppler shift of the line, selecting a subset of pixels on each velocity channel with Keplerian velocities equal to the expected Doppler shift enhances the S/N of the final integrated intensity map. To achieve this, we first calculate the projected radial velocity on each pixel using a stellar mass value of $2.3 M_{\odot}$ (van den Ancker et al. 1997). We create a mask cube with the same dimensions as the data spectral cube and select, for each spectral plane, the pixels that have a projected radial velocity greater than the correspondent Doppler-shifted velocity v_r of the spectral plane and lower than $v_r + \delta v$, where δv is the spectral resolution of the cube. Finally, each spectral plane of the mask cube is convolved with the synthesized beam to create a final mask that accounts for the smearing of the disk as seen in Fig 5.7.

A similar approach has already been used by Yen et al. (2016), stacking azimuthal regions that are corrected by their Keplerian velocity. They reconstruct integrated intensity maps by Doppler-shifting a selected azimuthal region within an inner and outer radius. Since both methods are flux conserving, the only difference lies in reduced noise for the latter in sacrifice of spatial information. The stacking method by Yen et al. (2016) achieves a S/N increase of a factor of ~ 4 for the weak lines N_2D^+ J=3–2 and DCN J=3–2. In contrast our method achieves an increase in S/N of a factor of ~ 2 but results in a much clearer integrated intensity map (see Fig. 5.1).

Bibliography

- Albertsson, T., Semenov, D. A., Vasyunin, A. I., Henning, T., & Herbst, E. 2013, *ApJS*, 207, 27
- Brinch, C., & Hogerheijde, M. R. 2010, *A&A*, 523, A25
- Butner, H. M., Lada, E. A., & Loren, R. B. 1995, *ApJ*, 448, 207
- Carney, M. T., Hogerheijde, M. R., Loomis, R. A., et al. 2017, *ArXiv e-prints*, arXiv:1705.10188
- Caselli, P., Walmsley, C. M., Zucconi, A., et al. 2002, *ApJ*, 565, 344
- Ceccarelli, C., Caselli, P., Herbst, E., Tielens, A. G. G. M., & Caux, E. 2007, *Protostars and Planets V*, 47
- Cleeves, L. I. 2016, *ApJ*, 816, L21
- Crapsi, A., Caselli, P., Walmsley, C. M., et al. 2005, *ApJ*, 619, 379
- Dalgarno, A., & Lepp, S. 1984, *ApJ*, 287, L47
- Dullemond, C. P., & Dominik, C. 2004, *A&A*, 417, 159
- Dumouchel, F., Faure, A., & Lique, F. 2010, *MNRAS*, 406, 2488
- Facchini, S., Birnstiel, T., Bruderer, S., & van Dishoeck, E. F. 2017, *ArXiv e-prints*, arXiv:1705.06235
- Favre, C., Bergin, E. A., Cleeves, L. I., et al. 2015, *ApJ*, 802, L23
- Flower, D. R. 1999, *MNRAS*, 305, 651
- Garufi, A., Quanz, S. P., Schmid, H. M., et al. 2014, *A&A*, 568, A40
- Gerner, T., Shirley, Y. L., Beuther, H., et al. 2015, *A&A*, 579, A80
- Guilloteau, S., Piétu, V., Dutrey, A., & Guélin, M. 2006, *A&A*, 448, L5

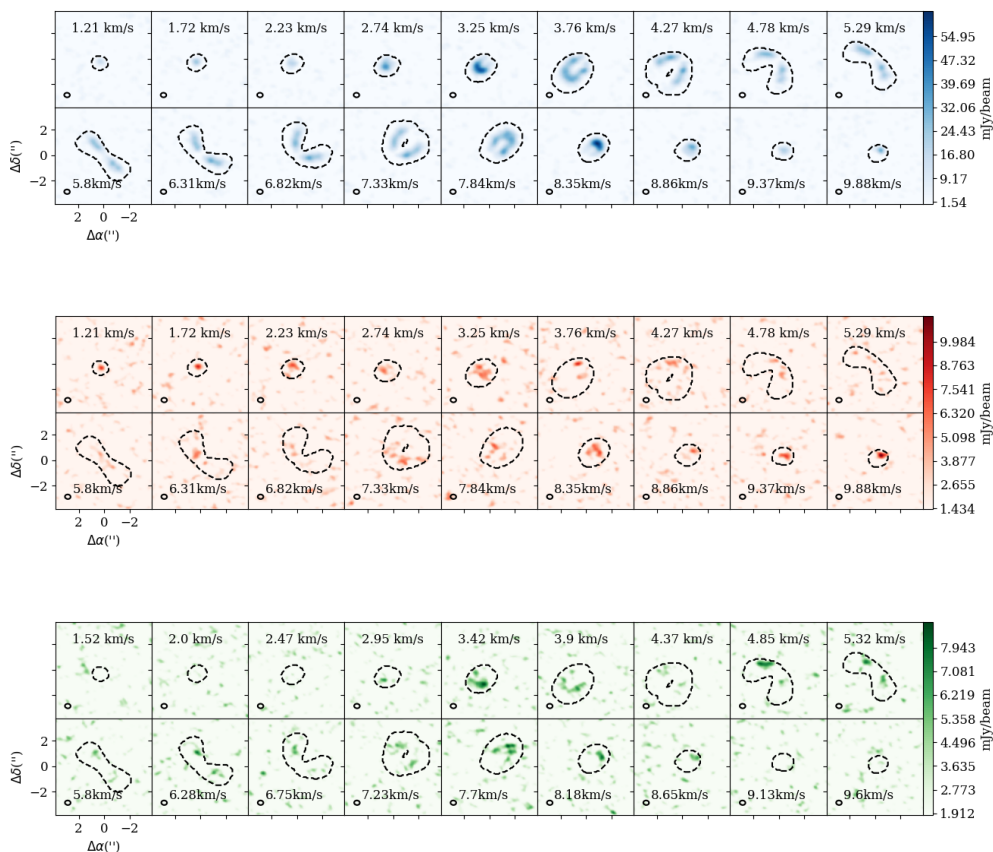
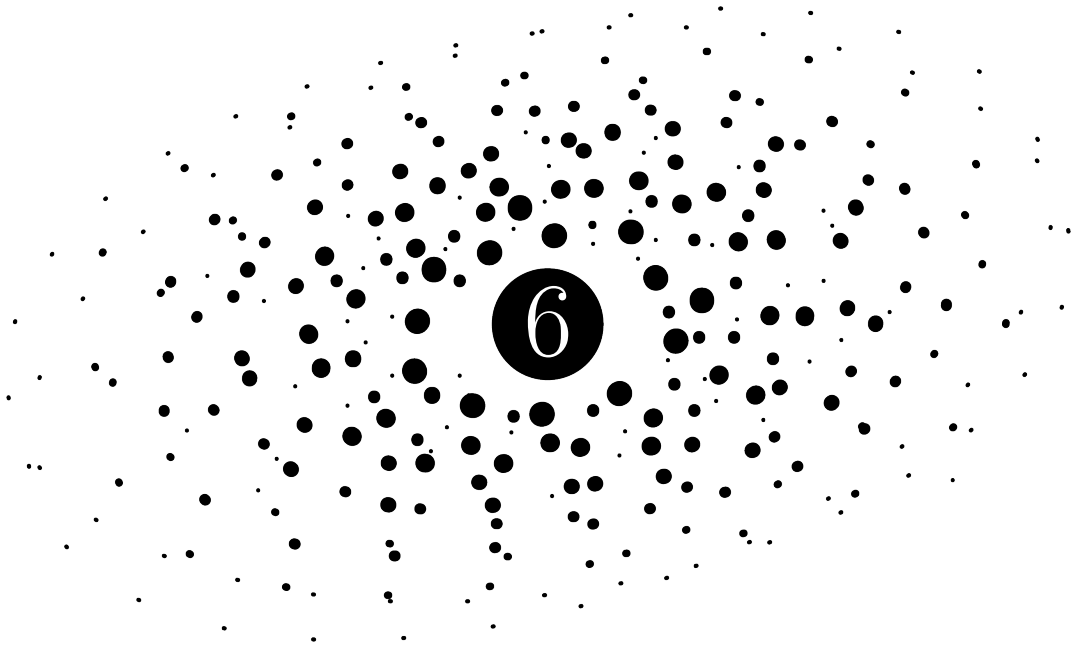


Figure 5.7: Overplotted Keplerian mask, in black dashed contours, and spectral maps of $\text{DCO}^+ J=3-2$, $\text{DCN } J=3-2$, and $\text{N}_2\text{D}^+ J=3-2$.

- Huang, J., & Öberg, K. I. 2015, *ApJ*, 809, L26
Huang, J., Öberg, K. I., Qi, C., et al. 2017, *ApJ*, 835, 231
Isella, A., Guidi, G., Testi, L., et al. 2016, *Phys. Rev. Lett.*, 117, 251101
Mathews, G. S., Klaassen, P. D., Juhász, A., et al. 2013, *A&A*, 557, A132
Millar, T. J., Bennett, A., & Herbst, E. 1989, *ApJ*, 340, 906
Mumma, M. J., & Charnley, S. B. 2011, *ARA&A*, 49, 471
Murillo, N. M., Bruderer, S., van Dishoeck, E. F., et al. 2015, *A&A*, 579, A114
Öberg, K. I., Boogert, A. C. A., Pontoppidan, K. M., et al. 2011, *ApJ*, 740, 109
Öberg, K. I., Furuya, K., Loomis, R., et al. 2015, *ApJ*, 810, 112
Öberg, K. I., Qi, C., Wilner, D. J., & Hogerheijde, M. R. 2012, *ApJ*, 749, 162
Öberg, K. I., Qi, C., Fogel, J. K. J., et al. 2010, *ApJ*, 720, 480
Perryman, M. A. C., Lindegren, L., Kovalevsky, J., et al. 1997, *A&A*, 323, L49
Qi, C., D'Alessio, P., Öberg, K. I., et al. 2011, *ApJ*, 740, 84
Qi, C., Öberg, K. I., Andrews, S. M., et al. 2015, *ApJ*, 813, 128
Qi, C., Wilner, D. J., Aikawa, Y., Blake, G. A., & Hogerheijde, M. R. 2008, *ApJ*, 681, 1396
Qi, C., Öberg, K. I., Wilner, D. J., et al. 2013, *Science*, 341, 630

- Remijan, A., Snyder, L. E., Friedel, D. N., Liu, S.-Y., & Shah, R. Y. 2003, *ApJ*, 590, 314
- Roberts, H., Fuller, G. A., Millar, T. J., Hatchell, J., & Buckle, J. V. 2002, *A&A*, 381, 1026
- Schöier, F. L., Jørgensen, J. K., van Dishoeck, E. F., & Blake, G. A. 2002, *A&A*, 390, 1001
- Schöier, F. L., van der Tak, F. F. S., van Dishoeck, E. F., & Black, J. H. 2005, *A&A*, 432, 369
- Tafalla, M., Santiago-García, J., Myers, P. C., et al. 2006, *A&A*, 455, 577
- Teague, R., Semenov, D., Guilloteau, S., et al. 2015, *A&A*, 574, A137
- Turner, B. E. 2001, *ApJS*, 136, 579
- van den Ancker, M. E., The, P. S., Tjin A Djie, H. R. E., et al. 1997, *A&A*, 324, L33
- van Dishoeck, E. F., Thi, W.-F., & van Zadelhoff, G.-J. 2003, *A&A*, 400, L1
- van't Hoff, M. L. R., Walsh, C., Kama, M., Facchini, S., & van Dishoeck, E. F. 2017, *A&A*, 599, A101
- Vidal-Madjar, A. 1991, *Advances in Space Research*, 11, 97
- Walmsley, C. M., Flower, D. R., & Pineau des Forêts, G. 2004, *A&A*, 418, 1035
- Watson, W. D. 1976, *Reviews of Modern Physics*, 48, 513
- Willacy, K. 2007, *ApJ*, 660, 441
- Wilson, T. L. 1999, *Reports on Progress in Physics*, 62, 143
- Wisniewski, J. P., Clampin, M., Grady, C. A., et al. 2008, *ApJ*, 682, 548
- Woods, P. M., & Willacy, K. 2009, *ApJ*, 693, 1360
- Wootten, A. 1987, in *IAU Symposium, Vol. 120, Astrochemistry*, ed. M. S. Vardya & S. P. Tarafdar, 311–318
- Yen, H.-W., Koch, P. M., Liu, H. B., et al. 2016, *ApJ*, 832, 204
- Zhang, K., Bergin, E. A., Blake, G. A., et al. 2016, *ApJ*, 818, L16
- Zhang, K., Bergin, E. A., Blake, G. A., Cleaves, L. I., & Schwarz, K. R. 2017, *Nature Astronomy*, 1, 0130



Exploring DCO^+ as a tracer of thermal inversion in the disk around the Herbig Ae star HD163296

Salinas, V. N., Hogerheijde, M. R., Murillo, N. M., Mathews, G. S., Qi, C., Williams, J. P., Wilner, D. J.
Submitted to A&A.

6.1 Introduction

DCO⁺ is a good tracer of the deuterium fractionation and ionization fraction of low temperature environments (Favre et al. 2015; Millar et al. 1989). Detections of DCO⁺, and other simple deuterated molecules, towards protoplanetary disks are present only in a handful of T Tauri disks (TW Hya (van Dishoeck et al. 2003), DM Tau (Guilloteau et al. 2006; Teague et al. 2015), AS 209, IM Lup V4046 Sgr and LkCa 15 (Öberg et al. 2010, 2011, 2015; Huang et al. 2017)) and in the disks around the Herbig Ae stars MWC 480 (Huang et al. 2017) and HD 163296 (Qi et al. 2008; Mathews et al. 2013; Qi et al. 2015; Yen et al. 2016; Salinas et al. 2017). High angular resolution observations of some of these disks have revealed a surprisingly complex radial structure. The chemistry involved in the gas-phase formation of DCO⁺ is thought to be well understood and has been previously studied in the ISM and in disks (Turner 2001; Willacy 2007; Roueff et al. 2013; Favre et al. 2015). In this paper, we attempt to determine whether our current understanding of the DCO⁺ chemistry is sufficient to reproduce the complex radial structure seen in protoplanetary disks, particularly in the disk surrounding the Herbig Ae star HD 163296.

DCO⁺ forms in the gas phase through two different regimes: a low temperature deuteration (henceforth cold deuteration, CD) and a warm deuteration (henceforth warm deuteration, WD) channel. The CD and WD regimes are gradually enhanced at temperatures lower than ~ 30 K and ~ 80 K, respectively (Millar et al. 1989; Albertsson et al. 2013). This enhancement is a direct consequence of the lower zero-point vibrational energy of simple deuterated molecules in comparison to their non-deuterated counterparts. The origin of highly deuterated species, and of DCO⁺, in the solar nebula can be attributed to in situ synthesis in the primordial disk or to being inherited from the interstellar medium (ISM). Deuterium is injected into the chemistry via ion-molecule reactions, and is kept active by the endothermic nature of the inverse reaction. For an effective enhancement of the deuterium fractionation ratio the environment must be cold (typically tens of degrees Kelvin), and ionized. In the dense shielded ISM, the ionization environment is mainly dominated by ultraviolet (UV) radiation from massive stars. In the cold outer regions of protoplanetary disks, where deuterium enrichment takes place, the ionization source comes from galactic cosmic rays (CRs) and to a lesser extent by radiation both from the host star and from external sources.

DCO⁺ was proposed first as a good CO snowline tracer in protoplanetary disks (Mathews et al. 2013). Recent chemical models (including the WD channel) conducted by Favre et al. (2015) have proposed DCO⁺ as a good tracer of the ionization degree in the inner regions of planet-forming disks rather than the temperature structure and the CO snowline. The WD channel formation channel involves ionized simple hydrocarbons, unlike the CD involving H₂D⁺ which is highly reactive with CO. If the CD dominates the formation of DCO⁺ in disks then it can be used as an indirect tracer of the CO snowline because of its parent molecule, H₂D⁺, is readily destroyed by CO in the gas-phase. The models of Favre et al. (2015) show that the WD channel enhances the column density of DCO⁺ by a factor of 5 in the warm regions of a T Tauri-like disk, where CO is still in the gas phase, and is responsible for the bulk of the abundance. Observations of significant emission of DCO⁺ in the inner parts of protoplanetary disks have been already reported (Qi et al. 2015; Huang et al. 2017). In particular, Salinas et al. (2017) have seen DCO⁺ extending from ~ 50 AU to ~ 300 AU in the disk surrounding the Herbig Ae star HD 163296.

HD 163296 has a massive ($0.089 M_{\odot}$) inclined (44°) disk and its gaseous content, probed by ¹²CO emission, extends at least to ~ 500 AU (Qi et al. 2013; Mathews et al. 2013). These attributes and its proximity (122 pc, van den Ancker et al. 1998) make it an excellent candidate to study both the radial and vertical distribution of deuterated species such as

DCO⁺. The disk has been observed in the millimeter regime revealing a distribution of mm-sized grains that extend up to ~ 230 AU with multiple rings and gaps (Isella et al. 2016).

The DCO⁺ radial distribution of the HD 163296 disk has been characterized by Salinas et al. (2017) using ALMA observations. The data are consistent with three regimes of different constant abundances defined by one inner radius at 50 AU and two breaks at 120 AU and 245 AU. They found that the first two regimes correlate well with the expected WD and CD channels traced by DCN and N₂D⁺. The third regime correlates with the extent of the mm-size dust grains which hints at a local decrease of UV opacity allowing photodesorption of CO and consequent DCO⁺ formation as proposed for the disk around IM Lup (Öberg et al. 2015). An interesting alternative to explain this excess DCO⁺ emission is releasing CO through thermal desorption (Cleeves 2016). Dust grain evolution models by Facchini et al. (2017) have predicted a thermal inversion of the dust temperature as a direct consequence of radial drift and settling in the disk surrounding HD 163296 given low turbulence values.

Our main goal is to implement a simple chemical network for the CD channel and a parametrized WD channel, to reproduce both the location and the amount of the observed DCO⁺ in HD163296. Specifically, we aim to constrain the relative contribution of the WD channel after taking into account the CD channel. We can also address the mechanisms that cause a decrease of DCO⁺ inside ~ 50 AU, the third ringlike feature at 245 AU and drop off at larger radii.

In Section 6.2 we briefly describe the data and explain our modeling strategy. Section 6.3 contains the results obtained from our different modeling approaches. Section 6.4 discusses the validity of these models and provides an interpretation for the models' parameters. Finally in section 6.5 we summarize our findings and conclusions.

6.2 Methods

6.2.1 Previous observation of HD 163296

This study uses data of DCO⁺ $J=3-2$ at 216.112 GHz in the disk surrounding the Herbig Ae star HD163296 ($\alpha_{2000} = 17^{\text{h}}56^{\text{m}}51^{\text{s}}.21$, $\delta_{2000} = -21^{\circ}57'22''.0$) obtained by the Atacama Large (sub-)Millimeter Array (ALMA) in Band 6 as a part of Cycle 2 on 2014 July 27-29 (project 2013.1.01268.S). The spectral resolution is 0.7 MHz corresponding to 0.085 km s⁻¹ with respect to the rest frequency of the line. The uv -coverage of the data ranges from 20 to 630 k λ .

The data were reduced as described by Salinas et al. (2017) and Carney et al. (2017). The DCO⁺ $J=3-2$ line was continuum subtracted in the visibility plane using a first-order polynomial fit and imaged using a Briggs weighting of 0.5. The resulting synthesized beam has dimensions of $0''.53 \times 0''.42$ and is shown along with the obtained channel maps in Appendix 6.A. Salinas et al. (2017) use a Keplerian mask to obtain an integrated intensity map. A radial emission profile can be constructed by taking the average value of concentric ellipsoids, centered at the star, in the integrated intensity map. The resulting DCO⁺ radial emission profile can be seen in Fig. 6.1. The observational analysis of Salinas et al. (2017) modeled DCO⁺ as a three-region radial structure. They argue that these radial regions correspond roughly to the WD channel, the CD channel and a third unidentified regime at larger radii ($\gtrsim 240$ AU). Their analysis treated each region independently and assumed that the bulk of the DCO⁺ emission comes from the midplane. These assumptions do not impact their ability to constrain the regimes radially, but do not allow to constrain the contribution of the WD channel in the HD163296 disk. Whereas Salinas et al. (2017) only derived vertically

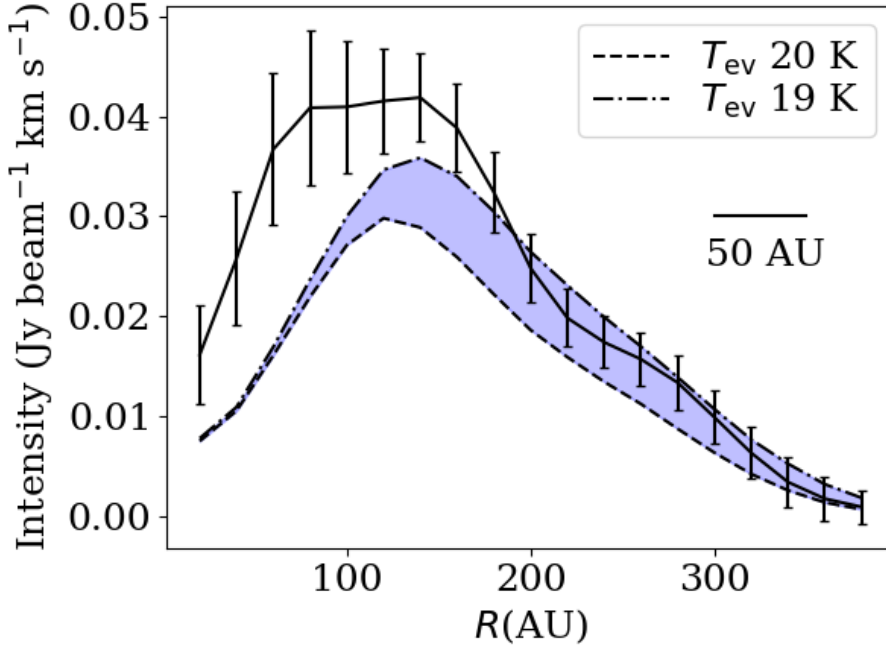
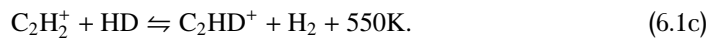
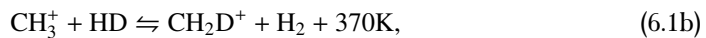
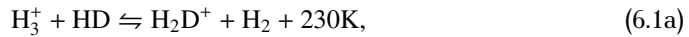


Figure 6.1: The black continuous line shows the observed DCO⁺ radial profile. These profiles are obtained by averaging the values of concentric ellipsoids of the integrated intensity maps. The error bars of the observed DCO⁺ radial profile corresponds to 3σ , where σ is the standard deviation of the values contained in the ellipsoid divided by the square root of the number of beams. The 50 AU bar corresponds to the semi-minor axis of the synthesized beam and serves as a measure of the spatial resolution. The dashed lines show radial profiles of the emission from models with two different evaporation temperature of CO $T_{\text{CO}}=19\text{-}20$ K and a constant abundance $X_{\text{in}}=5.0\times 10^{-5}$

averaged DCO⁺ abundances, here we carry out fully 2D (radius and height) modeling of the chemistry. Because deuteration, and the formation of DCO⁺, is a temperature dependent process, a vertical treatment of its abundance is needed in disks due to their strong vertical temperature gradient. For our analysis, we will assume that the WD channel remains active where the CD channel operates, but its contribution to the DCO⁺ emission in the outer regions of the disk is negligible. If this is the case, reproducing the emission at large radii alone can provide a constraint on the amount of DCO⁺ produced by the CD channel.

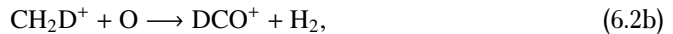
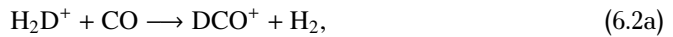
6.2.2 Chemical model

Deuterium is incorporated into the gas chemistry mainly through the following ion molecule reactions (Gerner et al. 2015; Turner 2001)

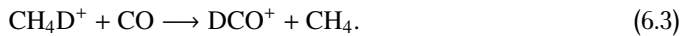


The right-to-left reactions of Equations 6.1a, 6.1b and 6.1c are endothermic and effectively enhance deuterium fractionation in low temperature environments. Equation 6.1a corresponds to the so-called CD channel and are active at temperatures ranging from 10-30 K (Millar et al. 1989; Albertsson et al. 2013). Eq. 6.1b and 6.1c, involving light hydrocarbons, correspond to the WD channel and is active at warmer temperatures ranging from 10-80 K.

DCO⁺ is formed in the gas-phase involving both the CD and WD channels through the reactions (Watson 1976; Wootten 1987; Favre et al. 2015)



or with products of CH₂D⁺ such as CH₄D⁺



We will model the CD channel using a simple chemical network, in 2D, and regard the WD channel as a constant abundance (X_{WD}) contribution that occurs at temperatures lower than an effective temperature (T_{eff}). The DCO⁺ chemical network involving the CD channel can be boiled down to only ten chemical reactions. This system can be solved analytically as proposed by Murillo et al. (2015). We use their prescription and simplified chemical network of the CD channel and apply it to HD163296. The input parameters are: the gas density ($n(\text{H}_2)$), the gas temperature (T_{gas}), the CO gas abundance ($X(\text{CO})$) and the HD gas abundance ($X(\text{HD})$). The ionization rate (ζ) is constant throughout the disk and equal to $1.3 \times 10^{-17} \text{ s}^{-1}$. We underestimate the ionization fraction at large heights above the midplane because we consider cosmic-rays to be the only ionizing agents. The ortho to para ratio of H₂ is considered to be in thermal equilibrium (LTE) and is approximated by the following expression,

$$\frac{o}{p} = 9 \exp\left(-\frac{170\text{K}}{T}\right). \quad (6.4)$$

We use a lower limit of 10^{-3} at low temperatures as described in Murillo et al. (2015). They contrasted their results to a full chemical network including gas-grain balance (freeze-out, thermal desorption, and cosmic-ray-induced photodesorption) confirming the general trend found by the simplified network. The advantage of using this simple network over a full chemical calculation, is that it allows us to more easily investigate the dependency of the DCO⁺ emission on individual model characteristics. Detailed chemical modeling, including the reactions shown in Eq. 6.1b and 6.1c would be needed to further investigate the DCO⁺ radial distribution, but this is beyond the scope of this paper.

6.2.3 Implementation

We adopt the gas density and dust temperature from the physical model used by Mathews et al. (2013) as inputs for the simple chemical network described above. This parametric model is an approximation of the model used by Qi et al. (2011) which fits both the SED and their millimeter observations. The density structure is defined by

$$\Sigma_d(R) = \begin{cases} \Sigma_C \left(\frac{R}{R_c}\right)^{-1} \exp\left[-\left(\frac{R}{R_c}\right)\right] & \text{if } R \geq R_{\text{in}} \\ 0 & \text{if } R < R_{\text{in}}, \end{cases}$$

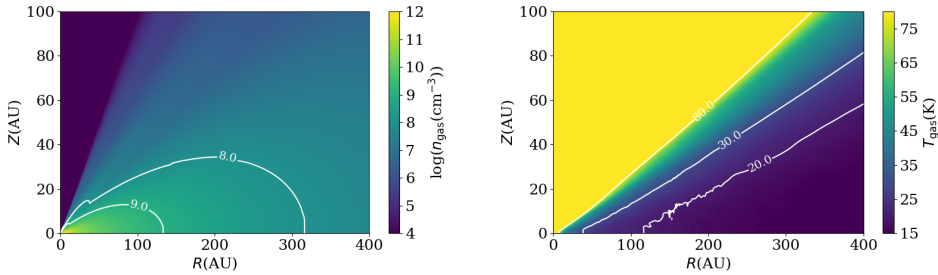


Figure 6.2: Visualization of the adopted physical model. The left panel shows the model density profile with white contours at 10^8 cm^{-3} and 10^9 cm^{-3} . The right panel shows the gas temperature structured clipped at 80 K to enhance the color gradient in the region of interest and white contours at 20, 30 and 80 K.

where Σ_C is determined by the total disk mass M_{disk} ($0.089 M_{\odot}$), R_C (150 AU) is the characteristic radius and R_{in} (0.6 AU) is the inner rim of the disk. The vertical structure is treated as a Gaussian distribution with an angular scale height defined by

$$h(R) = h_C \left(\frac{R}{R_C} \right)^{\psi},$$

where ψ (0.066) is the flaring power of the disk and h_C is the angular scale height at the characteristic radius R_C that can take different values for the gas and the dust distribution (see appendix A; Mathews et al. 2013). The dust temperature profile was computed by the 2D radiative transfer code RADMC (Dullemond & Dominik 2004) and is shown in Fig. 6.2 along with the gas density profile.

In addition to the gas density and dust temperature structure, CO and HD abundance profiles are required as inputs for the simple chemical network. We use a CO abundance profile described by three parameters: an effective dust temperature where CO starts to evaporate and becomes optimal for DCO^+ formation (T_{CO}), and two constant abundances for gas-phase CO inside (X_{low}) and outside (X_{high}) the freeze-out zone. We set $X_{\text{low}} = 0.01 X_{\text{high}}$ for all our models. We assume that the dust temperature (T_{dust}) equals the gas temperature (T_{gas}), which is a reasonable assumption in the dense regions that we focus on. We set the HD abundance, with respect to the nuclei density $n_{\text{H}} = 2n_{\text{H}_2}$, constant through the entire disk and equal to the cosmic D/H ratio $\sim 10^{-5}$ (Vidal-Madjar 1991).

6.2.4 Radiative transfer

We used LIME (v1.5), a 3D radiative transfer code in non-LTE (Brinch & Hogerheijde 2010) to compare our DCO^+ observations to the DCO^+ abundance model obtained using the prescription described above. LIME can produce line and continuum radiation from a physical model, an abundance distribution and the rate coefficients for a given molecular transition. We use the rate coefficients from the Leiden Atomic and Molecular Database (Schöier et al. 2005)¹ for DCO^+ . These are the same collision rates as those listed for HCO^+ (Flower 1999). The Einstein A coefficients taken are from CDMS and JPL. We use a grid of 100000 points that are created applying a weighted random selection in R using a logarithmic scale. This weighted random selection favors denser gas regions and will

¹www.strw.leidenuniv.nl/moldata/

always select a random point where the DCO^+ abundance of the model is higher than 10^{-15} . Establishing a convergence criteria on encompassing all of the grid points is difficult. We manually set the number of iterations to 20 and confirm convergence by comparing consecutive iterations.

The resulting model cube is continuum subtracted using the first channel as a continuum estimator. Then, each spectral plane of the model is convolved with the synthesized beam of the DCO^+ data cube. This is equivalent to simulate the visibilities from a sky model since the uv -space is well sampled (see the result in Appendix 6.A).

6.3 Results

6.3.1 Standard model (CD)

We chose a standard CO abundance model with a constant abundance $X_{\text{high}}=5.0 \times 10^{-5}$ at temperatures above an evaporation temperature of $T_{\text{CO}}=19$ K. This evaporation temperature corresponds to ~ 150 AU at the midplane in our adopted temperature structure and correlates well with the second emission ring thought to be produced by the CD channel (Salinas et al. 2017). The adopted CO abundance is similar to previous models of CO isotopologues (Qi et al. 2015; Carney et al. 2017). We also include a radial cut off at 300 AU where the DCO^+ abundance drops to zero because the emission disappears at ~ 300 AU. We further discuss this value in Sec. 6.4.1.

The resulting DCO^+ $J=3-2$ emission radial profile for the standard model is shown in Fig. 6.1. The figure also shows our standard model with $T_{\text{CO}}=20$ K keeping X_{high} at the same value to illustrate the model dependency on this parameter. Note that by changing the CO abundance the model is capable of compensating the difference in evaporation temperature because these two parameters are degenerate. A higher CO abundance will produce less DCO^+ , due to the competition of reactions $\text{CO} + \text{H}_3$ and $\text{HD} + \text{H}_3^+$, and vice versa. The adopted CO abundance of 5×10^{-5} correspond to a moderate carbon depletion consistent with other warmer disks such as HD100546 (Kama et al. 2016).

We can obtain an estimate of the emission contribution from the WD channel subtracting the standard model from the data. We perform a channel by channel subtraction from the data cube and the convolved model cube to calculate a residual cube (see example in Appendix 6.A). Figure 6.3 shows the residual radial curve from the standard models with $T_{\text{CO}}=19$ K and $T_{\text{CO}}=20$ K and their correspondent abundance estimate. The residual radial profile is obtained applying a Keplerian mask (see Appendix in Salinas et al. 2017) to the residual cube and each of the radial bins correspond to concentric ellipsoids projected to be equidistant to the central star. At $R \gtrsim 180$ AU we can only provide an upper limit of about a few 10^{-12} . At $R \lesssim 180$ AU the abundance is a few 10^{-13} and starts declining at ~ 50 AU.

The radial abundance estimate is calculated assuming LTE and that the emission is optically thin. If we regard the emission as coming from an isothermal medium in LTE we can calculate the correspondent column density at different radii assuming an excitation temperature by using the analytical formula of Remijan et al. (2003). This 1D analysis was previously performed by Salinas et al. (2017) and we use the same prescription and excitation temperature profile for DCO^+ . Finally, we divide the column density estimate by the surface density profile in Eq. 6.2.3 to get a vertically averaged abundance. The radial abundance profile only provides a lower limit to the actual DCO^+ because it emits from a layer set by the activation temperature of the CD and WD channel and the CO evaporation temperature constraining its vertical extent. The simple chemical model of the CD channel

can reproduce the DCO^+ emission in the disk around HD163296 at large radii ($R > 180$ AU), but requires additional DCO^+ , of a few 10^{-12} in abundance, to account for the inner emission produced by the WD channel and a radial cut-off at ~ 300 AU.

6.3.2 Thermal inversion model (CD+TI)

The standard model uses a radial cutoff to suppress the emission of DCO^+ in the outer disk, but a thermal inversion (TI) could prevent the CD channel from being active (Cleeves 2016). Temperatures higher than the activation barrier for the CD (and WD) channel would prevent the reactions shown in Eq. 6.1a and 6.1b, reducing DCO^+ formation. A thermal inversion is produced by the dust evolution modeling of Facchini et al. (2017) as a direct consequence of grain growth and settling. Considering both processes results in a radial decrease of the scale height of the dust because the turbulence is less capable of stirring up the grains that are decoupled from the gas in regions with low density. This leads to a radial temperature drop. At larger radii, where almost all of the big grains have migrated inward, the small dust is stirred back to the disk surface, out of the shadow cast in intermediate radii, intercepting more radiation.

We modify the temperature structure of our standard model to mimic this effect using the following parametrization

$$T'(R) = 25K \left(1 - \exp \left(-\frac{R - R_1}{R_2 - R_1} \right)^2 \right) + T(R), \quad (6.5)$$

where $R_1 = 240$ AU is the inflection point at which the TI occurs and $R_2 = 300$ AU a characteristic radius. We choose these values so that the temperature at ~ 290 AU reaches >30 K and effectively blocks the CD channel. We also use a CO abundance parameter of $X_{\text{high}}=2.0 \times 10^{-7}$, keeping T_{CO} at 19 K, to better match the shape of DCO^+ at larger radii. This value is much lower than the 5×10^{-5} of the fiducial model.

The adopted simple chemical network reaches a maximum in DCO^+ production for CO abundances of 1×10^{-5} . Higher values result in lower DCO^+ abundances because the gas-phase CO abundance surpasses the assumed HD abundance blocking its reaction with H_3^+ (Eq. 6.1a). Similarly, lower values than 1×10^{-5} result in lower DCO^+ abundances because CO in the gas-phase is required for Eq. 6.2a to proceed. If the gradient of the CO abundance is steep and smaller or comparable to our resolution, we can think of the X_{high} parameter of our simple step abundance model as an effective CO abundance that accounts for the production gradient of DCO^+ . The thermal inversion parametrization region in our model has a steep temperature gradient that results in a steep second desorption front of CO in the midplane, at ~ 240 -300 AU, comparable in size to our resolution. Our preferred value of $X_{\text{high}}=2.0 \times 10^{-7}$ is an effective CO abundance that reproduces the DCO^+ emission for such a steep gradient.

The first CO desorption front occurs much further in. Our CD+TI model places this desorption front at about ~ 150 AU, corresponding to a temperature of ~ 19 K in our adopted model, where the CO starts to evaporate with modest abundances of $\sim 2 \times 10^{-7}$. Observations of C^{18}O and N_2H^+ place the CO snowline at ~ 90 AU (Qi et al. 2015), corresponding to a temperature of ~ 22 K in our adopted model, where the bulk of CO is released into the gas-phase with abundances of $\sim 5 \times 10^{-5}$. Coincidentally, CO abundances of $\sim 5 \times 10^{-5}$ and $\sim 2 \times 10^{-7}$ produce the same amount of DCO^+ at temperatures where the CD channel operates. This explains why in Sec.6.3.1 the CD model reproduces the DCO^+ emission with a CO abundance of $\sim 5 \times 10^{-5}$ and a desorption front at ~ 150 AU. We find that to reconcile the CO snowline location at 90 AU, with an abundance of 5×10^{-5} , and the observed DCO^+

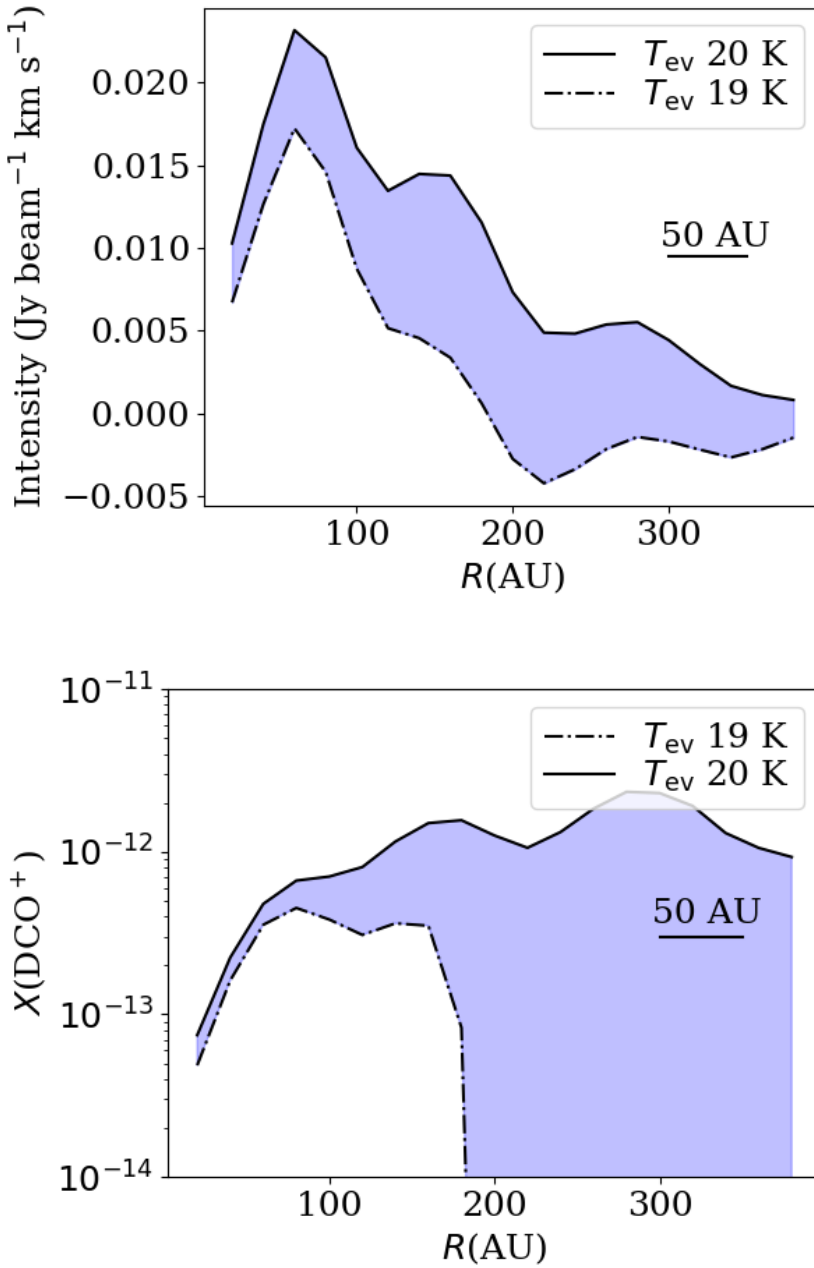


Figure 6.3: The top panel shows the residual radial profiles from the models shown in Fig. 6.1 with an evaporation temperature of CO $T_{CO}=19\text{K}-20\text{K}$ and a constant abundance $X_{in} = 5.0 \times 10^{-5}$. The bottom panel shows a vertically averaged abundance estimate of the radial curves of the top panel using the same excitation temperature profile and prescription proposed by Salinas et al. (2017) to convert emission to column densities. The 50 AU bar corresponds to the semi-minor axis of the synthesized beam and serves as a measure of the spatial resolution.

emission our CO abundance profile requires a zone between 90 AU and 150 AU with an effective abundance of 2×10^{-7} which we interpret as the onset of the thermal release of CO into the gas-phase.

The resulting DCO⁺ abundance, gas density and emission profile are shown in the middle panels of Fig. 6.4. DCO⁺ is confined between 30 K and 19 K, corresponding to the temperature where the CD channel starts to be efficient and to the temperature where CO freeze out passes 99% respectively. The DCO⁺ abundance increases radially as a consequence of the radial increase of the ionization fraction which is $\propto \frac{1}{\sqrt{n}}$ if the ionization rate ζ is constant. The thermal inversion parametrization of this model, coupled with the simple chemical network for CD channel, can reproduce the radial shape of the DCO⁺ in the disk around HD163296 at $R > 180$ AU and the lack of emission at $R > 300$ AU.

6.3.3 The CD+WD+TI model

Finally, we add a WD channel component to our CD+TI model by modifying the obtained DCO⁺ abundance in the following parametrization

$$X_{\text{DCO}^+}(r, t) = \begin{cases} X_{\text{CD+TI}}(r, t) + X_{\text{WD}} & \text{if } T(r, t) \leq T_{\text{eff}} \\ X_{\text{CD+TI}}(r, t) & \text{if } T(r, t) > T_{\text{eff}} \end{cases}, \quad (6.6)$$

where X_{WD} is a constant abundance parameter describing the WD channel contribution and T_{eff} the effective temperature for the WD channel at which the the WD channel switches on. The T_{eff} is not the temperature where WD starts to operate (which is 80 K), but rather where reaches its full effectiveness. Just like the CD channel, the WD channel does not switch on abruptly, but gradually increases toward lower temperatures. The right column of Fig. 6.4 show the modified DCO⁺ abundance, temperature and emission profile of the CD+WD+TI model using $X_{\text{WD}} = 3.2 \times 10^{-12}$ and $T_{\text{eff}} = 32$ K and the parameters from the CD+TI model. These values are taken to match the inner DCO⁺ emission at $R \lesssim 150$ AU. Note that the parameter $T_{\text{eff}} = 32$ K is tracing the location of an effective isothermal surface where WD starts to operate. This location is effectively constrained from the data and corresponds to ~ 40 AU in the midplane. The exact value of the parameter T_{eff} cannot be constrained without a gas temperature model and only represents the location of the isothermal surface. On the other hand, the X_{WD} parameter is much better constrained by our modelling because it does not depend strongly on the assumed gas temperature. The CD+WD+TI model reproduces simultaneously the inner and outer features of the DCO⁺ radial profile. The residual (and model) channel maps can be seen in Appendix 6.A.

For comparison, the left column of Fig. 6.4 shows the DCO⁺ abundance, temperature and emission profile of model CD. The emission profile of model CD does not include the radial cut off of our standard model. This radial cut off is shown as a hatched region in the DCO⁺ abundance profile of model CD. Without reducing the amount DCO⁺ at larger radii the CD channel alone overproduces the observed emission. The CD+WD+TI model effectively reproduces the DCO⁺ radial emission profile, at large and small radii, of the disk around HD163296 including the lack of emission at $R > 300$ AU.

6.4 Discussion

6.4.1 DCO⁺ Outer radius

Our standard model uses a radial cutoff in the DCO⁺ abundance to reproduce the absence in DCO⁺ emission at $R \gtrsim 300$ AU. In this section we discuss several possibilities to explain

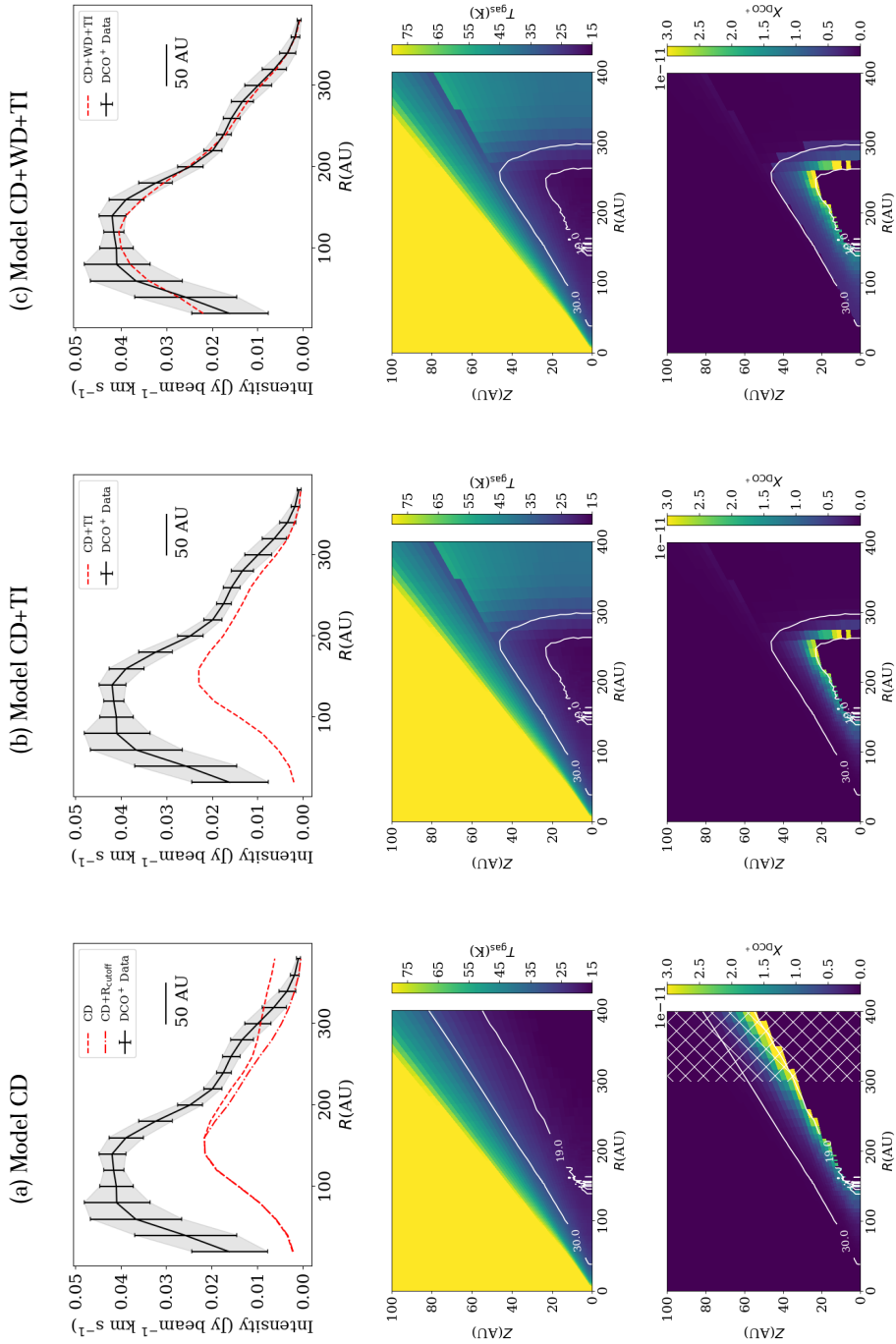


Figure 6.4: The top panels show the resulting radial profile of the DCO⁺ integrated intensity map of both models and data. The error bars on the data corresponds to 3σ , where σ is calculated as the standard deviation of a single ellipsoid divided by the square root of the number of beams. The middle panels show the models' temperature profile with contours at 19 and 30 K. The bottom panel shows the DCO⁺ abundance profile over-plotted with temperature contours at 19 and 30 K. The hatched region in the DCO⁺ abundance from model CD marks the radial cut off used in our standard model to reproduce the absence of emission at $R > 300$ AU.

such a drop, namely: a drop in total gas density, a local increase in the o/p ratio of H_2 , photodesorption or thermal desorption of CO and photodissociation.

First, the emission drop could be the consequence of a drop in total gas density. Observations of CO isotopologues at very high angular resolution (Isella et al. 2016) show that the ^{12}CO , ^{13}CO and C^{18}O emission abruptly diminish at different radii; ~ 630 AU, ~ 510 AU and ~ 360 AU respectively. If C^{18}O (the least abundant CO isotopologue) is tracing the total gas density, the radial cutoff of DCO^+ might be due to a lack of total gas density at a similar radius at which the C^{18}O emission drops. However, isotope selective dissociation of C^{18}O is a more likely explanation of its drop off at 360 AU (Miotello et al. 2014; Visser et al. 2009). If we adopt a plausible model of the CO column density profile, such as the one obtained by Facchini et al. (2017) (left panel of their Fig.8), the column density of C^{18}O at $R \gtrsim 360$ AU is not high enough to self-shield from UV radiation assuming the canonical ISM $\text{C}^{18}\text{O}/^{12}\text{CO}$ ratio of 550. This would be consistent with the different radii at which the emission of ^{12}CO , ^{13}CO and C^{18}O drop. It is therefore unlikely that the drop off of DCO^+ is due to an overall drop in gas surface density.

A second explanation comes from the difference in the zero-point energies of ortho and para H_2 . Since o- H_2 has more energy than p- H_2 , the endothermic reaction that introduces deuterium via the latter has a lower energy barrier than the former, enhancing the deuterium fractionation more efficiently at cold temperatures for a thermal o/p ratio of H_2 . This means that a local increase in the o/p ratio of H_2 could result in a drop of DCO^+ abundance. However, it is unclear why H_2 would have a spin temperature much higher (80 K) than the region where DCO^+ forms (< 30 K).

Thirdly, desorption of CO at large radii, either thermally or through photodesorption, can raise the CO abundance above the value where the formation of DCO^+ is quenched. The distinctive feature at ~ 260 AU, where the DCO^+ emission shows a 'bump', is a natural consequence of this. Both in a model with a thermal inversion and in a model with increased photodesorption through increased UV penetration, the layer of DCO^+ folds back to the midplane. Increased excitation and column density lead to a maximum in emission. The presence of this 'bump', in our data, therefore strongly supports this scenario. Small scale structures in CO abundance, gas temperature or H_2 o/p ratio could also produce the observed emission excess at 250 AU, but not as naturally as a thermal inversion. An extreme case of this scenario can also explain the DCO^+ emission rings seen in other disks such as IM Lup (Öberg et al. 2015). If the inflection point of the temperature profile occurs at large heights, at low gas densities, the emission could hide below the noise level and come back again at larger radii where the DCO^+ comes back to the midplane. This would give the illusion of two DCO^+ rings at low sensitivities.

The shape of our modified temperature profile resembles qualitatively the models of Facchini et al. (2017) but their results are heavily model dependent, in particular to the turbulent parameter α . The thermal inversion effect is most pronounced at lower alpha parameters (10^{-3} - 10^{-4}). The temperature inversion in these models is smoother than our proposed parametrization. The CO ice in their models is confined from ~ 200 to ~ 400 AU, with $\alpha = 10^{-4}$, whereas our models confine CO ice from ~ 150 AU to ~ 260 AU. A different temperature structure with a slightly hotter disk could also shape the CO ice region differently. Our constraining CD+WD+TI model applied to the DCO^+ data reveals the location of the thermal inversion and the temperature structure at large radii.

Instead of thermal desorption, photodesorption of CO by increased UV penetration can yield a similar cutoff to the DCO^+ emission profile. This has been invoked for the DCO^+ ring seen in IM Lup and full chemical models, of typical disks around T Tauri stars, show that this is a plausible scenario (Öberg et al. 2015). Our modeling cannot distinguish this

from thermal desorption. Additional observations are needed, either constraining the temperature (e.g via multiple transitions of the rotational lines of optically thin species such as H_2CO (Carney et al. 2017)), or through UV tracers and/or modeling of the dust. Both thermal and photodesorption could be occurring, potentially creating even more complex structures.

Finally, a higher electron density at radii $R > 300$ AU cannot significantly destroy DCO^+ resulting in the observed absence of emission. If no thermal inversion is invoked and CO remains in the gas-phase above 19 K (model CD), the required ionization rate to completely quench the DCO^+ production at $R > 300$ AU is at least 8 orders of magnitude higher than the assumed canonical value of $1.36 \times 10^{-17} \text{ s}^{-1}$. This implies an electron abundance of a few 10^{-4} much higher than expected for the warm molecular layer.

6.4.2 Low vs high temperature deuteration pathways

Our preferred CD+WD+TI model uses a constant abundance $X_{\text{WD}} = 3.2 \times 10^{-12}$ and an effective temperature of $T_{\text{eff}} = 32$ K to parametrize the contribution and onset of the WD channel. From Fig. 6.4 the abundance of model CD is about 1.2×10^{-11} at larger radii corresponding to a ratio between the DCO^+ column densities produced by the WD and the CD channel of 0.2. This ratio agrees well with the detailed chemical modeling of Favre et al. (2015) which is on average about 0.25 outside the CO snowline. Since the amount of DCO^+ produced by the CD channel depends on the CO abundance, an appropriate CO gradient can maximize the DCO^+ produced via the CD channel and minimize the contribution of the WD channel to $\sim 10\%$. This limit is only slightly lower than the 20% found by our CD+WD+TI model, which is therefore a robust number. The adopted T_{eff} , where the WD channel is fully operative, is effectively defined by the innermost drop off of the DCO^+ emission. Provided that the contribution of the WD channel can be constrained, DCO^+ can trace the temperature structure and CO snowline of a protoplanetary disk through their CD channel formation pathway.

6.5 Summary

In this work, we implemented a simple chemical network for cold deuteration and a parametrized treatment of warm deuteration, and carry out a 2D modeling of the DCO^+ emission in the disk around HD163296. The following points summarize the conclusions of this work:

- We found that a simple chemical model of the CD channel using a CO constant abundance of 2.0×10^{-7} , above an effective dust temperature of 19 K where CO starts to evaporate, coupled with thermal inversion at around ~ 260 AU can reproduce the DCO^+ emission in the outer regions of the disk surrounding HD163296.
- In addition, modeling the contribution of the WD channel with constant abundance of 3.2×10^{-12} and an effective temperature of 32 K, describing an isothermal surface corresponding to a midplane radius of ~ 40 AU, reproduces the DCO^+ emission in the inner disk where the CD channel is not yet active. The ratio of the amount of DCO^+ produced by the WD and CD channels outside the CO snowline in this model is 0.2, consistent with previous full chemical models of DCO^+ .
- With the CD channel tracing the CO abundance at 2.0×10^{-7} for radii < 150 AU, DCO^+ is a tracer of the onset of CO evaporation. The bulk of the evaporation of CO occurs

at radii < 90 AU, where temperatures are too high for the CD channel to be efficient. This opens possibilities to probe the binding energy of CO ice and its evaporation process.

- We conclude that the formation and destruction mechanisms of DCO^+ are very temperature sensitive, both through the efficiency of the CD channel and the CO abundance. With proper treatment of the DCO^+ production through the WD channel, DCO^+ can be used as tracer of the location of the CO snowline and the temperature structure, and specifically its gradient, at the outer disk.

Acknowledgements. The authors acknowledge support by Allegro, the European ALMA Regional Center node in The Netherlands, and expert advice from Luke Maud in particular. We also thank Prof. Karin Öberg and Dr. Stefano Facchini for their very useful discussions that helped improve this paper. This work was partially supported by grants from the Netherlands Organization for Scientific Research (NWO) and the Netherlands Research School for Astronomy (NOVA). This paper makes use of the following ALMA data: ADS/JAO.ALMA# 2013.1.01268.S. ALMA is a partnership of ESO (representing its member states), NSF (USA) and NINS (Japan), together with NRC (Canada), NSC and ASIAA (Taiwan), and KASI (Republic of Korea), in cooperation with the Republic of Chile. The Joint ALMA Observatory is operated by ESO, AUI/NRAO and NAOJ.

6.A Residual channel maps

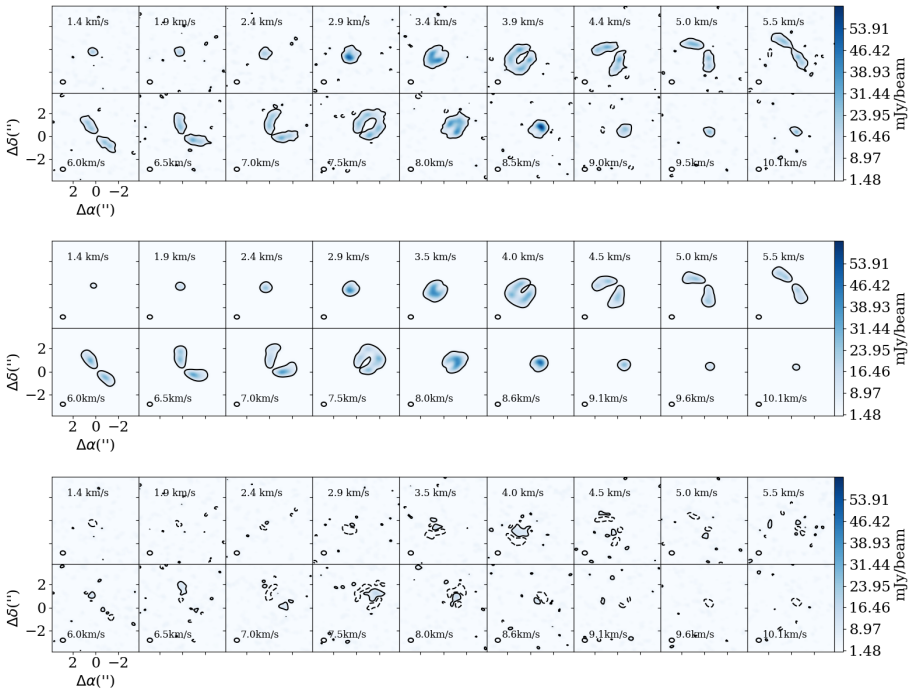


Figure 6.5: Top panel shows the $\text{DCO}^+ J=3-2$ data channel maps. The middle panel map shows the CD+WD+TI model. The bottom panel shows the residual channels. Contours are 3σ , where σ corresponds to the standard deviation of a line free channel. The channel maps presented here are binned in velocity to enhance signal to noise.

Bibliography

Albertsson, T., Semenov, D. A., Vasyunin, A. I., Henning, T., & Herbst, E. 2013, *ApJS*, 207, 27

- Brinch, C., & Hogerheijde, M. R. 2010, *A&A*, 523, A25
- Carney, M. T., Hogerheijde, M. R., Loomis, R. A., et al. 2017, *ArXiv e-prints*, arXiv:1705.10188
- Cleeves, L. I. 2016, *ApJ*, 816, L21
- Dullemond, C. P., & Dominik, C. 2004, *A&A*, 417, 159
- Facchini, S., Birnstiel, T., Bruderer, S., & van Dishoeck, E. F. 2017, *ArXiv e-prints*, arXiv:1705.06235
- Favre, C., Bergin, E. A., Cleeves, L. I., et al. 2015, *ApJ*, 802, L23
- Flower, D. R. 1999, *MNRAS*, 305, 651
- Gerner, T., Shirley, Y. L., Beuther, H., et al. 2015, *A&A*, 579, A80
- Guilloteau, S., Piétu, V., Dutrey, A., & Guélin, M. 2006, *A&A*, 448, L5
- Huang, J., Öberg, K. I., Qi, C., et al. 2017, *ApJ*, 835, 231
- Isella, A., Guidi, G., Testi, L., et al. 2016, *Phys. Rev. Lett.*, 117, 251101
- Kama, M., Bruderer, S., van Dishoeck, E. F., et al. 2016, *A&A*, 592, A83
- Mathews, G. S., Klaassen, P. D., Juhász, A., et al. 2013, *A&A*, 557, A132
- Millar, T. J., Bennett, A., & Herbst, E. 1989, *ApJ*, 340, 906
- Miotello, A., Bruderer, S., & van Dishoeck, E. F. 2014, *A&A*, 572, A96
- Murillo, N. M., Bruderer, S., van Dishoeck, E. F., et al. 2015, *A&A*, 579, A114
- Öberg, K. I., Boogert, A. C. A., Pontoppidan, K. M., et al. 2011, *ApJ*, 740, 109
- Öberg, K. I., Furuya, K., Loomis, R., et al. 2015, *ApJ*, 810, 112
- Öberg, K. I., Qi, C., Fogel, J. K. J., et al. 2010, *ApJ*, 720, 480
- Qi, C., D'Alessio, P., Öberg, K. I., et al. 2011, *ApJ*, 740, 84
- Qi, C., Öberg, K. I., Andrews, S. M., et al. 2015, *ApJ*, 813, 128
- Qi, C., Wilner, D. J., Aikawa, Y., Blake, G. A., & Hogerheijde, M. R. 2008, *ApJ*, 681, 1396
- Qi, C., Öberg, K. I., Wilner, D. J., et al. 2013, *Science*, 341, 630
- Remijan, A., Snyder, L. E., Friedel, D. N., Liu, S.-Y., & Shah, R. Y. 2003, *ApJ*, 590, 314
- Roueff, E., Gerin, M., Lis, D. C., et al. 2013, *Journal of Physical Chemistry A*, 117, 9959
- Salinas, V., Hogerheijde, M., Mathews, G., et al. 2017, *In Prepr.*
- Schöier, F. L., van der Tak, F. F. S., van Dishoeck, E. F., & Black, J. H. 2005, *A&A*, 432, 369
- Teague, R., Semenov, D., Guilloteau, S., et al. 2015, *A&A*, 574, A137
- Turner, B. E. 2001, *ApJS*, 136, 579
- van den Ancker, M. E., de Winter, D., & Tjin A Djie, H. R. E. 1998, *A&A*, 330, 145
- van Dishoeck, E. F., Thi, W.-F., & van Zadelhoff, G.-J. 2003, *A&A*, 400, L1
- Vidal-Madjar, A. 1991, *Advances in Space Research*, 11, 97
- Visser, R., van Dishoeck, E. F., & Black, J. H. 2009, *A&A*, 503, 323
- Watson, W. D. 1976, *Reviews of Modern Physics*, 48, 513
- Willacy, K. 2007, *ApJ*, 660, 441
- Wooten, A. 1987, in *IAU Symposium, Vol. 120, Astrochemistry*, ed. M. S. Vardya & S. P. Tarafdar, 311–318
- Yen, H.-W., Koch, P. M., Liu, H. B., et al. 2016, *ApJ*, 832, 204

Samenvatting

De mensheid heeft zich altijd vragen gesteld over zijn oorsprong en plaats in het universum. Onze voorouders keerden zich naar de hemel en zochten naar antwoorden in de sterren. Talloze mythen en legendes zijn doorgedrongen in de grote beschavingen uit het verleden en dienden als een verklaring voor fundamentele vragen over de oorsprong van het universum en de mensheid. Het is pas sinds kort dat de moderne astrofysica geprobeerd heeft om met rationeel denken de oorsprong van de aarde en het leven in het zonnestelsel te verklaren.

De meest geaccepteerde ster- en planeetvormings-theorie begint met een moleculaire wolk van gas en stof, die massief genoeg is om onder zijn eigen zwaartekracht ineen te storten. Tijdens dit proces ontstaat er een schijf, omdat materiaal dat van verder weg komt een meer rotatie heeft (of hoekmoment, zoals natuurkundigen dit noemen). Deze schijf is oorspronkelijk ingesloten in een omhulsel van gas en stof. Na ~ 0.5 miljoen jaar wordt de envelop weggeblazen door uitstromen, die worden aangedreven door de centrale ster. Deze uitstromen openen een holte uit het omhulsel en laten een schijf achter. Er wordt gedacht dat planeten zich vormen in deze circumstellaire schijven, die daarom de naam protoplanetaire schijven dragen. Deze schijven zijn ontdekt rond vele jonge sterren in verschillende evolutionaire stadia met zeer verschillende fysische en chemische eigenschappen.

Het gas- en stofgehalte van protoplanetaire schijven kan worden onderzocht met behulp van waarnemingen van spectrale lijnen van moleculen in de gasfase en waarnemingen van de thermische straling die wordt uitgestraald door het stof, wat een continuüm-spectrum oplevert. Tijdens zijn typische levensduur van ~ 10 Myrs ondergaat de schijf vele dynamische processen die zijn structuur veranderen, wat uiteindelijk leidt tot de vorming van planeten en de dissipatie van het gas. Bovendien vertonen protoplanetaire schijven een rijke chemie die voornamelijk wordt aangedreven door ultraviolette- en röntgenstraling en die intrinsiek kan worden verbonden met de fysische evolutie van de componenten van de schijf (zie Fig.7.1). Het doel van dit proefschrift is om een verklaring te geven voor de waargenomen morfologie van de emissie van belangrijkste stikstof-, zuurstof- en koolstofhoudende moleculaire soorten door ze te vergelijken met de morfologie van het dichtheidsprofiel van het stof. Het doel van dit proefschrift is om antwoord te vinden op de volgende twee vragen:

- Waar zitten de belangrijkste zuurstof- en stikstofhoudende soorten, namelijk water en ammoniak, in planeetvormende schijven?
- Hoe verhouden fysische structuren, zoals temperatuurgradiënten en substructuren in de dichtheid van het stof veroorzaakt door stofevolutieprocessen, zich tot de vorming en chemie van veelvoorkomende moleculen?

Dit proefschrift

Hoofdstuk 1 van dit proefschrift geeft een algemene inleiding van stervormingstheorie en protoplanetaire schijven, met de nadruk op de evolutie van het stof en de verschillende chemische regimes binnen deze schijven. De analyse is gericht op twee goed bestudeerde protoplanetaire schijven, TW Hya en HD163296. Beide schijven zijn uitstekende laboratoria vanwege hun nabijheid en hun enorm zware en heldere schijven. In dit proefschrift worden zowel infraroodwaarnemingen van de *Herschel Space Telescope* als (sub)millimeter waarnemingen van de Atacama Large Millimeter Array (ALMA) gebruikt. *Herschel* was uitgerust met een enkele spiegel van 3.5 m doorsnede en had drie instrumenten die bij elkaar een golflengte-bereik hadden tussen $\sim 50 \mu\text{m}$ en $\sim 600 \mu\text{m}$. Gegevens uit het waarnemingsprogramma "Water in stervormingsregio's met *Herschel*" (WISH), genomen met het HIFI-instrument aan boord van *Herschel*, werden in dit werk gebruikt. ALMA is een radiotelescoop bestaande uit zesenzestig antennes met een ongekeerd ruimtelijk oplossend vermogen en gevoeligheid. Voor onze twee bronnen zijn met ALMA zowel continuüm emissie als moleculairelijn emissie waargenomen, die worden gepresenteerd in dit proefschrift.

In Hoofdstuk 2 worden ALMA-waarnemingen op een golflengte van 1.3 mm gebruikt om te onderzoeken waar stofdeeltjes van ongeveer 1 mm groot zich in de schijf rond TW Hya bevinden. In planeetvormende schijven klonteren kleine stofdeeltjes ($\sim \mu\text{m}$) samen en groeien uit tot grotere stofdeeltjes (mm, cm en groter) om uiteindelijk planeten te vormen. Terwijl stofdeeltjes van μm -formaat goed aan het gas zijn gekoppeld, zullen grotere stofdeeltjes naar binnen bewegen als gevolg van de wrijving met het gas. De waarnemingen laten zien dat de mm-formaat stofdeeltjes voorkomen tot $\sim 47 \text{ AU}$ vanaf de ster, waarna

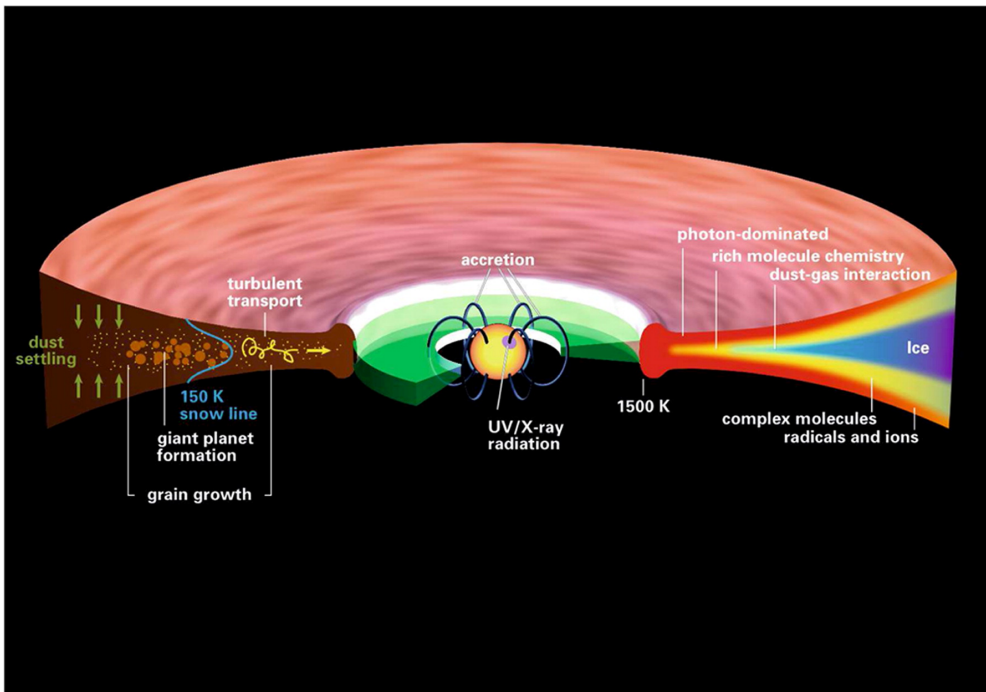


Figure 7.1: Cartoon van stofevolutie en chemische gebieden in de schijf. Figuur uit Henning & Semenov (2013).

hoeveelheid van deze deeltjes snel daalt. Een dergelijke sterke daling wordt voorspeld door theoretische berekeningen van de samenklontering van stofdeeltjes en hun transport door de schijf. Voor typische realistische stofevolutiemodellen van T Tauri-schijven zijn de waargenomen omvang van deze stofdeeltjes en hun totale hoeveelheid echter te groot voor een schijf van 8-10 Myrs. Mogelijke verklaringen hiervoor zijn een veel hogere initiële schijfgrootte en -massa, een gat in de stofdichtheid, geopend door een tot nu toe nog niet waargenomen planeet, die de radiële migratie van het mm-formaat stof stopt of een lokale overproductie van mm-stofdeeltjes tegenhoudt, geholpen door de aanwezigheid van ijzige stofdeeltjes in gebieden waar CO is bevroren, die efficiënter groeien dan kale stofdeeltjes.

Hoofdstuk 3 presenteert de allereerste detectie van ammoniak in een planeetvormende schijf. De $o\text{-NH}_3$ $1_0\text{-}0_0$ overgang werd waargenomen met het HIFI-instrument aan boord van *Herschel* samen met emissielijnen van $o\text{-H}_2\text{O}$ en $p\text{-H}_2\text{O}$ in TW Hya. Er worden vier verschillende modellen voor de verdeling van deze moleculen onderzocht, ervan uitgaande dat water en ammoniak gemengd zijn en dat ze tegelijkertijd aan de gasfase worden afgegeven. Alleen de meest radieel en verticaal compacte verdeling van zowel water als ammoniak in de gasfase, die volgt uit de omvang van de emissie van het mm-stof ($r \leq 60$ AU), is consistent met de ammoniak-waterverhouding ($\sim 5\%$ - 10%) gevonden in het interstellaire medium en objecten in het zonnestelsel. Andere configuraties die verder uitgestrekt zijn in de radiële of verticale richting kunnen alleen in overeenstemming worden gebracht met de waarden van de interstellaire medium en het zonnestelsel als extra formatieroutes van ammoniak worden toegevoegd. Het afgeleide reservoir van ammoniak en water in de gasfase in elk van deze modellen is slechts een klein deel van het geschatte totale reservoir, wat aangeeft dat het grootste deel van deze moleculen is opgesloten in het ijs.

Verwacht wordt dat het koude gas reservoir van planeetvormende schijven een grote hoeveelheid deuterium-dragende moleculen zoals NH_2D bevat. Hoofdstuk 4 analyseert zowel *Herschel* waarnemingen van de $o\text{-NH}_3$ $1_0\text{-}0_0$ overgang en ALMA-waarnemingen van de $p\text{-NH}_2\text{D}$ $1_0\text{-}0_0$ overgang voor de schijf rond HD 163296. Beide overgangen werden niet gedetecteerd vanwege de bescheiden integratietijden. Dit hoofdstuk onderzoekt twee verschillende radiële verdelingen van het $o\text{-NH}_3$ en $p\text{-NH}_2\text{D}$ gas om limieten te stellen aan hun de sterktes van hun lijnmissie en op hun totale massa. De bovengrenzen die zijn afgeleid voor de totale massa van het $o\text{-NH}_3$ en $p\text{-NH}_2\text{D}$ gas voor deze schijf zijn tien keer lager die voor de ongeveer even zware schijf van TW Hya, wanneer deze waardes worden uitgerekend in hoofdstuk 3 voor het best werkende model gebruik makende van een $\text{NH}_3/\text{NH}_2\text{D}$ -ratio van 10%. Dit suggereert dat de schijf rond HD 163296 NH_3 -arm is met ten minste een factor 5 in vergelijking met de schijf rond TW Hya. Andere stikstofhoudende moleculen gedetecteerd in de richting van deze schijven vertonen verschillende relatieve verhoudingen die niet overeen komen met die voor ammoniak. Dit suggereert dat het gevonden verschil in de totale hoeveelheid $o\text{-NH}_3$ gas tussen deze schijven te wijten is een verschil in de formatie van ammoniak en niet aan een verschil in de totale hoeveelheid stikstof tussen deze twee schijven.

De focus van Hoofdstuk 5 is de analyse en radiële karakterisatie van drie eenvoudige gedeutereerde moleculen in een planeetvormende schijf. DCO^+ , DCN en N_2D^+ werden waargenomen en gedetecteerd in Band 6 met ALMA voor de schijf rond HD 163296. Dit hoofdstuk vertaalt het radiële emissieprofiel van deze drie moleculen naar radiële dichtheden onder simpele aannames. De DCO^+ radiële emissie kan worden gereproduceerd door een model met drie opeenvolgende radiële gebieden en verschillende constante abundanties tussen ~ 50 AU en ~ 316 AU met twee radiële sprongen bij ~ 118 AU en ~ 245 AU. De eerste twee radiële gebieden van het best passende model van de DCO^+ -emissie correleren ruimtelijk met de best passende modellen die de radiële emissieprofielen van DCN en

N_2D^+ beschrijven. Dit kan worden geïnterpreteerd als een weerspiegeling van het feit dat er verschillende manieren zijn om deuterium in de chemie te injecteren. Eén route werkt alleen bij de laagste temperaturen en produceert N_2D^+ ; een andere werkt op iets hogere temperaturen en produceert DCN. DCO^+ vormt zich via beide routes. De oorsprong van de derde regio van DCO^+ -emissie bij ~ 260 AU is onbekend, maar het zou kunnen wijzen op een hogere temperatuur in dit gebied die er voor zorgt dat CO op deze grote radiële afstand van de ster sublimiert waarna het kan reageren om DCO^+ te vormen.

Hoofdstuk 6 probeert de waargenomen DCO^+ -emissie te reproduceren die wordt gepresenteerd in Hoofdstuk 5 met behulp van een meer verfijnd, maar nog steeds eenvoudig netwerk van chemische reacties voor de vorming van DCO^+ in koude omgevingen en een parametrisch model voor de vorming van DCO^+ in warmere omgevingen. De DCO^+ -emissie wordt gereproduceerd door een model met zowel een CO-abondantie van 2×10^{-7} in regio's waar de gastemperatuur hoger is dan 19 K als een bijdrage van 20% van de warme vormingsroute in gebieden waar beide formatieroutes actief zijn. Op grotere radiële afstanden kunnen de waargenomen grootte en vorm van de DCO^+ -emissie worden gereproduceerd door een temperatuurgradiënt te gebruiken die lijkt op de temperatuurgradiënt die wordt voorspeld door modellen van de evolutie van stofdeeltjes in de aanwezigheid van radiaal binnenwaartse migratie van mm-formaat stofdeeltjes.

Algemene conclusies

De analyse gepresenteerd in Hoofdstukken 3 en 4 geeft een antwoord op de eerste vraag die dit proefschrift probeerde te beantwoorden. Het water en ammoniak gas in TW Hya volgt de locatie van het bevroren water en ammoniak reservoir dat is gevangen in grotere stofdeeltjes en planetoïden die zijn neergedaald en naar binnen zijn getransporteerd. De locatie van dit reservoir wordt bepaald door de radiële inwaartse beweging van stofdeeltjes die enige groei hebben ondergaan en vervolgens zijn opgenomen in grotere rotsen. Dit scenario kan worden bevestigd door NH_2D en HDO te observeren in de richting van TW Hya en HD 163296. Hoofdstukken 5 & 6 trekken conclusies over het effect van fysieke structuren op de verdeling van eenvoudige moleculen. Temperatuurgevoelige soorten, zoals DCO^+ , kunnen substructuren volgen in het temperatuurprofiel van planeetvormende schijven. Hoewel de belangrijkste factor in de temperatuurstructuur van de schijf de verwarming door de centrale ster is, wijzigen substructuren als gevolg van stofgroei, en het neerdalen en de inwaartse beweging van stofdeeltjes de temperaturen. Moleculen als DCO^+ kunnen worden gebruikt om indirect de invloed van stofgrootte op de morfologie van de schijf te achterhalen. Het omgekeerde proces, dat wil zeggen de invloed van de locatie van eenvoudige moleculen op de evolutie van stof, wordt onderzocht in hoofdstuk 2 en kan worden bestudeerd door de vorm van de millimetercontinuümemissie en de locatie van de sneeuwlijn van de belangrijkste moleculaire soorten zoals CO met elkaar te vergelijken. Nieuwe instrumenten voor infrarood- en zichtbaar licht in faciliteiten zoals de toekomstige James Webb Space Telescope (JWST) of de Extremely Large Telescope (ELT) zullen in staat zijn om belangrijke moleculen waar te nemen in de warme omgevingen van de schijf, ijseigenschappen af te leiden en opgeloste afbeeldingen te maken van het door klein stof weerkaatste sterlicht. Dit stelt ons in staat om de verschillende scenario's te onderscheiden die in dit proefschrift worden onderzocht. Grootschalige systematische onderzoeken van planeetvormende schijven zouden de verschillen tussen individuele objecten helpen wegnemen en de algemene trends in hun structuur en evolutie naar voor brengen, wat zal leiden tot een beter begrip van de processen van planeet- en stervorming.

English Summary

Humanity has always wondered about its origin and place in the Universe. Our ancestors turned to the skies and searched for answers in the stars. Countless myths and legends have permeated across the great civilizations of the past and served as an explanation to fundamental questions about the origin of the Universe and humankind. It has been only recently that modern astrophysics tried to employ rational thinking to explain the origin of Earth and life within the Solar System.

The most widely accepted star (and planet) formation theory starts with a gravitationally unstable molecular cloud of gas and dust. As the cloud collapses under its own gravity, a disk quickly forms as more distant material falls in with larger amounts of rotation (or angular momentum, as physicists call this). This disk is initially embedded in an envelope of gas and dust. After ~ 0.5 Myr the envelope is cleared out by outflows, driven by the central star, that pierce a cavity within the envelope and leave behind a disk. It is in this circumstellar disk where planets are thought to be formed, thus bearing the name of protoplanetary disks. These disks have been detected around many young stars at different evolutionary stages with very different physical and chemical properties.

The gas and dust content of protoplanetary disks can be probed by observing spectral lines from molecules in the gas-phase and the thermal radiation emitted by the dust resulting in a continuum spectrum. During their typical life span of ~ 10 Myrs the disk undergoes many dynamical processes that transform its structure, eventually leading to the formation of planets and the dissipation of the gas. In addition, protoplanetary disks exhibit rich chemistry mainly driven by ultraviolet and X-ray radiation that may be intrinsically connected to the physical evolution of the disk components (see Fig.8.1). The aim of this thesis is to provide an explanation for the observed morphology of the emission of major nitrogen-, oxygen- and carbon-bearing molecular species by comparing them to the morphology of the dust density profile. In particular, this thesis sets to answer two questions:

- Where are the main oxygen- and nitrogen-bearing species, namely water and ammonia, located within planet-forming disks?
- How do physical structures, such as temperature gradients and substructures in the density of the dust caused by grain evolution processes, relate to the formation and chemistry of common molecular species?

This Thesis

Chapter 1 of this thesis gives an overall introduction of star formation theory and protoplanetary disks with an emphasis on the dust evolution process and the different chemical regimes within disks. The analysis is focused on two well-studied protoplanetary disks,

TW Hya and HD163296. Both disks are excellent laboratories because of their proximity and their massive and bright disks. This thesis uses both infrared data from the *Herschel Space Telescope* and (sub)millimeter data from the Atacama Large Millimeter Array (ALMA). *Herschel* was equipped with a 3.5 m single mirror and had three instruments that covered wavelengths ranging from $\sim 50 \mu\text{m}$ to $\sim 600 \mu\text{m}$. Data from the key program "Water In Star-forming regions with *Herschel*" (WISH), taken with the HIFI instrument on board *Herschel* were used in this work. ALMA is a radio telescope consisting of sixty six antennas with unprecedented spatial resolution and sensitivity that was used to observe both the continuum and line molecular emission presented in this thesis toward our sources.

In Chapter 2, ALMA observations at a wavelength of 1.3 mm are used to investigate where grains of about 1 mm in size are located in the disk around TW Hya. In planet forming disks, small grains ($\sim \mu\text{m}$) stick together and grow into larger grains (mm, cm, and beyond) to ultimately form planets. While μm -sized grains are well coupled to the gas, larger grains will drift inward due to the friction with the gas. The observations show that the mm-sized grains are found out to ~ 47 AU from the star, after which their amount rapidly drops. Such a steep drop is predicted by theoretical calculations of grain growth and their transport in the disk. However, for typical realistic dust evolution models of T Tauri disks, the observed extent of the grains and their total amount are too large for a disk of 8-10 Myrs. Possible explanations for this include a much higher initial disk size and mass, a dust density gap stopping the radial migration of the mm-sized dust opened by an unseen planet companion or a local overproduction of mm-sized grains aided by the presence of icy grains in regions where CO is frozen out that grow more efficiently than

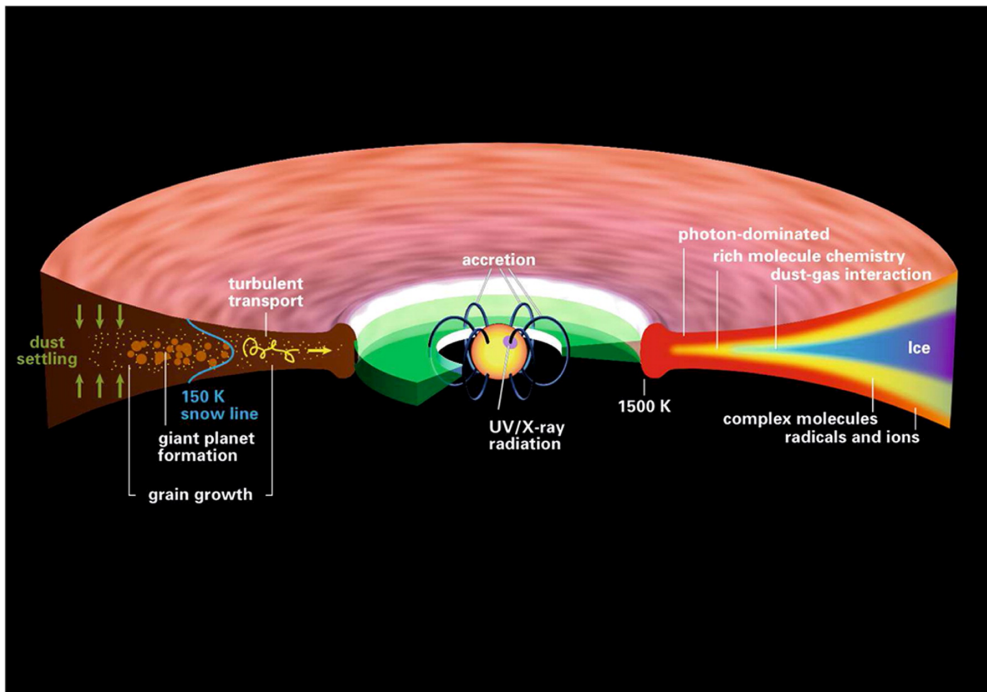


Figure 8.1: Cartoon of dust evolution and chemical regions in the disk. Figure from Henning & Semenov (2013).

bare dust grains.

Chapter 3 presents the very first detection of ammonia toward a planet forming disk. The o-NH_3 1_0-0_0 line was observed with the HIFI instrument on board *Herschel* together with emission lines of $\text{o-H}_2\text{O}$ and $\text{p-H}_2\text{O}$ in TW Hya. Four different models for the distribution of these molecules are explored assuming that water and ammonia ices are intermixed and released to the gas-phase simultaneously. Only the most compact and settled distribution of both water and ammonia in the gas-phase, following the millimeter continuum emission radial extent of $r \lesssim 60$ AU, is consistent with the ammonia to water ratio found in the gas between the stars of our galaxy and Solar System bodies of $\sim 5\%$ - 10% . Other configurations, at larger radii or heights, can only be reconciled with the interstellar and Solar System values if additional formation pathways of ammonia are invoked. The derived gas-phase reservoir of ammonia and water in any of this models is only a tiny fraction of the estimated total reservoir, indicating that most of these molecules are locked up in ices.

The cold gas environment of planet forming disks is expected to host a large amount of deuterium-bearing species such as NH_2D . Chapter 4 analyzes both *Herschel* data of the o-NH_3 1_0-0_0 line and ALMA data of the $\text{p-NH}_2\text{D}$ 1_0-0_0 line toward the disk around HD 163296. Both resulted in non-detections given their modest integration times. This chapter explores two different radial distributions of gas-phase o-NH_3 and $\text{p-NH}_2\text{D}$ to put limits on their line strengths and total masses. The upper limits derived for the total mass of gas-phase o-NH_3 and $\text{p-NH}_2\text{D}$ towards this disk are ten times lower than the values toward the similar-mass disk of TW Hya, derived in Chapter 3 for the preferred model, assuming a $\text{NH}_3/\text{NH}_2\text{D}$ ratio of 10% . This suggests that the disk around HD 163296 is NH_3 -poor by at least a factor of 5 compared to the disk around TW Hya. Other nitrogen-bearing species detected towards these disks show different relative amounts than those found for ammonia. This suggest that the difference observed in the total mass of the gas-phase o-NH_3 between these disks is due to its formation pathway and not an overall lack of elemental nitrogen.

The focus of Chapter 5 is the analysis and radial characterization of three simple deuterated species toward a planet-forming disk. DCO^+ , DCN , and N_2D^+ were observed and detected in Band 6 with ALMA toward the disk around HD 163296. This chapter translates the radial emission profile of these three molecules to radial densities under simplifying assumptions. The DCO^+ radial emission can be reproduced by a model with three consecutive radial regions and different constant abundances from ~ 50 AU to ~ 316 AU with two radial breaks at ~ 118 AU and ~ 245 AU. The first two radial regions of the best-fit model of the DCO^+ emission correlate spatially with the best-fit models describing the radial emission profiles of DCN and N_2D^+ . This can be interpreted as a reflection of the fact that there are multiple ways to inject deuterium into the chemistry. One path operates only at the lowest temperatures, and produces N_2D^+ ; another operates at slightly higher temperatures, and produces DCN . DCO^+ forms through both paths. The origin of the third region of DCO^+ emission at ~ 260 AU is unknown but it could be tracing higher temperatures allowing CO to evaporate at large radii, where it can react to form DCO^+ .

Chapter 6 tries to reproduce the observed DCO^+ emission presented in Chapter 5 using a more sophisticated, but still simple network of chemical reactions for the formation of DCO^+ in cold environments and a parametric model for its formation in warm environments. The DCO^+ emission is reproduced by a model with a CO abundance of 2×10^{-7} , in regions where the gas temperature exceeds 19 K, and a contribution from the warm environment formation of 20% in regions where both formation pathways are active. At larger radii, the extent and shape of the DCO^+ emission can be reproduced by considering a temperature gradient similar to those predicted by models of dust grain evolution in the

presence of inward radial migration of mm-sized dust grains.

Overall Conclusions

The analysis presented in Chapters 3 & 4 provides an answer to the first question this thesis sought to answer. The gas-phase water and ammonia in TW Hya follows the location of their icy reservoir trapped in larger bodies that have settled and drifted inwards. The location of this reservoir is set by the radial drift of grains that have undergone some growth, and subsequently were incorporated in larger rocks. This scenario can be confirmed by observing NH_2D and HDO toward TW Hya and HD 163296. Chapters 5 & 6 draw conclusions on the effect of physical structures on the distribution of simple molecules. Temperature-sensitive species, such as DCO^+ , can trace substructures in the temperature profile of planet-forming disks. While the most important factor in the disk's temperature structure is the illumination by the central star, substructures resulting from grain growth, settling and drift modify the temperatures. Species like DCO^+ can be used to indirectly trace the impact of grain evolution on the disk's morphology. The inverse process, i.e. the impact of the the location of simple molecules on dust evolution, is explored in Chapter 2 and can be studied by comparing the shape of the millimeter continuum emission and the location of the snowline of main molecular species such as CO. New infrared and visible light instruments in facilities such as the future James Webb Space Telescope (JWST) or the Extremely Large Telescope (ELT) will be able to observe key molecules in the warm environments of the disk, ice features and resolved scattered light emission allowing us to distinguish the different scenarios explored in this thesis. Large surveys of planet forming disks would help to average out the differences between individual sources and bring forward the general trends in their structure and evolution leading to a comprehensive understanding of the planet and star formation processes.

Resumen en Español

La humanidad se ha preguntado siempre sobre su origen y lugar en el Universo. Nuestros ancestros observaron los cielos en busca de respuestas. Incontables mitos y leyendas han permeado a través de las grandes civilizaciones del pasado, y han servido de explicación para las preguntas fundamentales sobre el origen del Universo y los seres humanos. Ha sido tan solo recientemente que la astrofísica moderna intentó emplear el pensamiento racional para explicar el origen de la Tierra y la vida dentro del Sistema Solar.

La teoría de formación estelar (y planetaria) más ampliamente aceptada comienza con una nube molecular de gas y polvo gravitacionalmente inestable. Mientras la nube colapsa bajo su propia gravedad, un disco se forma rápidamente a medida que material lejano con grandes cantidades de rotación (o momento angular, como es conocido en física) se desploma hacia el centro del sistema. Este disco está inicialmente inserto en una envoltura de gas y polvo. Luego de ~ 0.5 millones de años esta envoltura es disipada por chorros y flujos bipolares, generados por la estrella central, que crean una cavidad en la envoltura dejando atrás un disco. Es en este disco circumestelar donde los planetas se forman, llevando así el nombre de disco protoplanetario. Estos discos han sido descubiertos alrededor de muchas estrellas jóvenes en distintas etapas evolutivas con propiedades físicas y químicas muy diferentes.

El contenido de gas y polvo de los discos protoplanetarios puede explorarse observando las líneas espectrales de las moléculas en estado gaseoso y la radiación térmica emitida por el polvo, lo que da como resultado un espectro continuo. Durante su tiempo de vida típico de ~ 10 millones de años, el disco se somete a muchos procesos dinámicos que transforman su estructura, conduciendo eventualmente a la formación de planetas y a la disipación de su contenido gaseoso. Adicionalmente, los discos protoplanetarios presentan una química diversa impulsada principalmente por la radiación ultravioleta y de rayos X que puede estar intrínsecamente conectada a la evolución física de los componentes del disco (ver Fig.9.1). El objetivo de esta tesis es proporcionar una explicación para la morfología que se observa en la emisión de especies moleculares portadoras de nitrógeno, oxígeno y carbono mediante su comparación con la morfología del perfil de densidad del polvo. En particular, esta tesis busca responder dos preguntas:

- ¿Dónde están ubicadas las principales especies portadoras de oxígeno y nitrógeno, concretamente agua y amoníaco, dentro de los discos formadores de planetas?
- ¿Cómo se relacionan las estructuras físicas, tales como los gradientes de temperatura y las subestructuras en la densidad del polvo causadas por los procesos de crecimiento granular, con la formación y la química de moléculas comunes?

Esta Tesis

El Capítulo 1 de esta tesis ofrece una introducción general a la teoría de formación estelar y a los discos protoplanetarios, con énfasis en el proceso de evolución del polvo y los diferentes regímenes químicos dentro de los discos. El análisis se centra en dos discos protoplanetarios bien estudiados, TW Hya y HD 163296. Ambos objetos son excelentes laboratorios debido a su proximidad y sus brillantes y masivos discos. Esta tesis utiliza datos infrarrojos del *Telescopio Espacial Herschel* y datos (sub)milimétricos del Gran Conjunto Milimétrico de Atacama (ALMA por sus siglas en inglés). *Herschel* estaba equipado con un único espejo de 3.5 metros y tenía tres instrumentos a bordo que cubrían longitudes de onda desde $\sim 50 \mu\text{m}$ a $\sim 600 \mu\text{m}$. En este trabajo se usaron los datos del programa clave “Agua en las regiones de formación estelar con Herschel” (WISH, por sus siglas en inglés), tomados con el instrumento HIFI a bordo de *Herschel*. ALMA es un radiotelescopio que consta de sesenta y seis antenas con una resolución espacial y sensibilidad sin precedentes que se utilizó para observar tanto la emisión molecular como el espectro continuo de los dos objetos seleccionados.

El Capítulo 2 utiliza observaciones de ALMA a una longitud de onda de 1.3 mm para investigar dónde se encuentran los granos de aproximadamente 1 mm de tamaño en el disco alrededor de TW Hya. En los discos formadores de planetas, los granos pequeños ($\sim \mu\text{m}$) se unen y se convierten en granos más grandes (mm, cm y mayores) para finalmente formar planetas. Mientras que los granos pequeños con tamaños aproximados de μm están bien acoplados al gas, los granos más grandes se desplazan hacia el centro del disco debido a la fricción con el gas. Las observaciones muestran que los granos de tamaño milimétrico

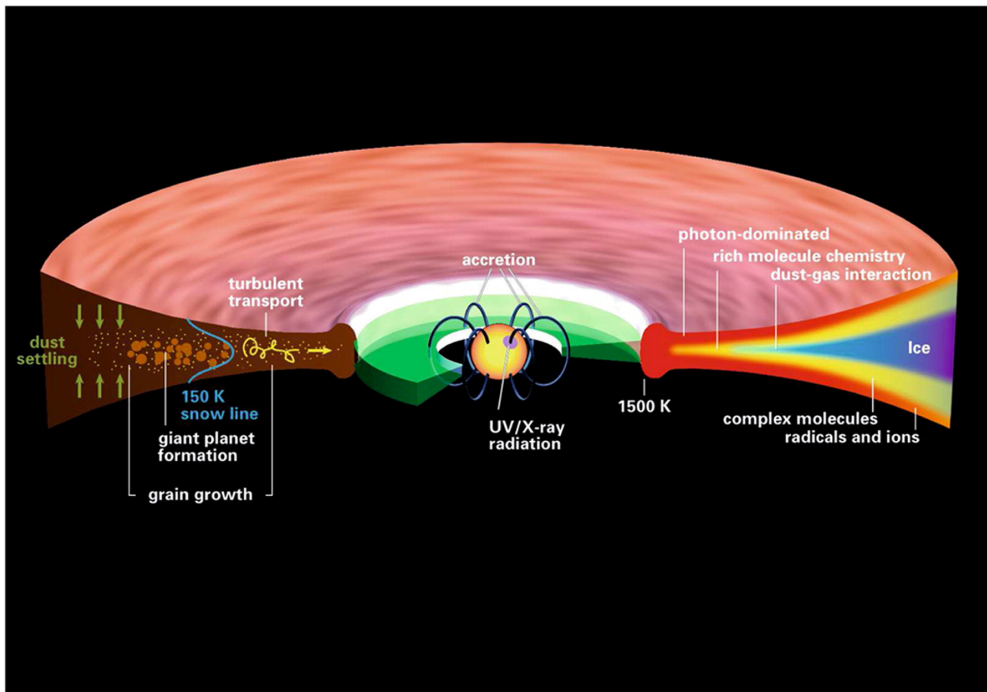


Figure 9.1: Caricatura de la evolución del polvo y las diferentes regiones químicas de un disco protoplanetario. Figura de Henning & Semenov (2013).

se encuentran hasta ~ 47 AU de la estrella central. A distancias más largas su cantidad disminuye rápidamente. Esta pronunciada caída se ha predicho, mediante cálculos teóricos, como consecuencia del crecimiento de los granos de polvo y su transporte en el disco. Sin embargo, para modelos de evolución de polvo realistas que son típicos de discos T Tauri, la extensión observada de los granos y su cantidad total son demasiado grandes para un disco de 8-10 millones de años de vida. Posibles explicaciones para esta aparente contradicción incluyen una masa y tamaño del disco inicial mucho mayor, una brecha en la densidad de polvo que detiene la migración radial del polvo de tamaño milimétrico abierta por un compañero planetario invisible o una sobreproducción local de granos de tamaño milimétrico generada por la presencia de granos cubiertos de hielo que crecen más eficientemente que los granos sin hielo en regiones donde el CO está congelado.

El Capítulo 3 presenta la primera detección de amoníaco en un disco formador de planetas. La línea $o\text{-NH}_3$ $1_0\text{-}0_0$ fue observada con el instrumento HIFI a bordo de *Herschel* junto con las líneas de emisión de $o\text{-H}_2\text{O}$ y $p\text{-H}_2\text{O}$ en el disco alrededor de TW Hya. Cuatro modelos diferentes para la distribución de estas moléculas fueron explorados, asumiendo que los hielos de agua y amoníaco se entremezclan y se liberan al medio gaseoso simultáneamente. Solo la distribución más compacta y decantada tanto del agua como del amoníaco en estado gaseoso, siguiendo la extensión radial de la emisión del continuo milimétrico de $r \lesssim 60$ AU, es consistente con la razón amoníaco/agua encontrada en el gas entre las estrellas de nuestra galaxia y cuerpos del Sistema Solar de $\sim 5\%$ - 10% . Otras configuraciones, a radios o alturas mayores, solo se pueden conciliar con los valores interestelares y del Sistema Solar si se invocan vías de formación adicionales para el amoníaco. La reserva de amoníaco y agua derivada de su estado gaseoso en cualquiera de estos modelos es solo una pequeña fracción de la reserva total, lo que indica que la mayoría de estas moléculas están contenidas en granos con hielo.

Se piensa que el gas frío de los discos formadores de planetas alberga una gran cantidad de especies portadoras de deuterio, como NH_2D . El Capítulo 4 analiza los datos de *Herschel* de la línea $o\text{-NH}_3$ $1_0\text{-}0_0$ y los datos de ALMA de la línea $p\text{-NH}_2\text{D}$ $1_0\text{-}0_0$ del disco alrededor de HD 163296. Ambas observaciones no pudieron detectar las líneas de emisión dado sus modestos tiempos de integración. Este Capítulo explora dos distribuciones radiales diferentes de $o\text{-NH}_3$ y $p\text{-NH}_2\text{D}$ en su estado gaseoso para poner límites en sus intensidades de línea y masas totales. Los límites superiores derivados para la masa total de $o\text{-NH}_3$ y $p\text{-NH}_2\text{D}$ en su estado gaseoso en este disco son diez veces inferiores a los valores en el disco de similar masa alrededor de TW Hya, de acuerdo al modelo preferido derivado en el Capítulo 3, asumiendo una razón $\text{NH}_3/\text{NH}_2\text{D}$ de un 10%. Esto sugiere que el disco alrededor de HD 163296 es pobre en NH_3 por un factor no menor a 5 en comparación con el disco alrededor de TW Hya. Otras especies portadoras de nitrógeno detectadas hacia estos discos muestran cantidades relativas diferentes a las encontradas para el amoníaco. Esto sugiere que la diferencia observada en la masa total de $o\text{-NH}_3$ en su estado gaseoso entre estos discos se debe a su vía de formación y no a una falta general de nitrógeno elemental.

El Capítulo 5 se enfoca en el análisis y caracterización radial de tres especies deuteradas simples en un disco formador de planetas. Las líneas de emisión de DCO^+ , DCN , y N_2D^+ se observaron y detectaron con ALMA en el disco alrededor de HD 163296. Este capítulo traduce el perfil de emisión radial de estas tres moléculas a densidades radiales bajo suposiciones que simplifican su cálculo. La emisión radial de DCO^+ puede ser reproducida por un modelo con tres regiones radiales consecutivas y diferentes abundancias constantes desde ~ 50 AU a ~ 316 AU con dos saltos radiales en ~ 118 AU y ~ 245 AU. Las dos primeras regiones radiales del modelo que mejor reproduce la emisión de DCO^+ se correlacionan

espacialmente con los modelos que mejor describen los perfiles de emisión radial de DCN y N_2D^+ . Esto puede interpretarse como un reflejo del hecho de que hay múltiples formas de inyectar deuterio en la química. Una de estas rutas es solo activada a temperaturas bajas y produce N_2D^+ ; la otra opera a temperaturas ligeramente más altas y produce DCN. DCO^+ se forma a través de ambas rutas. El origen de la tercera región de emisión DCO^+ a ~ 260 AU es incierto, pero podría estar correlacionado con temperaturas altas permitiendo que el CO se evapore a distancias lejanas, donde puede reaccionar para formar DCO^+ .

El Capítulo 6 trata de reproducir la emisión de DCO^+ presentada en el Capítulo 5 usando una sencilla red de reacciones químicas, pero un poco más sofisticada que el tratamiento del Capítulo 5, para la formación de DCO^+ en ambientes fríos y un modelo paramétrico para su formación en ambientes más cálidos. La emisión de DCO^+ puede ser reproducida por un modelo con una abundancia de CO de 2×10^{-7} , en regiones donde la temperatura del gas excede los 19 K, y una contribución de la formación de DCO^+ en ambientes más cálidos del 20% en regiones donde ambas vías de formación están activas. A mayores distancias de la estrella central, la extensión y forma de la emisión de DCO^+ puede reproducirse considerando un gradiente de temperatura similar a los predichos por los modelos de evolución y crecimiento de los granos de polvo en presencia de migración radial de los granos de tamaño milimétrico hacia el centro del sistema.

Conclusiones generales

El análisis presentado en los Capítulos 3 & 4 proporciona una respuesta a la primera pregunta que esta tesis trató de responder. El agua y amoníaco en estado gaseoso alrededor de TW Hya siguen la estructura espacial de sus reservas de hielo. Estas reservas se encuentran atrapadas en cuerpos grandes que se han asentado y desplazado hacia el centro del sistema. La ubicación de este reservorio es determinada por la migración radial de los granos de polvo que han experimentado algún crecimiento, y que posteriormente se incorporaron en rocas más grandes. Observaciones de NH_2D y HDO hacia TW Hya y HD 163296 podrían confirmar este escenario. Los Capítulos 5 & 6 sacan conclusiones sobre el efecto de las estructuras físicas del disco en la distribución de moléculas simples. Especies sensibles a la temperatura, como DCO^+ , pueden rastrear las subestructuras en el perfil de temperatura de los discos formadores de planetas. Si bien el factor más importante en la estructura de la temperatura del disco es la iluminación por la estrella central, las subestructuras producidas por la evolución y crecimiento de los granos de polvo pueden modificar el perfil térmico del disco. Especies como DCO^+ se pueden utilizar para rastrear indirectamente el impacto de la evolución y el crecimiento de los granos de polvo sobre la morfología del disco. El proceso inverso, es decir, el impacto de la ubicación de moléculas simples en la evolución del polvo, es estudiado en el Capítulo 2 comparando la forma de la emisión del continuo milimétrico y la ubicación de la *snowline* de las principales especies moleculares como por ejemplo el CO. Nuevos instrumentos de luz infrarroja y visible en instalaciones tales como el futuro Telescopio Espacial James Webb (JWST, por sus siglas en inglés) o el Telescopio Extremadamente Grande (ELT, por sus siglas en inglés) podrán observar moléculas clave en ambientes cálidos dentro del disco, características del hielo que cubre a los granos de polvo e imágenes espacialmente resueltas de luz en dispersión permitiéndonos distinguir los diferentes escenarios explorados en esta tesis. Observaciones de múltiples discos protoplanetarios podrían ayudar a promediar las diferencias entre fuentes individuales y dilucidar las tendencias generales en su estructura y evolución, conduciendo finalmente a una comprensión integral de los procesos involucrados en la formación de estrellas y planetas.

Curriculum Vitae

I was born in Santiago de Chile on a very hot day (even for Chilean standards) in the summer of 1990. I lived with my grandparents, my mother and my little brother in a quiet residential area. A few years later I moved to a countryside area very close to the city known for its excellent wines. For as long as I can remember my mother encouraged me to explore her artistic and scientific interests: music and astronomy. I started playing piano when I was 5 years old and I even briefly attended the Music Conservatory of the Pontificia Universidad Católica. At first, the piano and I were not the best of friends. Today, playing the piano is a wonderful gift that I have learned to appreciate and love. Knowing how to express yourself through a musical instrument is one of the greatest joys in life. In a very similar fashion, my mother's obsession with stars and the Universe (and in particular Carl Sagan's COSMOS) started rubbing off on me at a very young age. The images of the tilted rings of Uranus and the huge rings of Saturn dazzled me. As a fully fledged nerd teenager I participated in math tournaments and attended public talks on physics and astronomy during my high school years. I enrolled in the bachelor programme of Science at Universidad de Chile and started my studies in 2008. This programme is designed to provide a strong foundation on math and physics, as well as a broad variety of subjects, ranging from economy to chemistry, during its first two years. My first real experience with astronomy came around May 2010 during my first astrophysics course, *Astronomía Experimental*, where I got to operate the GOTO telescope at the Cerro Calán Observatory in Santiago. The pixelated image of Jupiter and its Galilean moons is engraved in my memory.

After finishing my bachelor's degree I was admitted to the master programme of Astronomy, at the same University, to work under the supervision of Prof. dr. Simón Casassus. During this time I was teaching assistant of two of my favorite physics topics: relativity and quantum mechanics. I also gave talks for the general public at the Cerro Calán Observatory. My master's research project consisted in implementing and designing an algorithm using principal component analysis (PCA) to improve the classical spectral deconvolution imaging (SDI) technique. This technique is used to directly image the circumstellar material and forming exoplanets around young stellar objects in the infrared regime. I devised a selection criterion that resulted in roughly twice the amount of throughput in comparison to the classical approach. In early 2013, I was invited to the PhD application round at Leiden University where I was offered a position to work with Prof. dr. Michiel Hogerheijde on the radial and vertical distribution of the gas and dust content of planet forming disks. During my PhD I analyzed data from the *Herschel Space Telescope* and the Atacama Large (sub)Millimeter Array (ALMA) toward two well-known protoplanetary disks around HD 163296 and TW Hya. My PhD dissertation focused on the link between the morphology of key gas-phase molecular species and grain evolution processes, probed by continuum observations in the (sub)millimeter regime, towards these two sources.

During my years in Leiden I got to travel to wonderful places to present my research

and I met many young and talented scientists. I participated in the traditional dutch borrel committee where I enjoyed many lively conversations with fellow PhDs and post-docs. Next year, I will continue my career at the University of Kagoshima in Japan as a specially appointed research staff for the NAOJ Chile Observatory working with Prof. dr. Shigehisa Takakuwa. This new project aims to use ALMA to understand the processes involved in the formation of planet forming disks which are still embedded in an envelope of gas and dust.

Acknowledgments

I apologize in advance if I forget to thank someone in specific, since I met so many wonderful and interesting people throughout this journey. Although so many of you have contributed in different ways to the completion of this dissertation I would like to start with the most obvious and sometimes (surprisingly) overlooked individual: my supervisor. I was truly lucky to have Michiel guide me through my PhD. You perfectly fit my archetypal view of a mentor. Thank you for your patience, for answering three (or many more) times the same question, and for never undermining my confidence. Without your constant support and understanding this would have seemed an impossible task.

Irene, Matteo, Marco, Berenice, Thanja, Silvia and Nicola were among the first people that welcomed me to Leiden. I enjoyed our baking club meetings and our constant complaining about the weather. Tiffany, my first office mate, thank you for your guidance during my chaotic first months. I also had the pleasure of meeting Nienke during my first year in Leiden. You have proven to be a valuable friend and I thank you for your support and unconditional friendship. I hope we continue to visit each other wherever life take us. Emanuelle, thanks for keeping things light and your funny but inappropriate jokes.

During my second year I found a very special group of people. We quickly bonded and we have shared numerous adventures together. Most memorably, the unforgettable trip to Barcelona and the NOVA school. Mike and Charlotte, I will miss our chats about cats and what is truly British. Thank you so much for decorating and lending us your tandem. Mieke, keep being your weird self, I will send goats from Japan. Aayush, we should keep playing tennis. Eleonora, whenever I drink a cappuccino around 6 pm I will think of you. Andrew, we will surely plan a trip to kiwi-land and we hope you are there to guide us. Chris and Zoe, we have managed to be away for all your pumpkin carving sessions, I hope we can be there for the next one. I also got to know Gabi with whom I share the passion of running. Gracias por todo pollita, estoy seguro que nos veremos en un futuro no muy distante.

My stay in Leiden would not have been complete without sharing an apartment in Kruitschip with two very special Danes. Ann-Sofie, thank you for your kindness. I love to hang out with you and freely be as geeky as possible, either discussing the Potter world or watching Love Actually. Special thanks to Jeroen and his knowledge about beer and dutch grammar. Christian, your enthusiasm, at times extreme, has impregnated our community. Thanks for all the lectures about bow ties and what is proper. I wish you and Iris the best in this new adventure and I hope we never lose touch.

As the saying goes "los chilenos están en todos lados". Seba and Javi, muchas gracias por su incondicional amistad. Javi extrañare tus noches de locura, nuestras selfies y cuchicheos. Seba, gracias por los incontables debates y conversaciones que pretendían arreglar el mundo. Pablo, gracias por los puchos y las noches de tertulia. Francisco, mi fuente inagotable de tabaco muchas gracias por la buena onda, te deseo éxito en todo lo

que tu y Nora se propongan. Pedro y Santi, mis queridos secuases borreleros, gracias por las parrilladas y por las lecciones de mexicano. Fran, aunque llegaste tarde fue como si siempre hubieras estado aquí, dejamos el borrelito en buenas manos. Yanett, Max, Cristi, Claudio, Cristóbal, Dani y toda la comunidad latina me han hecho sentir en casa.

A special thanks to our small (but growing) research group, Mason, Eva, Leon and Jeroen, for keeping up our morning meetings fun and interesting. A special thanks to Leon who proofread my samenvatting. Mason and Allie, sharing a traumatic experience is among one of the few things that create an unbreakable bond. I think the agony of taking that train back to Munich qualifies as such. We will be waiting for your visit (and this time having a selfie stick will be a prerequisite). Allison and Alex, thanks for your support, for never having a boring conversation and for the series & movies recommendations. Now you enter a new chapter in your lives and I could not be happier for both of you.

My dear Eva, I was trying to pick just one moment with you to immortalize in these pages, but there are so many of them. Instead, I just want to thank you for all the support and love you have given me. I have seen your PhD journey from the beginning and I have had the pleasure of sharing it with you. I hope we continue making memories for a life time. A special thanks to Niels for sharing my passion for horror movies when no one else did. Mi amorosa Heather, las palabras de gratitud sobran. Personas como tu hay pocas, con una sonrisa bordada en la cara frente toda adversidad. Gracias por ser mi amiga y confidente, espero que los años nos traigan mejores momentos, mas risas y muchos gokus en el cielo. Without my family I would have never been where I am today. Gracias a mis abuelos, que desde muy pequeño, han reafirmado mi confianza he impulsado a soñar en grande. Mama, eres sin lugar a duda la coautora invisible de estas páginas, gracias por creer en mi, cultivar mi curiosidad y ser el sustento que siempre has sido.

Finally, I want to thank my husband Wijnand who designed the cover of this thesis and translated my summary. You have endured my ups and downs. You have watched me closely and have supported every decision I have made. Coming home to you (and Shaffy) is an instant stress-cure. You and your family, now also my own, have received me with open arms and I am very grateful to have found you. This is only the start of our adventure, and knowing I can rely on you makes me stronger. Thank you for your love mi varkentje, ik houd van jou.